X-ray radiographic and tomographic investigations of cycled lithium ion batteries

vorgelegt von
Master of Science
Fu Sun
geb. in Shandong

von der Fakultät III – Prozesswissenschaften der Technischen Universität Berlin
zur Erlangung des akademischen Grades

Doktor der Naturwissenschaften

-Dr. rer. nat.-

Genehmigte Dissertation

Promotionsausschuss:

Vorsitzender: Prof. Dr. Walter Reimers
Gutachter: Prof. Dr. John Banhart
Gutachter: Dr. Yan Lu

Tag der wissenschaftlichen Aussprache: 3. February 2017

Berlin 2017

Abstract

Lithium ion batteries (LIBs) have become the predominant power supplies in portable electronic devices such as cell phones, laptops and tablets. They are regarded as promising candidates to power future electric vehicles and to store the intermittent and fluctuating energy harvested from solar and wind sources. Unfortunately, the current LIB technology fails to meet the growing energy demand required by the automotive industry and operators of power stations. In addition, safety concerns prevent a simple scale-up from the currently small scale LIBs to future large-scale LIBs. Future LIB technology will undoubtedly rely on a sound understanding of underlying work principles of current LIBs. In this dissertation, X-ray imaging both utilizes X-ray tube and synchrotron sources is employed to investigate the underlying reactions of operating LIBs.

Firstly, lithium dendrites which are in-homogeneously deposited/stripped on/from the surface of lithium (Li) electrodes during cycling are characterized. The morphological evolution of lithium dendrites is investigated. In addition, it is observed that both lithium dissolution during lithium stripping and lithium deposition during lithium plating contribute to the formation of the porous lithium interface (PSI). Secondly, the commercialized trilayer Celgard® 2325 separator is investigated during battery cycling. It is observed that the trilayer separator can delaminate under mechanical forces arising from growing lithium microstructures. In addition, partial melting of the separator resulting from an internal short circuit (ISC) is demonstrated. Thirdly, gas development inside an operating LIB is investigated. It is found that gas is preferentially generated in regions close to the separator. Moreover, it is observed that gas generation is a continuous process extending over many cycles. Fourthly, degradation of LIBs based on Si particles has been studied. The volume expansion during lithiation and volume contraction during delithiation of Si particles have been observed. It is found that the distribution of fractured Si particles is heterogeneous. Furthermore, electrochemical deactivation of originally electrochemically active Si particles is observed. Moreover, electrochemically inactive Si particles are believed to decrease the energy density of an LIB. Fifthly, different (de)lithiation behaviors of Sn particles are presented. In addition to the conventional “core-shell” reaction mode, an unusual fracture of a Sn particle is observed during cycling. It is observed that some Sn particles need some “incubation” time to become electrochemically active.

Kurzfassung

Lithium-Ionen-Batterien (aus dem englischen: Lithium ion batteries LIBs) haben sich als vorherrschende Energiequelle in portablen elektronischen Geräten, wie zum Beispiel Smartphones, Laptops und Tablets, etabliert. Sie werden als vielversprechende Möglichkeit betrachtet, zukünftige elektrische Autos anzutreiben als auch überschüssige Energie aus Solar- und Windkraftanlagen zwischenzuspeichern. Die heutige LIB-Technologie schafft es derzeitig nicht den technischen Anforderungen der Automobilindustrie und der Energiewirtschaft gerecht zu werden. Hinzu kommen Sicherheitsbedenken großvolumige LIBs zu betreiben. In der Zukunft wird diese Technologie zweifelsohne auf dem fundierten Verständnis der zugrunde liegenden Prozesse derzeitiger LIBs basieren. In dieser Dissertation werden bildgebende Verfahren mittels einer kommerziellen Röntgen-CT Anlage als auch mittels Synchrotron Röntgenstrahlung angewendet, um die grundlegenden Reaktionen in LIBs während des Be-und Entladens zu untersuchen.

Im ersten Teil wurden Lithium-Dendrite charakterisiert, die während des Zyklierens inhomogen auf der Lithiumelektrodenoberfläche abgeschieden und abgetragen werden. Die morphologische Entwicklung der Lithium-Dendrite wurde dabei untersucht. Es wurde dabei beobachtet, dass sowohl das Auflösen während des Abtragens als auch die Beschichtung während des Abscheidens zur Bildung einer porösen Lithiumoberfläche beitragen. Im zweiten Teil wurde ein kommerziell erhältlicher dreilagiger Celgard® 2325 Separator während des Zyklierens untersucht. Dabei wurde beobachtet, dass der dreilagige Separator durch die mechanischen Kräfte der anwachsenden Lithiumstrukturen delaminieren kann. Zusätzlich wird ein teilweises Schmelzen des Separators durch einen internen Kurzschluss beobachtet. Der dritte Teil widmet sich der Gasentwicklung in LIBs während des Zyklieren. Es konnte gezeigt werden, dass Gas überwiegend in Separator-nahen Regionen erzeugt wird. Die Gasentstehung wird als kontinuierlicher Prozess charakterisiert, der sich über viele Zyklen erstreckt. Im vierten Teil wurde die Degradation von Silizium-basierten LIBs studiert. Die Expansion während der Lithiierung und die Kontraktion während der Delithiierung wurden im Detail quantitativ analysiert. Die Reaktion der Siliziumpartikel ist dabei räumlich heterogen, das heißt, die Partikel reagieren individuell auf verschiedene Weise und zu verschiedenen Zeitpunkten. Darüber hinaus wurde eine elektrochemische Deaktivierung von ursprünglich aktiven Partikeln beobachtet, was darauf hindeutet, dass elektrochemisch inaktive Partikel die Energiedichte der LIBs entscheidend verringern. Schließlich, im fünften Teil, wird das (De-)Lithiierungsverhalten von Sn-Partikeln untersucht. Zusätzlich zur konventionellen „core-shell“ Reaktion, wurdd ein ungewöhnliches Verhalten bei der Degradation der Sn-Partikel während des Zyklierens beobachtet: Unter anderem hat sich gezeigt, dass einige Sn-Partikel eine gewisse „Inkubationszeit“ benötigen um elektrochemisch aktiv zu werden.

Contents

1 Introduction

1.1 Introduction to lithium ion batteries

Since the successful commercialization by SONY in 1991 and a joint venture of Asahi Kasei and Toshiba in 1992, the lithium ion battery (LIB) has penetrated ubiquitously into our daily life [1]. The predominant reason that LIB can revolutionize portable energy storage technology is due to its higher energy density compared with other battery systems such as lead-acid and Ni-MH (nickel-metal hybride), as shown in Fig. 1a [2]. In contrast to other battery systems, LIBs do not suffer from the memory effect problem. In addition, LIBs have voltages nearly three times these of typical Ni-based batteries. The high single-cell voltage obtained from a LIB reduces the number of cells required in a battery system. Finally, the self-discharge rate in LIBs is very low (< 5% per month) compared with Ni-based batteries (~ 20-30% per month).
Moreover, in 2005, SONY launched the Nexelion hybrid LIB, which further increased the battery energy density by 30% compared to conventional LIBs [3]. With such high energy density, coupled with their long cycle life and rate capability, LIBs are now considered promising candidates to power the upcoming electric vehicles (EVs) or plug-in hybrid electric vehicles (PHEVs) [4]. Another important potential market for LIBs is to store intermittent and fluctuating green energy supplies from renewable sources such as solar and wind sources [5]. From Fig. 1b, one can observe that the market for various kinds of LIBs has expanded significantly from 2000 to 2015 [6] and this trend is going to continue.

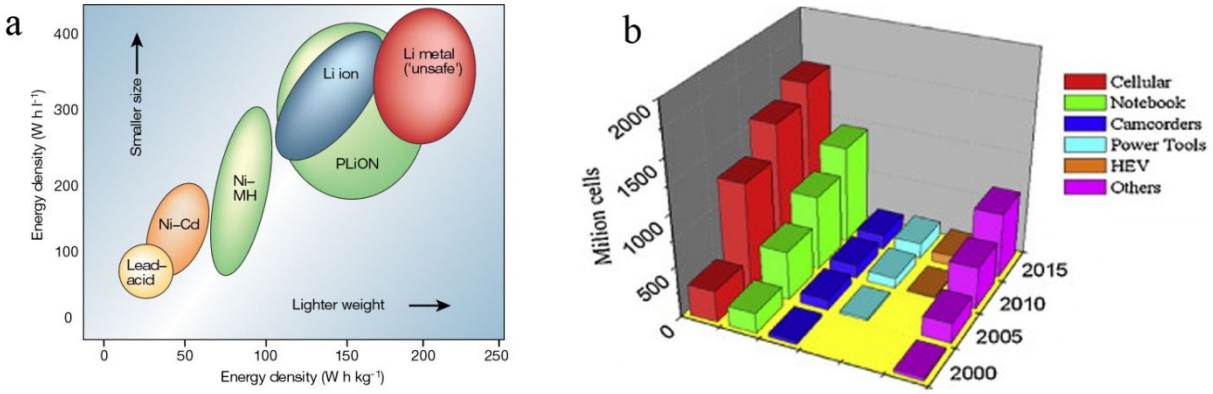

Fig. 1 a) Comparison of different battery types in terms of energy density. Reprinted with permission from Ref. 2. b) Evolution of the lithium ion battery sale in various markets. Reprinted with permission from Ref.6.

A more detailed historical evolution and present review of LIBs can be found elsewhere [2, 6]. Typically, a basic LIB consists of a cathode (positive electrode), an anode (negative electrode), electrolyte containing lithium ions and a separator isolating the anode from the cathode. The components of the first commercialized LIB are schematically illustrated in Fig. 2 [7]. During

discharge and charge, lithium ions shuttle between the anode and the cathode while electrons are transported through the external circuit. The driving force for discharge of LIBs is the different electrochemical potential μ_A and μ_C of the anode and the cathode. The open-circuit voltage of a cell can be expressed by [7]:

$$V = \frac{\mu_A - \mu_C}{e} \tag{1.1}$$

More details of the open circuit voltage with relation to the Fermi energy level and Gibbs free energy of electrde materials can be found in previous reports [2, 8]. The effect of lithium ion tranportation behavior within electrode materials on open circuit voltage can also be found in previous investigations [9, 10].

During the charging process, the two electrodes are connected externally to an electrical supply. The electrons are forced to be released from the cathode and transported externally to the anode side. Simultaneously, lithium ions move internally from the cathode to the anode through the electrolyte. Hence, the external energy is electrochemically stored in the battery in form of chemical energy in both the anode and cathode [5]. During the discharge process, electrons move from the anode back to the cathode through external load to do work and lithium ions move through the electrolyte. The stored chemical energy inside the battery is released via electrochemical reactions at two electrodes.

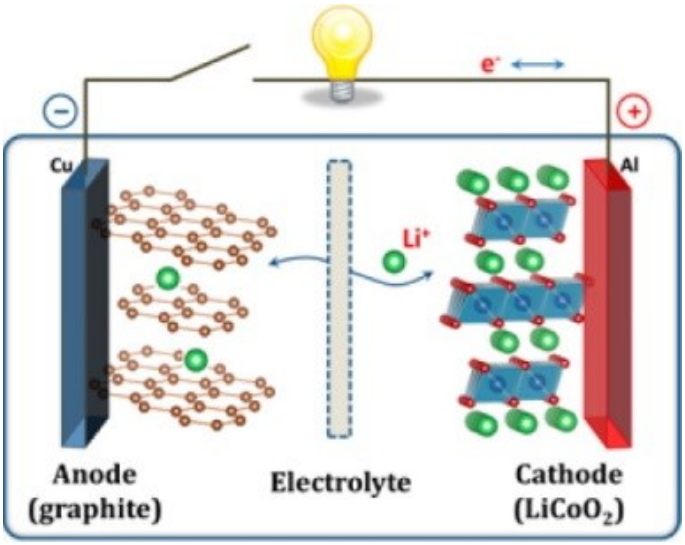

Fig. 2 Schematic illustration of the first lithium ion battery. Reprinted with permission from Ref. 7.

The amount of electrical energy that can be converted by the electrochemical reaction of LIB electrodes during discharge can be expressed either per unit of weight (Wh/kg) or per unit of volume (Wh/l). This electrical energy that a battery can deliever is a function of the open-cell potential (V) and specific capacity (Ah/kg or mAh/g) [2]. The specific energy (Wh/kg) can be obtained by multiplying the specific capacity with the operating battery voltage. The specific capacity measures the amount of charge that can be reversibly stored/released per unit mass. It is

closely related to the number of electrons transferred during electrochemical reactions and the atomic weight of the electrode material. The theoretical capacity of electrode materials can be estimated based on electrochemical reactions. For example, the reversible electrochemical reaction of a graphite anode LIB is [6]:

$$Li^+ + e^- + 6C \leftrightarrow LiC_6 \tag{1.2}$$

The theoretical specific capacity (mAh/g) of a graphite anode can be estimated as:

$$C_{specific} = xF/nM = 1 \times (96485\ C/mol)/6 \times (12g/mol) = 372\ mAh/g \tag{1.3}$$

where x is the number of electrons transferred in formula (1.2), F = 96485 C/mol is Faraday's constant, n is the number of moles of the chosen graphite anode taking place in the reaction and M is the molecular weight of graphite. In practice, to evaluate the specific capacity of a battery, not only integration of cathode and anode materials have to be taken into consideration, but also other essential componets such as binders, conductive enhancers, separators, electrolytes, current collectors, cases, tabs as well as battery management systems. As a result, the practical energy density is always less than that estimated one based only on battery chemistry.

Cyclability of a battery measures the reversibility of lithium ion insertion and extraction processes in terms of the number of charge and discharge cycles before a battery fails or can no longer sustain devices [5]. Specifically, the cycle life of LIBs is closely affected by the state of charge (SoC) and depth of discharge (DoD) as well as operating temperature and current rate. It has been demonstrated that the cycle life can be enhanced by a shallow DoD and a lower SoC [11].

Finally, abuse tolerance of a Li-ion battery is a critical requirement for practical applications expecially for high-energy and high-density EVs and PHEVs. Before commercialization, mechanical, thermal and electrical abuse evaluations have to be conducted on prototypes of Li-ion batteries to evaluate abuse tolerance. Typically, mechanical abuse evaluation includes roll-over, nail penetration, mechanical shock and drop and immersion in water tests. The thermal abuse evaluation includes thermal stability test, radiant heat test, overheat test and extreme cold test. The electrical abuse evaluation includes short circuit, overcharge and over-discharge tests. Those abuse tolerance tests are extremely import before final commercializaion. Actually, the fire catastrophe of the Boeing 787 Dreamliner is reported to have resulted from short circuits of employed LIBs [12].

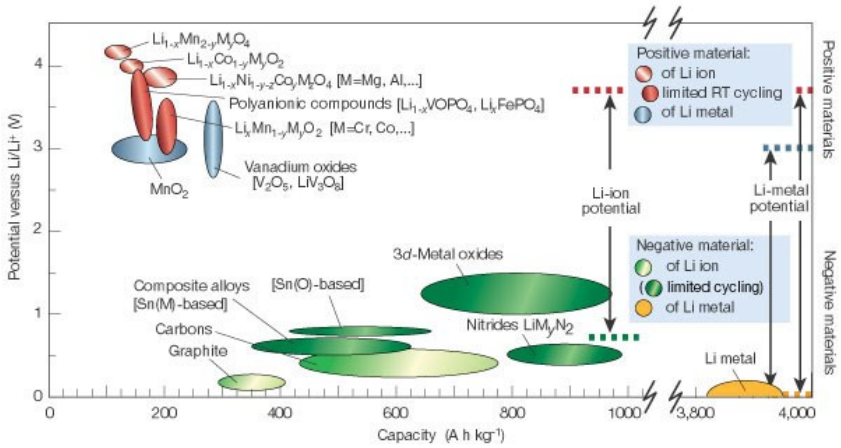

Fig. 3 Voltage versus capacity for negative and positive electrode materials presently used or under condideration for the next-generation of LIBs. Reproduced with permission from Ref.[2]

The voltage range and capacity of different electrode materials are shown in Fig. 3. In the following, the focus will be on a brief introduction to cathode, electrolyte, anode and separator, followed by an introduction of primary studies of the present dissertation.

1.1.1 Cathode material

Generally speaking, cathode materials are typically oxides of transition metals, which can experience oxidation to higher valences when lithium is removed during charge [13]. While oxidation of the transition metal can conserve charge neutrality in the compound, large compositional changes can lead to phase changes. As a result, cathode materials have to be crystal-structurally stable over wide ranges of composition. During discharge, lithium is inserted into the cathode along with electrons from the anode to reduce the transition metal ions in the cathode to a lower valence [14]. The rate of this oxidation and reduction of cathode materials as well as the rate of transporation of lithium ions in the electrolyte control the maxium discharge current. It has to be noted that exchange of lithium ions between cathode and electrolyte occurs at electrode-electrolyte interfaces, so cathode performance depends directly on electrode architecture and morphology as well as on electrochemical properties of cathode materials[14]. From the perspective of materials, there are a number of candidates that have been investigated as cathode materials for LIBs. The cathode materials can be categorized based on their voltage versus Li/Li^+, namely [5]: TiS_2 and MoS_2 with 2-D layered structure (~2 Volt); MnO_2 and V_2O_5 (~3 Volt); $LiCoO_2$, $LiNiO_2$ with 2-D layered structure and 3-D spinel $LiMn_2O_4$ and olivine $LiFePO_4$ (~4 Volt); olivine $LiMnPO_4$, $LiCoPO_4$ and $Li_2MxMn_{4-x}O_8$ (M=Fe, Co) spinel 3-D structure (~5 Volt). Typically, high cathode voltage is desirable for electrode materials because the energy density is proportional to cell voltage. Currently, $LiCoO_2$ and $LiFePO_4$ are most widely used in commercial LIBs because of their excellent cycle life and capacity retention. However, investigation of cathode materials is not the focus in the current dissertation.

1.1.2 Electrolyte

The electrolyte is crucial for LIBs. First of all, the electrolyte has to be chemically and electrochemically stable to withstand a redox environment at both the cathode and anode sides besides possessing high ionic conductivity for lithium ions. In addition, the electrolyte has to be inert and stable in an acceptable temperature range. A detailed description of the potential window of the electrolyte with respect to the electrochemical potentials of electrodes can be found in previous reports [15].

In commercial Li-ion batteries, typically a liquid electrolyte is a solution of lithium salts in organic solvents. However, it should be noted that there are other types of electrolyte such as ionic electrolytes and inorganic solid electrolytes [16]. Most of the existing organic liquid electrolytes can potentially catch fires under conditions of thermal runaway or short circuit due to the volatile and flammable nature of the solvents. On the one hand, polar aprotic organic solvents such as carbonate solvents with a high dielectic constant are selected to solve lithium salts at a high concentration (normally 1 M) [5]. On the other hand, solvents with a low viscosity and low melting point are necessary to meet the requirement for high ionic mobility during cycling. Until now, various organic solvents have been explored for battery usage such as dimethyl carbonate, diethyl carbonate, ethyl methyl carbonate, ethylene carbonate, etc [17]. In addition, many lithium salts have been investigated such as $LiPF_6$, $LiBF_4$, $LiAsF_6$, $LiClO_4$, etc [18]. Currently, the widely used electrolyte for LIBs is a lithium hexafluorophosphate solution ($LiPF_6$): 1 M $LiPF_6$ in EC/DMC (ethylene carbonate and dimethyl carbonate, v/v=50/50) or 1M $LiPF_6$ in EC/EMC (ethylene carbonate and ethyl methyl carbonate, v/v=50/50), commercialized by different companies [5]. These electrolytes offer reasonable stability over a wide range of potential. Nevertheless, during cycling of LIBs containg these electrolytes, a SEI (solid electrolyte interface) forms from the side reactions of the electrolyte with the electrodes [19]. Meanwhile, a significant amount of gas is generated [20]. The generated gas can cause an internal pressure build-up and even result in severe gas leakage [21].

Various characterization tools have been employed to investigate the decomposition of electrolyte such as gas chromatography, a flame ionization detector and a thermal conductive detector [18, 22]. Until now, the decomposition of solvent and lithium salts during battery operation has been thoroughly studied. In the following, the decomposition of EMC, DMC, EC and $LiPF_6$ salt will be presented.

Reduction of ethyl methyl carbonate (EMC) following one-electron reduction:

$$CH_3CH_2O(C{=}O)OCH_3 + e^- \rightarrow CH_3CH_2O(C\bullet - O^-)OCH_3 \quad (1.4)$$

Then $CH_3CH_2O(C\bullet - O^-)OCH_3$ reacts with Li^+ to produce CH_3CH_2OLi according to:

$$CH_3CH_2O(C\bullet - O^-)OCH_3 + e^- + 2Li^+ \rightarrow LiO(C{=}O)CH_3 + CH_3CH_2OLi \quad (1.5)$$

Alternatively, a two-electron reduction process can occur as for dimethyl carbonate (DMC):

$$CH_3OCO_2CH_3 + 2e^- + 2\,Li^+ \rightarrow Li_2CO_3\downarrow + C_2H_{6(g)}\uparrow \quad (1.6)$$

Reduction of ethylene carbonate (EC) involves:

$$(CH_2O)_2CO + 2e^- + 2Li^+ \rightarrow Li_2CO_3\downarrow + C_2H_{4(g)}\uparrow \quad (1.7)$$

Or alternatively:

$$(CH2O)_2CO + 2e^- + 2Li^+ \rightarrow (CH_2OCO_2Li)_2\downarrow + CH_2{=}CH_{2(g)}\uparrow \quad (1.8)$$

The $LiPF_6$ salt dissociates into LiF and the lewis acid PF_5:

$$LiPF_6 \leftrightarrow LiF + PF_5 \quad (1.9)$$

or a Li^+ and anion PF_6^- as below:

$$LiPF_6 \leftrightarrow Li^+ + PF_6^- \quad (1.10)$$

The dissociated lewis acid PF_5 can react with H_2O:

$$PF_5 + H_2O \rightarrow 2HF + POF_3 \quad (1.11)$$

$$PF_5 + H_2O \rightarrow PF_4OH + HF \quad (1.12)$$

The Lewis acid PF_5 can also react with dialkylcarbonate to form a variety of decomposition products [23].
Apart from these extensive characterizations of decomposed products by compositional characterizations, neutron radiography imaging was also employed to investigate gas generation and movement inside LIBs [20]. Unfortunately, radiographic imaging always yields two-dimensional (2D) information only, which prevents us from further comprehending gas evolution kinetics in its inherent three-dimension (3D) state and from further quantitatively analyzing its complex evolution. In the current dissertation, section 2.3 presents a detailed study of three-dimensional gas evolution in an operating LIB using non-destructive synchrotron X-ray tomography.

1.1.3 Anode material

Anode materials have been extensively investigated and there are many different materials and candidate materials. Different anode materials exhibit different electrochemical performance such

as cyclability, current rate and energy density. From the material point of view, there are basically three types of materials based on their reaction types with Li [4, 24, 25]:
1, Li intercalation/de-insertion materials such as carbon-based materials (porous carbon, carbo nanotubes and graphene) and TiO_2;
2, alloying/de-alloying systems such as Ge, Sn, Si Al, Bi and SnO_2;
3, conversion materials such as transition metal oxide materials (Mn_xO_y, NiO, Fe_xO_y, CuO, Cu_2O and MoO_2), metal sulphides, metal phosphides and metal nitrides (M_xX_y, here X= S, P, N).
Since the first commercialization of carbonaceous anodes, carbon is still dominant in commercial LIBs due to its excellent cycle performance. Graphitic carbon with a layered structure can effectively store and release lithium ions from its lattice space, resulting in excellent cyclability. However, carbon anodes have been approaching their theoretical capacity of 372 mAh/g over the past two decades of development. During the search for high energy density anode materials, conversion materials and alloy materials have been discovered [26, 27]. In the following section, we will mainly focus on the alloying/de-alloying anode materials as they normally possess higher energy density than conversion materials, specifically, tin and silicon. But before that, lithium metal as an anode material for LIBs is briefly reviewed and discussed.

1.1.3.1 Lithium anode

The motivation for using lithium metal as anode is because lithium is the most electronegative (-3.04 V versus standard hydrogen electrode) and the lightest (equivalent weight M = 6.94 g/mol, and specific gravity ρ = 0.53 g/cm^{-3}) metal, thus facilitating the design of storage systems with high energy density (theoretical capacity is 3860 mAh/g) [28]. The usage of lithium metal was first demonstrated in the 1970s in primary (non-rechargeable) lithium cells [29]. In 1972, Exxon embarked on a large project using TiS_2 as the positive electrode, lithium metal as the negative electrode in a rechargeable lithium cell [30]. However, they soon encountered the disadvantages of a lithium metal/liquid electrolyte combination: the uncontrolled growth of dendritic lithium microstructures during each discharge/charge cycle as shown in Fig. 4a. The electrochemically generated lithium microstructures such as dendrites, fibers and moss during inhomogeneous lithium stripping/plating results in an internal short circuit leading to battery failure [31]. A review of lithium dendrite formation can be found elsewhere [32]. To circumvent the safety issues associated with the usage of lithium metal, an alternative approach of substituting metallic lithium by a insertion material was proposed, which led to the discovery of the highly reversible, low-voltage Li intercalation-deintercalation carbonaceous material as schematically shown in Fig. 4b [33].

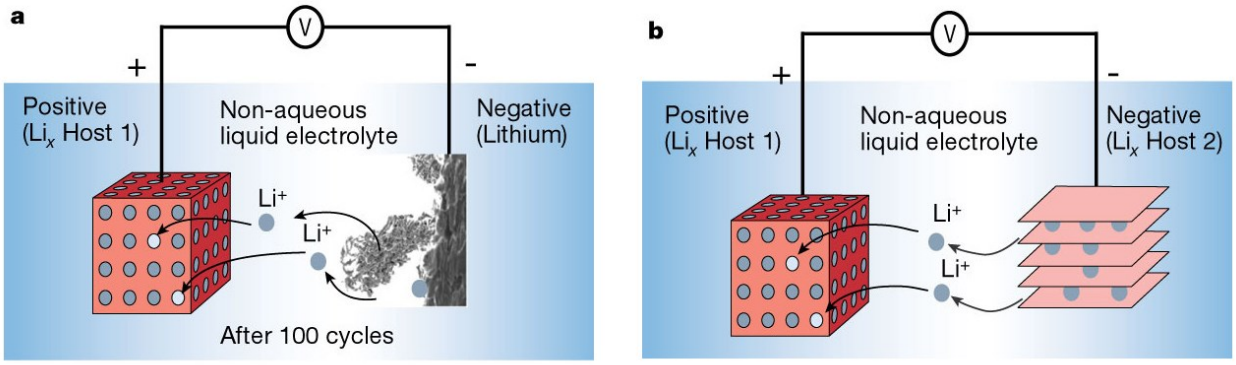

Fig. 4 Schematic illustration of lithium batteries. a) lithium dendrite growth during cycles. b) proposed approach of using an intercalation-deintercalation host material as a negative electrode. From ref.[2]

Recently, metallic lithium has again attracted research attention from all over the world because of its potential use in next-generation technologies such as Li-S and Li-O_2 batteries. Various characterization tools such as optical microscopy [34], atomic force microscopy (AFM) [35], scanning electron microscope (SEM) [36], transmission electron microscopy (TEM) [37], nuclear magnetic resonance (NMR) [38] and magnetic resonance imaging (MRI) [39] have been employed to understand the growth of the lithium microstructure (LmS) in lithium-ion batteries. Meanwhile, different strategies such as employing Li surface coating [40], additives [41], polymer- [42] and/or inorganic-based [28] electrolytes and employing different electrode/cell configurations [43] have been adopted to reduce and/or control the growth of lithium microstructures during cycling. Despite these intensive efforts, a fundamental understanding of the underlying evolution mechanisms remains elusive. Herein, in section 2.1, synchrotron in-line phase contrast X-ray tomography was employed to investigate the morphological evolution of electrochemically deposited/dissolved lithium microstructures non-destructively. For the first time, we present a 3D characterization of electrochemically stripped Li electrodes with regards to electrochemically plated lithium microstructures. We also clarify fundamentally the origin of the porous lithium interface growing towards Li electrodes.

1.1.3.2 Silicon anode

Since Dey *et al*. demonstrated in 1971 that Li metal can electrochemically alloy with other metals such as Sn, Pb, Al, Zn, Si, etc. at room temperature, Li alloying/de-alloying materials have been intensively investigated during the past few decades [44]. Among various alloying partners for Li, Si has been considered as one of the most promising candidates for next-generation LIBs due to its high specific capacity (3500 mAh/g) [45], low cost, abundance and environmentally benign properties. Moreover, the discharging potential is about 0.1 V with respect to Li/Li^+, which is lower than for most of other alloy-type and conversion metal oxide anodes [46].
The mechanism of electrochemical lithiation of Si is critical to improve the performance of a Si anode. The Li-Si alloying/de-alloying process during discharge/charge has been extensively

investigated by several groups [46, 47]. It has been found that the reactions follow the equilibrium Li-Si binary phase diagram at high temperature, forming different intermetallic compounds and showing distinct voltage plateaus [48]. The detailed reaction investigated by X-ray diffraction (XRD) analysis is explained as follows [49]:
During discharge:

$$Si\ (crystalline) + xLi^+ + xe^- \rightarrow yLi^+ + ye^- + Li_{15}Si_4(crystalline) \quad (1.13)$$

During charge:

$$Li_{15}Si_4(crystalline) \rightarrow Si\ (amorphous) + yLi^+ + ye^- + Li_{15}Si_4(residual) \quad (1.14)$$

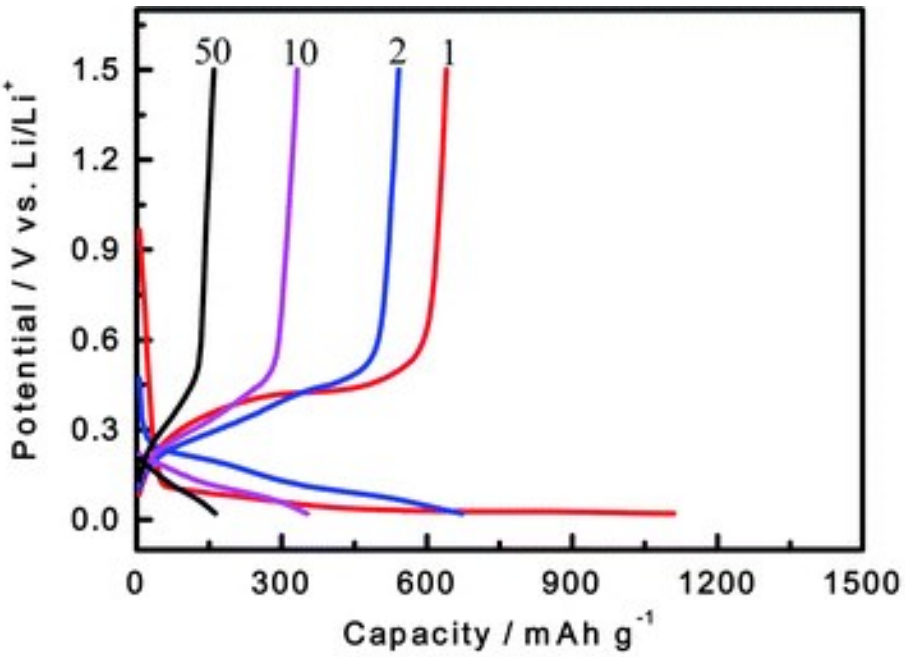

Fig. 5 Voltage-capacity curve of Si-based LIB. Revised from ref [50]

The typical discharge curve of a Si-based LIB is shown in Fig. 5. The crystalline Si becomes an amorphous Li-Si alloy during the first lithiation and the highly lithiated amorphous Li_xSi phase is suddenly found to crystallize into $Li_{15}Si_4$ phase. A typical long voltage plateau at 0.1 V is also clearly shown (1st discharge curve, red line). During delithiation, the formed crystalline $Li_{15}Si_4$ turns into amorphous Si and only a small fraction of $Li_{15}Si_4$ phase remains. After the first cycle, Li ions react with the amorphous Si formed at the end of the first delithiation. During the abovementioned Li storage and release process, the Si electrode undergoes volume expansion ~400% [51]. This significant volume expansion contributes to the capacity degradation of Si-based LIBs. In order to alleviate the significant volume expansion leading to irreversible capacity decay, the underlying morphological change of the Si electrode with regard to the electrochemical behavior should be investigated. In the current dissertation, section 2.4 presents

the detailed investigation of the failure mechanisms of ~100-µm-sized Si particle LIBs by using a laboratory X-ray source. Section 2.5 presents a detailed study of the fracture behavior of ~20-µm-sized Si particle LIBs by using synchrotron X-ray source.

1.1.3.3 Tin anode

Compared with Si, the theoretical specific capacity of Sn is calculated to be 990 mAh/g [52] when lithiated to $Li_{4.4}Sn$. The volume expansion of a Sn electrode during lithium insertion and de-insertion is reported to be around 300% [53], which is smaller than for Si. Actually, the Nexelion LIB launched by SONY in 2005 was based on Sn due to its high specific capacity and relatively low volume expansion. Even though, current LIB technology falls short of meeting the demands by energy systems because of its poor cycle performance. Significant capacity decay has been observed in Sn-based LIBs during prolonged cycle tests [45, 54].
The electrochemical reduction of a Sn electrode leads to the subsequent formation of a number of intermetallic phases Li_xSn_y at room temperature. The detailed Li-Sn alloy reaction during discharge has been suggested as follows:

$$5Sn + 2Li \rightarrow Li_2Sn_5 \quad (1.15)$$

$$Li_2Sn_5 + 3Li \rightarrow 5LiSn \quad (1.16)$$

$$5LiSn + 17Li \rightarrow Li_{22}Sn_5 \quad (1.17)$$

Some studies also reveal that the formation of $Li_{22}Sn_5$ from LiSn also involves other intermediate phases [55]. The corresponding discharge curve of a Sn electrode is shown in Fig. 6.

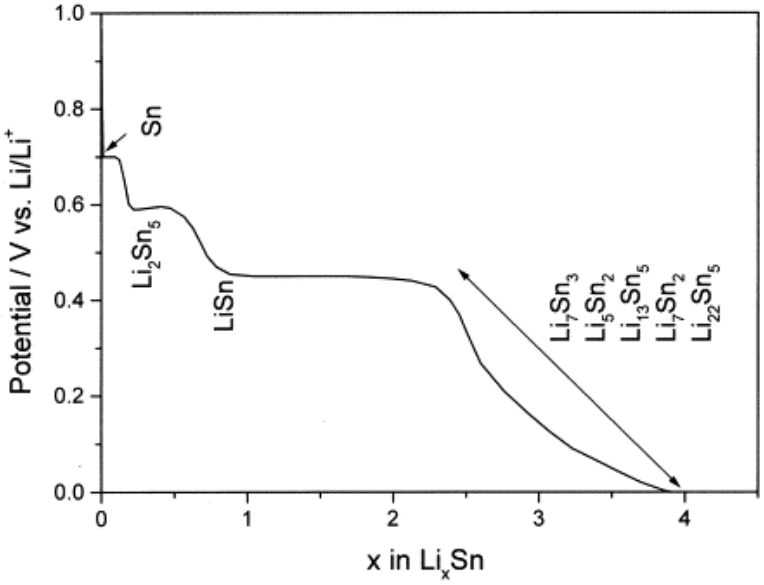

Fig. 6 Discharge curve of Sn based LIB. Revised from ref. [56]

Similar to the Si anode, the detailed knowledge of the morphological changes of Sn electrodes with regard to the electrochemical behavior can guide future battery design for next-generation Sn anode LIBs. In the current dissertation, section 2.6 presents detailed (de)lithiation behavior of Sn particles during (dis)charge by in situ synchrotron X-ray radiography.

1.1.4 Separator

The separator plays an important role in LIBs. The primary function of a separator is to prevent physical contact between anode and cathode to prevent an internal short circuit (ISC). Meanwhile, the separator allows the lithium ions to pass through to finish (dis)charge process. Generally, separators with sub-micro pore sizes have proven adequate to block any penetration of electrode particles while providing efficient transport of lithium ions [57]. Although the separator itself does not take part in the cell reaction, its structure and properties directly affect battery capacity, cycle life and safety. In addition, an ideal separator has to be electronically isolative, mechanically, dimensionally, chemically and electrochemically stable. Furthermore, the separator should not produce impurities, which could cause interference with the function of batteries. In some applications, separators have to withstand the corrosive nature of the electrolyte at elevated temperatures [58-60].
The major manufacturers of LIB separators along with their typical products are listed in Table 1 [59].

Table 1 Commercial separator properties from different companies. Reprinted with permission from Ref. 58.

Table 1. Commercial separator properties.

Separator manufacturers[a]	ASAHI	TORAY	CELGARD	UBE	ENTEK
Product	HIPORE	SETELA	Celgard	UPORE	Teklon
thickness [μm]	≥25	7–25	ML PP: 16-25 ML PE: 16-20 TL PP/PE/PP: 12-38	–	25
single (SL)/multilayer (ML)	SL	SL	SL/ML	SL	SL
composition[b]	PE	PE	SL: PP, PE ML: PP/PE/PP	PP, PE	PE
process	wet extruded	wet extruded	dry extruded	dry extruded	wet extruded

[a] Separator specifications are found on data sheets for each product. [b] PE: polyethylene, PP: polypropylene.

The detailed requirements for a suitable separator in LIBs are listed below:
1, the separator material must be chemically stable against the electrolyte especially, under the strongly reductive environment of the anode and the oxidative environment of the cathode when the battery is fully charged. At the same time, the separator should not degrade and lose mechanical strength during battery operation. An easy way to verify chemical stability is by calendar life testing.

2, the separator should possess a high wettability. Separators should have the ability to absorb significant amounts of liquid electrolyte and also to retain the electrolyte during cell operation in order to facilitate ion transportation.
3, a low thickness of a separator is beneficial for high energy and high rate capability. However, this adversely affects mechanical strength and safety. In current technologies, the standard thickness of separators for consumer rechargeable LIBs is ~ 25 μm. In addition, thickness homogeneity is also desirable as variations in thickness may lead to cell failure.
4, an appropriate porosity is necessary to hold sufficient liquid electrolyte and ensure ionic conductivity between the cathode and anode. A too low porosity will retain less electrolyte, leading to internal resistance increase. However, a too high porosity will adversely impact the mechanical performance of the separator. Typically, the separators for LIBs have a porosity of 40% [59].
5, a uniform pore size distribution is desirable within the total area of a separator film to avoid performance decay. In addition, the pore size must be smaller than the particle size of electrode materials so no electrode particles can be transported. In practical cases, sub-μm pore size have proven adequate in reducing the possibility of an internal short circuit by blocking the penetration of larger electrode particles meanwhile providing efficient conductivity for lithium ions [57].
6, a separator should possess a mediate permeability for lithium ions, i.e. the separator should not limit the transportation of lithium ions during battery operation. Typically, the presence of a separator increases the effective resistance of electrolyte by a factor of 4-5 [57]. The separator with uniform permeability is essential for long cycle life of a battery. Variations in permeability will lead to an uneven current density distribution, which has been verified as one of the reasons for the formation of lithium dendrites on the anode [61].
7, a separator should possess a high mechanical strength and a high dimensional stability. Mechanical strength is characterized in terms of tensile strength along the machine direction and the transverse direction, the tear resistance and the puncture strength. The puncture strength is defined as the maximum load required for a given needle to puncture the separator. The standard minimum requirement for the mechanical and puncture strength is 100 kg/cm^{-2} and 300 g for a 25 μm separator [61].
Lastly, the separator should possess a low thermal shrinkage. In practice, the separator tends to shrink when the temperature rises to the softening temperature. For example, polyethylene (PE) can shrink as much as 10% when exposed to a temperature of 120 ℃ for 10 min. Thermal shrinkage should be minimized. For LIBs, shrinkage of a separator is required to be not more than 5% after 60 min at 90℃ [61].
From the point view of composition and structure, battery separators can be broadly categorized into:
1, microporous polymer separators,
2, non-woven mats,
3, composite membranes and
4, gel-poymer electrolyte separators [59].

Among them, the microporous polymer separators have been widely used in liquid electrolyte batteries due to their comprehensive advantages of performance, safety and cost [58]. In the following section, we will focus on the trilayer separator developed by Celgard®.

1.1.4.1 Celgard® 2325 separator

The purpose of the proposed trilayer structure is to enhance inherent battery safety by shutting down the pores of the PE layer (135 ℃ melting temperature) while maintaining the mechanical stability of the separator through two PP (polypropylene) layers (165 ℃ melting temperature) in case of internal chort circuit [58]. Fig.7 shows the currently investigated three-layered PP/PE/PP Celgard® 2325 separator.

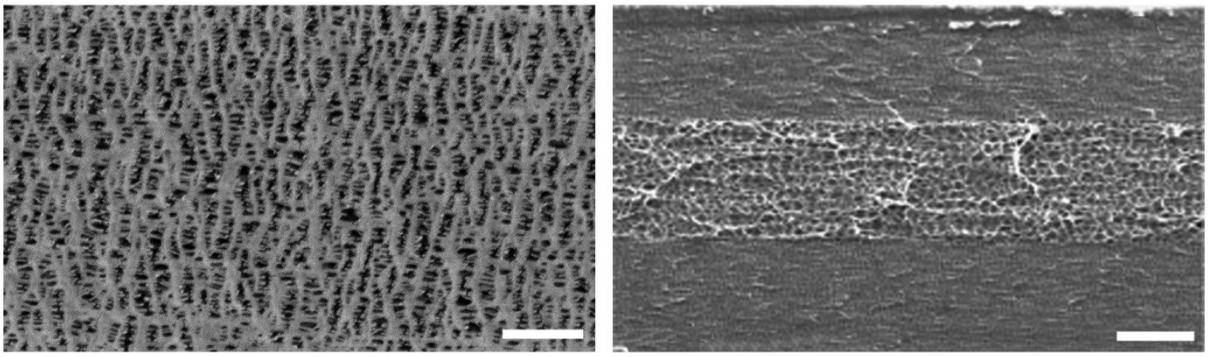

Fig. 7 Top view and cross-sectional view of the Celgard® 2325 separator characterized by scanning electron microscopy (SEM). Scale bars in left and right figure are 1 μm and 5 μm, respectively. The image are revised from ref. [58]

In the case of over-heating, the middle PE layer will shut down the cell automatically by blocking ionic pathways upon melting, while the two PP layers can still provide mechanical strength to prevent physical contact of the electrodes. From our investigation, it is concluded that the proposed three-layer structure of the separator cannot withstand the force arising from the growing lithium microstructures. Actually, delamination of the trilayer Celgard® 2325 separator into three native layers can develop under the high pressure exerted by the growing lithium microstructures. In addition, melting of the PE separator can occur due to localized excessive Joule heating resulting from ISC. Section 2.2 presents a detailed investigation of this topic.

1.2 X-ray imaging setup

Recently, X-ray imaging based on either a laboratory X-ray source or a synchrotron X-ray source has been widely used as a powerful characterization tool in material science [62, 63]. Specifically, X-ray imaging enables researchers to obtain fundamental insights into the evolution of electrodes non-destructively. In the current dissertation, all the investigations are conducted by X-ray radiography or tomography.

The underlying working principle of X-ray imaging is based on different X-ray absorption coefficients of different materials. During X-ray imaging, an X-ray beam produced by the X-ray tube or the synchrotron X-ray facility passes through the LIB to be characterized. Different materials such as the cathode, anode and separator inside the LIB have different X-ray absorption coefficients. The attenuated X-ray is finally captured by a detector. Then the obtained picture is further analyzed. In conventional X-ray radiography, one 2D image is obtained [64]. Through X-ray tomography, three dimensional structures of internal components of LIBs can be obtained [65].

1.2.1 laboratory X-ray imaging setup

The laboratory X-ray imaging setup used in this dissertation is shown in Fig. 8 and is located at the Helmholtz-Zentrum Berlin, Germany.

Fig. 8 Photography of the employed laboratory X-ray imaging setup

The employed laboratory X-ray imaging setup consists of an X-ray tube (Hamamatsu, L8121-03) and a flat panel detector (Hamamatsu, C7942SK-05). The micro focus X-ray source produces a cone beam which allows for different ratios in dependence of the relation between source-detector and source-sample distances. In this way, the field of view and the spatial resolution are

tunable. The detailed parameters for the laboratory X-ray tomography and radiography (section 2.4) are: 60 kV and 166 µA for the X-ray tube voltage and current, 58 mm and 500 mm for the source-to-sample distance and source-to-detector distance. Each pixel represents 5.76 µm of the sample. The obtained datasets are then normalized, filtered and reconstructed. More detailed information can be found in section 2.4.

1.2.2 Synchrotron X-ray imaging setup

The schematic illustration of the BAMline used for synchrotron X-ray imaging is shown in Fig. 9.

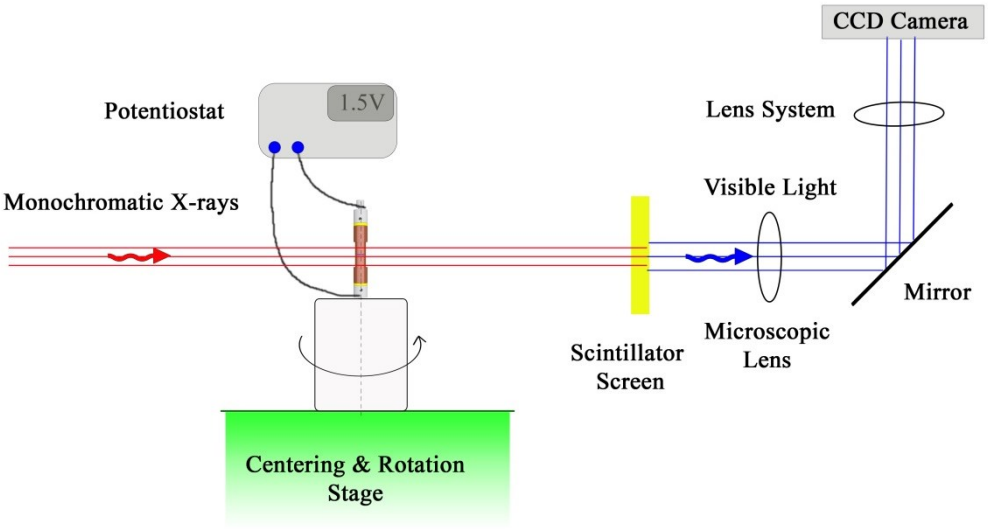

Fig. 9 Schematic illustration of the employed synchrotron X-ray imaging setup at the BAMline.

The synchrotron beam was monochromatized to 20 keV using a double multilayer monochromator with an energy resolution of about 1.5 %. The detector system comprised a 60-µm thick $CdWO_4$ scintillator, a microscopic optic and a pco4000 camera equipped with a 4008×2672 pixels CCD chip that is kept out of the direct beam by using a mirror. In the present dissertation, the synchrotron X-ray imaging setup is employed to characterize:

1, the morphological evolution of lithium microstructures in LIBs(section 2.1);

2, the break-down of the commercial Celgard® 2325 separator during cycles (section 2.2);

3, the three dimensional development of gas inside an operating battery (section 2.3);

4, the fracture behavior of ~ 20 µm sized Si particles investigated by synchrotron X-ray tomography (section 2.5);

5, different (de)lithiation behaviors of Sn particles investigated by in situ synchrotron X-ray radiography.

The detailed parameters for the above measurements can be found in each section.

1.3 The customized cells

In order to characterize LIBs by X-ray imaging, special LIBs had to be designed and fabricated because commercially available LIBs are not compatible with this technique. For this purpose, two prototypes of a tomography cell (tomo-cell) and a radiography cell (radio-cell) are fabricated as shown in Fig. 10, along with the schematic illustrations.

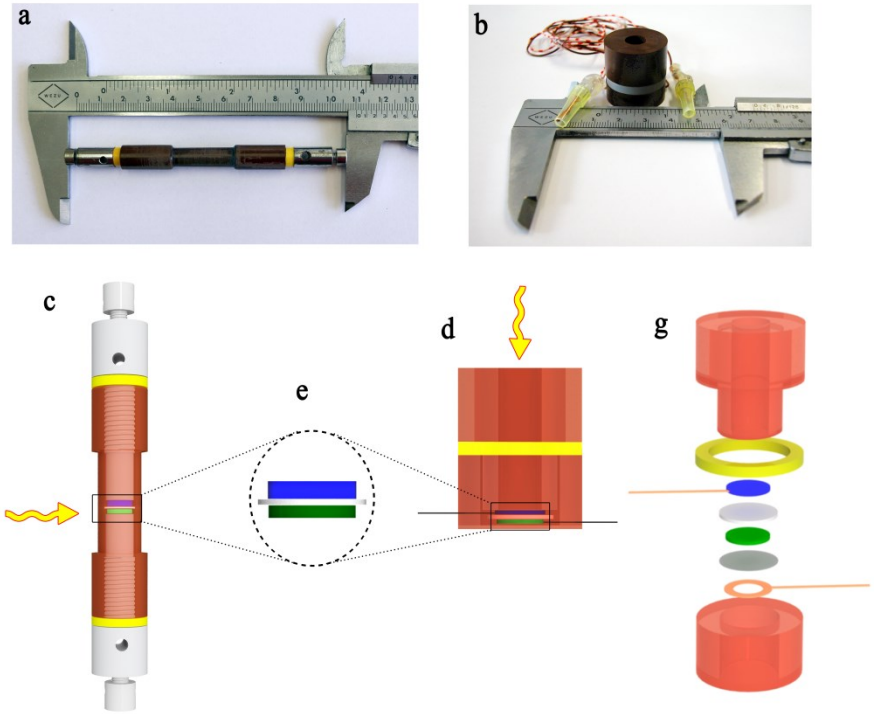

Fig. 10 Photography and schematic illustration of the two cell prototypes employed. a), b) photography of the fabricated tomo-cell and radio-cell, respectively. c), schematic illustration of the tomo-cell. d) and g) schematic illustration of the radio-cell. e) enlarged electrode part of both cells.

Both cell prototypes are made of polyamide-imide due to its low X-ray absorption. Specifically, the tomo-cell consists of a polyamide-imide housing (brown), two screw electrodes and a retaining screws each on top (light grey), two sealing rings (yellow), a negative electrode (blue), a porous separator (white) and the counter positive electrode (green), as shown in Fig. 10c. For the radio-cell, from top to bottom, it consists of an upper housing (orange), sealing ring (yellow), a negative electrode (blue) with copper wire, separator (light gray), a positive counter electrode (green), a titanium foil current collector (gray), an annular copper current collector (copper), a lower housing (orange), as shown in Fig. 10g. The direction of the penetrating X-ray is illustrated by yellow arrows in Fig. 10c and Fig. 10d. More detailed information can be found in each section of chapter 2.

2 Published parts of work

2.1 Morphological evolution of lithium microstructures (paper titled "Morphological evolution of electrochemically plated/stripped lithium microstructures investigated by synchrotron X-ray phase contrast tomography", ***ACS NANO***, **2016**, 10: 7990)

2.1.1 Supporting information

2.2 Break-down of the separator (paper titled "Study of the Mechanisms of Internal Short Circuit in a Li/Li cell by Synchrotron X-ray Phase Contrast Tomography", ***ACS Energy Letters***, **2016**, 2: 94)

2.3 Gas development (paper titled "Three dimensional visualization of gas evolution and channel formation inside a lithium-ion battery", ***ACS Applied Materials & Interfaces***, **2016**, 8: 7156)

2.3.1 Supporting information

2.4 Degradation of lithium ion batteries based on ~100-µm-sized Si particles (paper titled "Investigation of failure mechanisms in silicon based half cells during the first cycle by micro X-ray tomography and radiography", ***Journal of Power Sources***, **2016**, 321: 174)

2.4.1 Supporting information

2.5 Fracture behavior of ~20-µm Si particles (paper titled "Synchrotron X-ray tomographic study of a silicon electrode before and after discharge and the effect of cavities on particle fracturing", ***ChemEltroChem***, **2016**, 3: 1170)

2.5.1 Supporting information

2.6 Different (de)lithiation behaviors of Sn particles (paper titled "In Situ Radiographic Investigation of (De)Lithiation Mechanisms in a Tin-Electrode Lithium-Ion Battery", ***ChemSusChem***, **2016**, 9: 946)

2.6.1 Supporting information

2.1 Morphological evolution of lithium microstructures

Morphological evolution of electrochemically plated/stripped lithium microstructures investigated by synchrotron X-ray phase contrast tomography

Fu Sun,[*†,§] Lukas Zielke,[‡] Henning Markötter,[†,§] Andre Hilger,[†,§] Dong Zhou,[†,§] Riko Moroni,[‡] Roland Zengerle,[‡] Simon Thiele,[‡,#] John Banhart[†,§] and Ingo Manke[§]

[†]Institute of Material Science and Technologies
Technical University Berlin
Strasse des 17. Juni 135, 10623 Berlin, Germany
[‡]Laboratory for MEMS Applications, IMTEK Department of Microsystems Engineering
University of Freiburg
Georges-Koehler-Allee 103, 79110 Freiburg, Germany
E-mail: Lukas.Zielke@imtek.de
[§]Helmholtz Centre Berlin for Materials and Energy
Hahn-Meitner-Platz 1,
14109 Berlin, Germany
[#]FIT, University of Freiburg
Georges-Köhler-Allee 105, 79110 Freiburg, Germany,
*Email: fu.sun@helmholtz-berlin.de

Due to its low redox potential and high theoretical specific capacity Li metal has drawn worldwide research attentions because of its potential use in next-generation battery technologies such as Li-S and Li-O_2. Unfortunately, uncontrollable growth of Li microstructures (LmSs, e.g. dendrites, fibers) during electrochemical Li stripping/plating has prevented their practical commercialization. Despite various strategies proposed to mitigate LmS nucleation and/or block its growth, a fundamental understanding of the underlying evolution mechanisms remains elusive. Herein, synchrotron in-line phase contrast X-ray tomography was employed to investigate the morphological evolution of electrochemically deposited/dissolved LmSs non-destructively. For the first time we present a 3D characterization of electrochemically stripped Li electrodes with regard to electrochemically plated LmSs. We clarify fundamentally, the origin of the porous lithium interface growing towards Li electrodes. Moreover, cleavage of the separator caused by growing LmS was experimentally observed and visualized in 3D. Our systematic investigation provides fundamental insights into LmS evolution and enables us to understand the evolution mechanisms in Li electrodes more profoundly.

2.1 Morphological evolution of lithium microstructures

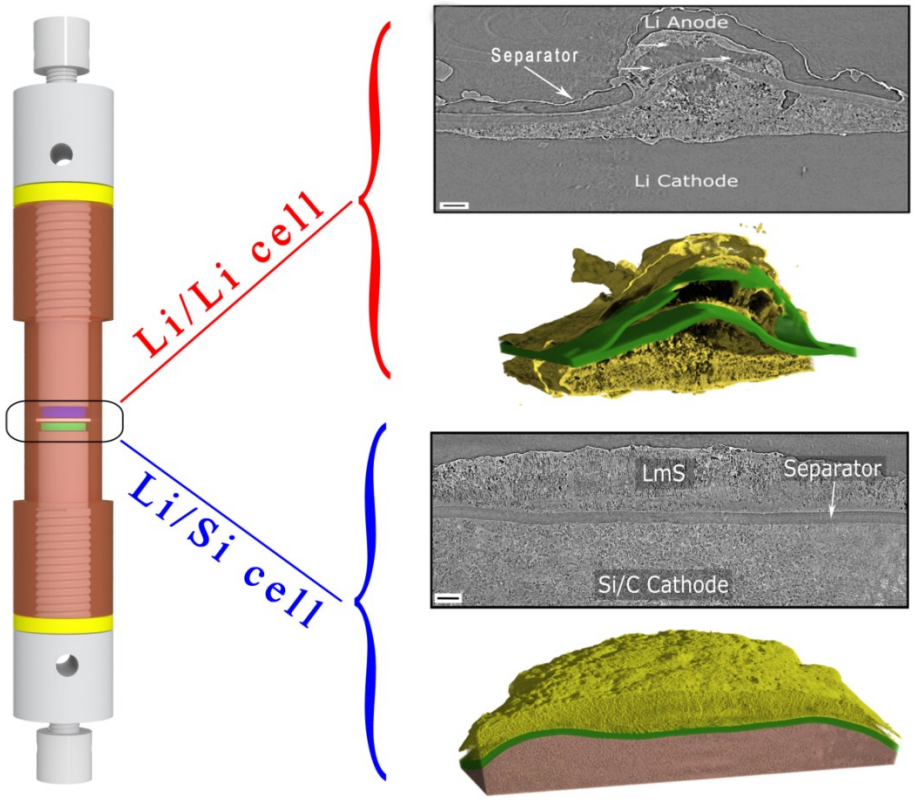

Abstract Graphic

Keywords: lithium microsctructures; morphological evolution; lithium ion battery; silicon; separator; lithium strip/plate

The further development of characterization methods has often promoted a better understanding of the structure and function of materials.[1] For example, optical microscopy,[2] atomic force microscopy (AFM),[3] scanning electron microscope (SEM),[4] transmission electron microscopy (TEM),[5] nuclear magnetic resonance (NMR)[6] and magnetic resonance imaging (MRI)[7] have been employed to understand the growth of the lithium microstructure (LmS) in lithium-ion batteries. Our apprehension of the growth mechanisms of LmSs has greatly improved[8] since usage of Li metal as negative electrode began in the 1970s.[9] Nevertheless, prior analytical tools are inherently limited. For instance, most techniques usually require prior sample removal from their *as grown* environment for analysis, which is problematic since accidental exposure of LmSs to air during sample transfer[10] and the Li-rinsing procedures applied for sample preparation[11] may fundamentally change their morphology. Furthermore, nuclear resonance techniques suffer from limited resolution of around 100 µm, the limited penetration depth of radiofrequency irradiation and additional concerns arising from artefacts introduced by metals.[12] Recently, Eastwood *et al.* have characterized the 3D microstructure of electrodeposited LmS by synchrotron in-line phase

contrast X-ray tomography at sub-µm resolution,[12] demonstrating that this method is a suitable and powerful tool for the study of LmSs. In another study, Harry *et al.* found that most Li dendrites reside within the electrode instead of the polymer separator during the early stage of dendrite development. They conclude that these dendrites preferentially grow from crystalline impurities existing within an electrode.[13]

In this work, we implement a further systematic study by using in-line phase contrast X-ray tomography. We propose that the Li dendrites residing on the surface of the electrode arise from the nascent electrochemically deposited LmS occupying the previously dissolved initial Li bulk electrode. Furthermore, the present study clarifies, from a fundamental point of view, the origin of the Porous Lithium Interface (PLI) growing towards the Li electrode, which has been discovered previously.[14] In addition, an unexpected cleavage of the separator caused by the growing LmS is experimentally shown for the first time. These unprecedented findings, which were not accessible from conventional microscopic characterizations and electrochemical measurements, fundamentally deepen our understanding of the evolution mechanism of the LmS during electrochemical stripping/plating. The insights obtained could open up the way towards new design principles and opportunities to further ameliorate or eliminate LmSs.

A proof-of-concept electrochemical cell, which is fully compatible with X-ray imaging and at the same time representative for commercial lithium-ion batteries (LIBs), was designed and manufactured as shown in Figure 1 along with a schematic illustration of the synchrotron X-ray imaging setup at BAM*line* of BESSY II, Berlin, Germany.[15] Two kinds of electrochemical cells were investigated: a Li electrode coupled with a silicon-based composite (Si/C) electrode (Li/Si half-cell) and a Li electrode coupled with a Li electrode (Li/Li symmetrical cell). All cells employed commercial Celgard® 2325 separators and were filled with 0.2 ml standard 1 M $LiPF_6$ in ethylene carbonate (EC) and ethyl methyl carbonate (EMC) (EC/EMC=50/50 (v/v)) electrolyte. Details of parameters and cycling routines of the investigated cells are given in the Methods section and the Supporting Information (SI). The validation of the electrochemical performance of this proof-of-concept cell can be found in a previous report.[16] The cycling curves of all the cells are shown in the SI. After cycling, the cells were transferred to the beamline to conduct tomography without prior disassembly. Every tomography was recorded with 2200 projections covering a 180° rotation angle. A detector system with 0.438 µm pixel size was used.[17] The field of view (FoV) is 1.7 × 1.2 mm^2 large (length × height), which enables the simultaneous imaging of morphological changes occurring in all components of the electrodes. The detailed normalization, tomography reconstruction and 3D presentation procedure is given in the Methods section and in SI.[18]

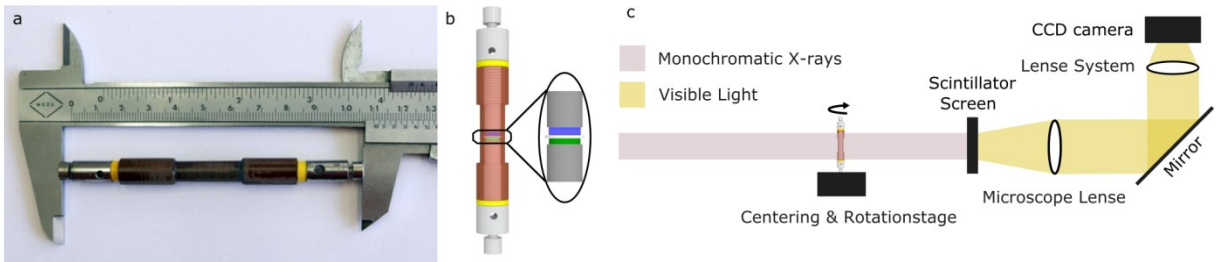

2.1 Morphological evolution of lithium microstructures

Figure 1 Schematic illustration of the proof-of-concept cell and the beamline setup. a, photograph and b, corresponding illustration of the electrochemical cell: polyamide-imide housing (brown), two screws serving as current collectors (light gray), two sealing rings (yellow), cathode (blue), separator (white) and anode (green). c, schematic representation of the experimental setup at BAMline BESSY II, Berlin, Germany. More information about the cell and the setup parameters can be found in Methods and SI.

Cross-sectional views of uncycled Li/Li (Li/Li-N: N denotes sample cell number. In this case, the sample is Li/Li-1) and Li/Si (Li/Si-N: N denotes sample cell number. In this case, the sample is Li/Si-1) cells are shown in Figure 2a-c and Figure 3a-c, respectively, where we can clearly discern the Li electrode, the separator and the counter Li electrode (Si/C electrode) by the light and dark interfaces between them arising from the in-line phase contrast.[19] In both cases, the interfaces between electrode and electrolyte of uncycled cells exhibit a few minor noticeable features (uneven surfaces shown in Figure 2c and Figure 3c) caused by the high electrochemical activity of Li.[13] The anode and cathode are labeled separately in Figure 2 and Figure 3 (the arrangement is taken only for easy demonstration: in sample Li/Li-2 (Figure 2d-l), the Li anode is the bottom electrode, while the Li cathode is the upper. In sample Li/Li-3 (Figure 2m-o), the Li anode is the top, the Li cathode the bottom electrode. For all Li/Si half cells, the Li anode is the top, the Si/C cathode the bottom electrode (Figure 3)). Figure 2d,e show images of the Li/Li-2 sample subjected to a constant current of $0.3\ mA \cdot cm^{-2}$ for 10 h. The corresponding 3D representation is shown in Figure 2f. Compared to Figure 2a-c, the initially flat electrode/electrolyte interfaces have turned into rugged interfaces with numerous electrochemically deposited LmSs on the cathode side. In addition, differently sized cavities can be observed in the partially electrochemically dissolved Li anode. It has been reported that the appearance of such cavities stems from the unevenly formed solid electrolyte interface (SEI) and that regions containing cavities are electrochemically more active than flat surfaces.[20] Furthermore, the separator deforms into an arched shape and adheres closely to the electrochemically dissolved porous structure, indicating that significant stress is generated during LmS formation.

In a next step, the Li/Li-2 sample was continuously discharged galvanostatically for another 19 h. Figure 2g-I illustrates that a large amount of Li is further dissolved from the Li anode and deposited onto the Li cathode, as indicated by the increased volume of cavities within the anode and by the increasing LmSs on top of the cathode. Consequently, some delamination between the separator and the two Li electrodes can be observed, which is comparable to previous reports.[11]

After charging the Li/Li-2 sample for 17 h, the structure shown in Figure 2j-l is obtained. One observes that: i) during Li stripping from the cathode, it is the remaining Li bulk instead of the electrochemically plated LmS that undergoes electrochemical Li dissolution, as indicated by the newly formed void in the Li cathode (indicated by white triangles in Figure 2j,k), ii) during plating of the anode with Li, Li deposition occurs preferentially in the system of cavities structures as indicated by the newly formed LmSs on the surface of the existing cavities (note white tetragons in Figure 2j,k). It has been reported that the nascent electrochemically inactive LmSs are still chemically active and can easily react with the electrolyte to form a new SEI

coverage.[14] Consequently, the SEI formed electrically insulates most of the nascent LmSs, thereby deactivating them electrochemically during Li stripping.[21] The reason for the preferential deposition of LmSs in cavity-containing regions is that such areas are electrochemically more active[22] or possess a high local ionic conductivity.[20]

Figure 2m-o shows a cross section of the Li/Li-3 sample which has been discharged at a constant current of 0.3 $mA \cdot cm^{-2}$ for 30 h. Here, the unexpected phenomenon of cleavage of the separator due to the puncture by the LmS is observed. The corresponding 3D representation is displayed in Figure 2o. The presence of Li filaments running across the separator is observed, as indicated by white arrows between the punctured separator in Figure 2m. The cleavage can be attributed to the anisotropic mechanical properties of the Celgard® separator in the transverse direction due to the manufacturing process employed to create the micro-porous membranes.[23] This is the first time that the puncture of a separator is reported experimentally and displayed in 3D. 3D representations of the morphological evolution of these cells are shown in Figure 2c, f, i, l, o. The locations of the cross sections shown in Figure 2, along with the corresponding videos displaying the 3D nature of LmSs are available in SI.

2.1 Morphological evolution of lithium microstructures

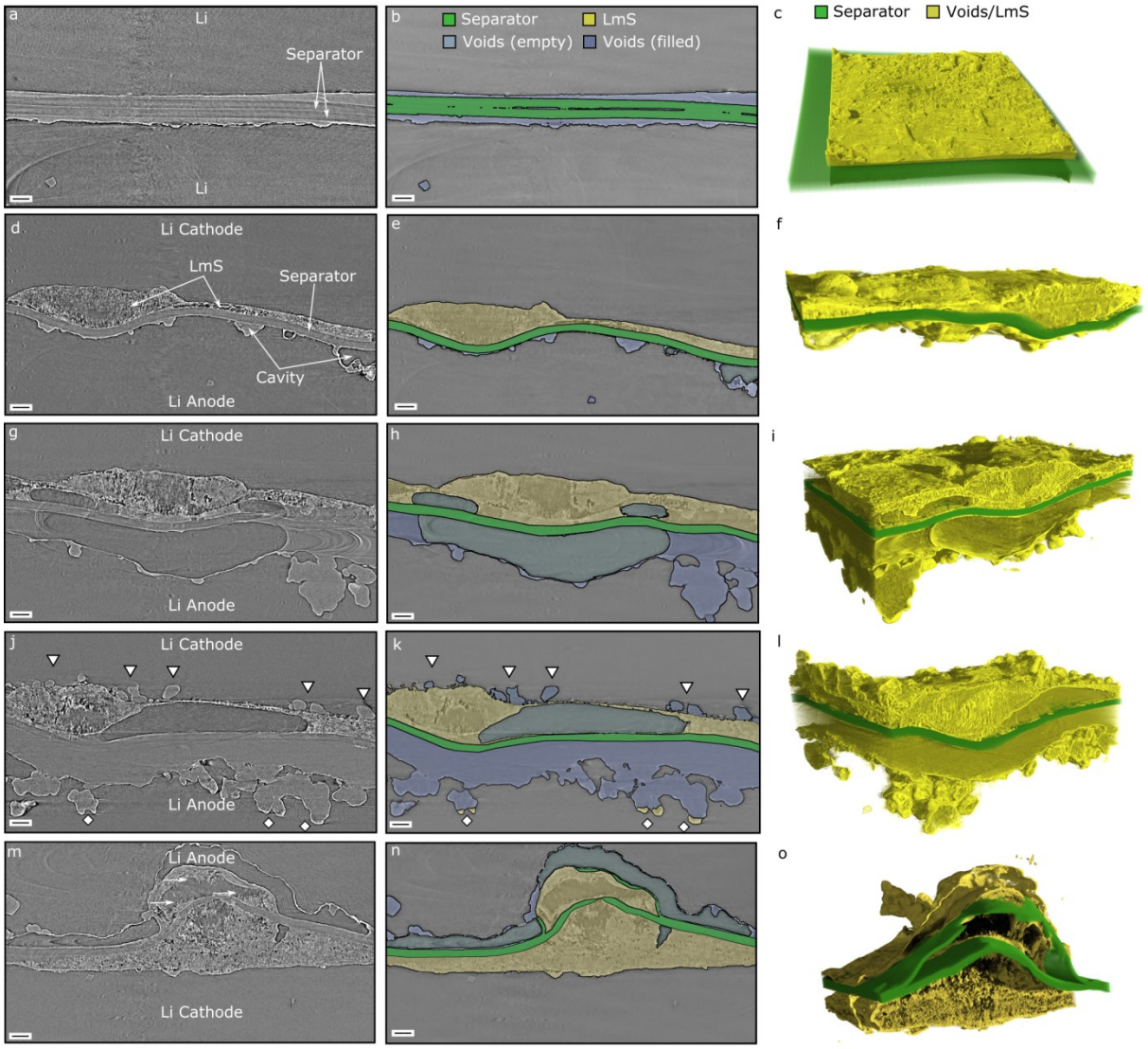

Figure 2 Morphological evolution of LmS in Li/Li symmetrical cells. a-c, uncycled pristine Li/Li-1 sample. The Celgard® separator is sandwiched between two Li electrodes. d-f, Li/Li-2 sample after galvanostatic discharge for 10 h at 0.3 mA·cm^{-2}. Li metal has been dissolved from the Li anode (evidenced by the visible cavities) and deposited onto the Li cathode (evidenced by the LmS). g-i, Li/Li-2 sample after galvanostatic discharge for another 19 h at 0.003 mA·cm^{-2}. An increasing amount of Li has been dissolved from the Li anode and deposited onto the Li cathode. j-l, Li/Li-2 cell after galvanostatic charge for 19 h at 0.3 mA·cm^{-2} showing that the residual Li bulk (indicated by white triangles) instead of LmSs has been dissolved and preferentially deposited onto the surface of existing cavities (marked by white tetragons). m-o, Li/Li-3 sample galvanostatically discharged for 30 h at 0.3 mA·cm^{-2} showing filamentous LmSs running across the separator (indicated by arrows) and the torn Celgard® separator. The first column (a, d, g, j, m) contains reconstructed X-ray tomographies. The second column (b, e, h, k, n) shows the same slice after a combination of manual and automated phase filtering and color labeling. The third column (c, f, i, l and o) shows the corresponding 3D representations. All the scale bars are 50 µm long. The cycling procedures of all cells, the detailed phase filtering procedure and 3D presentation methods are described in Methods and SI.

2.1 Morphological evolution of lithium microstructures

More information about the evolution of LmSs can be obtained from tomographies showing the Li/Si half-cells. Figure 3d-f displays cross-sectional views of the Li/Si-2 sample that was galvanostatically discharged for 15 h at 0.3 mA·cm^{-2}. Compared to the uncycled Li electrode sample (Figure 3a-c), a good deal of Li has been electrochemically stripped from the bulk anode Li (evidenced by the cavities formed as marked by white triangles in Figure 3d,e) and subsequently alloyed with Si particles (evidenced by the cracks formed as marked by white diamonds in Figure 3d,e). Moreover, after the Li/Si-1 sample has been discharged for 15 h and then charged for 5 h at 0.7 mA·cm^{-2}, some but not all voids generated during electrochemical dissolution are dominated by the nascent electrochemically deposited LmSs, as shown in Figure 3g-i. This non-uniform filling of voids may be the result of the uneven distribution of Li ion flux.[8b] Finally, the Li/Si-3 sample, which has experienced 5 cycles, is shown in Figure 3j-l. We observe that a nearly 100-µm thick portion of the initial Li anode has been dissolved and is thereafter occupied by electrochemically generated LmSs. On the Si cathode, almost all of the Si particles have been fully lithiated to $SiLi_x$ ($1<x<4$) and are no longer observable due to the low X-ray attenuation coefficient.[24] 3D representations of the morphological evolution of the LmS formed in Li/Si cells are shown in Figure 3c, f, i, l. The locations of the cross sections shown in Figure 3, along with the corresponding videos showing the 3D nature of the LmS are available in SI.

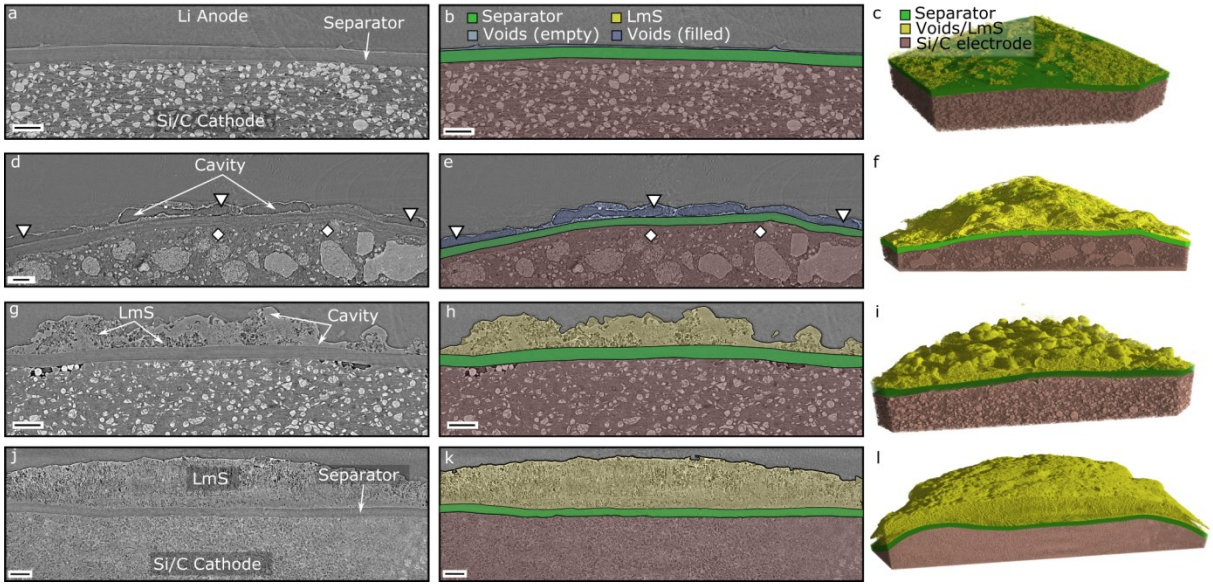

Figure 3 Morphological evolution of LmS in Li/Si half cells. a-c, uncycled pristine Li/Si-1 cell. The Celgard® separator is sandwiched between the Li anode and the Si/C composite cathode. d-f, Li/Si-2 sample that has been galvanostatically discharged for 15 h at 0.3 mA·cm^{-2}. Here, Li has been dissolved from the Li anode (evidenced by cavity/void, white triangles) and alloyed with the Si/C cathode (evidenced by Si crack formation, white tetragons). g-i, Li/Si-1 cell after 15 h of discharge and 5 h of charge at 0.7 mA·cm^{-2}. The cavities formed are partially occupied by newly formed LmSs. j-l, Li/Si-3 cell that has experienced 5 cycles (see SI). Here, nearly half of the original Li anode has been dissolved and is now occupied by deposited LmSs. The first column (a, d, g, j) contains reconstructed tomography slices. The second column (b, e, h, k) shows the same slice after a combination of manual and automated phase

filtering and color labeling. The third column (c, f, i, l) contains the corresponding 3D representations. All the scale bars are 50 μm long. The cycling procedures of all cells can be found in SI.

Based on these systematic investigations, we suggest a model that describes the phenomena observed in Figures 2 and 3. A schematic illustration of the proposed evolution is shown in Figure 4. During the 1st electrochemical Li stripping, a significant amount of Li dissolves from the Li anode (yellow), and numerous cavities (white) are generated. Meanwhile, these Li ions, i) are electrochemically deposited into the LmS on the hostless Li cathode (as observed in Figure 2) or, ii) form an alloy with the Si/C composite electrode (as observed in Figure 3). The purple-yellow color gradient in Figure 4 indicates the two cases observed in Figure 2 and Figure 3. During subsequent electrochemical Li plating, the Li ions are transported back to the Li anode and are preferentially deposited in the previously formed cavities due to the high electrochemical local activity there. However, during the following (the 2nd) Li stripping from the anode, it is the remaining bulk Li (yellow) that undergoes electrochemical dissolution instead of the nascent electrochemically deposited LmS (ocre, formed during previous Li plating) which is covered by electron-blocking SEI. Summarizing this process one can say that the initial bulk Li anode is electrochemically dissolved continuously in each Li stripping step, which results in numerous cavities. During subsequent Li plating, large amounts of the LmS are generated and form the PLI, which occupies the voids formed during previous Li dissolution. It has been reported that a continuously growing PLI can substantially increase the internal resistance of a cell, which eventually results in poor cell performance and ultimately in cell failure.[14] Meanwhile, thin LmS protruding from the PLI towards the separator conducts high currents and consequently experiences large localized Joule heating, which results in the melting of the separator and finally puncture of the separator.[25]

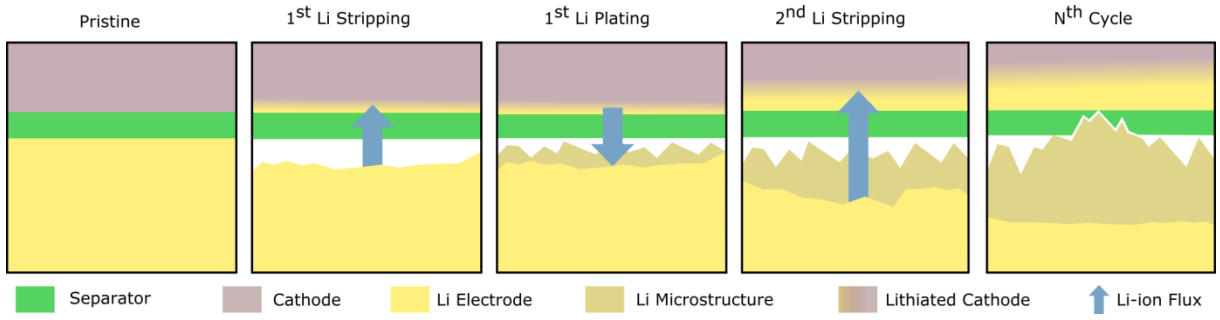

Figure 4 Schematic illustration of the morphological evolution of LmSs in a Li anode: from left to right, a pristine state cell; Li anode then undergoes the 1st stripping during discharge; Li anode undergoing the 1st plating during charge; Li anode undergoing the 2nd stripping during another discharge; Li anode after Nth stripping/plating (N⩾2).

The observations of the evolution of electrochemically stripped/plated LmSs presented here shed new light on a range of processes that previously have not been acknowledged or barely

considered. Firstly, the proposed mechanism of LmS evolution can explain the origin of the electrochemically generated PLI that grows towards the Li bulk electrode. Based on our observations, both the electrochemical dissolution of the initial Li bulk electrodes and the following electrochemical deposition of nascent LmSs contribute to the inward growth of the PLI. Secondly, the evaluation of using Coulombic efficiency to investigate the cycling efficiency of Li in Li symmetrical cells is compromised by the electrochemically inert LmSs.[20] According to our observations, a significant amount of Li is stripped from the initial Li bulk instead from the generated nascent (electrochemically inactive) LmSs to compensate for the depletion of Li ions in the electrolyte used to be plated. Thirdly, concerns about using Li metal as a standard counter electrode for the evaluation of the performance of new battery materials using half-cells are raised. In fact, it has been confirmed that the PLI, which continuously grows in each cycle, can markedly increase the inner cell resistance and is the actual origin of the onset of cell degradation and failure.[14] Finally, considering that the dissolution of the initial Li bulk electrodes and the deposition of nascent LmSs (necessitated by the charge transfer within cells) remain intrinsic and unavoidable, the present results suggest that novel fundamental strategies that involve direct engineering of Li electrodes are desirable and necessary. For example, strategies such as introducing surface patterns to the Li electrode to direct and control Li deposition,[26] replacing conventional Li foil electrodes by organic-coated Li powder[27] or employing different substrates to selectively deposit and then encapsulate the LmS,[28] appear more suitable than conventional mechanical suppression or formation of protective passivation layers.[29]

Our work represents a major step forward in understanding the evolution of electrochemically stripped/plated LmSs and may speed up the process of introducing Li into commercial lithium metal batteries (LMBs) with enhanced performance. On the one hand, ground breaking electrolytes are highly needed to facilitate the nascent electrochemically deposited LmSs to plate smoothly onto the Li bulk electrode instead of forming a highly resistive PLI. On the other hand, it is also worth investigating electrochemical Li stripping to enable a more uniform accessibility of Li ions from not only the initial bulk Li electrode but also from the electrochemically plated LmS. In addition, engineering a sophisticated architecture of the Li electrode will be technologically crucial. Finally, new separators with high ion conductivities and improved rigidities are highly desirable.

Materials and Methods

Materials

Lithium, carbon black, Polyvinylidene difluoride (PVDF) binder and Celgard separator were purchased from MTI Cor. USA. Silicon (Si) was received from Elkem AS, Norway. Electrolyte 1M $LiPF_6$ in a volume-ratio mixture (1:1) of ethylene carbonate (EC) and ethyl methyl carbonate (EMC) was purchased from Sigma Aldrich as well as N-methyl pyrrolidone solvent (NMP). The housing of the proof-of-concept beamline battery is made of polyamide-imide (Torlon) provided by Drake Plastics Europe.

Battery Preparation

The lithium electrodes in both Li/Li symmetrical cells and Li/Si half cells were punched out (2.5 mm diameter) from a lithium plate (1 mm thick). The Si composite electrode was made of electrode slurries containing weight ratios of Si:carbon black:binder of 70:20:10 in NMP. Two kinds of Si/C electrodes were prepared: electrodes containing i) Si particles with a diameter of ~20 µm (for Li/Si-1 and Li/Si-3); ii) Si particles with diameters of ~20, ~80 and ~150 µm in a weight ratio of 1:1:1 (for Li/Si-2). The slurry was cast onto copper foil. To remove the NMP, the cast copper foils were dried in an oven at 60 ℃ for 12 h. After drying, the composite electrode was diced into small blocks of around 1.7 mm × 1.7 mm × 0.2 mm size with a razor blade. For the Li/Si half cells, Li was used as the anode and a Si/C electrode as the cathode. For the Li/Li symmetrical cells, Li was used both as anode and cathode. All cells (6 in total, 3 Li/Li cells from Li/Li-1 to Li/Li-3, 3 Li/Si cells with Li/Si-1 to Li/Si-3) were assembled in an argon-filled glovebox with humidity and oxygen levels below 0.1 ppm. The polymer separator (3.5 mm in diameter and ~25 µm thick) was placed between the Li/Li electrode (in Li/Li cells) and the Li/Si electrode (in Li/Si cells). All cells were assembled manually without exerting force. Finally, both cells were filled with the liquid electrolyte and were sealed off before taking out of glovebox.

Electrochemical Measurement

Galvanostatic charge and discharge of all the batteries was carried out using an IviumStat from Ivium Technologies, Netherlerlands. The cells were subjected to different current densities for discharge and charge. The cycling procedure for each cell is detailed in SI.

Setting of Tomography Measurement

Synchrotron X-ray tomography was carried out at the BAMline at BESSY II of the Helmholtz-Centre Berlin, Germany. The synchrotron beam was monochromatized to 20 keV using a double multilayer monochromator with an energy resolution of about 1.5 %. The detector system comprised a 60-µm thick $CdWO_4$ scintillator, a microscopic optic and a pco4000 camera equipped with a 4008×2672 pixels CCD chip that is kept out of the direct beam by using a mirror. For tomography measurements of all cells, 2200 projections within a 180° battery rotation were recorded. For the Li/Li symmetrical cells, the exposure time was 2.5 s, for Li/Si half cells 3 s.

Data Processing

The raw tomography data was filtered, normalized and reconstructed using code programmed in IDL 8.2. Three-dimensional segmentations of the separators were made using a grid of manually marked points that were fitted with a biharmonic equation using MATLAB. For the segmentation of LmSs and voids, the statistical region merger tool implemented in Fiji[30] was used followed by manual removal of the bulk lithium background. For the three-dimensional presentations in Figure 2 and 3, the segmentation of all materials except the Li bulk (Li bulk set to 0, all other materials to 1) was used as a mask for the according X-ray dataset in order to be able to show LmSs and voids without the Li bulk in the background. Two-dimensional segmentations were made by first manually segmenting the separator, followed by a statistical region merging and

manual removal of the Li bulk background. The tomograms shown in the first column of Figure 2 are absorption contrast tomograms while the second column displays the averages of the according absorption and phase contrast tomograms. All remaining tomograms show absorption contrast only.

Remark concerning the experimental program

The effect of the pressure subjected to both cells and the electrode morphology on LmS formation was currently not the scope of this paper. Moreover, we have used a relatively small current and long cycle time to induce as much as possible Li dissolution and deposition. The effect of different C rates on the morphology of Li dissolution and deposition was not investigated. Nevertheless, these important parameters are worth to be studied in the future.
A quantitative analysis of the amount of lithium that has been dissolved from the Li anode and the amount of LmS that has been deposited onto the surface of the Li cathode (alloyed with the Si/C cathode) has presently not been conducted mainly because the currently used Li electrode (2.5 mm diameter) is bigger than the field of view (FoV), which is 1.7 mm wide. The current that passes through the chemical workstation may give rise to dissolution or deposition of Li outside the FoV. Considering this, the present research focuses on the qualitative analysis of the morphological evolution of LmSs in Li electrodes. However, cells assembled with Li electrodes smaller than the FoV could be measured in the future and analysed quantitatively.

Acknowledgements

We thank Dr. Heinrich Riesemeier, the beamline scientist at BESSY II, for his valuable assistance and engineer Norbert Beck for fabricating the beamline battery. We also thank Elkem AS for providing us with the Si particles. This work is sponsored by the Helmholtz Association and the China Scholarship Council.

Author Contributions

Fu Sun, Henning Markötter and Ingo Manke designed the cell. Fu Sun, Henning Markötter and Dong Zhou assembled and tested the cells. Andre Hilger and Henning Markötter aided in synchrotron characterizations and the discussion of results. Lukas Zielke, Andre Hilger, Roland Zengerle, Riko Moroni and Simon Thiele reconstructed the data and prepared the figures. Fu Sun, Henning Markötter, Ingo Manke and John Banhart contributed to the data interpretation and the discussion of the results. Fu Sun, Henning Markötter, Ingo Manke and John Banhart composed the manuscript. Ingo Manke and John Banhart directed the work.

Additional information

Supplementary information is available.

Competing Financial Interests statement

The authors declare no competing financial interests.

References

1. Withers, P. J., Mechanical Failure: Imaging Cracks in Hostile Regimes. *Nat Mater* **2013,** *12*, 7-9.
2. Steiger, J.; Kramer, D.; Mönig, R., Mechanisms of Dendritic Growth Investigated by in Situ Light Microscopy During Electrodeposition and Dissolution of Lithium. *J. Power Sources* **2014,** *261*, 112-119.
3. Cohen, Y. S.; Cohen, Y.; Aurbach, D., Micromorphological Studies of Lithium Electrodes in Alkyl Carbonate Solutions Using in Situ Atomic Force Microscopy. *J. Phys. Chem. B* **2000,** *104*, 12282-12291.
4. Dollé, M.; Sannier, L.; Beaudoin, B.; Trentin, M.; Tarascon, J.-M., Live Scanning Electron Microscope Observations of Dendritic Growth in Lithium/Polymer Cells. *Electrochem. Solid-State Lett.* **2002,** *5*, A286-A289.
5. Leenheer, A. J.; Jungjohann, K. L.; Zavadil, K. R.; Sullivan, J. P.; Harris, C. T., Lithium Electrodeposition Dynamics in Aprotic Electrolyte Observed in Situ Via Transmission Electron Microscopy. *ACS Nano* **2015,** *9*, 4379-4389.
6. Bhattacharyya, R.; Key, B.; Chen, H.; Best, A. S.; Hollenkamp, A. F.; Grey, C. P., In Situ Nmr Observation of the Formation of Metallic Lithium Microstructures in Lithium Batteries. *Nat Mater* **2010,** *9*, 504-510.
7. Chandrashekar, S.; Trease, N. M.; Chang, H. J.; Du, L.-S.; Grey, C. P.; Jerschow, A., 7li Mri of Li Batteries Reveals Location of Microstructural Lithium. *Nat Mater* **2012,** *11*, 311-315.
8. (a) Xu, W.; Wang, J.; Ding, F.; Chen, X.; Nasybulin, E.; Zhang, Y.; Zhang, J.-G., Lithium Metal Anodes for Rechargeable Batteries. *Energy Environ. Sci.* **2014,** *7*, 513-537; (b) Liang, Z.; Zheng, G.; Liu, C.; Liu, N.; Li, W.; Yan, K.; Yao, H.; Hsu, P.-C.; Chu, S.; Cui, Y., Polymer Nanofiber-Guided Uniform Lithium Deposition for Battery Electrodes. *Nano Lett.* **2015,** *15*, 2910-2916.
9. Ji, X.; Liu, D.-Y.; Prendiville, D. G.; Zhang, Y.; Liu, X.; Stucky, G. D., Spatially Heterogeneous Carbon-Fiber Papers as Surface Dendrite-Free Current Collectors for Lithium Deposition. *Nano Today* **2012,** *7*, 10-20.
10. Stark, J. K.; Ding, Y.; Kohl, P. A., Dendrite-Free Electrodeposition and Reoxidation of Lithium-Sodium Alloy for Metal-Anode Battery. *J. Electrochem. Soc.* **2011,** *158*, A1100-A1105.
11. Orsini, F.; Du Pasquier, A.; Beaudoin, B.; Tarascon, J. M.; Trentin, M.; Langenhuizen, N.; De Beer, E.; Notten, P., In Situ Scanning Electron Microscopy (Sem) Observation of Interfaces within Plastic Lithium Batteries. *J. Power Sources* **1998,** *76*, 19-29.
12. Eastwood, D. S.; Bayley, P. M.; Chang, H. J.; Taiwo, O. O.; Vila-Comamala, J.; Brett, D. J. L.; Rau, C.; Withers, P. J.; Shearing, P. R.; Grey, C. P.; Lee, P. D., Three-Dimensional Characterization of Electrodeposited Lithium Microstructures Using Synchrotron X-Ray Phase Contrast Imaging. *Chem. Commun.* **2015,** *51*, 266-268.
13. Harry, K. J.; Hallinan, D. T.; Parkinson, D. Y.; MacDowell, A. A.; Balsara, N. P., Detection of Subsurface Structures Underneath Dendrites Formed on Cycled Lithium Metal Electrodes. *Nat Mater* **2014,** *13*, 69-73.
14. Lu, D.; Shao, Y.; Lozano, T.; Bennett, W. D.; Graff, G. L.; Polzin, B.; Zhang, J.; Engelhard, M. H.; Saenz, N. T.; Henderson, W. A.; Bhattacharya, P.; Liu, J.; Xiao, J., Failure Mechanism for Fast-Charged Lithium Metal Batteries with Liquid Electrolytes. *Adv. Energy Mater.* **2015,** *5*, 1400993-1401000.
15. (a) Manke, I.; Banhart, J.; Haibel, A.; Rack, A.; Zabler, S.; Kardjilov, N.; Hilger, A.; Melzer, A.; Riesemeier, H., In Situ Investigation of the Discharge of Alkaline Zn–Mno2 Batteries with Synchrotron X-Ray and Neutron Tomographies. *Appl. Phys. Lett.* **2007,** *90*, 214102-214105; (b) Sun, F.; Markötter, H.; Zhou, D.; Alrwashdeh, S. S. S.; Hilger, A.; Kardjilov, N.; Manke, I.; Banhart, J., In Situ Radiographic Investigation of (De)Lithiation Mechanisms in a Tin-Electrode Lithium-Ion Battery. *ChemSusChem* **2016,** *9*, 946-950.
16. (a) Sun, F.; Markötter, H.; Manke, I.; Hilger, A.; Kardjilov, N.; Banhart, J., Three-Dimensional Visualization of Gas Evolution and Channel Formation inside a Lithium-Ion Battery. *Acs Appl. Mater. Interfaces* **2016,** *8*, 7156-7164; (b) Sun, F.; Markötter, H.; Dong, K.; Manke, I.; Hilger, A.; Kardjilov, N.;

Banhart, J., Investigation of Failure Mechanisms in Silicon Based Half Cells During the First Cycle by Micro X-Ray Tomography and Radiography. *J. Power Sources* **2016,** *321*, 174-184.
17. Zielke, L.; Barchasz, C.; Waluś, S.; Alloin, F.; Leprêtre, J. C.; Spettl, A.; Schmidt, V.; Hilger, A.; Manke, I.; Banhart, J.; Zengerle, R.; Thiele, S., Degradation of Li/S Battery Electrodes on 3d Current Collectors Studied Using X-Ray Phase Contrast Tomography. *Sci. Rep.* **2015,** *5*, 10921-10933.
18. Zielke, L.; Hutzenlaub, T.; Wheeler, D. R.; Chao, C.-W.; Manke, I.; Hilger, A.; Paust, N.; Zengerle, R.; Thiele, S., Three-Phase Multiscale Modeling of a Licoo2 Cathode: Combining the Advantages of Fib–Sem Imaging and X-Ray Tomography. *Adv. Energy Mater.* **2015,** *5*, 1401612-1401620.
19. Eastwood, D. S.; Bradley, R. S.; Tariq, F.; Cooper, S. J.; Taiwo, O. O.; Gelb, J.; Merkle, A.; Brett, D. J. L.; Brandon, N. P.; Withers, P. J.; Lee, P. D.; Shearing, P. R., The Application of Phase Contrast X-Ray Techniques for Imaging Li-Ion Battery Electrodes. *Nucl. Instrum. Meth. B* **2014,** *324*, 118-123.
20. Li, W.; Zheng, H.; Chu, G.; Luo, F.; Zheng, J.; Xiao, D.; Li, X.; Gu, L.; Li, H.; Wei, X.; Chen, Q.; Chen, L., Effect of Electrochemical Dissolution and Deposition Order on Lithium Dendrite Formation: A Top View Investigation. *Faraday. Discuss.* **2014,** *176*, 109-124.
21. Arakawa, M.; Tobishima, S.-i.; Nemoto, Y.; Ichimura, M.; Yamaki, J.-i., Lithium Electrode Cycleability and Morphology Dependence on Current Density. *J. Power Sources* **1993,** *43*, 27-35.
22. Grande, L.; von Zamory, J.; Koch, S. L.; Kalhoff, J.; Paillard, E.; Passerini, S., Homogeneous Lithium Electrodeposition with Pyrrolidinium-Based Ionic Liquid Electrolytes. *Acs Appl. Mater. Interfaces* **2015,** *7*, 5950-5958.
23. Love, C. T., Thermomechanical Analysis and Durability of Commercial Micro-Porous Polymer Li-Ion Battery Separators. *J. Power Sources* **2011,** *196*, 2905-2912.
24. Gonzalez, J.; Sun, K.; Huang, M.; Lambros, J.; Dillon, S.; Chasiotis, I., Three Dimensional Studies of Particle Failure in Silicon Based Composite Electrodes for Lithium Ion Batteries. *J. Power Sources* **2014,** *269*, 334-343.
25. Jana, A.; Ely, D. R.; García, R. E., Dendrite-Separator Interactions in Lithium-Based Batteries. *J. Power Sources* **2015,** *275*, 912-921.
26. Ryou, M.-H.; Lee, Y. M.; Lee, Y.; Winter, M.; Bieker, P., Mechanical Surface Modification of Lithium Metal: Towards Improved Li Metal Anode Performance by Directed Li Plating. *Adv. Funct. Mater.* **2015,** *25*, 834-841.
27. Heine, J.; Krüger, S.; Hartnig, C.; Wietelmann, U.; Winter, M.; Bieker, P., Coated Lithium Powder (Clip) Electrodes for Lithium-Metal Batteries. *Adv. Energy Mater.* **2014,** *4*, 1300815-1300822.
28. Yan, K.; Lu, Z.; Lee, H.-W.; Xiong, F.; Hsu, P.-C.; Li, Y.; Zhao, J.; Chu, S.; Cui, Y., Selective Deposition and Stable Encapsulation of Lithium through Heterogeneous Seeded Growth. *Nat. Energy.* **2016,** *1*, 16010-16018.
29. Zheng, G.; Lee, S. W.; Liang, Z.; Lee, H.-W.; Yan, K.; Yao, H.; Wang, H.; Li, W.; Chu, S.; Cui, Y., Interconnected Hollow Carbon Nanospheres for Stable Lithium Metal Anodes. *Nat Nano* **2014,** *9*, 618-623.
30. Abramoff, M. D.; Magalhães, P. J.; Ram, S. J., Image Processing with Imagej. *Biophotonics international* **2004,** *11*, 36-42.

2.1 Morphological evolution of lithium microstructures

2.1.1 Supporting information

Morphological evolution of electrochemically plated/stripped lithium microstructures investigated by synchrotron X-ray phase contrast tomography

Fu Sun,[*†,§] Lukas Zielke,[‡] Henning Markötter,[†,§] Andre Hilger,[†,§] Dong Zhou,[†,§] Riko Moroni,[‡] Roland Zengerle,[‡] Simon Thiele,[‡,#] John Banhart[†,§] and Ingo Manke[§]

[†]Institute of Material Science and Technologies
Technical University Berlin
Strasse des 17. Juni 135, 10623 Berlin, Germany
[‡]Laboratory for MEMS Applications, IMTEK Department of Microsystems Engineering
University of Freiburg
Georges-Koehler-Allee 103, 79110 Freiburg, Germany
E-mail: Lukas.Zielke@imtek.de
[§]Helmholtz Centre Berlin for Materials and Energy
Hahn-Meitner-Platz 1,
14109 Berlin, Germany
[#]FIT, University of Freiburg
Georges-Köhler-Allee 105, 79110 Freiburg, Germany,
*Email: fu.sun@helmholtz-berlin.de

This section includes:

Detailed cycling procedures for all cells

Figures S1-S8

Captions for the Supplementary Movies

Figure S1 and S2 specify the locations of the cross-sections of the Li/Li symmetrical cells shown in Figure 2 and Figure 3, respectively.
All the symmetrical Li/Li cells and Li/Si half cells are galvanostaticly discharged and charged using an IviumStat electrochemical workstation. The Li/Li-2 cell was discharged at 0.3 mA cm^{-2} for 10 h and a tomography was conducted as shown in Figure 2d-f. The corresponding discharge curve is displayed in Figure S3a. After this, the Li/Li-2 cell was continued to be galvanostatically discharged for 19 h at 0.3 mA cm^{-2} and another tomography was conducted, as shown in Figure 2g-i. The corresponding discharge curve is shown in Figure S3b. Finally, the Li/Li-2 cell was charged for 19 h at 0.3 mA cm^{-2} and the third tomography of this cell was conducted as shown in Figure 2j-l. The corresponding charge curve is shown in Figure S3c. Note that during the

prolonged discharge and charge process, there is a rise in the discharge or charge voltage. The observed rise in the overpotential is similar to that reported previously[1] and the reason may be a continuous electrolyte loss during prolonged cycling[2].

The Li/Li-3 cell was discharged at a constant current of 0.3 mA cm^{-2} for 30 h and after that a tomography was conducted as shown in Figure 2m-o. The corresponding discharge curve is shown in Figure S4. It has to be noted that the voltage fluctuation may arise from the growing LmS in agreement with previous reports[3].

For the Li/Si-1cell, a pristine-state (without any discharge or charge) tomography was conducted as shown in Figure3a-c. After that, the Li/Si-1 cell was discharged for 15 h and then charged for 5 h at 0.7 mA cm^{-2}. After this cycle, another tomography was conducted as shown in Figure 3g-i. The corresponding discharge and charge curve is shown in Figure S5.

The Li/Si-2 cell was galvanostatically discharged for 15 h at 0.3 mA cm^{-2} and then a tomography was conducted as shown in Figure 3d-f. The corresponding discharge curve is shown in Figure S6.

For Li/Si-3 cell, it experienced 5 cycles with different current densities: for the 1st cycle the current was of 0.714 mA cm^{-2} for 1.3 hours; for the 2nd cycle the current was of 0.706 mA cm^{-2} for 1.7 hours; for the 3rd cycle the current was of 0.3 mA cm^{-2} for 2.4 hours; for the 4th cycle the current was of 0.159 mA cm^{-2} for 13 hours; for the 5th cycle the current was of 0.083 mA cm^{-2} for 44 hours. The discharge/charge curves are shown in Figure S7. After these procedures, one tomography was conducted as shown in Figure 3j-l.

For a 3D representation of Li/Li symmetrical cells it is useful to enhance the phase contrast between LmS, lthium and separator[4]. We used a phase backpropagation filter prior to tomographic reconstruction of all the Li/Li cells as displayed in Figure S8.

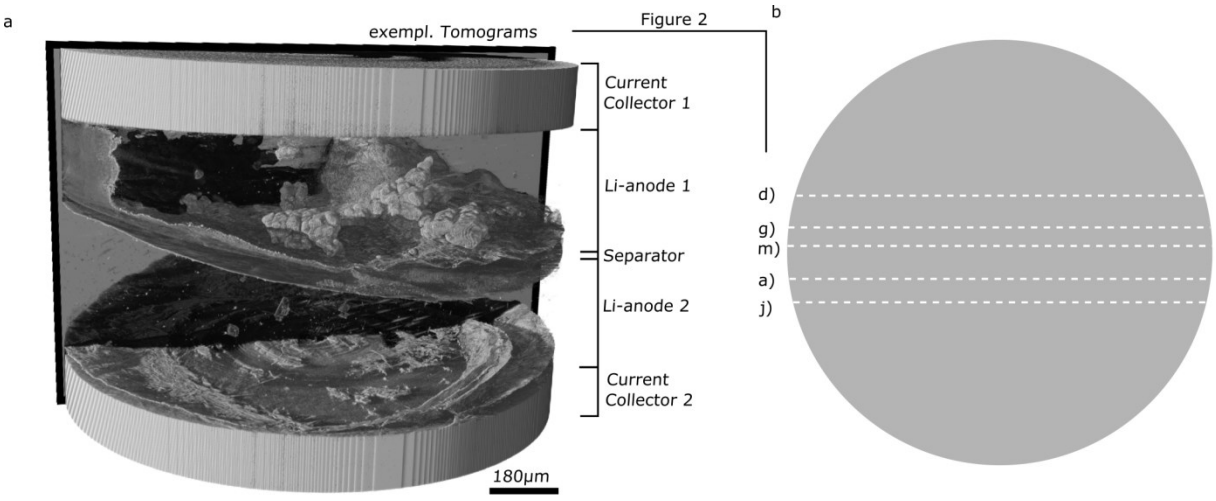

Figure S1 Location of the cross-sections shown in Figure 2 in the main text. a, a 3D presentation of the assembled Li/Li cells. b, the dashed lines a), d), g), j) and m) are indicative of the locations of the cross-section planes shown in Figure 2a, d, g, j and m.

2.1 Morphological evolution of lithium microstructures

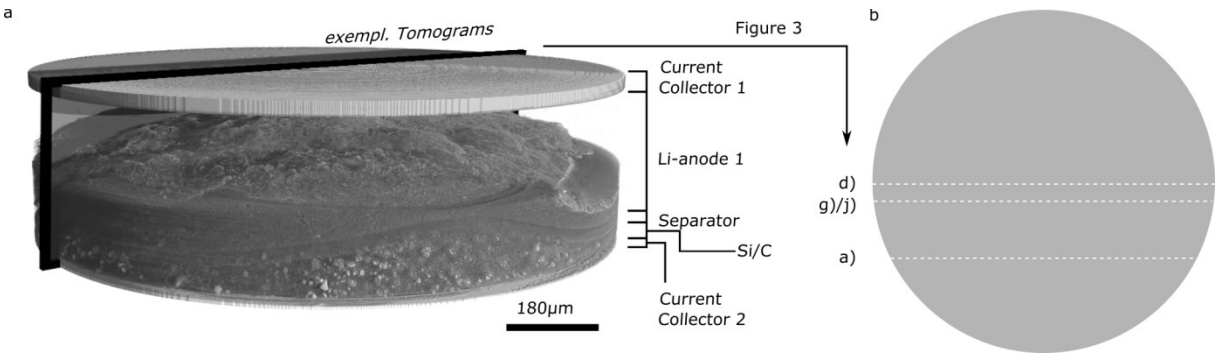

Figure S2 Location of the cross-sections shown in Figure 3 in the main text. a, a 3D presentation of the assembled Li/Si cells. b, the dashed a), d), and g)/j) lines are indicative of the locations of the cross-section planes in Figure 3a, d, g and j.

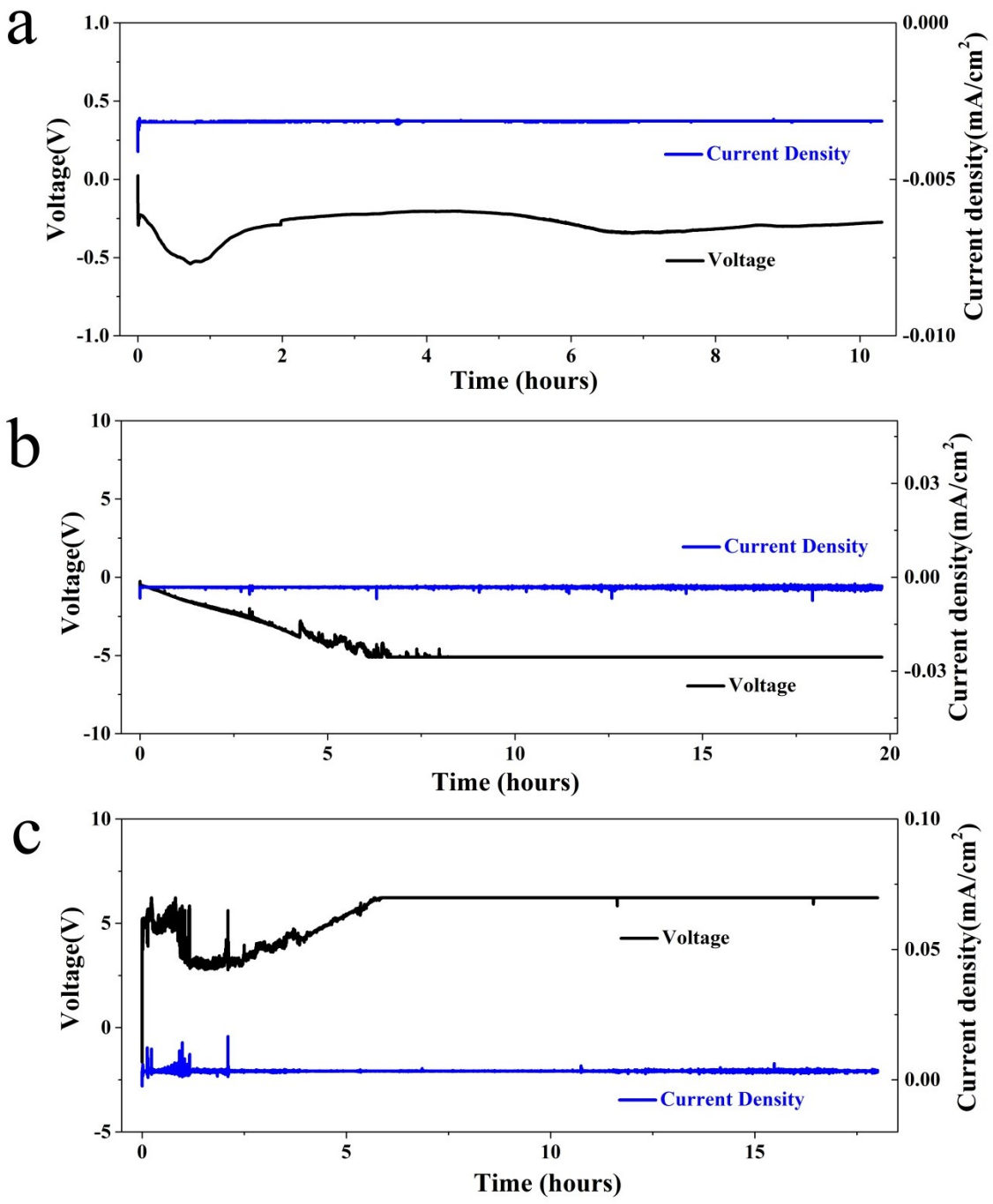

Figure S3 Cycling profiles of Li/Li-2 cell. a, discharged at 0.3 mA cm^{-2} for 10 h. b, discharged for another 19 h at 0.3 mA cm^{-2}. c, finally charged for 19 h at 0.3 mA cm^{-2}.

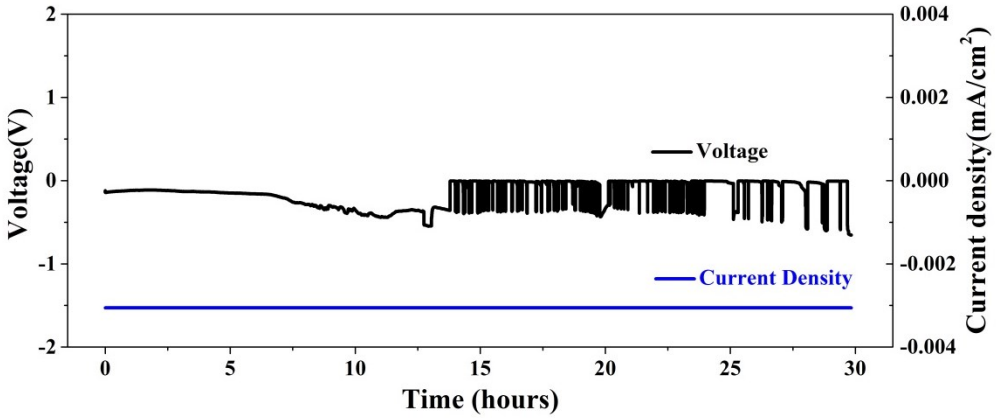

Figure S4 Cycling profiles of Li/Li-3 cell discharged at 0.3 mA cm^{-2} for 30 h.

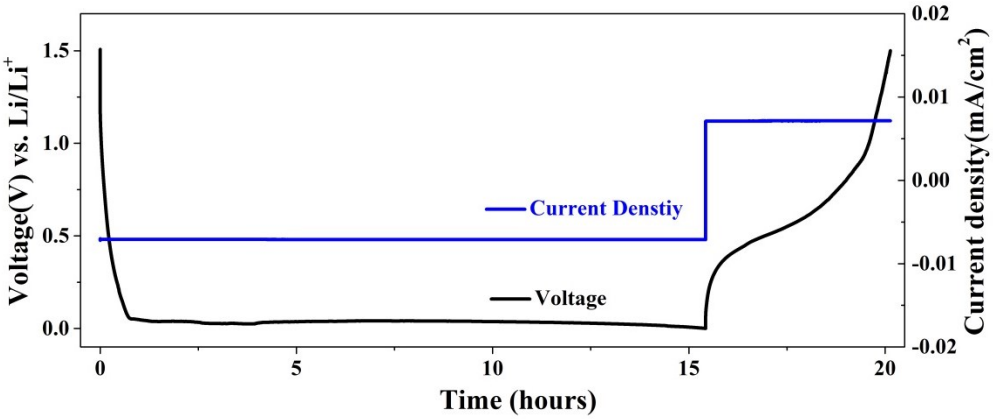

Figure S5 Cycling profiles of Li/Si-1 cell first discharged for 15 h and then charged for 5h at 0.7 mA cm^{-2}.

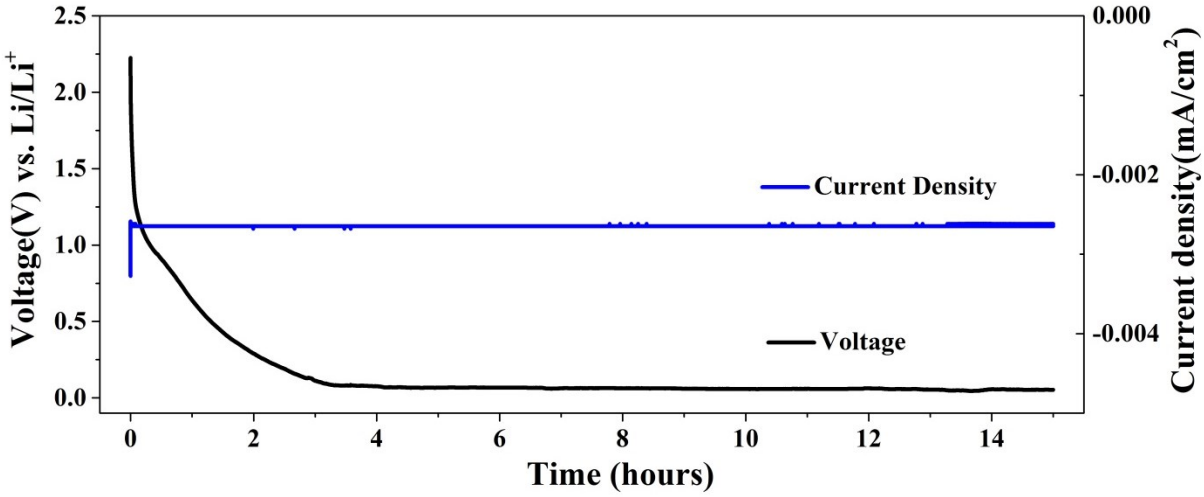

Figure S6 Cycling profile of Li/Si-2 cell discharged for 15 h at 0.26 mA cm^{-2}.

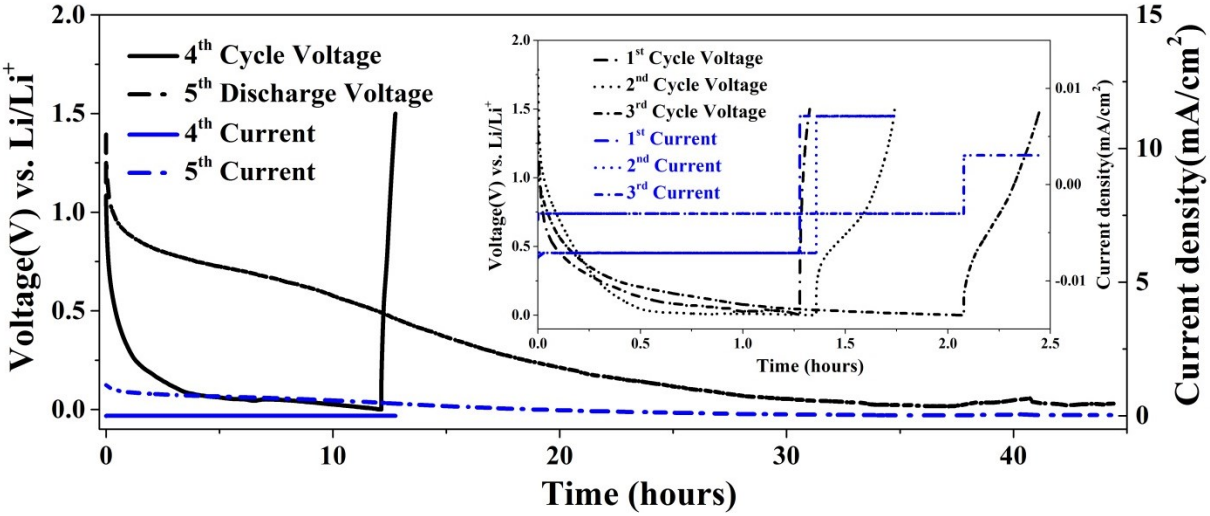

Figure S7 Cycling profiles of Li/Si-3 cell. The inset shows the 1st, 2nd and 3rd cycle; the 4th cycle and 5th discharge curve are shown in the main figure.

2.1 Morphological evolution of lithium microstructures

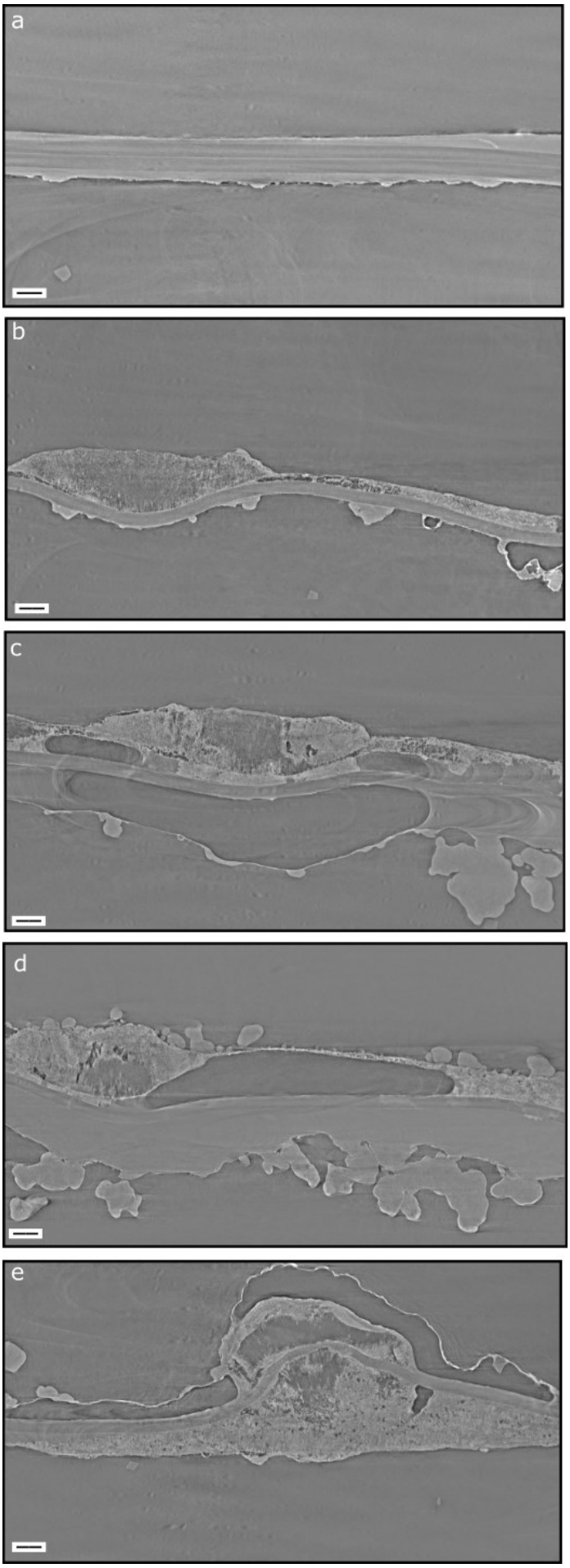

Figure S8 Cross-sections of reconstructed Li/Li symmetrical cells after using phase backpropagation filtering. a, tomography of pristine Li/Li-1 cell. b, tomography slice of Li/Li-2 cell after 10 h of discharge at 0.3 mA cm^{-2}. c, tomography slice of Li/Li-2 cell after another 19 h of discharge at the same current density. d, tomography slice of Li/Li-2 cell after 19 h of charge at the same current density. e, tomography slice of Li/Li-3 sample after 30 h of discharge at 0.3 mA cm^{-2}.

Captions for the Supplementary Movies

http://pubs.acs.org/doi/abs/10.1021/acsnano.6b03939

SM-1-Li-Li-1_Pristine
SM-1-Li-Li-1_Pristine-Colored-Figure2a-c
SM-2-Li-Li-2_Discharge for 10 Hours
SM-2-Li-Li-2_Discharge for 10 Hours-Colored-Figure 2d-f
SM-3-Li-Li-2_Discharge for another 19 Hours
SM-3-Li-Li-2_Discharge for another 19 Hours-Colored
SM-4-Li-Li-2_Charge for 17 Hours
SM-4-Li-Li-2_Charge for 17 Hours-Colored-Figure 2j-l
SM-5-Li-Li-3_Discharge for 30 Hours
SM-5-Li-Li-3_Discharge for 30 Hours-Colored-Figure 2m-o
SM-6-Li-Si-1_Pristine
SM-6-Li-Si-1_Pristine-Colored-Figure 3a-c
SM-7-Li-Si-2_Discharged for 15 Hours
SM-7-Li-Si-2_Discharged for 15 Hours-Colored-Figre 3d-f
SM-8-Li-Si-1_Discharged for 15 Hours and then Charged for 5 Hours
SM-8-Li-Si-1_Discharged for 15 Hours and then Charged for 5 Hours-Colored-Figure 3g-i
SM-9-Li-Si-3_Cycled for 5 cycles
SM-9-Li-Si-3_Cycled for 5 cycles-Colored

References

1. Harry, K. J.; Hallinan, D. T.; Parkinson, D. Y.; MacDowell, A. A.; Balsara, N. P., Detection of Subsurface Structures Underneath Dendrites Formed on Cycled Lithium Metal Electrodes. *Nat Mater* **2014,** *13*, 69-73.
2. (a) Sarasketa-Zabala, E.; Aguesse, F.; Villarreal, I.; Rodriguez-Martinez, L. M.; López, C. M.; Kubiak, P., Understanding Lithium Inventory Loss and Sudden Performance Fade in Cylindrical Cells During Cycling with Deep-Discharge Steps. *J. Phys. Chem. C* **2015,** *119*, 896-906; (b) Cai, L.; An, K.; Feng, Z.; Liang, C.; Harris, S. J., In-Situ Observation of Inhomogeneous Degradation in Large Format Li-Ion Cells by Neutron Diffraction. *J. Power Sources* **2013,** *236*, 163-168.
3. Wu, H.; Zhuo, D.; Kong, D.; Cui, Y., Improving Battery Safety by Early Detection of Internal Shorting with a Bifunctional Separator. *Nat Commun* **2014,** *5*, 5193-5199.
4. Eastwood, D. S.; Bayley, P. M.; Chang, H. J.; Taiwo, O. O.; Vila-Comamala, J.; Brett, D. J. L.; Rau, C.; Withers, P. J.; Shearing, P. R.; Grey, C. P.; Lee, P. D., Three-Dimensional Characterization of Electrodeposited Lithium Microstructures Using Synchrotron X-Ray Phase Contrast Imaging. *Chem. Commun.* **2015,** *51*, 266-268.

2.2 Break-down of the separator

A Study of the Mechanisms of Internal Short Circuit in a Li/Li cell by Synchrotron X-ray Phase Contrast Tomography

Fu Sun,*[,†,§] Riko Moroni,[‡] Kang Dong,[†,§] Henning Markötter,[§] Dong Zhou,[†,§] André Hilger,[§] Lukas Zielke,[‡] Roland Zengerle,[‡] Simon Thiele,[‡,#] John Banhart,[†,§] and Ingo Manke[§]

[†]Institute of Material Science and Technologies
Technical University Berlin
Strasse des 17. Juni 135, 10623 Berlin, Germany
[‡]Laboratory for MEMS Applications, IMTEK Department of Microsystems Engineering
University of Freiburg
Georges-Koehler-Allee 103, 79110 Freiburg, Germany
[§]Helmholtz Centre Berlin for Materials and Energy
Hahn-Meitner-Platz 1,
14109 Berlin, Germany
[#]FIT, University of Freiburg
Georges-Köhler-Allee 105, 79110 Freiburg, Germany

ABSTRACT

Synchrotron in-line phase contrast X-ray tomography was employed to investigate the underlying internal cell deformation and degradation caused by an internal short circuit (ISC). By comparing the reconstructed tomography of one uncycled Li/Li cell and one short-circuited Li/Li cell for the first time, we experimentally demonstrate: 1) most of the electrochemically deposited lithium microstructures (LmSs) are electrochemically inert during the following Li stripping, 2) the electrochemical stripping and plating process during discharge and charge are highly inhomogeneous, 3) delamination into three native layers and the partial melting of the commercial trilayer Celgard® 2325 separator can develop during real ISC event, 4) decomposition of the solid electrolyte interface (SEI) covering LmSs and partial melting and re-solidifying of porous LmS can also occur due to the localized excessive Joule heating resulted from the ISC event. These unexpected insights into the internal cell degradation and deformation mechanisms caused by ISC shed new lights on enhancing the properties of separators and could open up new design principles and opportunities to fundamentally improve the reliability and safety of current- and/or next-generation LIBs.

2.2 Break-down of the separator

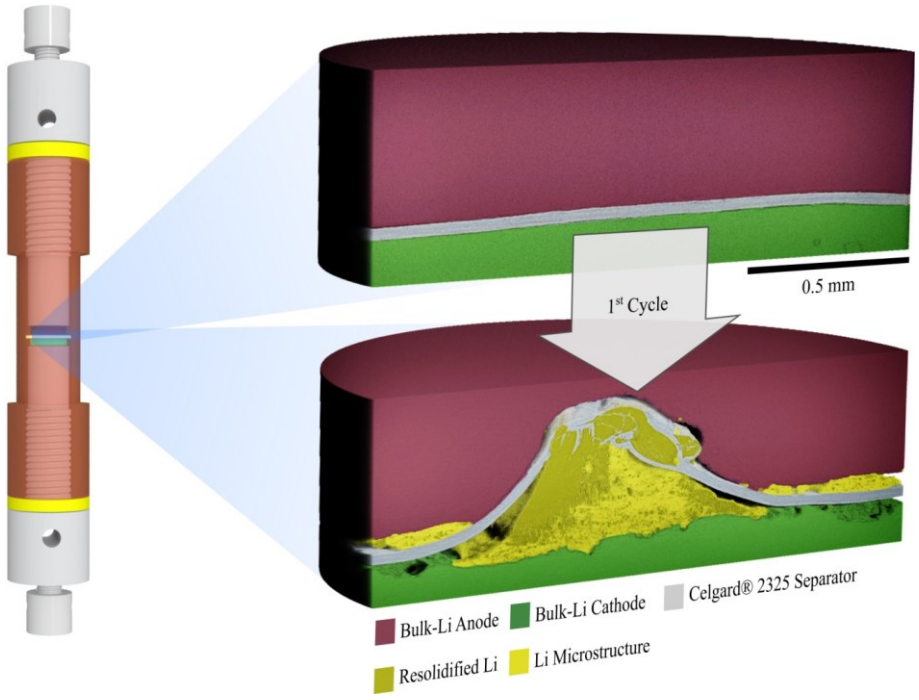

Abstract Graphic

Keywords: lithium microstructure; internal short circuit; dendrites; separator; lithium ion battery; synchrotron X-ray phase contrast tomography

Introduction

Safety and reliability of lithium ion batteries (LIBs) that are targeted for high power and high energy applications are of major concern.[1-8] For example, the most promising Li metal-based battery technologies such as lithium-sulphur and lithium-air batteries have not been successfully commercialized mainly because of the uncontrolled growth of lithium microstructures (LmSs) such as dendrites, fibers, whiskers and moss etc., which can cause internal short circuit (ISC) of a cell and result in catastrophic fires or even explosions.[9-11] Recent field incidents such as fires on a Boeing 787 Dreamliner flight and in a Tesla electric vehicle (EV) or even the Samsung note 7 phone's exploding are believed to be closely linked to ISC in LIBs.[12-14] Furthermore, the soaring number of EVs in use additionally adds tremendous weight to safety and reliability in present- and next-generation LIB technology. In order to gain a detailed understanding of internal cell deformation and degradation leading to ISCs, various testing techniques such as using a blunt rod to indent a cell as developed by the Underwrites Laboratory and the U.S. Advanced Battery Consortium, surface indentation or pinch test developed by Motorola, and the forced ISC approach developed by the Battery Association of Japan have been employed.[15] The purpose of these tests is to create a small break in the separator by exerting an external force, mimicking the ISC events that may lead to failed accidents in LIBs. Unfortunately, recent investigations have demonstrated that such mechanical intrusion methods are not entirely representative of true spontaneous ISCs due to the destructive and post-mortem nature of characterization, which

eliminates much of the *in situ* deformation information.[16, 17] Although a non-mechanical approach to initiate an ISC has been reported by Christopher *et al.* by using different melting point metals and metal alloys,[15] the challenge of a detailed characterization of an ISC by sophisticated characterization tool in a non-destructive way remains.

To this end, various investigations employing light microscopy,[18] nuclear magnetic resonance[19] (NMR) and ^{7}Li magnetic resonance imaging[20] (MRI), scanning electron microscopy[21, 22] (SEM) and transmission electron microscopy[23, 24] (TEM) have been carried out to characterize the complicated LmS growth, which is regarded to lead to the ultimate ISC event. However, these reports mainly focus on the growth of LmSs and ignore the accompanying morphological evolution of the separators as well as the correlation between growing LmS and cell failure. Hitherto, no experiments have been reported in the battery community that aims at investigating the mechanisms of ISCs leading to (internal) cell degradation. Whilst different strategies have been proposed to avoid ISC-induced battery failures,[25-32] it remains of fundamental interest to directly visualize the ISC caused by growing LmSs in order to fundamentally understand the failure mechanism of LIBs and thereafter be able to improve their properties for current and future usage.

Recently, synchrotron X-ray imaging has evolved into a powerful characterization tool in materials science[33] and has enabled battery researchers to obtain unprecedented insights into the underlying degradation mechanisms of LIBs non-destructively.[34, 35] Among these, Eastwood *et al*. have characterized the 3D microstructure of electrodeposited LmSs by synchrotron in-line phase contrast X-ray tomography, demonstrating that this technique is a suitable tool for investigating LmSs without removing the sample from its as-grown environment.[36] Moreover, Harry *et al*. have characterized the LmS and the LmS-punctured separator simultaneously, further demonstrating that this technique is also a suitable and powerful tool for studying the LmS and the separator simultaneously in a short circuited cell.[37] Nevertheless, Harry *et al*. have employed a self-made polystyrene-block-poly (ethylene oxide) copolymer electrolyte as separator and they conducted their characterization *ex situ*. From a practical point of view though, non-destructive investigations using widely adopted commercial separators would allow for more general conclusions on how and why separators fail and ISC develops. Obviously, fundamental research on actual kinematic processes of ISC associated with commercial separators is highly desired.

Currently, the most widely used commercial separators in LIBs are made of polyolefin materials such as polyethylene (PE) and polypropylene (PP) due to their proper pore structure, good mechanical strength and acceptable costs.[26, 28] In this work, the commercially available trilayer Celgard® 2325 separator[38, 39] is employed and its failure mechanism leading to an internal ISC, caused by the growing LmS, is investigated via in-line phase contrast X-ray tomography. The separator investigated here is made of a PE layer of a low melting point (m.p. 135°C), sandwiched between two PP layers of higher melting point (m.p. 165°C). In the case of over-heating, the middle PE layer will shut down the cell automatically by blocking ionic pathways upon melting, while the two PP layers can still provide mechanical strength to prevent physical contact of the electrodes. This proposed shutdown function is meant to dispel safety concerns related to ISCs in LIBs.

2.2 Break-down of the separator

Here, we present a non-destructive characterization of an ISC in a Li/Li symmetrical cell for the first time. We demonstrate that: 1) most of the electrochemically deposited LmSs are electrochemically inert during ensuing Li stripping, 2) electrochemical stripping and plating during discharge and charge are highly inhomogeneous, 3) delamination into three native layers and partial melting of the trilayer Celgard® 2325 separator can develop in a real ISC event, 4) decomposition of the solid electrolyte interface (SEI) covering LmSs and partial melting and re-solidifying of porous LmSs can also occur due to localized excessive Joule heating resulting from the ISC. These unexpected findings, which are not accessible by conventional electrochemical and morphological characterizations, shed new light on the kinematic process of ISC and could open up new design principles and opportunities to fundamentally improve the safety and reliability of current- and next-generation LIBs.

Cell preparation, imaging setup and data acquisition

A proof-of-concept cell that is compatible with synchrotron X-ray tomography is designed and fabricated, as shown in Figure 1 along with a schematic illustration of the synchrotron setup at the BAMline, BESSY II in Berlin, Germany.[40-42] The electrochemical validation of the presently designed cell can be found in our previous reports.[43, 44] SEM images of the surface and cross-section of the employed trilayer Celgard® 2325 separator are shown in Figure 2. From Figure 2a, the distinct slit-pore structure that results from extrusion and unidirectional stretching during the dry process manufacture method is clearly observed.[38] The three-layer structure of the PP/PE/PP sandwich with a total thickness of ~25 μm is shown in Figure 2b.[38, 39] Symmetrical cells made of Li metal electrodes, the trilayered separator and the standard electrolyte (1 M $LiPF_6$ in ethylene carbonate (EC) and ethyl methyl carbonate (EMC) (EC/EMC=50/50 (vol/vol)) were assembled. Two Li symmetrical cells were investigated here, one being the pristine state (without any cycling, hereafter named Li/Li-1) and the other one being short circuited after 13.4 h charge (evidenced by a sudden voltage drop shown in Figure 2d, hereafter named Li/Li-2). Both cells were mounted on the set-up for characterization without prior disassembly. Every tomography was recorded by a detector system with 0.438 μm pixel size with 2200 projections covering 180° rotation angle. The field of view (FoV) was (1.7 × 1.2) mm^2 (length × height). Detailed cycling parameters and the procedure of normalization, tomography reconstruction and 3D presentation are given in Experimental Methods.[45, 46]

2.2 Break-down of the separator

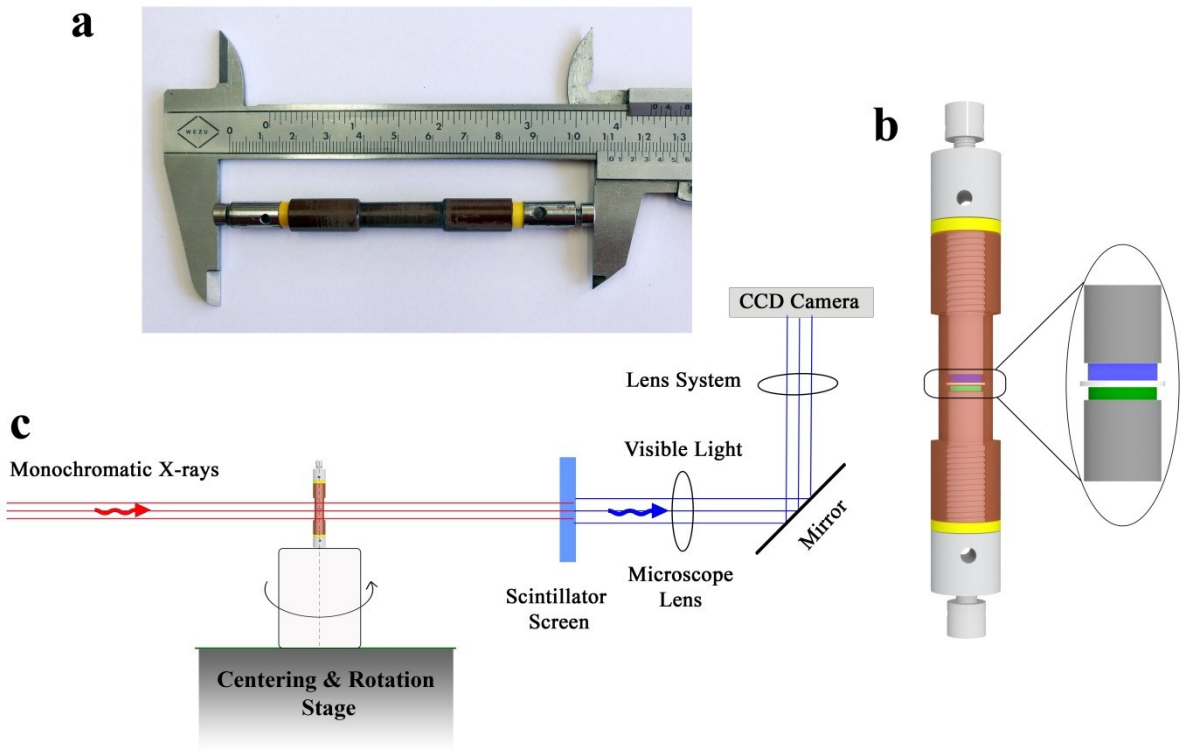

Figure 1. a) Photograph of the fabricated proof-of-concept cell. b) Corresponding schematic representation of the cell consisting of a polyamide-imide housing (brown), two screw electrodes and retaining screws each on top (light grey), two sealing rings (yellow), a porous separator (white) sandwiched between two electrodes (blue and green). c) Schematic representation of the experimental setup of the tomography station at the BAM*line* at BESSY II, Helmholtz-Zentrum Berlin, Germany. Figure 1 is adapted from ref[44], with permission from the American Chemical Society.

Morphological characterization of Li/Li-1 cell and electrochemical characterization of Li/Li-2 cell

A cross-sectional X-ray tomographic slice of the uncycled Li/Li-1 cell is shown in Figure 2c, in which the two Li electrodes and the separator are clearly discernable due to the light and dark boundaries between them arising from in-line phase contrast.[36, 47] The interface between the Li electrode and the separator of Li/Li-1 cell is flat and gapless. The Li/Li-2 cell was galvanostatically "cycled" until an internal short circuit occurred. The voltage curve of the Li/Li-2 cell measured at a current density of 0.3 mA cm^{-2} for 18 h of discharge and then for 13.4 h of charge is shown in Figure 2d (discharge corresponds to Li stripping from the Li anode, charge corresponds to Li plating onto the Li anode. The anode and cathode are defined during the 1st discharge and are also used during the 1st charge). As indicated by two black arrows, there is a steep voltage dip at the beginning of Li metal deposition during both discharge and charge. The observed overpotential here is typical of a nucleation mechanism, which signifies the initiation of the growth of Li nuclei.[48, 49] During the charge process, the sudden voltage drop pointed by the red arrow in Figure 2d indicates that ISC has occurred. The cross section of the short-circuited Li/Li-2 cell displays a significantly different morphology compared to that of the Li/Li-1 cell. A

panoramic view of this situation is shown in Figure 3 (Figure 3b is a reconstructed raw data tomogram allowing for a comparison with Figures 3c-h showing data after filtering and segmentation). Enlarged details are shown in Figure 4 showing both reconstructed raw data as well as segmented data. The complete three-dimensional visualization of the internal structure of the Li/Li-1 and Li/Li-2 cells is shown in a supporting movie.

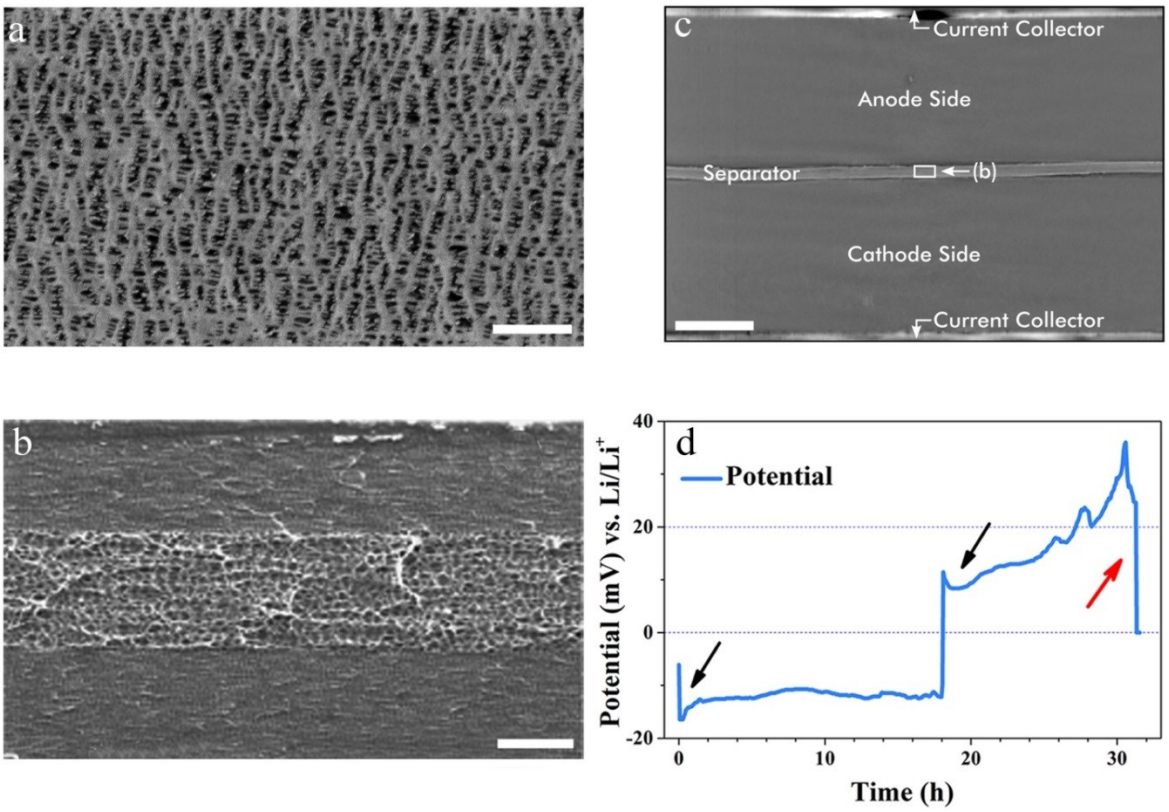

Figure 2. a) Plane view and b) Cross-sectional view of the investigated trilayer Celgard® 2325 separator as obtained by scanning electron microscopy (SEM). c) Reconstructed in-line X-ray phase contrast tomography slice of the pristine Li/Li-1 cell. d) Electrochemical characterization of the investigated Li/Li-2 cell (the black arrows point an abrupt voltage dip; the red arrow points a sudden internal short circuit). Scale bars in a), b), and c) are 1 µm, 5 µm, and 125 µm long, respectively. Figure 2b is adopted from Ref.[38], with permission from the American Chemical Society.

Preliminary inspection of morphological structures inside Li/Li-2 cell

Based on our previous investigation of morphological evolution of electrochemically plated/stripped LmSs in Li/Li symmetrical cells,[43] kinetic ISC formation induced by growing LmSs in Li/Li-2 cell is elaborately studied. Figures 3 and 4 show various horizontal and cross-sectional slices of the short-circuited Li/Li-2 cell. The initially flat electrode/separator interfaces have turned into distinctively rugged interfaces with a large cavity within the Li anode and

numerous electrochemically deposited LmSs on the surface of the Li cathode as shown in Figure 3b-e and Figure 4a,f (middle area of dark and light yellow LmS and deformed separator of gray). During the 1st discharge, the total electron transfer (calculated from the external circuit) is 0.986 C (with the assumption that the total charge transfer of Li^+ inside the Li/Li-2 sample during the 1st discharge occurs within the FoV, the same assumption for the 1st charge), this results in $M_{cathode} = 10^{-5}$ mol of Li that is stripped from the anode (generating a large cavity) and subsequently plated onto the surface of the Li cathode (developing numerous LmSs). Simultaneously, the separator is stretched and pushed into the cavity formed within the anode by the growing LmSs. These phenomena are clearly shown in Figure 3 and Figure 4. Furthermore, as can be clearly observed from Figure 3c,d (pink arrows) and Figure 4e (light blue lines), cleavage of the separator into its three native layers takes place, which contributes to a decreased chord length of the separator, see Figure 5b (orange line). The significant deformation and unexpected cleavage of the separator implies that enormous mechanical stresses are generated by the growing LmSs. According to the manufacturer,[38, 39] the Celgard® separator has a high mechanical strength (in terms of tensile strength along both the machine direction (MD, 1900 kg/cm^2) and the transverse direction (TD, 135 kg/cm^2)) and puncture strength (300 g/cm^2).[39] This observation suggests that the current mechanical property of the separator cannot withstand the enormous mechanical stress caused by the growing LmSs and thus has to be further improved. During the 1st charge, the total charge transfer after the immediate short circuit is 0.788 C, i.e. about $M_{anode} = 0.82\times10^{-5}$ mol of Li is stripped from the cathode and then plated onto the surface of the Li anode.

Notably, two observations regarding the previously formed LmSs (on the surface of the Li cathode, beneath the separator) and newly formed LmSs (on the surface of the Li anode, above the separator) are noted: 1) most of the previously formed LmS undergoes no electrochemical dissolution (evidenced by the remaining LmSs, beneath the separator in the middle of the FoV, dark yellow and light yellow shown in Figure 3b-e and Figure 4a,f). It is the original Li bulk cathode to compensate for the depletion of Li ions in the electrolyte used to conduct charge transfer (as evidenced by the nascently formed cavities within the Li cathode as shown by the white diamonds in Figure 3c-e and enlarged Figure 4d); 2) It is the peripheral region of the Li anode onto which newly LmS is preferentially electrochemically deposited (above the separator, shown by the white triangles in Figure 3c-e and enlarged Figure 4d), in correspondence to the regions of nascently formed cavities within the Li cathode (as marked by white diamonds in Figure 3c-e and Figure 4d). The inhomogeneous Li stripping/plating during the 1st cycle is clearly shown in Figure 3h where LmSs in the middle surrounded by the separator are generated during the 1st discharge by deposition onto the surface of the Li cathode; in the regions outside the separator, the LmSs are generated during the 1st charge by deposition onto the surface of the Li anode. By further calculating the volume fraction of LmSs (deposited on the cathode during the 1st discharge and deposited on the anode during the 1st charge) as a function of radius r with respect to the central point located along z direction as shown in Figure 5a, one obtains volume fractions (blue straight line and dashed line) distribution as shown in Figure 5b. Obviously, the

cathode LmSs are concentrated in the middle while the anode LmSs are distributed in the peripheral region. From Figure 5b (orange line), one can also observe the calculated chord length of the separator (orange line): the separator located in the middle (small r) has delaminated into layers with small average thickness as deduced from the low average chord length. The reason lies that the separator in the middle undergoes cleavage (see above) and partial melting (see below for more detailed explanation), while the separator in the peripheral region (large r) is nearly intact. The observed fluctuations between ~25 µm to ~30 µm result from its morphological distortion.

2.2 Break-down of the separator

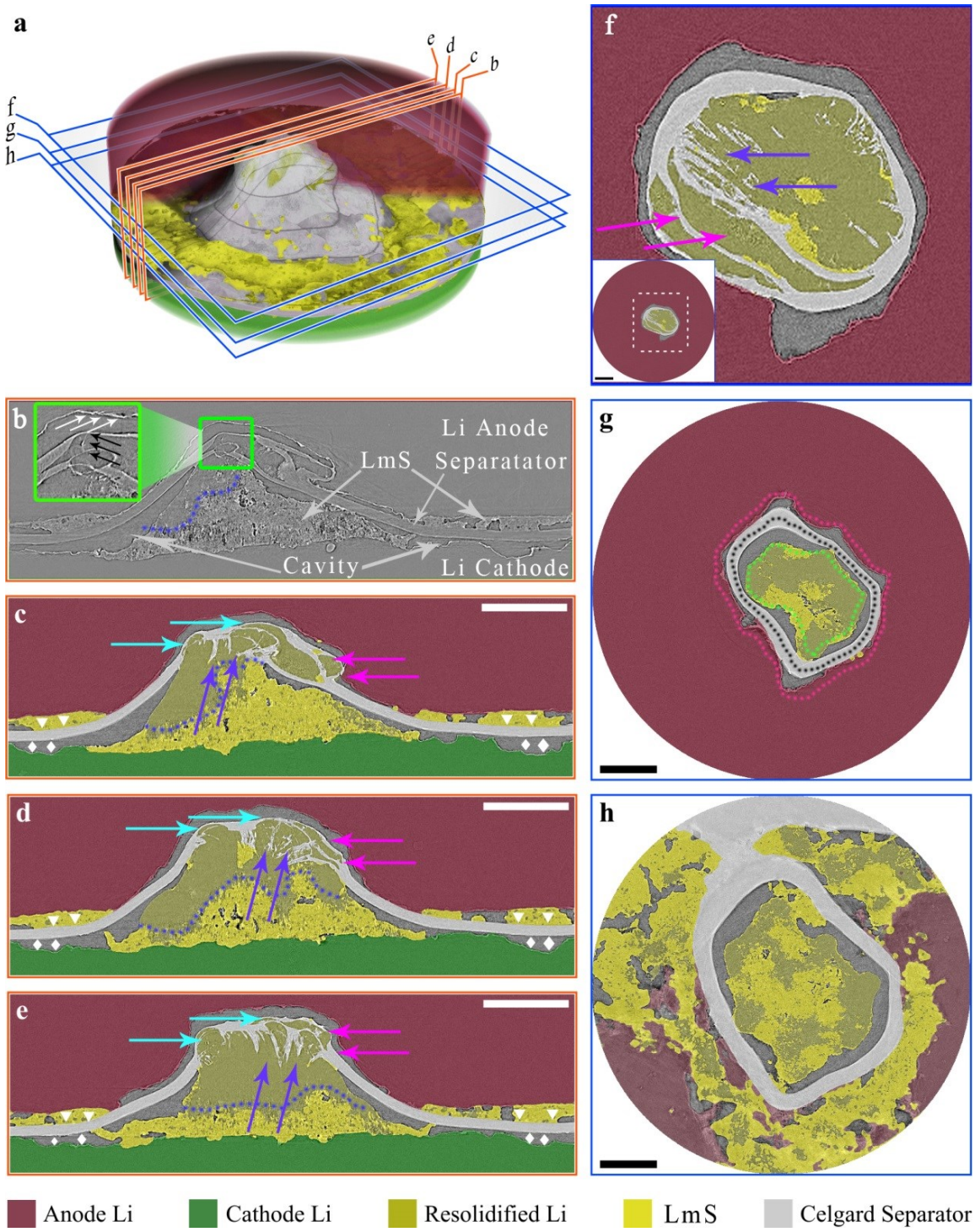

Figure 3. a) 3D visualization of the short circuited Li/Li-2 cell. Letters b-e denote selected cross-sectional planes; letters f-h selected horizontal planes. These planes of Figure b)-h) are all defined in a). b) Reconstructed raw data to which neither phase filter nor segmentation is applied, serves as comparison for the segmented figures c)-h). In the enlarged green rectangle, black arrows point at a fiber that may be the remnant of a Li dendrite or a molten separator, white arrows point at an irregular boundary resulting probably from a fused lithium dendrite. In c)-f), light blue arrows point at the partially molten separator; purple arrows point at dangling separator fibers; pink arrows point at the cleavage of the separator. The purple dotted line separates the resolidified Li and the porous LmSs. The interesting region in figure f) is

enlarged as indicated by white dotted rectangle in inset figure. In g), the pink, black and green dotted lines denote the contour of the anodic Li, the separator or the LmSs, respectively. In h), the electrochemically deposited LmSs clearly appears heterogeneous. All scale bars are 250 μm long.

Comparison of the amount of LmS between morphological and electrochemical characterizations

It has been reported that the electrochemically formed LmSs are still chemically active and that they can easily react with the electrolyte to form a solid electrolyte interface (SEI) coverage.[50] As a result, the SEI formed on the surface of LmSs during the 1st discharge electrically insulates most of the LmSs, thereby deactivating them electrochemically during the 1st charge.[51] Further confirmation of the electrochemical inertness of newly formed LmSs during ensuing electrochemical reaction is conducted by comparing the volume ratio of LmSs (plated onto the cathode and LmSs plated onto the anode, both calculated from X-ray tomography), with that of the amount of quantity ratio of LmSs (calculated from the external electron transfer during the 1st discharge and charge). The calculation of the volume ratio of the amount of LmSs via the reconstructed tomography dataset was done by counting the number of voxels belonging to the LmSs deposited onto the cathode ($V_{cathode}$) and the LmSs deposited onto the anode (V_{anode}). The reconstructed volume ratio $V_{cathode}$: V_{anode} = 10:5.5 is obtained. The ratio calculated from the electrochemical characterization with $M_{cathode}$: M_{anode} being 10:8. The tendency of the apparent deviation between these two ratios is expected and the reason stems from the limited FoV (see above). Nevertheless, the comparison between these two ratios confirms that most of the electrochemically formed LmSs during 1st discharge become electrochemically inactive during 1st charge, forming the well-know "dead LmSs".[50] This is the first time that the amount of electrochemically deposited LmSs calculated from morphological characterizations is directly correlated with the amount of external electron transfer measured electrochemically. Concerning the locations of preferential Li dissolution and LmS deposition during cycling, it has been suggested that such locations are electrochemically more active[9] or possess a high local ionic conductivity.[21] Li/Li cells employing differently shaped[52, 53] Li electrodes are planned to be further investigated in the future.

2.2 Break-down of the separator

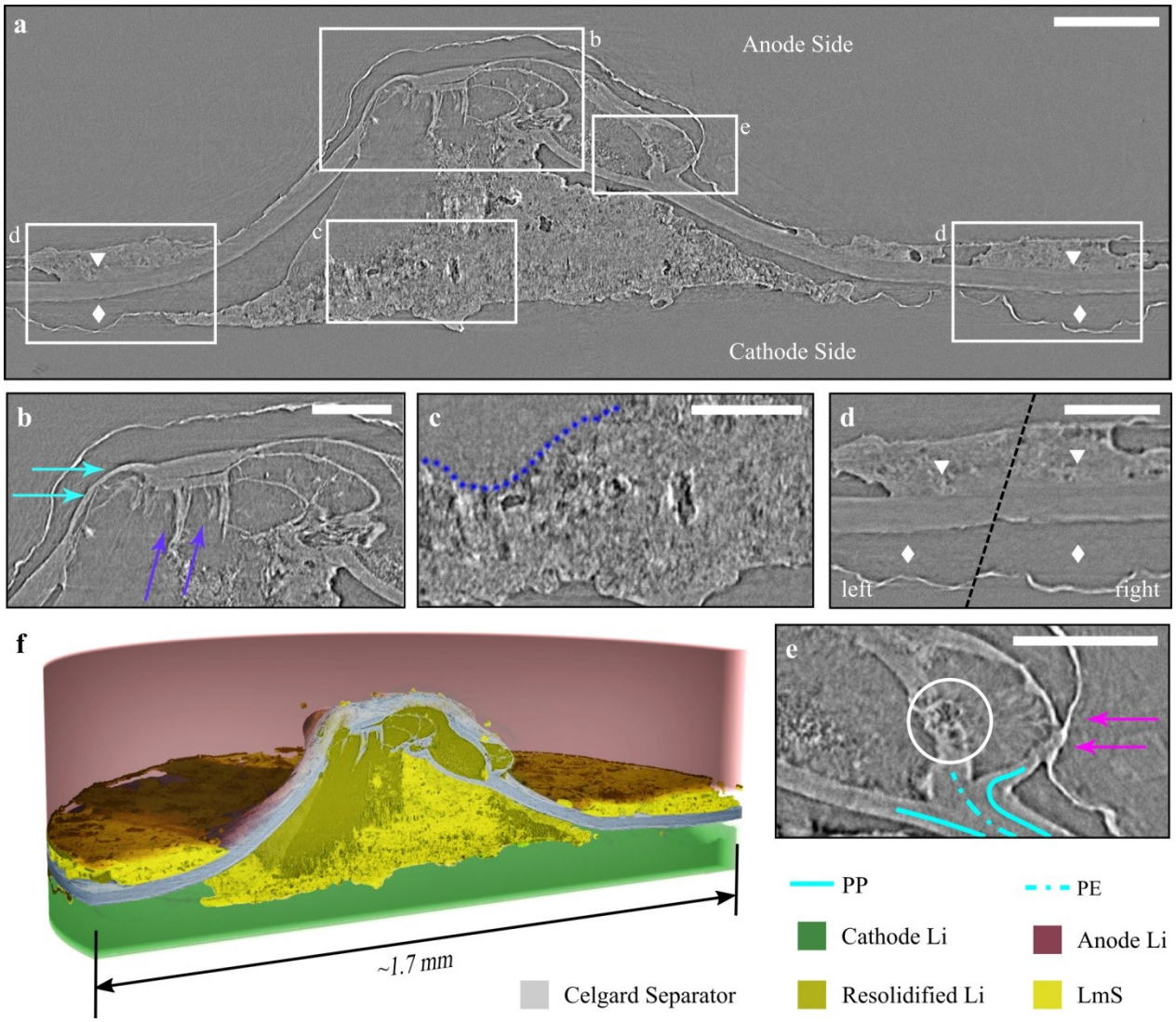

Figure 4. a) Exemplary tomogram of the short circuited Li/Li-2 cell. b)-e) Zoom in into regions defined in a). b) The original Li anode is electrochemically dissolved and partially filled by the separator and LmSs. The partially molten separator forming dangling fibers can also be seen (light blue and purple arrows). c) Exemplary slice shows electrochemically plated LmSs formed during the first discharge. Deposited porous LmS and compact solid LmS can be observed (separated by a purple dotted line). d) Newly formed cavities (diamonds) and LmSs (triangles) during the first charge. e) Cleavage and partial melting of the separator. Figures 4a-e are reconstructed raw data without phase filtering and segmentation. f) Three-dimensional visualization of the segmented data set. The scale bar in a) is 150 µm and scale bars in b)-e) are 75 µm long.

Close-up inspection of morphological structures inside Li/Li-2 cell

Apart from these findings, a close-up inspection of Figure 3 and Figure 4 further demonstrates: 3), there are two different phases of electrodeposited LmSs, one being porous LmS and the other being solid and compact LmS (both are shown in Figure 3b-e and Figure 4c,f by light yellow and dark yellow, respectively, separated by purple dotted line); 4) Some of the originally intact separator has completely disappeared (light blue arrows in Figure 3c-e and enlarged Figure 4b).

2.2 Break-down of the separator

At other positions the separator has molten into filamentary fibers that dangle into the solid and the compact LmS phase (purple arrows in Figure 3c-e and enlarged Figure 4b). This also contributes to the decreased average chord length of the separator in the middle region, see Figure 5b (orange line). The currently observed porous LmS phase agrees well with previous characterizations[36] and the highlighted pore structures are attributed by Eastwood *et al.* to the high-surface area lithium (HSAL) compound that is composed of decomposed lithium salt precipitates.[36] We assume that these HSAL compound are porous LmSs composed of SEI formed during electrochemical plating of Li and numerous voids within.[50] If one compares the porous LmS (light yellow) with the solid and compact LmS (dark yellow) one can conclude that the SEI and the voids in the porous LmS have been completely dissolved or depleted. Richard and Dahn have indeed identified an exothermic peak due to SEI decomposition at ~100 °C in accelerating rate calorimetry (ARC) studies of the thermal stability of LIBs.[54] Furthermore, Maleki *et al.* have also confirmed the exothermic SEI decomposition peak at ~100 °C by differential scanning calorimetry (DSC).[55] The currently observed disappearance of SEI and voids in porous LmS may be attributed to high temperature melting. Regarding the disappearance and the meltdown of the separator, Cai *et al.*[56] and Malekei *et al.*[57] have independently observed separator melting around the ISC location inside LIBs by post-mortem light microscopy. They concluded that the thermal energy induced by an ISC is sufficient to locally increase the temperature of a cell by 200 K, which can easily melt the PE (m.p. 135 °C), PP (m.p. 165 °C) and Li (m.p. 180 °C).[58] Considering the decomposition of SEI and the melting of the separator together with the electrochemical characterization (a sudden voltage drop in Figure 2d), it can be safely concluded that an ISC occurs during charge. This is the first experimental demonstration of the melting of the separator and the porous LmS phase in a non-destructive and three-dimensional way.

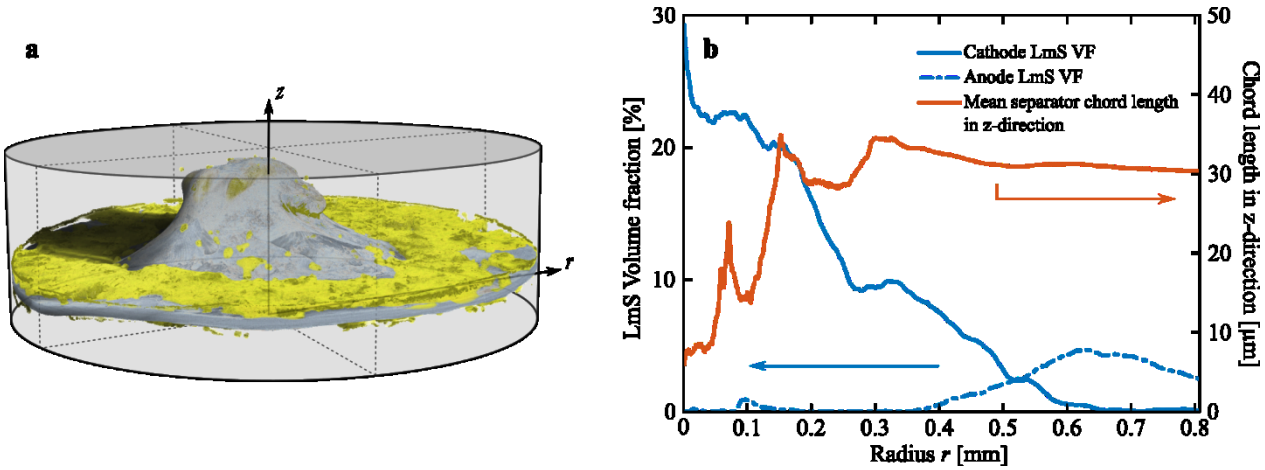

Figure 5. a) 3D demonstration of the calculated LmS volume fraction (VF) deposited on both the cathode (here invisible, beneath the gray separator) and the anode (light yellow, above the separator). The r and z directions are also shown. b) Calculated LmS volume fraction (VF) deposited on both the Li cathode (blue solid line) and Li anode (blue dashed line) as a function of r; the calculated chord length of the separator in the z direction as a function of r is also shown by the orange line (the chord length of the separator in

the central region is small due to partial separator cleavage and melting, is large in the peripheral region because the separator is intact there).

Discussion based on inspection of short-circuited Li/Li-2 cell

By checking intensively the separator break-down region, it is notable to find that one fiber remnant is located inside the delaminated separator, pointing to the cathode LmS with surrounding separator molten away. This phenomenon is marked by black arrows in the green rectangle in Figure 3b. In the green rectangle, the irregular boundaries, pointed by white arrows, is also shown. The diameter of this fiber is about 2 μm. We suspect that the irregular boundaries probably result from the fusing of some Li dendrites and that the remnant fiber is closely related to the ISC (due to the similar X-ray absorption this fiber cannot be assigned to the separator or to Li with certainty). During charging most of the LmSs are electrochemically deposited preferentially in the outer region, but one dendrite is electrochemically generated in this specific area (lithium is probably supplied from the electrolyte). During its growth it can easily penetrate through the pores of this part of the separator since the separator has already been significantly stretched and its mechanical robustness has already been weakened by the LmS growing during discharge.[38] Once this dendrite eventually perforates the separator and bridges the Li anode and cathode the entire cell current (0.015 mA) concentrates only on ~2 μm diameter piercing-through dendrite, which results in a significantly high current density of about 470 A cm^{-2} and pronounced localized Joule heating around the ISC location. According to previous calculation,[59] within less than ~0.1 s the induced Joule heat will lead to the decomposition of the SEI and the melting of both the separator and porous LmS phase. Most of the energy is dissipated by the endothermic porous LmS and separator melting events and within ~0.4 s, the temperature drops sharply.[59] The above-observed results agree well with previous simulations.[9, 60, 61] Additionally, the direct internal view of the electrochemically short circuited Li/Li-2 cell suggests that the shutdown mechanism provided by the sandwich structure can hardly provide any protection from a real ISC, i.e. the considerable force accompanied by the growing LmSs and the ISC-induced high Joule heating easily destroy the trilayer separator which is made by laminating PP and PE layers together by adhesion or welding.[39],[62] The decomposition of the SEI and the melting of the porous LmS to a more compact resolidified LmS will release lots of the mechanical stress that acted on the separator (the conformal gaps between the contours of LmSs, separator and Li anode, as marked by green dot line, black dot line and pink dot line in Figure 3g, act as tracers of the movement of the separator under stress relief). In the investigated Li/Li-2 cell, most of the Joule heat is dissipated by the endothermic separator melting[63] after the penetrating Li dendrite has been fused.[64] However, in real commercial LIBs containing normal cathode materials such as $LiCoO_2$, $LiMn_2O_4$ and $LiFePO_4$ etc. and anode materials such as lithiated carbon, an ISC-induced Joule heating will initiate the exothermic decomposition of some of the active materials including the release of oxygen and flammable gas.[62] Such reactions can further increase the inner temperature to above 200 ℃ and lead to the exothermic decomposition or ignition of the flammable electrolyte.[14, 65] Ultimately, without an effective heat dissipation or propagation

within LIBs, the lithium-dendrite induced ISC can eventually result in serious incidents. Table 1 summary some particular parameters of commercial LIB components.[38, 66, 67]

Table 1. Specific property parameters of selected commercial LIB components.

	Tensile strength (kg cm^{-2})	Puncture strength (g cm^{-2})	Melting temperature (°C)	Decomposition temperature (°C)
Celgard® 2325 PP/PE/PP separator	1900/135 (MD/TD)	300	135/165 (PE/PP)	-
SEI (solid electrolyte interface)	-	-	-	90-120[b]
Electrolyte	-	-	-	130-230[a]
Lithium	-	-	180	-
Carbon (fully charged)	-	-	-	100-130
$LiCoO_2$ (fully charged)	-	-	-	178-250

a, electrolyte decomposition temperature varies among different electrolyte, this temperature range is based on PC/EC/DMC (1/1/3)+$LiPF_6$ (1M)[66][PC: $C_4H_6O_3$; EC: $C_3H_4O_3$; DMC: $C_3H_6O_3$]
b, SEI decomposition temperature depends on the electrolyte used, more information can be found elsewhere.[14]

Conclusion

In summary, for the first time the underlying internal cell deformation and degradation caused by an ISC is experimentally visualized by using synchrotron X-ray phase contrast tomography. From the battery engineer's point of view, the present study suggests three potential ways to further enhance the safety and reliability of current- and/or next-generation LIBs: i) LmSs that are electrochemically plated on the surface of Li electrodes should be perfectly manipulated and/or even completely avoided. There have been reports about the direct controlled plating of LmSs on the surface of Li electrodes[52, 68] and the direct engineering of Li electrodes.[69] ii) New kinds of separators with considerably improved mechanical and puncture strength as well as higher thermal stability (m.p. above 165°C) are highly desired. Promising candidates are ceramic separators which combine the characteristics of flexible polymers and excellent thermal stability.[70, 71] iii) Novel electrolytes with enhanced thermal stability and non-flammability are desired. Although adding fire retardant (FR) additives to lower the flammability of the liquid electrolytes can, to some extent, reduce the liquid organic electrolyte flammability,[14] yet the recently emerging solid state electrolytes, which function as both electrolyte and separator, may be the most promising option for current- and/or next-generation LIBs with enhanced safety and reliability.[6, 72-74] From the battery tester's point of view, the present investigation may open up new opportunities for future standard battery testing procedures. Conventional mechanical

evaluation techniques have been predominantly criticized by the fact that they only show how the cells behave under an abuse condition instead of truly replicating the conditions of a filed failure.[16] The firstly successful direct visualization of an ISC conducted by synchrotron X-ray imaging may help updating existing testing standards and creating new ones for next-generation LIB technology.

EXPERIMENTAL METHODS

Lithium and Celgard®2325 separator were purchased from MTI Corp. USA. The electrolyte is 1M $LiPF_6$ in a volume-ratio mixture (1:1) of ethylene carbonate (EC) and ethyl methyl carbonate (EMC) and was purchased from Sigma Aldrich. The housing of the proof-of-concept beamline battery was made of polyamide-imide (Torlon) provided by Drake Plastics Europe.

The lithium electrodes in both Li/Li cells (2.5 mm diameter) were punched out from a 1-mm thick lithium plate. Both cells were assembled in an argon-filled glovebox with humidity and oxygen levels below 0.1 ppm. The trilayer Celgard®2325 separator (3.5 mm in diameter and ~25 µm thick) was placed between the Li/Li electrodes. All cells were assembled manually without exerting force. Finally, both cells were filled with the standard liquid electrolyte and were sealed off before taking them out of the glovebox.

Galvanostatic charge and discharge of the Li/Li-2 battery was carried out using an IviumStat from Ivium Technologies, Netherlands. The cells were discharged for 18 h and charged for 13.4 h at a current density of 0.3 $mA \cdot cm^{-2}$.

Synchrotron X-ray tomography was carried out at the BAMline at BESSY II of the Helmholtz-Centre Berlin, Germany. The synchrotron beam was monochromatized to 20 keV using a double multilayer monochromator with an energy resolution of about 1.5 %. The detector system comprised a 60-µm thick $CdWO_4$ scintillator, a microscopic optic and a pco4000 camera equipped with a 4008×2672 pixels CCD chip that is kept out of the direct beam by using a mirror. For tomography measurements of both cells, 2200 projections with each 2.5 s exposure time within a 180° battery rotation were recorded.

The raw tomography data was filtered, normalized and reconstructed using code programmed in IDL 8.2. Three-dimensional segmentations of the separators were made using a grid of manually marked points that were fitted with a biharmonic equation using MATLAB. For the segmentation of LmSs, the statistical region merger tool implemented in Fiji[75] was used followed by manual removal of the bulk lithium background.

ACKNOWLEDGEMENTS

We thank Dr. Heinrich Riesemeier, the beamline scientist at BESSY II, for his valuable assistance and engineer Norbert Beck for fabricating the beamline battery. We also thank Christiane Förster for preparing the SEM sample and Manzoni Anna for conducting the SEM measurement. This work is sponsored by the Helmholtz Association and the China Scholarship Council.

REFERENCES

[1] C. Zu, A. Manthiram, *J. Phys. Chem. Lett.* **2014**, *5*, 2522.
[2] Y. Zhao, X. Liu, H. Li, T. Zhai, H. Zhou, *Chem. Commun.* **2012**, *48*, 5079.
[3] B. Lim, J. Jin, J. Yoo, S. Y. Han, K. Kim, S. Kang, N. Park, S. M. Lee, H. J. Kim, S. U. Son, *Chem. Commun.* **2014**, *50*, 7723.
[4] F. Sun, K. Huang, Y. Liu, T. Gao, Y. Han, J. Zhong, *Appl. Surf. Sci.* **2013**, *266*, 300.
[5] F. Sun, K. Huang, X. Qi, T. Gao, Y. Liu, X. Zou, X. Wei, J. Zhong, *Nanoscale* **2013**, *5*, 8586.
[6] Y. Wang, W. D. Richards, S. P. Ong, L. J. Miara, J. C. Kim, Y. Mo, G. Ceder, *Nat Mater* **2015**, *14*, 1026.
[7] B. Sun, K. Huang, X. Qi, X. Wei, J. Zhong, *Adv. Funct. Mater.* **2015**, *25*, 5633.
[8] F. Sun, K. Huang, X. Qi, T. Gao, Y. Liu, X. Zou, J. Zhong, *Ceram. Int.* **2014**, *40*, 2523.
[9] L. Grande, J. von Zamory, S. L. Koch, J. Kalhoff, E. Paillard, S. Passerini, *ACS Appl. Mater. Interfaces* **2015**, *7*, 5950.
[10] Z. Liang, G. Zheng, C. Liu, N. Liu, W. Li, K. Yan, H. Yao, P.-C. Hsu, S. Chu, Y. Cui, *Nano Lett.* **2015**, *15*, 2910.
[11] H. Wu, D. Zhuo, D. Kong, Y. Cui, *Nat Commun* **2014**, *5*, 5193.
[12] D. Deng, *Energy Sci. Eng.* **2015**, *3*, 385.
[13] F. Ren, T. Cox, H. Wang, *J. Power Sources* **2014**, *249*, 156.
[14] Q. Wang, P. Ping, X. Zhao, G. Chu, J. Sun, C. Chen, *J. Power Sources* **2012**, *208*, 210.
[15] C. J. Orendorff, E. P. Roth, G. Nagasubramanian, *J. Power Sources* **2011**, *196*, 6554.
[16] J. Lamb, C. J. Orendorff, *J. Power Sources* **2014**, *247*, 189.
[17] H. Wang, S. Simunovic, H. Maleki, J. N. Howard, J. A. Hallmark, *J. Power Sources* **2016**, *306*, 424.
[18] J. Steiger, D. Kramer, R. Mönig, *Electrochim. Acta* **2014**, *136*, 529.
[19] R. Bhattacharyya, B. Key, H. Chen, A. S. Best, A. F. Hollenkamp, C. P. Grey, *Nat Mater* **2010**, *9*, 504.
[20] S. Chandrashekar, N. M. Trease, H. J. Chang, L.-S. Du, C. P. Grey, A. Jerschow, *Nat Mater* **2012**, *11*, 311.
[21] W. Li, H. Zheng, G. Chu, F. Luo, J. Zheng, D. Xiao, X. Li, L. Gu, H. Li, X. Wei, Q. Chen, L. Chen, *Faraday. Discuss.* **2014**, *176*, 109.
[22] F. Orsini, A. Du Pasquier, B. Beaudoin, J. M. Tarascon, M. Trentin, N. Langenhuizen, E. De Beer, P. Notten, *J. Power Sources* **1998**, *76*, 19.
[23] H. Ghassemi, M. Au, N. Chen, P. A. Heiden, R. S. Yassar, *Appl. Phys. Lett.* **2011**, *99*, 123113.
[24] X. H. Liu, L. Zhong, L. Q. Zhang, A. Kushima, S. X. Mao, J. Li, Z. Z. Ye, J. P. Sullivan, J. Y. Huang, *Appl. Phys. Lett.* **2011**, *98*, 183107.
[25] Y. S. Jung, A. S. Cavanagh, L. Gedvilas, N. E. Widjonarko, I. D. Scott, S.-H. Lee, G.-H. Kim, S. M. George, A. C. Dillon, *Adv. Energy Mater.* **2012**, *2*, 1022.
[26] J. Zhang, Z. Liu, Q. Kong, C. Zhang, S. Pang, L. Yue, X. Wang, J. Yao, G. Cui, *ACS Appl. Mater. Interfaces* **2013**, *5*, 128.
[27] W. Xu, Z. Wang, L. Shi, Y. Ma, S. Yuan, L. Sun, Y. Zhao, M. Zhang, J. Zhu, *Acs Appl. Mater. Interfaces* **2015**, *7*, 20678.
[28] X. Zhu, X. Jiang, X. Ai, H. Yang, Y. Cao, *ACS Appl. Mater. Interfaces* **2015**, *7*, 24119.
[29] J. Kalhoff, G. G. Eshetu, D. Bresser, S. Passerini, *ChemSusChem* **2015**, *8*, 2154.
[30] F. Huang, Y. Xu, B. Peng, Y. Su, F. Jiang, Y.-L. Hsieh, Q. Wei, *ACS Sustainable Chem. Eng.* **2015**, *3*, 932.
[31] X. Ji, D.-Y. Liu, D. G. Prendiville, Y. Zhang, X. Liu, G. D. Stucky, *Nano Today* **2012**, *7*, 10.
[32] J.-J. Woo, Z. Zhang, K. Amine, *Adv. Energy Mater.* **2014**, *4*, 1301208.
[33] H. A. Bale, A. Haboub, A. A. MacDowell, J. R. Nasiatka, D. Y. Parkinson, B. N. Cox, D. B. Marshall, R. O. Ritchie, *Nat Mater* **2013**, *12*, 40.
[34] M. Ebner, F. Marone, M. Stampanoni, V. Wood, *Science* **2013**, *342*, 716.
[35] D. S. Eastwood, V. Yufit, J. Gelb, A. Gu, R. S. Bradley, S. J. Harris, D. J. L. Brett, N. P. Brandon, P. D. Lee, P. J. Withers, P. R. Shearing, *Adv. Energy Mater.* **2014**, *4*, 1300506.

[36] D. S. Eastwood, P. M. Bayley, H. J. Chang, O. O. Taiwo, J. Vila-Comamala, D. J. L. Brett, C. Rau, P. J. Withers, P. R. Shearing, C. P. Grey, P. D. Lee, *Chem. Commun.* **2015**, *51*, 266.
[37] K. J. Harry, D. T. Hallinan, D. Y. Parkinson, A. A. MacDowell, N. P. Balsara, *Nat Mater* **2014**, *13*, 69.
[38] P. Arora, Z. Zhang, *Chem. Rev.* **2004**, *104*, 4419.
[39] S. S. Zhang, *J. Power Sources* **2007**, *164*, 351.
[40] F. Sun, H. Markötter, D. Zhou, S. S. S. Alrwashdeh, A. Hilger, N. Kardjilov, I. Manke, J. Banhart, *ChemSusChem* **2016**, *9*, 946.
[41] I. Manke, J. Banhart, A. Haibel, A. Rack, S. Zabler, N. Kardjilov, A. Hilger, A. Melzer, H. Riesemeier, *Appl. Phys. Lett.* **2007**, *90*, 214102.
[42] A. Haibel, I. Manke, A. Melzer, J. Banhart, *J. Electrochem. Soc.* **2010**, *157*, A387.
[43] F. Sun, L. Zielke, H. Markötter, A. Hilger, D. Zhou, R. Moroni, R. Zengerle, S. Thiele, J. Banhart, I. Manke, *ACS Nano* **2016**, *10*, 7990.
[44] F. Sun, H. Markötter, I. Manke, A. Hilger, N. Kardjilov, J. Banhart, *ACS Appl. Mater. Interfaces* **2016**, *8*, 7156.
[45] L. Zielke, C. Barchasz, S. Waluś, F. Alloin, J. C. Leprêtre, A. Spettl, V. Schmidt, A. Hilger, I. Manke, J. Banhart, R. Zengerle, S. Thiele, *Sci. Rep.* **2015**, *5*, 10921.
[46] L. Zielke, T. Hutzenlaub, D. R. Wheeler, C.-W. Chao, I. Manke, A. Hilger, N. Paust, R. Zengerle, S. Thiele, *Adv. Energy Mater.* **2015**, *5*, 1401612.
[47] P. Cloetens, M. Pateyron-Salomé, J. Y. Buffière, G. Peix, J. Baruchel, F. Peyrin, M. Schlenker, *J. Appl. Phys.* **1997**, *81*, 5878.
[48] K. Yan, Z. Lu, H.-W. Lee, F. Xiong, P.-C. Hsu, Y. Li, J. Zhao, S. Chu, Y. Cui, *Nat. Energy.* **2016**, *1*, 16010.
[49] H. Porthault, C. Decaux, *Electrochim. Acta* **2016**, *194*, 330.
[50] D. Lu, Y. Shao, T. Lozano, W. D. Bennett, G. L. Graff, B. Polzin, J. Zhang, M. H. Engelhard, N. T. Saenz, W. A. Henderson, P. Bhattacharya, J. Liu, J. Xiao, *Adv. Energy Mater.* **2015**, *5*, 1400993.
[51] M. Arakawa, S.-i. Tobishima, Y. Nemoto, M. Ichimura, J.-i. Yamaki, *J. Power Sources* **1993**, *43*, 27.
[52] M.-H. Ryou, Y. M. Lee, Y. Lee, M. Winter, P. Bieker, *Adv. Funct. Mater.* **2015**, *25*, 834.
[53] S.-T. Hong, J.-S. Kim, S.-J. Lim, W. Y. Yoon, *Electrochim. Acta* **2004**, *50*, 535.
[54] M. N. Richard, J. R. Dahn, *J. Electrochem. Soc.* **1999**, *146*, 2068.
[55] H. Maleki, G. Deng, A. Anani, J. Howard, *J. Electrochem. Soc.* **1999**, *146*, 3224.
[56] W. Cai, H. Wang, H. Maleki, J. Howard, E. Lara-Curzio, *J. Power Sources* **2011**, *196*, 7779.
[57] H. Maleki, J. N. Howard, *J. Power Sources* **2009**, *191*, 568.
[58] M. J. Brand, S. F. Schuster, T. Bach, E. Fleder, M. Stelz, S. Gläser, J. Müller, G. Sextl, A. Jossen, *J. Power Sources* **2015**, *288*, 62.
[59] C.-S. Kim, J.-S. Yoo, K.-M. Jeong, K. Kim, C.-W. Yi, *J. Power Sources* **2015**, *289*, 41.
[60] K. Nishikawa, T. Mori, T. Nishida, Y. Fukunaka, M. Rosso, T. Homma, *J. Electrochem. Soc.* **2010**, *157*, A1212.
[61] A. Jana, D. R. Ely, R. E. García, *J. Power Sources* **2015**, *275*, 912.
[62] T. H. Dubaniewicz Jr, J. P. DuCarme, *J. Loss. Prevent. Proc.* **2014**, *32*, 165.
[63] P. Ping, Q. Wang, P. Huang, K. Li, J. Sun, D. Kong, C. Chen, *J. Power Sources* **2015**, *285*, 80.
[64] M. Dollé, L. Sannier, B. Beaudoin, M. Trentin, J.-M. Tarascon, *Electrochem. Solid-State Lett.* **2002**, *5*, A286.
[65] T. Kawamura, A. Kimura, M. Egashira, S. Okada, J.-I. Yamaki, *J. Power Sources* **2002**, *104*, 260.
[66] P. Biensan, B. Simon, J. P. Pérès, A. de Guibert, M. Broussely, J. M. Bodet, F. Perton, *J. Power Sources* **1999**, *81–82*, 906.
[67] R. Spotnitz, J. Franklin, *J. Power Sources* **2003**, *113*, 81.
[68] K. Yan, Z. Lu, H.-W. Lee, F. Xiong, P.-C. Hsu, Y. Li, J. Zhao, S. Chu, Y. Cui, *Nat. Energy.* **2016**, *1*, 16010.
[69] Y.-S. Lee, J. H. Lee, J.-A. Choi, W. Y. Yoon, D.-W. Kim, *Adv. Funct. Mater.* **2013**, *23*, 1019.
[70] M. Kim, G. Y. Han, K. J. Yoon, J. H. Park, *J. Power Sources* **2010**, *195*, 8302.
[71] M. He, X. Zhang, K. Jiang, J. Wang, Y. Wang, *ACS Appl. Mater. Interfaces* **2015**, *7*, 738.

[72] A. Aboulaich, R. Bouchet, G. Delaizir, V. Seznec, L. Tortet, M. Morcrette, P. Rozier, J.-M. Tarascon, V. Viallet, M. Dollé, *Adv. Energy Mater.* **2011**, *1*, 179.
[73] N. Kamaya, K. Homma, Y. Yamakawa, M. Hirayama, R. Kanno, M. Yonemura, T. Kamiyama, Y. Kato, S. Hama, K. Kawamoto, A. Mitsui, *Nat Mater* **2011**, *10*, 682.
[74] Y. Kato, S. Hori, T. Saito, K. Suzuki, M. Hirayama, A. Mitsui, M. Yonemura, H. Iba, R. Kanno, *Nat. Energy.* **2016**, *1*, 16030.
[75] M. D. Abramoff, P. J. Magalhães, S. J. Ram, *Biophotonics international* **2004**, *11*, 36.

2.3 Gas development

Three Dimensional Visualization of Gas Evolution and Channel Formation inside a Lithium-ion Battery

Fu Sun*[,†,‡], Henning Markötter[†,‡], Ingo Manke[‡], Andre Hilger[‡], Nikolay Kardjilov[‡] and John Banhart[†,‡]

[†]Institute of Materials Science and Technology
Technische Universität Berlin
10623 Berlin, Germany
[‡]Helmholtz Centre Berlin for Materials and Energy
Hahn-Meitner-Platz 1
14109 Berlin, Germany
*Corresponding Author: fu.sun@helmholtz-berlin.de

Abstract

Gas generation within lithium ion batteries (LIBs) gives rise to safety concerns that question their applicability. By employing synchrotron X-ray imaging, the gas and channel evolution occurring in an operating LIB have been directly visualized in their inherent 3D state as a function of discharge and charge. Using the spatial 3D distribution of gas bubbles and channels, the active particles that dictate the performance of a functional LIB were identified and visualized in 3D. Delithiation and lithiation are interpreted as the process of activating particles continuously in a step-by-step way. The present work not only demonstrates the generation and evolution of gas within LIB in 3D, but also reveals the distribution of active particles for the first time. These fundamentally findings presented here shed light on a range of processes that could not previously be characterized in 3D and can provide practical guidance for the design of next-generation LIBs with improved safety.

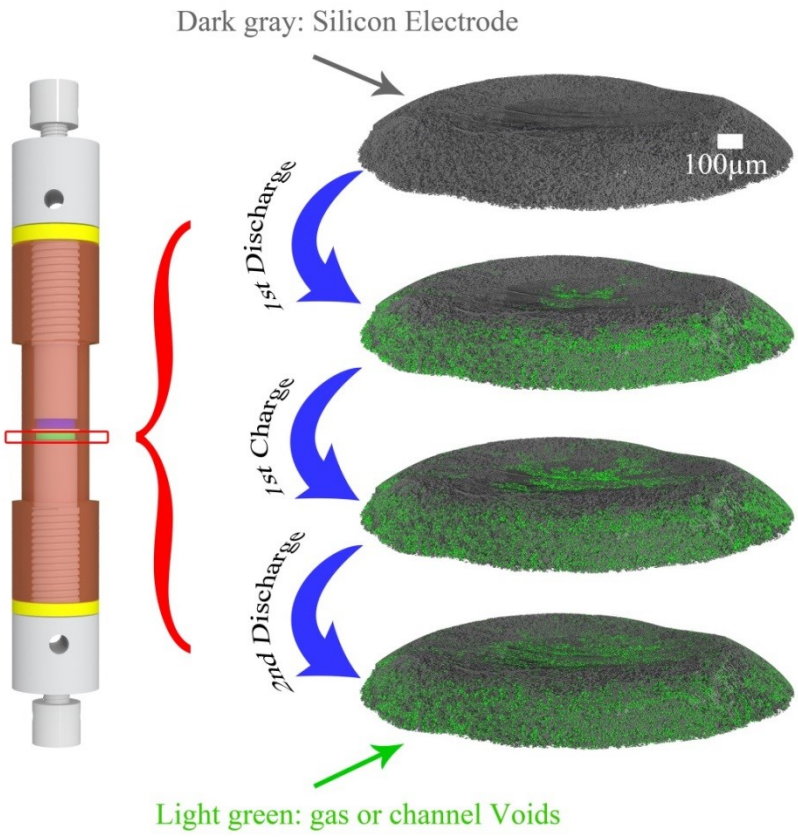

Abstract Graphic

KEYWORDS

gas evolution; channel formation; lithium ion battery; synchrotron X-ray imaging; tomography; radiography; silicon anode

INTRODUCTION

Rechargeable lithium-ion batteries (LIBs) have penetrated profoundly into products such as portable electronic devices, electric vehicles or other large-sized power sources.[1-5] However, safety concerns still limit the full practical utilization of these batteries.[6] Especially gas evolution is a formidable technological and fundamental challenge[7] since gas generated in hermetically sealed batteries can lead to detrimental effects: on the one hand, gas generation during storage results in a diminished shelf life and eventually a markedly reduced cycle lifetime.[8] On the other hand, gas evolution during cycling leads to electrolyte displacement,[9] which causes a decrease of Li-ion diffusion and/or Li-ion conduction in the electrolyte and ultimately contributes to a tremendous increase of battery resistance.[10] In both cases, the internal pressure build-up may also induce battery bulging, mechanical stress inside the electrodes and even severe gas leakage,[11] all of which are detrimental to longevity and reliability of energy storage battery systems. Therefore,

understanding the gas evolution mechanisms are of great importance from a practical point of view.

To date, many experimental investigations have been carried out in extensive detail and, as a result, our knowledge of the gas evolution mechanism has substantially deepened. For instance, it is already known that the gas evolution, which is intimately related with solid electrolyte interphase (SEI) formation in the electrochemical battery,[12] originates from reductive and oxidative electrolyte decomposition reactions due to the fact that the electrochemical potential of both electrode materials is far beyond the thermodynamic stability window of the commonly used organic electrolytes.[13] Actually, significant evolution of gaseous products such as CO_2, CO, O_2, H_2, CH_4, C_2H_4, C_2H_6, C_3H_6 and C_3H_8 from the decomposition of carbonate solvents and lithium during battery operation has been detected by various characterization techniques.[14-21] In addition, utilizing isotope analysis, Onuk *et al.* have unambiguously identified the origin of gases evolving in LIBs.[22] Furthermore, by adopting in situ transmission electron microscopy (TEM)[23] and neutron radiography (NR),[9, 11] the generation of gaseous bubbles channels formed by the gas have recently been visualized. These studies have enhanced our understanding of gas evolution but, unfortunately, the applied radiographic imaging techniques yield two-dimensional (2D) information and do not help us in further comprehending gas evolution kinetics in its inherently three-dimensional (3D) state and in quantitatively analyzing its complex evolution. Moreover, no study of the spatial gas distribution in relation to the electrochemically active particle population[24] in electrodes has been conducted so far, even though it is the active particles that directly determine battery performance and cycle life.[25]

Due to the high fluxes generated by synchrotron sources, synchrotron X-ray imaging has evolved into a powerful characterization tool in the field of materials science.[26-36] Especially synchrotron X-ray tomography has enabled researchers to obtain unprecedented insights into LIBs from the level of individual particles to the scale of entire electrodes.[37-40] Most recently, Ebner *et al.*, have directly observed and quantified electrochemical and mechanical degradation in a SnO anode.[41]

Using a non-destructive 3D X-ray imagining technique, herein we investigate in 3Ds the gas evolution scenario in a LIB based on a silicon (Si) electrode since Si is considered one of the most promising anode materials for next-generation power sources.[42-43] This is the first study that also visualizes the distribution of electrochemically active electrode particles with respect to the spatial gas development and interprets delithiation and lithiation as a process of activating particles in a step-by-step way. This work sets a refined example for the 3D gas evolution investigation and the spatially evolved active particle distribution, providing in-depth knowledge for the electrode engineers and numerical simulation experts.

EXPERIMENTAL SECTION

Materials. Active silicon particles were received from Elkem AS, Norway. Conductive carbon black, Polyvinylidene fluoride (PVDF) binder, Celgard separator and lithium were purchased from MTI Cor. USA. N-methyl pyrrolidone solvent (NMP) and 1M $LiPF_6$ in a volume-ratio (1:1)

mixture of ethylene carbonate (EC) and dimethyl carbonate (DMC) were purchased from Sigma Aldrich. The housing of the proof-of-concept beamline battery is made of polyamide-imide (Torlon), from McMaster-Carr.

Materials characterization. Scanning electron microscopy (SEM) images were taken using a Zeiss ultraplus microscope. The particle size distribution of Si particles was measured by laser diffraction using a Malvern Mastersizer 2000 analyzer.

Battery preparation. The electrode is made of electrode slurries with weight ratios of Si:carbon black:binder of 80:10:10 in NMP. The slurry was cast directly onto the head of the bottom screw shown in Figure 1. To remove the NMP, the cast slurry was dried in an oven at 60 ℃ overnight. Before and after casting, the screw was weighed to determine the mass of the electrode materials. The proof-of-concept battery (shown in Figure 1a) designed for beamline use was assembled in an argon filled glovebox with humidity and oxygen levels below 0.1 ppm. Metallic lithium was placed onto the head of the top screw in Figure 1a acting as both a counter and reference electrode. A polymer separator soaked with the electrolyte was placed between the lithium electrode and the Si electrode. Current leads are connected to a potentiostat for electrochemical tests.

Electrochemical measurements. Cyclic voltametry (CV) and galvanostatic charge/discharge of the battery were carried out using an IviumStat voltameter. A fresh battery after assembly was measured for CV curves from 0 V to 2.5 V at a scan rate of 1 mV/s. During galvanostatic cycling at the beamline, the assembled battery was measured at 1.75 Ag^{-1} based on the mass of active silicon. Different discharge and charge current rates will be used to further investigate the correlation between the current rate and the gas releasing and channel formation behavior.

Settings of tomography and radiography. Synchrotron X-ray tomography and radiography were recorded at the BAMline at the storage ring BESSY II of the Helmholtz-Zentrum Berlin, Germany. The synchrotron beam was monochromatized to 20 KeV using a double multilayer monochromator with an energy resolution of about 1.5 %. The detector system comprised a 60-µm thick $CdWO_4$ scintillator, a microscopic optic and a pco4000 camera with a 4008×2672 $pixel^2$ CCD chip that is kept out of the direct beam by using a mirror. For tomography, 2200 projections during a 180° battery rotation each with 4 s exposure time were recorded before/after discharge/charge. The battery was radiographically imaged during discharge and charge with 4 s exposure time. 4 s exposure time was required because of the relative low photon flux provided by the BAMline compared to other imaging stations. It has to be noted that in order to characterize the morphological change of the whole Si based electrode (3.2 mm × 0.4 mm, length × width), we have used an optic and camera combination with a corresponding field of view of 3.3 mm × 2.2 mm. And the resultant voxel resolution is ~0.876 µm. However, -10 er camera system with higher resolution of ~0.438 µm will be used in future investigations.

Data processing. Filtering, binarization and segmentation was performed in ImageJ and Avizo Fire. Data visualization was done using VGStudio MAX and Avizo Fire. Analysis of the particles is conducted by ImageJ. The procedure is presented in Supporting Information.

RESULTS AND DISCUSSION

2.3 Gas development

An electrochemical cell that can fully represent a working battery and at the same time is compatible with synchrotron X-ray imaging is crucial for the characterization of gas evolving during operation. For this purpose, we developed an electrochemical cell that is X-ray transparent so that imaging can be conducted in operando to directly study gas evolution during dis/charge processes, allowing us to correlate the gas evolution with electrochemical activity. Figure 1 displays a photograph and the corresponding schematic illustration of the battery as well as a schematic representation of the synchrotron X-ray tomography setup. [44]

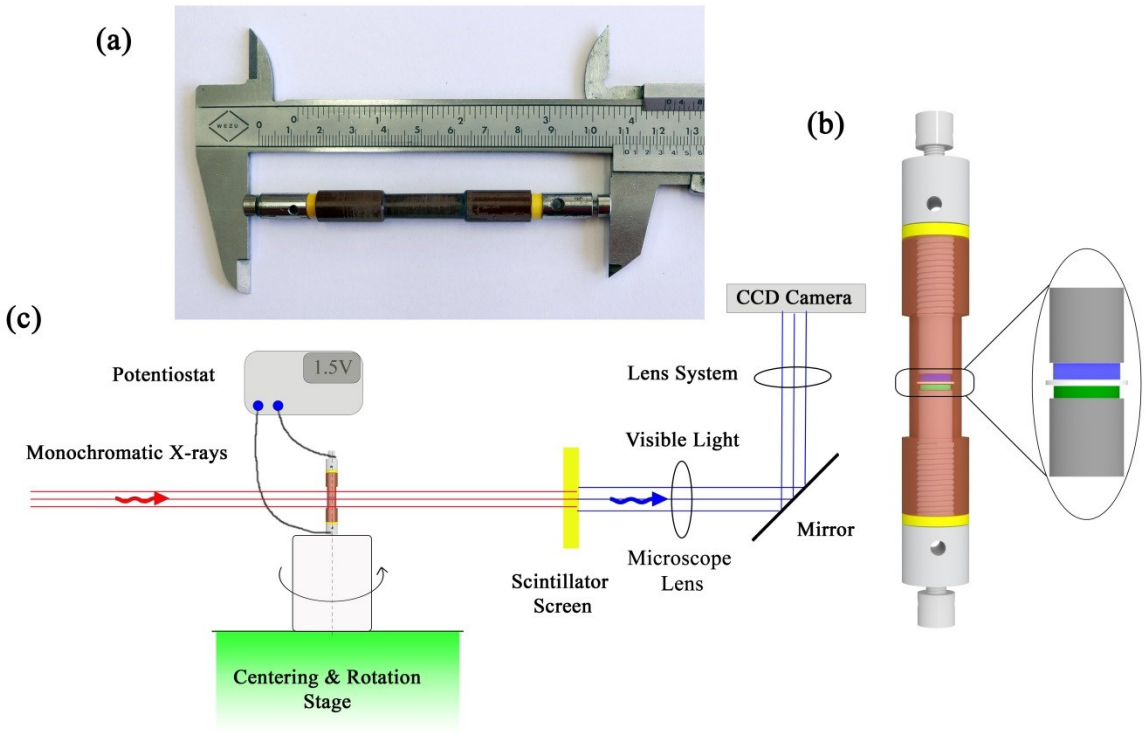

Figure 1. The customized electrochemical battery and the employed X-ray tomography setup: a) Photograph of the battery investigated. b) Corresponding schematic representation of the battery cell consisting of a polyamide-imide housing (brown), two screw electrodes and a retaining screws each on top (light grey), two sealing rings (yellow), a lithium metal electrode (blue), a porous separator (white) and the Si-based anode (green). c) Schematic representation of the experimental setup of the tomography station at the BAM*line* at BESSY II, Helmholtz-Zentrum Berlin, Germany

After assembly of the battery, cyclic voltametry (CV) was performed to verify the reduction and oxidation characteristics of silicon. Figure 2a shows CV curves of the battery scanned at a rate of 1 mVs^{-1} in the potential window of 0-2.5 V. The cathodic current increase from 1.4 V to 0.7 V in the CV curves is related to small-scale reduction of electrolyte and/or surface contaminations such as trace water.[45] The small hump around 0.5 V is attributed to a strong reductive decomposition of the electrolyte associated to the release of large amounts of gases,[46] while the peak above 0 V is related to Li alloying with Si. During delithiation, the anodic peak observed slightly above 0.5 V is for de-alloying of Li-Si phase and the broad anodic peak at 1.0 V is related to the oxidation of electrolyte and/or compounds previously reduced during the

cathodic process. The results are in good agreement with previously reported Si/carbon composites,[43, 47] thus confirming the electrochemical reactions inside the battery.

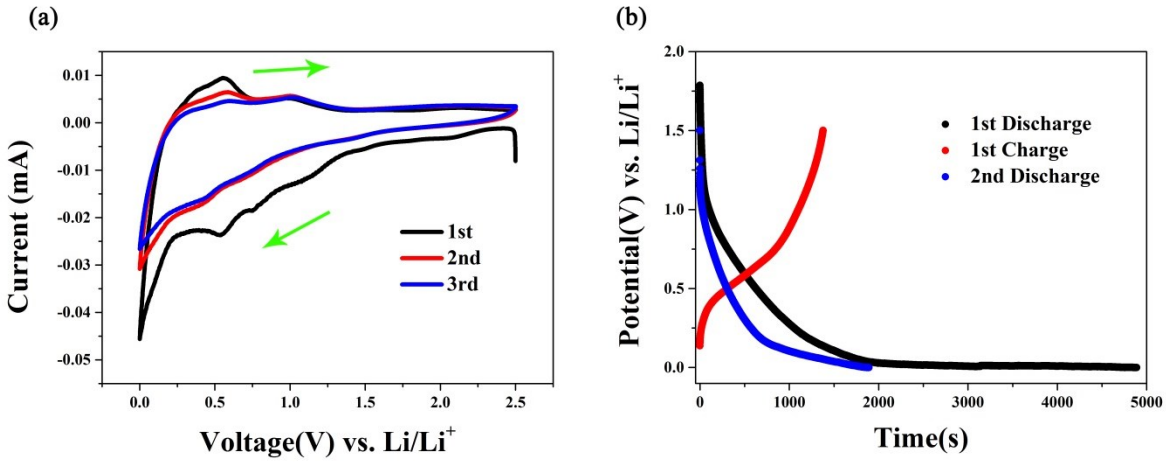

Figure 2. Electrochemical characterization of the investigated battery: a) CV curves of the first three cycles of the battery at a scan rate of 1 mVs^{-1}. b) The first discharge, the first charge and the second discharge voltage-time profiles of the battery at 1.75 Ag^{-1} rate.

After this, we conducted X-ray radiography while simultaneously galvanostatically discharging or charging the cell at a rate of 1.75Ag^{-1} as shown in Figure 2b. The discharge and charge curves are also in good agreement with previous results for Si electrodes.[43] In addition, another battery was galvanostatically discharged/charged at a small current of 0.01Ag^{-1} for more than 20 h as shown in Supporting Information (SI) Figure S1, showing typical characteristic features of Si. Thus, the battery design used for tomographic measurements exhibits an authentic electrochemical behavior.

High-resolution synchrotron X-ray tomographic imaging grants us the ability to probe the internal structure and the distribution of elements in the electrode nondestructively.[40] First, the pristine battery without being exposed to any discharge or charge is characterized. The typical procedure of tomographic data acquisition and processing is demonstrated in Figure 3. Figure 3a shows a projection image of the Li electrode/separator/Si electrode assembly. While the Li electrode and the porous plastic separator appear nearly invisible due to their low X-ray absorption coefficients, the Si electrode is clearly visible. As the battery rotates during tomography, a series of projections are recorded, which are later reconstructed into a three dimensional volume. Figure 3b shows a horizontal slice image through the reconstructed volume, which displays that the Si particles are well mixed with the carbon black. In order to further analyze the Si particles, the grayscale slices were segmented into binary images, yielding Figure 3c, in which the bright regions correspond to higher-absorbing material, the Si particles, whereas the black regions are assigned to less-absorbing material such as carbon black and polymer binder. Segmentation is performed via a combined approach of filtering and thresholding[48] and produces Figure 3d after labeling. In order to validate the X-ray tomography

results qualitatively and quantitatively we compare scanning electron microscopy images (SEM) (Figure 3e) with grayscale slice images as well as the particle size distribution (PSD) measured using laser diffraction with the PSD obtained from the tomographic data (Figure 3f). The good agreement between the experimentally and numerically obtained results indicates that the segmentation applied accurately captures the electrode material properties. Finally, a full-view 3D representation of the segmented particles is shown in Figure 3g and in the Supporting Movie 1 (SM 1) (More details can be found in the SI.)

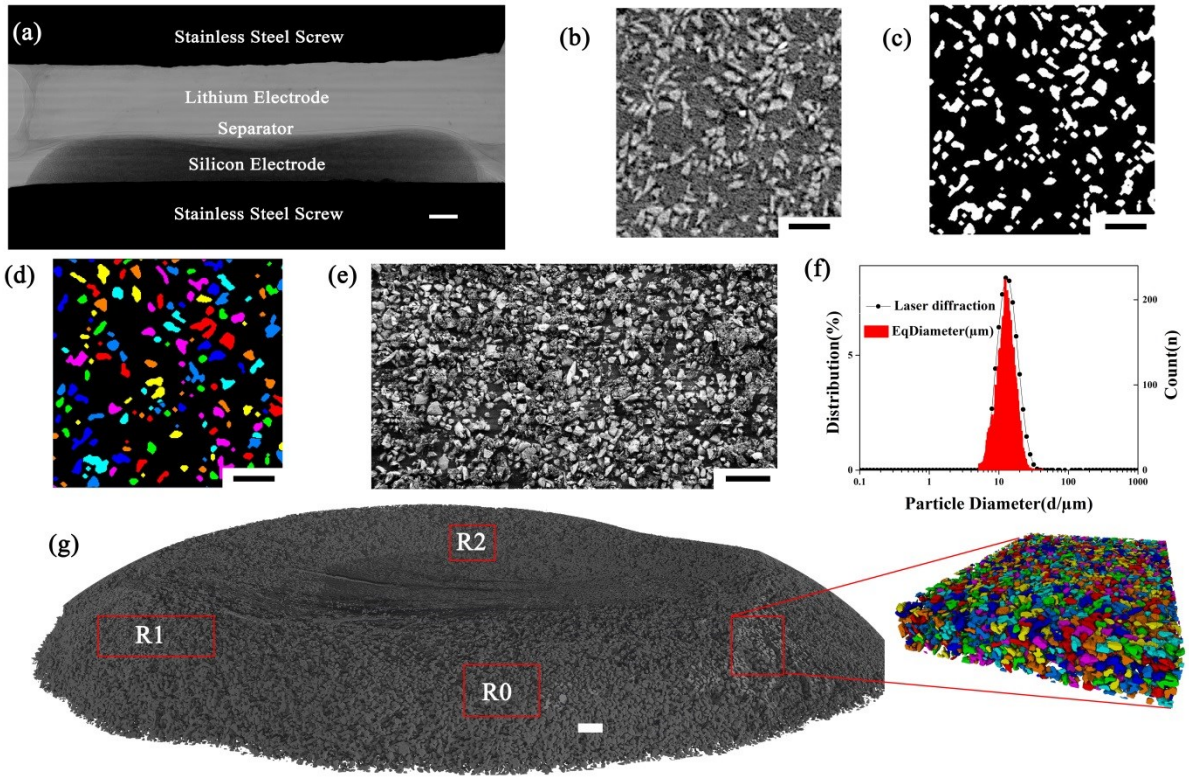

Figure 3. a) X-ray projection image of the assembled Li electrode/separator/Si electrode stack within the battery. The scale bar is 200 µm long. b) Example of a reconstructed grayscale slice image. c) Same slice after binarization. d) Slice after separation and labeling. e) Scanning electron micrographs (SEM) of the mixed Si and carbon. Scale bars in b) – e) are 50 µm long. f) Particle size distribution (PSD) obtained from the labeled particles (red) compared to values measured by laser diffraction (black). g) 3D visualization of all Si particles with labeled regions R0, R1 and R2. The scale bar is 100 µm long.

Gas evolution is directly observed in 3D after each discharge or charge step and the reconstructed gas evolution is straightforwardly correlated to the electrochemical process. During data processing, we can easily separate the gas evolved of the channel from the solid materials due to the near zero absorption of gas. After the first discharge process, we captured the internal morphological change by tomographic imaging. In Figure S2, different 3D views of the composite of Si electrode and gas or channel are displayed. Figure 4a shows a cropped region after the first discharge, labeled as R0 in Figure 3g, in which Si particles are shown in gray and

gas or channel in green. We then charge the battery and obtain the first charged state tomogram. The corresponding 3D renderings are displayed in Figure S2b and SM 2b and the corresponding cropped region is shown in Figure 4b. In the final step, we discharge the battery again and acquire the second discharged state tomogram shown in Figure S2c, SM 2c and Figure 4c. In addition, during the discharge and charge process, we simultaneously capture the gas movement inside the battery in 2D by in situ X-ray radiography. The results are shown in Figure 5 and SM 3.

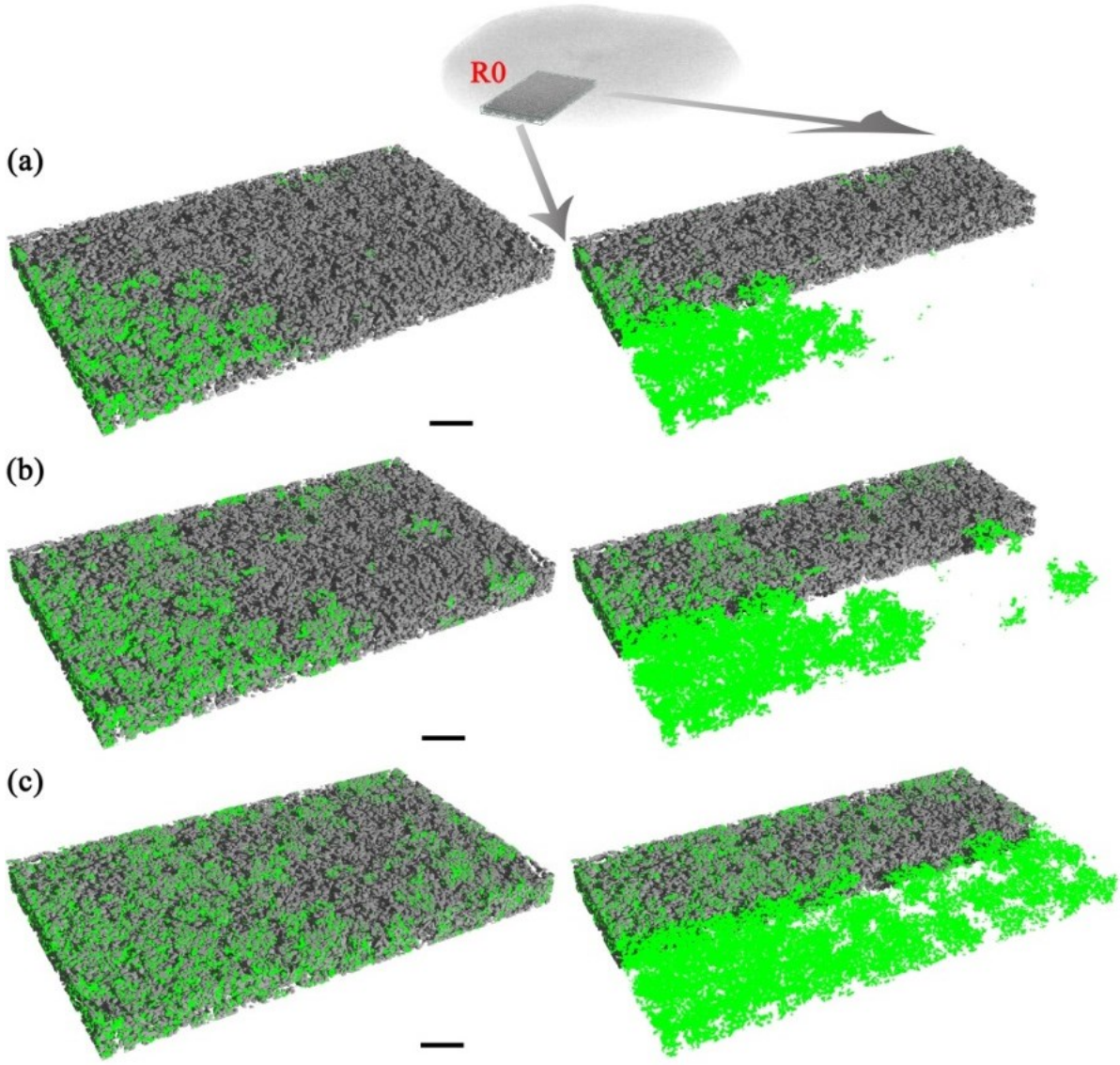

Figure 4. 3D visualization of gas evolution in a cutout at position R0 in the battery after each discharge or charge process (see Figure 3g). a) After the first discharge. b) After the first charge. c) After the second discharge. In all pictures, from left to right is from the periphery to the central part of the electrode. The left column shows the Si particles (gray) and the gas or channel (green) in a composite image. In the right

column, one half of the particles is rendered transparent to show the gas part. The scale bar is 100 µm long in all the pictures.

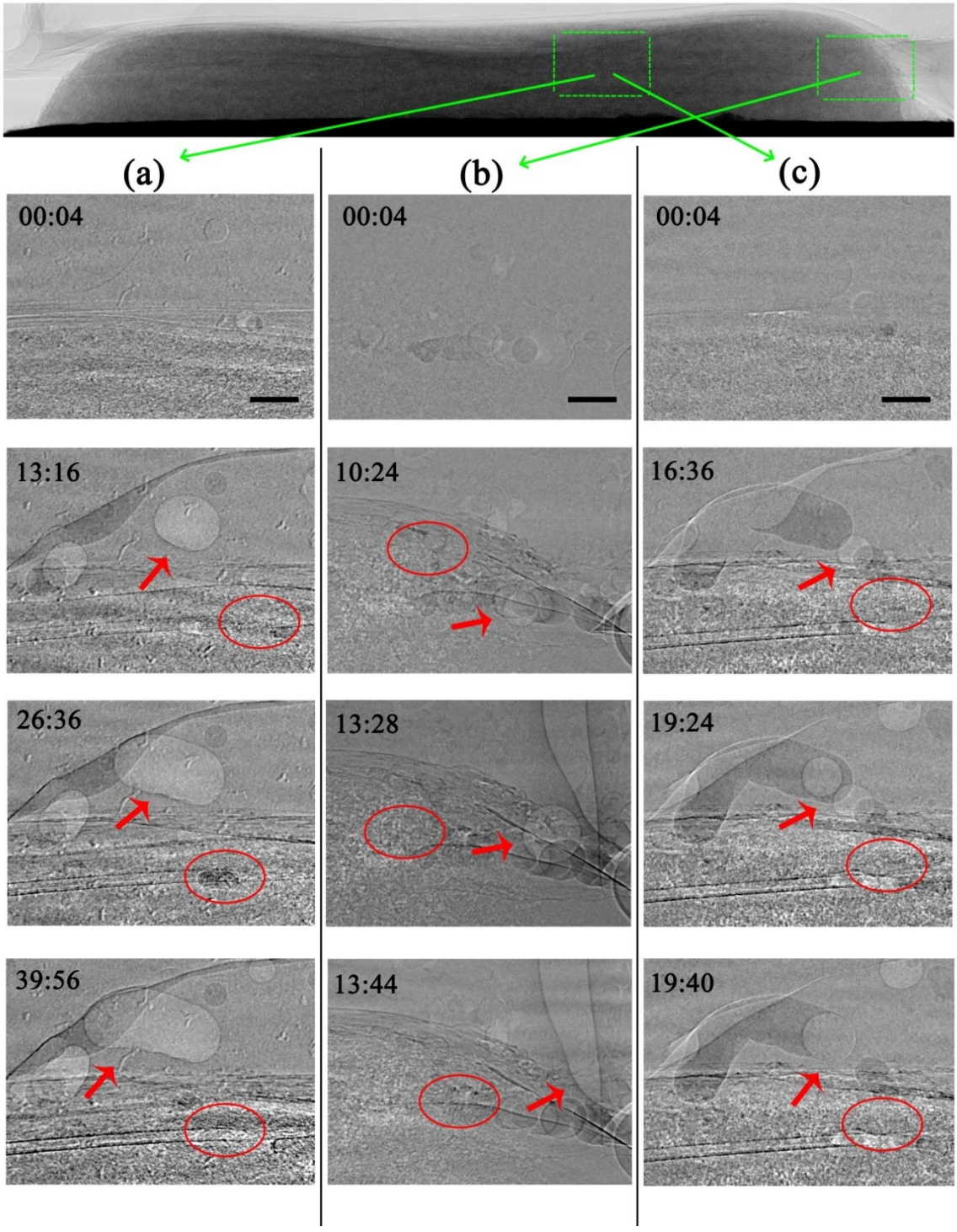

Figure 5. A series of projections showing the movement of gas as imaged by X-ray radiography. a) First discharge step. b) First charge step. c) Second discharge step. The scale bar is 100 µm long in all the

pictures. Ellipses mark areas of gas generation, arrows point at areas where gas bubbles have moved to. Columns a) and c) are in the middle, column b) near the edge of the electrode. See more in SI and SM 3.

During cycling, lithium ions will pass through the separator, reduce or oxidize the electrolyte on the surface of the electrode, form a solid electrolyte interface (SEI) layer containing a large amount of generated gas, and finally lithiate or delithiate the electrode[49]. In Figure S2, Figure 4, and Figure 5 as well as in the in operando 2D movie SM 3, it is clearly shown that a pronounced gas generation and accumulation takes place within the electrode during the first discharge step, which is consistent with previous experimental results.[15, 50] However, some phenomena were observed that are in contradiction to what had been assumed previously. One is the non-uniform distribution of gas generation sites. During electrolyte reduction/oxidization by active lithium, on the one hand, the reductive/oxidative decomposed products form the SEI layer with organic carbonate outer surface and an inner inorganic salt[45] fully covering the electrode. On the other hand, notable amounts of gas are released. The polymer SEI layer remains on the surfaces of the electrodes and to some extent shapes into the wall of the channels through which the newly generated gas readily migrates out and finally merges with the accumulated gas, which eventually displaces the electrolyte and then takes the form of a skeleton structure within the electrode as clearly shown in Figure S2a and Figure 4a. Actually, because of the higher flow of electrochemically reactive Li ions it is plausible to find larger gas agglomerations close to the separator and wide channels grow into the electrode from the separator, which is consistent with the literature.[18] However, there are also a large number of gas bubbles or channels that are generated in the periphery of the electrode. The reason for this may stem from the high Li ion concentration in the electrolyte, which surrounds the electrode.[51] Another reason may stem from the Si electrode morphology that can modify the distribution of the electric field in the electrode. As shown in Figure 3a and g, the surface of the Si electrode is not flat, with the circumferential edge slightly higher than the center. Actually, it has been simulated that the electric filed has its highest value in the electrolyte at the tip of lithium dendrites.[52] In our case, the non-flat Si electrode morphology may result in an inhomogeneous electric field, with higher intensity in the circumferential edge than the center area. As a result, the lithium ions, driven by the different electric field, will preferentially react with the electrode materials in the periphery region. In the region near the current collector, the development of gas bubbles or channels is also observed, most likely because the Li ions are transported via the contacted particles[53] or by interstitials or vacancies in the SEI.[54] In a series of radiographic images during the first discharge process, see Figure 5a and SM 3a, we can clearly observe the gas movement. Figure 5b and SM 3b along with Figure 5c and SM 3c show the first charge and the second discharge process, respectively. They also clearly reveal unexpected dynamics of gas evolution and channel development during the electrochemical process. Note that radiographic images might give misleading information on the direction of gas movement because of the ignored third dimension. In contrast, the full view of gas evolution in 3D provided by tomography allows us access the three dimensional channel structures.

2.3 Gas development

Another unexpected phenomenon is the continuous production of gas in successive cycles. Contrary to the widespread belief that lithium ions diffuse uniformly from the separator to the current collector and form a lithiation front extending through the entire electrode,[55] the bubbles evolve successively from the circumferential surface into the bulk of the inner electrode and form a branched system of gas bubbles and channels. It follows from the observed gas evolution after delithiation or lithiation – as clearly shown in Figure S2b-c and Figure 4b-c –that lithium ions preferentially enter the electrode in an inwardly radial passage. The direct full-view visualization of the three-dimensional gas evolution presented here suggests diffusion pathways of lithium ions inside the anode material that are non-uniformly distributed.

In fact, recently more and more attentions are being devoted to the investigation of the electrochemically active particles in relation to the overall electrode current and/or the degree of current homogeneity.[24-25, 56] For example, a discrepancy is observed between electrochemical measurements that represent the overall state of the cell and spectroscopic data that represent a local state.[57-58] A recent experiment by Delmas *et al.* showed the coexistence of fully lithiated and fully delithiated individual $LiFePO_4$ cathode particles by X-ray diffraction after full lithiation.[59] Sugar *et al.* and Brunetti *et al.* further concluded that at any given time during cycling, only a small fraction of the total ensemble of particles is actively charged or discharged.[57, 60] Li *et al.* conducted an in-depth characterization and observed that only 5% to 8% of particles are actively intercalating during lithiation, while during delithiation the active population ranges from 8 to 32%.[24] They further confirm that the current is heterogeneously distributed in the electrode, that is to say, only a small number of active particles carries most of the current regardless of the total electrode current. Taking into account that lithiation of Si will not occur until the native silicon oxide is at least partially reduced by Li ions[49] and the gas evolution behavior presented here, we assume that diffusion of Li ions takes place as follows: during lithiation, Li ions that pass though the separator and/or the native Li ions in the native lithium salt electrolyte will first diffuse to the potentially active electrode particles, reduce the electrolyte and/or lithium salts with the obtain of electrons from the electrode and successively reduce the native silicon oxide, thus forming the SEI layer with inorganic inner species and organics outer species, releasing gas, and finally lithiate the active particles of the electrode, leaving non-active local regions intact.[10] Vice versa during delithiation. Using this picture, we can convincingly correlate gas evolution and channel formation with the active or potentially active particles during electrochemical delithiation and lithiation. More specifically, where gas is generated, where the active particles are, where the electrochemical current is concentrated. This finding is fundamental. For the first time, the spatially distributed electrochemically active particles in an operated LIB are directly visualized via the gas evolution.

For a more convenient visualization of the distributed population of active particles and/or potentially active particles, we separated them from the remaining particles. The results are shown in Figure 6b and Table 1. After each delithiation and lithiation step, the active particle population increases concurrently with the electrochemical process. From above analysis, we interpret delithiation and lithiation as a process of progressively activating potentially active particles.

2.3 Gas development

Table 1. Relative gas or channel volume fraction and number of active particles (both in %) as a function of the cycle state in region 1 and region 2 (see Figure 3g).

Fraction / State Name	First discharge	First charge	Second discharge
Region 1 Gas/Channel	20	31	39
Region 2 Gas/Channel	14	20	39
Region 1 Active Particles	29	46	64
Region 2 Active Particles	18	29	57

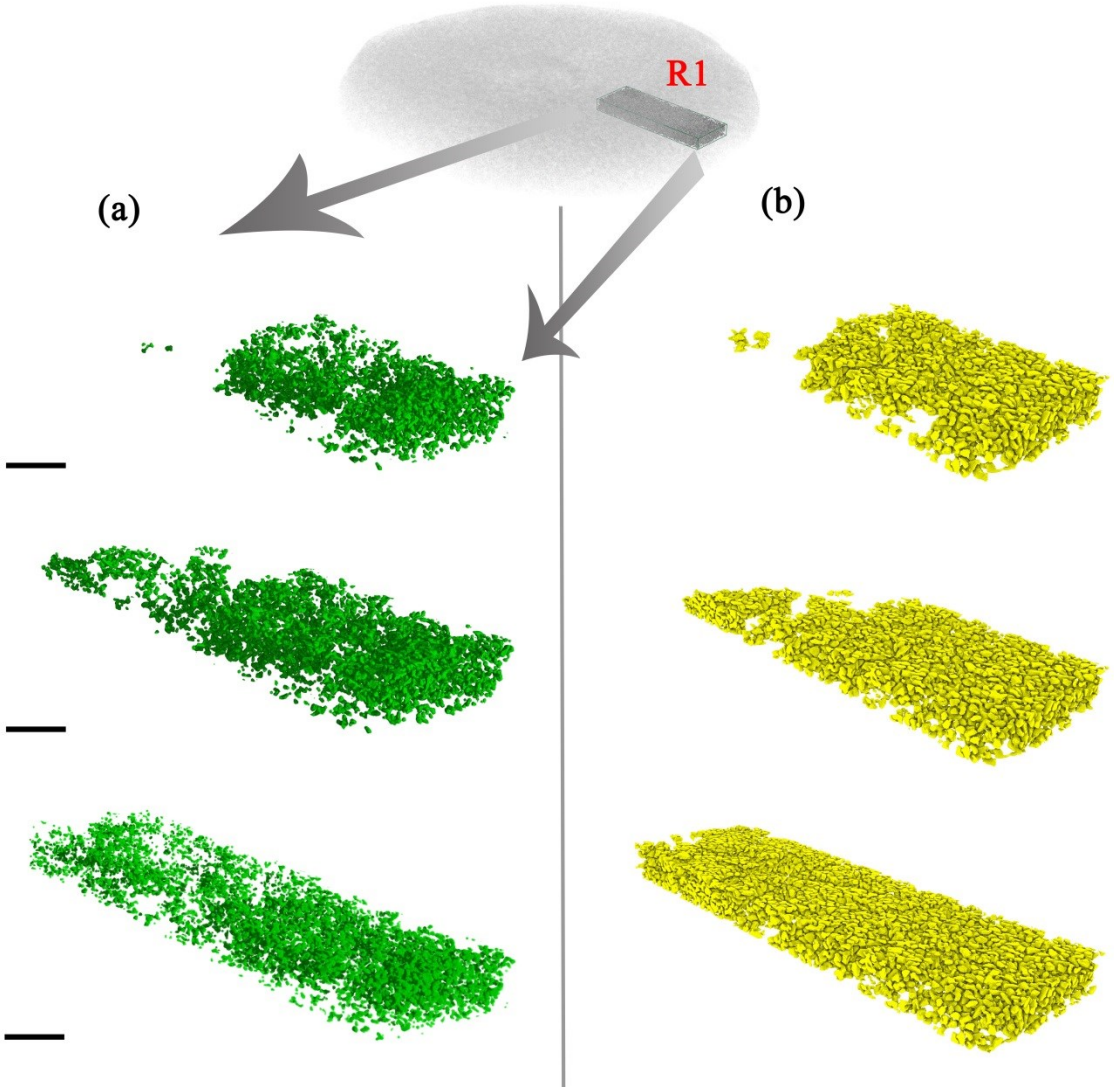

Figure 6. 3D visualization of region1as defined in Fig. 3g. a) gas or channel. b) active particles. From top to bottom: after first discharge, after first charge, after second discharge. The scale bar is 100 µm long in all the pictures.

To further quantify the relationship between both gas or channel volume changes and the population of active particles with electrochemical reactions, we calculated the volume fraction of gas or channel volume and the fraction of active particles after each charge and discharge process. Two independent regions – labeled R1 and R2 in Figur 3g – are extracted for quantitative analysis. The evolution of the gas or channel volume in region R1 is presented in Table 1 and in Figure 6a. After the first discharge step, the fraction of gas or channel volume is only 20% compared to 31% after the first charge step. After the second discharge step, the gas or channel volume fraction is ~39%. Along with these changes of gas or channel volume fraction, the increase of the fraction of active particles is evident in Figure 6b and Table 1, from 29% in the first discharged state to 46% in the first charged state and 64% in the second discharged state. Both trends imply the aforementioned delithiation/lithiation activation mechanism that progresses in each cycle. The analysis of R2 yields a similar result, increasing confidence in the applicability of the mechanism to the entire electrode.

The experiment conducted here connects the gas bubble or channel evolution with the evolution of effectively or potentially active particles in a functional LIB. This opens new perspectives in optimizing the overall performance of a battery. From the viewpoint of electrode engineering, it is important to find optimal battery operating conditions or to develop new materials with reduced gas formation. There are already some reports of adding electrolyte additives[8, 10] and using new electrolytes[13] to control gas generation and increase Li ion transport rates to enhance the LIBs's reversible performance. It is also crucial to optimize the electrode architecture to significantly increase the population of active particles to sustain the overall galvanostatic current and at the same time to improve the homogeneity of the distribution of active particles to prevent the extent of shocks and fractures induced by high local currents.[24] From the perspective of numerical simulation, it is important to identify the impact of SEI formation with the associated gas release within the electrode on the transport properties of Li ions and cycling performance of LIBs during discharge and charge[12] to further speed up the optimization of electrode structures. Altogether, the three dimensional microscale investigations of gas in the present study contribute to the understanding of the complex discharge and charge processes.

CONCLUSIONS

Novel insights into the spatial distribution and kinetics of gas evolution are unraveled by 3D synchrotron X-ray imaging for the first time. The knowledge obtained here enriches our understanding of the electrochemical activity in a real functional LIB. The gas evolution and channel formation occurring in a functional LIB have been directly visualized in a full-3D view after discharge and charge. Gas channels successively evolve from the surface of the anode

material into the bulk of the electrode and form a branched system of gas bubbles and channels. The observed gas evolution points at an activation of individual particles progressing from cycle to cycle. These novel findings presented here also highlight the unique synchrotron X-ray characterization tool for revealing underlying mechanisms of LIBs and shed light on a whole range of processes that could not previously be characterized in 3D. Indeed, our results and the value of information we obtained should speed up the optimization of the architecture and/or material of the current LIBs to design more stable electrodes to further enhance their performance for next-generation demand.

ACKNOWLEDGEMENTS

The assistance of the beamline scientist of the BAMline, Dr. Heinrich Riesemeier, is gratefully acknowledged. We thank Norbert Beck for fabricating the beamline battery and Elkem AS for providing us with Si particles. This work is sponsored by the Helmholtz-Zentrum Berlin and China Scholarship Council.

ASSOCIATED CONTENT

Supporting Information Available: including Methods, Data Processing, Figure S1-S3 and captions for the Supporting Movies. This material is available free of charge via the Internet at http://pubs.acs.org.

REFERENCES

(1) Yuk, J. M.; Seo, H. K.; Choi, J. W.; Lee, J. Y. Anisotropic Lithiation Onset in Silicon Nanoparticle Anode Revealed by in Situ Graphene Liquid Cell Electron Microscopy. *ACS Nano* **2014,** *8*, 7478-7485.

(2) Lin, F.; Markus, I. M.; Nordlund, D.; Weng, T.-C.; Asta, M. D.; Xin, H. L.; Doeff, M. M. Surface Reconstruction and Chemical Evolution of Stoichiometric Layered Cathode Materials for Lithium-Ion Batteries. *Nat Commun* **2014,** *5*, 3529-3538.

(3) Sun, F.; Huang, K.; Liu, Y.; Gao, T.; Han, Y.; Zhong, J. Hierarchical Structure of Co3o4 Nanoparticles on Si Nanowires Array Films for Lithium-Ion Battery Applications. *Appl. Surf. Sci.* **2013,** *266*, 300-305.

(4) Lv, D.; Shao, Y.; Lozano, T.; Bennett, W. D.; Graff, G. L.; Polzin, B.; Zhang, J.; Engelhard, M. H.; Saenz, N. T.; Henderson, W. A.; Bhattacharya, P.; Liu, J.; Xiao, J. Failure Mechanism for Fast-Charged Lithium Metal Batteries with Liquid Electrolytes. *Adv. Energy Mater.* **2014,** *5*, 1400993-1401000.

(5) Sun, F.; Huang, K.; Qi, X.; Gao, T.; Liu, Y.; Zou, X.; Zhong, J. Enhanced 3d Hierarchical Double Porous Co3o4/Graphene Architecture for Superior Rechargeable Lithium Ion Battery. *Ceram. Int.* **2014,** *40*, 2523-2528.

(6) Browning, K. L.; Baggetto, L.; Unocic, R. R.; Dudney, N. J.; Veith, G. M. Gas Evolution from Cathode Materials: A Pathway to Solvent Decomposition Concomitant to Sei Formation. *J. Power Sources* **2013,** *239*, 341-346.
(7) Vetter, J.; Holzapfel, M.; Wuersig, A.; Scheifele, W.; Ufheil, J.; Novák, P. In Situ Study on Co2 Evolution at Lithium-Ion Battery Cathodes. *J. Power Sources* **2006,** *159*, 277-281.
(8) Wuersig, A.; Scheifele, W.; Novák, P. Co2 Gas Evolution on Cathode Materials for Lithium-Ion Batteries. *J. Electrochem. Soc.* **2007,** *154*, A449-A454.
(9) Lanz, M.; Lehmann, E.; Imhof, R.; Exnar, I.; Novák, P. In Situ Neutron Radiography of Lithium-Ion Batteries During Charge/Discharge Cycling. *J. Power Sources* **2001,** *101*, 177-181.
(10) Seo, J. H.; Park, J.; Plett, G.; Sastry, A. M. Gas-Evolution Induced Volume Fraction Changes and Their Effect on the Performance Degradation of Li-Ion Batteries. *Electrochem. Solid-State Lett.* **2010,** *13*, A135-A137.
(11) Goers, D.; Holzapfel, M.; Scheifele, W.; Lehmann, E.; Vontobel, P.; Novák, P. In Situ Neutron Radiography of Lithium-Ion Batteries: The Gas Evolution on Graphite Electrodes During the Charging. *J. Power Sources* **2004,** *130*, 221-226.
(12) Rashid, M.; Gupta, A. Mathematical Model for Combined Effect of Sei Formation and Gas Evolution in Li-Ion Batteries. *ECS Electrochem. Lett.* **2014,** *3*, A95-A98.
(13) Etacheri, V.; Haik, O.; Goffer, Y.; Roberts, G. A.; Stefan, I. C.; Fasching, R.; Aurbach, D. Effect of Fluoroethylene Carbonate (Fec) on the Performance and Surface Chemistry of Si-Nanowire Li-Ion Battery Anodes. *Langmuir* **2011,** *28*, 965-976.
(14) Aurbach, D.; Markovsky, B.; Shechter, A.; Ein‐Eli, Y.; Cohen, H. A Comparative Study of Synthetic Graphite and Li Electrodes in Electrolyte Solutions Based on Ethylene Carbonate‐Dimethyl Carbonate Mixtures. *J. Electrochem. Soc.* **1996,** *143*, 3809-3820.
(15) Kumai, K.; Miyashiro, H.; Kobayashi, Y.; Takei, K.; Ishikawa, R. Gas Generation Mechanism Due to Electrolyte Decomposition in Commercial Lithium-Ion Cell. *J. Power Sources* **1999,** *81–82*, 715-719.
(16) Lee, K. H.; Song, E. H.; Lee, J. Y.; Jung, B. H.; Lim, H. S. Mechanism of Gas Build-up in a Li-Ion Cell at Elevated Temperature. *J. Power Sources* **2004,** *132*, 201-205.
(17) Agubra, V. A.; Fergus, J. W. The Formation and Stability of the Solid Electrolyte Interface on the Graphite Anode. *J. Power Sources* **2014,** *268*, 153-162.
(18) Shin, J.-S.; Han, C.-H.; Jung, U.-H.; Lee, S.-I.; Kim, H.-J.; Kim, K. Effect of Li2co3 Additive on Gas Generation in Lithium-Ion Batteries. *J. Power Sources* **2002,** *109*, 47-52.
(19) Kong, W.; Li, H.; Huang, X.; Chen, L. Gas Evolution Behaviors for Several Cathode Materials in Lithium-Ion Batteries. *J. Power Sources* **2005,** *142*, 285-291.
(20) Imhof, R.; Novák, P. In Situ Investigation of the Electrochemical Reduction of Carbonate Electrolyte Solutions at Graphite Electrodes. *J. Electrochem. Soc.* **1998,** *145*, 1081-1087.
(21) Gireaud, L.; Grugeon, S.; Laruelle, S.; Pilard, S.; Tarascon, J.-M. Identification of Li Battery Electrolyte Degradation Products through Direct Synthesis and Characterization of Alkyl Carbonate Salts. *J. Electrochem. Soc.* **2005,** *152*, A850-A857.
(22) Onuki, M.; Sakata, Y.; Yanagidate, M.; Otake, Y.; Kinoshita, S.; Ue, M.; Deguchi, M. Identification of the Source of Evolved Gas in Li-Ion Batteries by Using 13c-Labeled Solvents. *ECS Trans.* **2008,** *11*, 43-47.
(23) Wang, C.-M.; Li, X.; Wang, Z.; Xu, W.; Liu, J.; Gao, F.; Kovarik, L.; Zhang, J.-G.; Howe, J.; Burton, D. J.; Liu, Z.; Xiao, X.; Thevuthasan, S.; Baer, D. R. In Situ Tem Investigation of Congruent Phase Transition and Structural Evolution of Nanostructured Silicon/Carbon Anode for Lithium Ion Batteries. *Nano Lett.* **2012,** *12*, 1624-1632.

(24) Li, Y.; El Gabaly, F.; Ferguson, T. R.; Smith, R. B.; Bartelt, N. C.; Sugar, J. D.; Fenton, K. R.; Cogswell, D. A.; Kilcoyne, A. L. D.; Tyliszczak, T.; Bazant, M. Z.; Chueh, W. C. Current-Induced Transition from Particle-by-Particle to Concurrent Intercalation in Phase-Separating Battery Electrodes. *Nat Mater* **2014,** *13*, 1149-1156.
(25) Dreyer, W.; Jamnik, J.; Guhlke, C.; Huth, R.; Moskon, J.; Gaberscek, M. The Thermodynamic Origin of Hysteresis in Insertion Batteries. *Nat Mater* **2010,** *9*, 448-453.
(26) Bale, H. A.; Haboub, A.; MacDowell, A. A.; Nasiatka, J. R.; Parkinson, D. Y.; Cox, B. N.; Marshall, D. B.; Ritchie, R. O. Real-Time Quantitative Imaging of Failure Events in Materials under Load at Temperatures above 1,600 °C. *Nat Mater* **2013,** *12*, 40-46.
(27) Moosmann, J.; Ershov, A.; Weinhardt, V.; Baumbach, T.; Prasad, M. S.; LaBonne, C.; Xiao, X.; Kashef, J.; Hofmann, R. Time-Lapse X-Ray Phase-Contrast Microtomography for in Vivo Imaging and Analysis of Morphogenesis. *Nat. Protocols* **2014,** *9*, 294-304.
(28) dos Santos Rolo, T.; Ershov, A.; van de Kamp, T.; Baumbach, T. In Vivo X-Ray Cine-Tomography for Tracking Morphological Dynamics. *Proc. Natl. Acad. Sci. U. S. A.* **2014,** *111*, 3921-3926.
(29) Möbus, G.; Inkson, B. J. Nanoscale Tomography in Materials Science. *Mater. Today* **2007,** *10*, 18-25.
(30) Manke, I.; Banhart, J.; Haibel, A.; Rack, A.; Zabler, S.; Kardjilov, N.; Hilger, A.; Melzer, A.; Riesemeier, H. In Situ Investigation of the Discharge of Alkaline Zn–Mno2 Batteries with Synchrotron X-Ray and Neutron Tomographies. *Appl. Phys. Lett.* **2007,** *90*, 214102-214105.
(31) Haibel, A.; Manke, I.; Melzer, A.; Banhart, J. In Situ Microtomographic Monitoring of Discharging Processes in Alkaline Cells. *J. Electrochem. Soc.* **2010,** *157*, A387-A391.
(32) Shearing, P. R.; Howard, L. E.; Jørgensen, P. S.; Brandon, N. P.; Harris, S. J. Characterization of the 3-Dimensional Microstructure of a Graphite Negative Electrode from a Li-Ion Battery. *Electrochem. Commun.* **2010,** *12*, 374-377.
(33) Zielke, L.; Hutzenlaub, T.; Wheeler, D. R.; Chao, C.-W.; Manke, I.; Hilger, A.; Paust, N.; Zengerle, R.; Thiele, S. Three-Phase Multiscale Modeling of a Licoo2 Cathode: Combining the Advantages of Fib–Sem Imaging and X-Ray Tomography. *Adv. Energy Mater.* **2015,** *5*, 1401612-1401620.
(34) Zielke, L.; Barchasz, C.; Waluś, S.; Alloin, F.; Leprêtre, J. C.; Spettl, A.; Schmidt, V.; Hilger, A.; Manke, I.; Banhart, J.; Zengerle, R.; Thiele, S. Degradation of Li/S Battery Electrodes on 3d Current Collectors Studied Using X-Ray Phase Contrast Tomography. *Sci. Rep.* **2015,** *5*, 10921-10933.
(35) Zielke, L.; Hutzenlaub, T.; Wheeler, D. R.; Manke, I.; Arlt, T.; Paust, N.; Zengerle, R.; Thiele, S. A Combination of X-Ray Tomography and Carbon Binder Modeling: Reconstructing the Three Phases of Licoo2 Li-Ion Battery Cathodes. *Adv. Energy Mater.* **2014,** *4*, 1301617-1301623.
(36) Ebner, M.; Geldmacher, F.; Marone, F.; Stampanoni, M.; Wood, V. X-Ray Tomography of Porous, Transition Metal Oxide Based Lithium Ion Battery Electrodes. *Adv. Energy Mater.* **2013,** *3*, 845-850.
(37) Shearing, P. R.; Brandon, N. P.; Gelb, J.; Bradley, R.; Withers, P. J.; Marquis, A. J.; Cooper, S.; Harris, S. J. Multi Length Scale Microstructural Investigations of a Commercially Available Li-Ion Battery Electrode. *J. Electrochem. Soc.* **2012,** *159*, A1023-A1027.
(38) Wang, J.; Chen-Wiegart, Y.-c. K.; Wang, J. In Situ Three-Dimensional Synchrotron X-Ray Nanotomography of the (De)Lithiation Processes in Tin Anodes. *Angew. Chem. Int. Ed.* **2014,** *53*, 4460-4464.

(39) Chen-Wiegart, Y.-c. K.; DeMike, R.; Erdonmez, C.; Thornton, K.; Barnett, S. A.; Wang, J. Tortuosity Characterization of 3d Microstructure at Nano-Scale for Energy Storage and Conversion Materials. *J. Power Sources* **2014,** *249*, 349-356.
(40) Wang, J. Watching Microstructures in Action in Lithium-Ion Batteries. *ChemElectroChem* **2014,** *1*, 329-331.
(41) Ebner, M.; Marone, F.; Stampanoni, M.; Wood, V. Visualization and Quantification of Electrochemical and Mechanical Degradation in Li Ion Batteries. *Science* **2013,** *342*, 716-720.
(42) Liu, X. H.; Zhong, L.; Huang, S.; Mao, S. X.; Zhu, T.; Huang, J. Y. Size-Dependent Fracture of Silicon Nanoparticles During Lithiation. *ACS Nano* **2012,** *6*, 1522-1531.
(43) Sun, F.; Huang, K.; Qi, X.; Gao, T.; Liu, Y.; Zou, X.; Wei, X.; Zhong, J. A Rationally Designed Composite of Alternating Strata of Si Nanoparticles and Graphene: A High-Performance Lithium-Ion Battery Anode. *Nanoscale* **2013,** *5*, 8586-8592.
(44) Görner, W.; Hentschel, M. P.; Müller, B. R.; Riesemeier, H.; Krumrey, M.; Ulm, G.; Diete, W.; Klein, U.; Frahm, R. Bamline: The First Hard X-Ray Beamline at Bessy Ii. *Nuclear Instruments and Methods in Physics Research Section A: Accelerators, Spectrometers, Detectors and Associated Equipment* **2001,** *467-468*, 703-706.
(45) Pereira-Nabais, C.; Światowska, J.; Chagnes, A.; Ozanam, F.; Gohier, A.; Tran-Van, P.; Cojocaru, C.-S.; Cassir, M.; Marcus, P. Interphase Chemistry of Si Electrodes Used as Anodes in Li-Ion Batteries. *Appl. Surf. Sci.* **2013,** *266*, 5-16.
(46) Nie, M.; Abraham, D. P.; Seo, D. M.; Chen, Y.; Bose, A.; Lucht, B. L. Role of Solution Structure in Solid Electrolyte Interphase Formation on Graphite with Lipf6 in Propylene Carbonate. *J. Phys. Chem. C* **2013,** *117*, 25381-25389.
(47) Zhou, X.; Yin, Y.-X.; Wan, L.-J.; Guo, Y.-G. Self-Assembled Nanocomposite of Silicon Nanoparticles Encapsulated in Graphene through Electrostatic Attraction for Lithium-Ion Batteries. *Adv. Energy Mater.* **2012,** *2*, 1086-1090.
(48) Arlt, T.; Maier, W.; Tötzke, C.; Wannek, C.; Markötter, H.; Wieder, F.; Banhart, J.; Lehnert, W.; Manke, I. Synchrotron X-Ray Radioscopic in Situ Study of High-Temperature Polymer Electrolyte Fuel Cells - Effect of Operation Conditions on Structure of Membrane. *J. Power Sources* **2014,** *246*, 290-298.
(49) Schroder, K. W.; Celio, H.; Webb, L. J.; Stevenson, K. J. Examining Solid Electrolyte Interphase Formation on Crystalline Silicon Electrodes: Influence of Electrochemical Preparation and Ambient Exposure Conditions. *J. Phys. Chem. C* **2012,** *116*, 19737-19747.
(50) Armstrong, A. R.; Holzapfel, M.; Novák, P.; Johnson, C. S.; Kang, S.-H.; Thackeray, M. M.; Bruce, P. G. Demonstrating Oxygen Loss and Associated Structural Reorganization in the Lithium Battery Cathode Li[Ni0.2li0.2mn0.6]O2. *J. Am. Chem. Soc.* **2006,** *128*, 8694-8698.
(51) Nadimpalli, S. P. V.; Sethuraman, V. A.; Dalavi, S.; Lucht, B.; Chon, M. J.; Shenoy, V. B.; Guduru, P. R. Quantifying Capacity Loss Due to Solid-Electrolyte-Interphase Layer Formation on Silicon Negative Electrodes in Lithium-Ion Batteries. *J. Power Sources* **2012,** *215*, 145-151.
(52) Jana, A.; Ely, D. R.; García, R. E. Dendrite-Separator Interactions in Lithium-Based Batteries. *J. Power Sources* **2015,** *275*, 912-921.
(53) Malik, R.; Abdellahi, A.; Ceder, G. A Critical Review of the Li Insertion Mechanisms in Lifepo4 Electrodes. *J. Electrochem. Soc.* **2013,** *160*, A3179-A3197.
(54) Lu, P.; Harris, S. J. Lithium Transport within the Solid Electrolyte Interphase. *Electrochem. Commun.* **2011,** *13*, 1035-1037.
(55) Ferguson, T. R.; Bazant, M. Z. Nonequilibrium Thermodynamics of Porous Electrodes. *J. Electrochem. Soc.* **2012,** *159*, A1967-A1985.

(56) Lin, F.; Nordlund, D.; Weng, T.-C.; Zhu, Y.; Ban, C.; Richards, R. M.; Xin, H. L. Phase Evolution for Conversion Reaction Electrodes in Lithium-Ion Batteries. *Nat Commun* **2014,** *5*, 3358-3367.
(57) Brunetti, G.; Robert, D.; Bayle-Guillemaud, P.; Rouvière, J. L.; Rauch, E. F.; Martin, J. F.; Colin, J. F.; Bertin, F.; Cayron, C. Confirmation of the Domino-Cascade Model by Lifepo4/Fepo4 Precession Electron Diffraction. *Chem. Mater.* **2011,** *23*, 4515-4524.
(58) Shin, H. C.; Chung, K. Y.; Min, W. S.; Byun, D. J.; Jang, H.; Cho, B. W. Asymmetry between Charge and Discharge During High Rate Cycling in Lifepo4 – in Situ X-Ray Diffraction Study. *Electrochem. Commun.* **2008,** *10*, 536-540.
(59) Delmas, C.; Maccario, M.; Croguennec, L.; Le Cras, F.; Weill, F. Lithium Deintercalation in Lifepo4 Nanoparticles Via a Domino-Cascade Model. *Nat Mater* **2008,** *7*, 665-671.
(60) Sugar, J. D.; El Gabaly, F.; Chueh, W. C.; Fenton, K. R.; Tyliszczak, T.; Kotula, P. G.; Bartelt, N. C. High-Resolution Chemical Analysis on Cycled Lifepo4 Battery Electrodes Using Energy-Filtered Transmission Electron Microscopy. *J. Power Sources* **2014,** *246*, 512-521.

2.3.1 Supporting Information

Three Dimensional Visualization of Gas Evolution and Channel Formation inside a Lithium-ion Battery

Fu Sun*[,†,‡], Henning Markötter[†,‡], Ingo Manke[‡], Andre Hilger[‡], Nikolay Kardjilov[‡] and John Banhart[†,‡]
[†]Institute of Materials Science and Technology
Technische Universität Berlin
10623 Berlin, Germany
[‡]Helmholtz Centre Berlin for Materials and Energy
Hahn-Meitner-Platz 1
14109 Berlin, Germany
*Corresponding Author: fu.sun@helmholtz-berlin.de

This section includes:

Methods

Battery Preparation:

A normally functioning battery is crucial for the synchrotron X-ray imaging technique. The widely used coin cell is not convenient for the X-ray because it blocks beam from characterization. During the rotation in the characterization, the battery has to be fully X-ray transparent to allow the imaging procedure. In addition, properly sealing is critical to ensure that the cell can work normally and meanwhile be stable during the characterization process. To satisfy the technological needs, we develop a polymeric tube proof-of-concept battery, as shown in Figure 1a. On the one hand, the polyamide-imide tube housing ensures high X-ray transmission. On the other hand, the proof-of-concept battery also has good sealing ability so that the electrochemical battery remains functional for months. To further improve X-ray

transmission though the battery, we machine a groove around the entire circumference of the tube housing.

A conventional electrode is made from the electrode slurries with weight ratios of Si:carbon black:binder of 80:10:10 in NMP. The slurry was cast directly onto the top of one of the screws. To remove the NMP, the casted screws were dried in an oven at 60 ℃ overnight. Before and after casting process, the screw was weighed to determine the weight of the electrode materials. Metallic lithium was placed on the top of another screw, as the counter and reference electrode. A polymer separator soaked with the electrolyte was placed between the lithium electrode and Si electrode. The beamline proof-of-concept battery was assembled in an argon filled glovebox with humidity and oxygen levels below 0.1 ppm.

Our developed proof-of-concept battery also allows performing various electrochemical characterizations and analysis such as cyclic voltagram and dis/charge profile. Furthermore, the beamline battery can undergo considerable stability during the characterization process.

Electrochemical Measurements:

Cyclic voltammetry (CV) and galvanostatic charge/discharge of the battery were carried out with IviumStat. A fresh battery after assembly was measured for CV curves from 2.5 V to 0 V at a scan rate of 1 mV/s. In the beamline, the battery is mounted on the centering and rotation table through the small screw on top of the electrode screw, thus confirming the full stability of the battery during the characterization process. Thin unclad copper wires are wrapped around the small screws connecting each electrode and are secured between the two small screws. The wires are then connected to the IviumStat potentiostat, as shown in Figure 1c. The wire lengths are also long enough to enable the cell to rotate in the beamline without any obstructions. During X-ray imaging process, electrochemical testing is performed by remotely controlling the potentiostat within the beamline hutch. The schematic illustration of the battery in XBAM*line* in BESSY is briefly described in Figure 1.

Tomography Settings and Data Acquisition:

The X-ray tomography and radiography imaging are conducted in the XBAM*line* in BESSY, Berlin, Germany. XBAM*line* is a dedicated tomography beamline, of which the usable X-ray spectrum is 5-100 KeV. In this experiment, monochromatic synchrotron radiation at 20 KeV (selected using a $[W/Si]_{100}$ multi-layer monochromator), a 20 µm $CdWO_4$ scintillator and an optical 10X objective in conjuction with a pco4000 camera (with a 4008 x 2672 $pixel^2$ CCD chip) are selected[1-2]. The ultimate resolution is 0.876 µm. For each tomography, 2200 projections over an angular range of 180° battery rotation with 4 s exposure time are recorded. As for the radiographies, the battery was directly imaged during the charge/discharge process with 4 s exposure time.

Data Processing

Data process & 3D visualization method:

2.3 Gas development

The obtained raw data are firstly flat- and darkfield corrected and rearranged into sinograms. A median filter with a kernel size of 3 ×3×3 voxels was applied to the original image for noise reduction. After that, the Si/Si_xLi and the other regions (carbon black and polymer binder) are labeled by simple threshold segmentation (Image J 1.49i). The histogram of the reconstruction images consist of two peaks for these Si/Si_xLi and the other regions and therefore the threshold value can be chosen as the minimum value between two peaks. The reconstructed volume is registered using commercial software Avizo Fire, version 8.0 and for 3D presentation. We also adopted commercial software VGStudio Max, version 2.2 for 3D visualization.

Analysis of (potentially) active particles:

After labeling process via Avizo Fire, a lot of properties of particles can be obtained through the bulilt-in measurements. Herein, the diameter of each particle is obtained by the built-in equivalent diameter: EqDiameter:

$$EqD=\sqrt{\frac{4\times Area}{\pi}}$$

To successfully separate the particles connected with the gas/channel from these particles that don't connect with void/channel, we use the commercial software Image J. The idea is this: suppose particle A is connected with void a, if we Maximize the diameter of void a, then the particle A will overlap with void a and we can use the Minimum operation between particle A and void a to get the overlap zone A'. So far, we have only small part A' of the particles that are connected with the voids. After that, we increase the gray value of A' and add it with all the particles. In the last step, we use the 3D Hysteresis Thresholding to discern the particles that has A' from those that do not have, namely the particles that are not connected with voids. Through this procedure, we can successfully separate the particles that are connected with voids from those that are not.

SI Figures

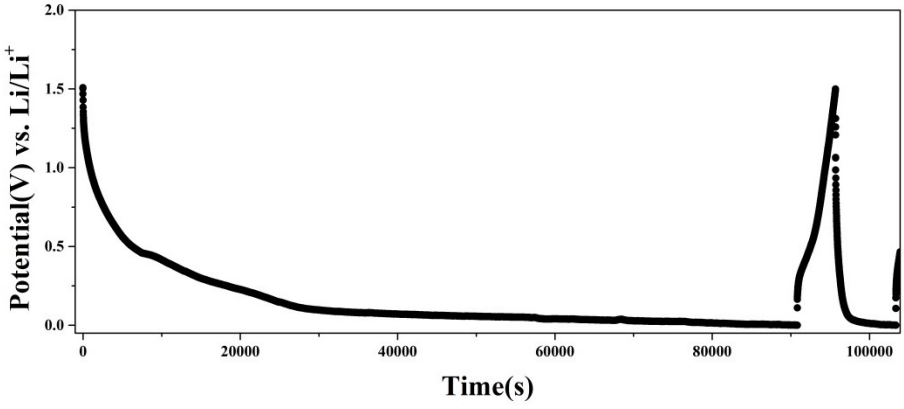

2.3 Gas development

Figure S1. The first discharge, the first charge and the second discharge voltage-time profiles of a beamline battery at $0.01 Ag^{-1}$.

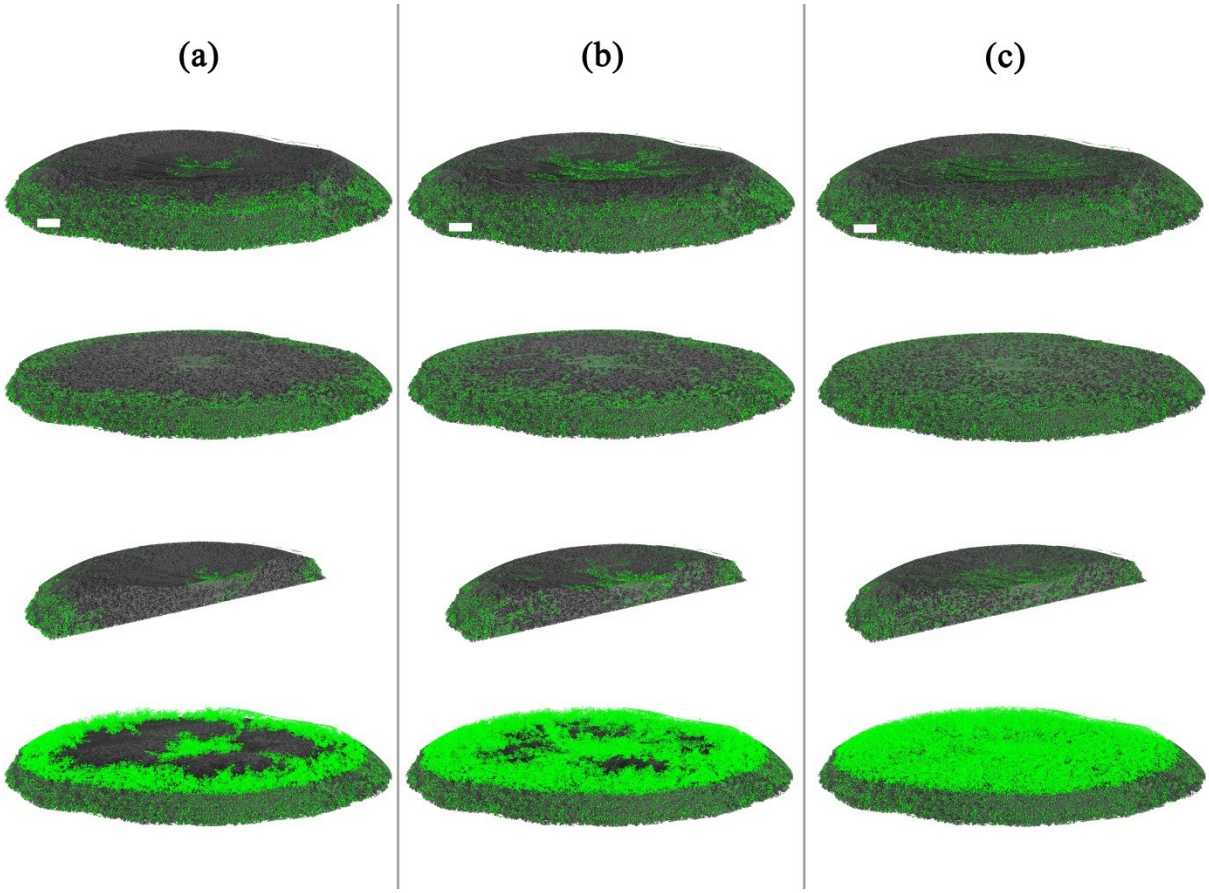

Figure S2. 3D visualization of the evolution of developed gas in the battery: a) After first discharge. b) After first charge. c) After second discharge. In all sections, from the top to the bottom, the row shows the 3D visualization, the plane view, the cross section view of the Si and gas/void composite and the solitary gas/void 3D rendering. The scale bar is 100µm in all pictures.

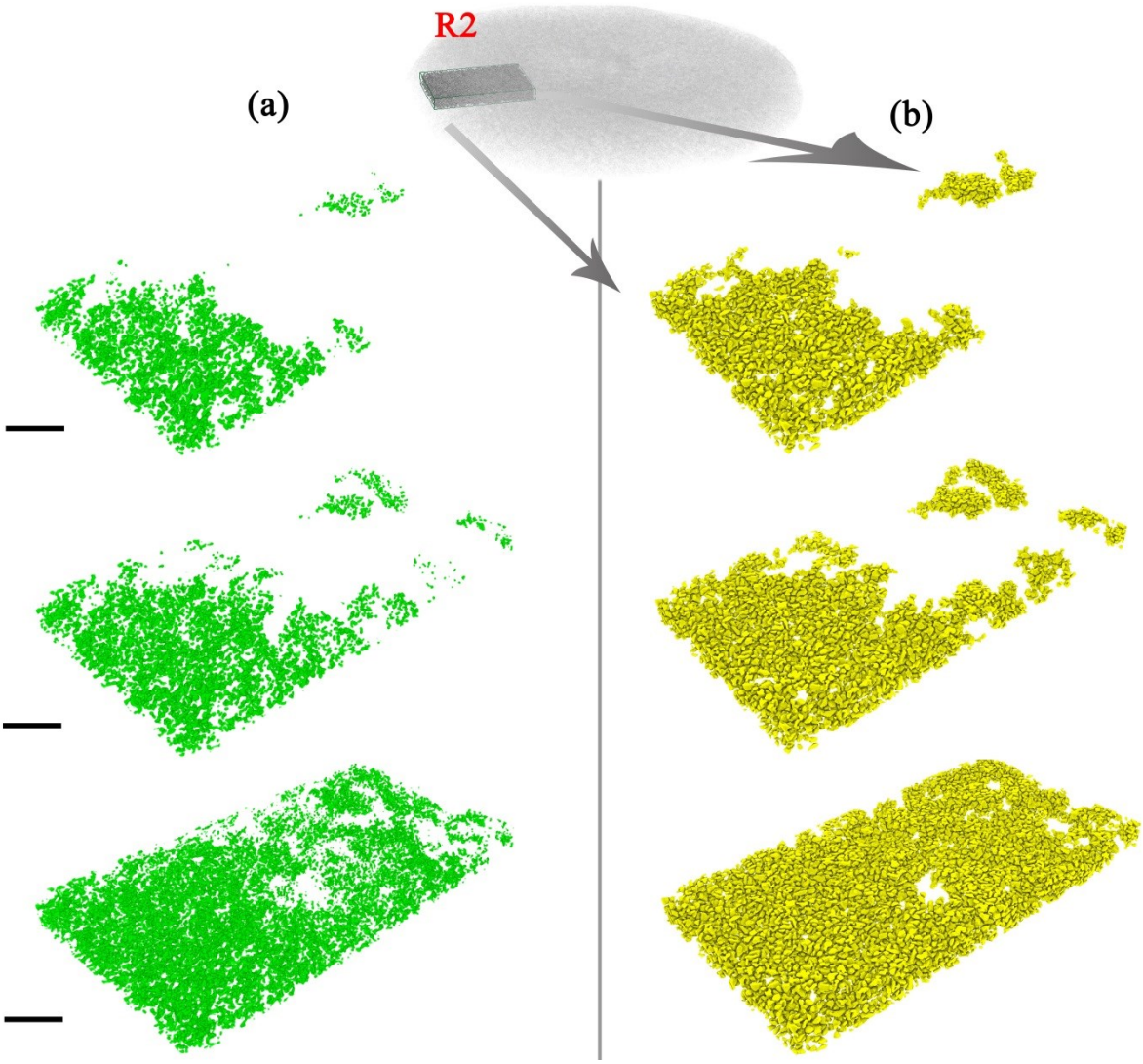

Figure S3. a) 3D visualization of the evolution of gas/channel on the left. b) and the active particle population, on the right in Region2: from top to bottom is the result of, after first discharge; after first charge; after second discharge. The scale bar is 100μm in all pictures.

Captions for the Supporting Movies

http://pubs.acs.org/doi/abs/10.1021/acsami.6b00708

SM1:
Three Dimension Visualization of Reconstructed Silicon Electrode

SM2:

SM2a-Three Dimension Visualization of Reconstructed Firstly Discharged Si Electrode
SM2b-Three Dimension Visualization of Reconstructed Firstly Charged Si Electrode

SM2c-Three Dimension Visualization of Reconstructed Secondly Discharged Si Electrode

SM3a:

SM3a-1-First-Discharge-Movie_Region_Left

SM3a-2-First-Discharge-Movie_Region_Right

SM3b:

SM3b-1-First-Charge-Movie_Region_Left

SM3b-2-First-Charge-Movie_Region_Right

SM3c:

SM3c-1-Second-Discharge-Movie_Region_Left

SM3c-2-Second-Discharge-Movie_Region_Right

References

(1) Arlt, T.; Maier, W.; Tötzke, C.; Wannek, C.; Markötter, H.; Wieder, F.; Banhart, J.; Lehnert, W.; Manke, I. Synchrotron X-Ray Radioscopic in Situ Study of High-Temperature Polymer Electrolyte Fuel Cells - Effect of Operation Conditions on Structure of Membrane. *J. Power Sources* **2014,** *246*, 290-298.

(2) Manke, I.; Banhart, J.; Haibel, A.; Rack, A.; Zabler, S.; Kardjilov, N.; Hilger, A.; Melzer, A.; Riesemeier, H. In Situ Investigation of the Discharge of Alkaline Zn–Mno2 Batteries with Synchrotron X-Ray and Neutron Tomographies. *Appl. Phys. Lett.* **2007,** *90*, 214102-214105.

2.4 Degradation of lithium ion batteries based on ~100 µm-sized Si particles

Reprinted with permission from **DOI**: 10.1016/j.jpowsour.2016.04.126.

Investigation of failure mechanisms in silicon based half cells during the first cycle by micro X-ray tomography and radiography

Fu Sun [a,b,], Henning Markötter [b], Kang Dong [a,b], Ingo Manke [b], Andre Hilger [b], Nikolay Kardjilov [b] and John Banhart [a,b]*

[a] Institute of Material Science and Technologies
Technical University Berlin
10623 Berlin, Germany

[b] Helmholtz Centre Berlin for Materials and Energy
Hahn-Meitner-Platz 1
14109 Berlin, Germany

*Corresponding Author: fu.sun@helmholtz-berlin.de

Abstract

Two proof-of-concept batteries were designed and prepared for X-ray microtomography and radiography characterizations to investigate the degradation mechanisms of silicon (Si) based half cells during the first cycle. It is highlighted here for the first time that, apart from the significant volume expansion-induced pulverization, the electrochemical "deactivation" mechanism contributes significantly to the capacity loss during the first charge process. In addition, the unexpected electrochemically inactive Si particles are also believed to substantially decrease the energy density due to the inefficient utilization of loaded active material. These unexpected findings, which cannot be deduced from macroscopic electrochemical characterizations, expand the inherent explanations for performance deterioration of Si-anode material based lithium ion batteries (LIBs) and emphasize the vital value of microscopic techniques in revealing the correlation between macroscopic electrode structure and the overall electrochemical performance.

Key words

lithium ion battery; silicon particles; degradation mechanisms; X-ray micro tomography; X-ray micro radiography

Introduction

Following their commercial introduction in the early 1990s, lithium ion batteries (LIBs) have penetrated ubiquitously into the market for energy storage systems, e.g. laptops and mobile phones [1, 2]. More recently, advanced LIBs with a larger specific energy, higher power density and longer cycle life have been considered for powering clean electric vehicles (EVs) and plug-in hybrid vehicles (PHVs), as well as for the storage and distribution of energy from sustainable sources, such as solar and wind energy [3-6]. The key to fabricate such next-generation LIB is to exploit high-performance electrode materials. From the material's point of view, silicon (Si) is a

promising candidate for the anode of LIBs because it possesses the highest theoretical capacity of 3579 mAh/g when lithiated to $Li_{21}Si_5$, that is about 10 times larger than the currently commercialized carbonaceous anode, which features 372 mAh/g for LiC_6 [7-9]. This promising potential of the high specific capacity has spurred considerable investigations of Si thin films [10], carbon mixed [11, 12] and metal coated [13] Si composites, along with various Si nanostructures, such as nanoparticles [14], nanowires [15], nanospheres [16] and nanotubes [17] that could serve as building blocks for high-performance anodes. Despite these extensive efforts, Si-based anode LIBs still inevitably suffer from substantial capacity decay during lithium insertion and extraction and thus they are now below the requirements for practical applications.

To shed light on the underlying degradation mechanisms, a range of investigation techniques such as scanning electron microscopy (SEM) [18], transmission electron microscopy (TEM) [19], X-ray diffraction (XRD) [20], nuclear magnetic resonance (NMR) [21] and Raman spectroscopy [22] have been adopted. As a result, our knowledge of the intrinsic behaviour of Si upon lithium insertion and extraction has been significantly enhanced [23] and various possible explanations for the performance deterioration have been proposed. For instance, it has been discovered that, apart from the loss of the lithium inventory and electrolyte/binder decomposition [24], the preferential volume expansion along Si [110] directions is as large as ~300% during lithium insertion and this extraordinary volume change has been proposed as the primary factor contributing to the fatal capacity decay [25]. Nevertheless, prior analytical tools are inherently limited. For example, most of the measurements abovementioned explore the degradation mechanisms on the atomic or single nanoparticle level, overlooking the interplays amongst a multitude of particles and the interactions between the active material and the conductive/binder agent. What is more, a particular battery design, such as open structure and specialized electrolyte that does not adequately simulate the real battery operating conditions is widely employed. On the other hand, most conventional tools only specialize in revealing the structural and compositional information without imaging capability, lacking effective spatially resolved information about the degradation mechanisms. In parallel, some investigations are carried out *ex situ*, i.e. post-mortem, as opposed to *in situ* characterizations of dynamic processes. Considering that a realistic composite electrode includes an assembly of ensembles of active particles, an organic polymeric binder and a conducting agent, the ability to probe the dynamic deterioration mechanisms on a multi-particle electrode level is of technological and practical importance. Therefore, it is crucial and emergent that fundamental research techniques are highly needed to further promote the exploration of electrode degradation.

Recently, X-ray imaging based on either laboratory X-ray or synchrotron X-ray sources has rapidly evolved into a powerful characterization tool in materials science [26-42]. Specifically, X-ray imaging has enabled researchers to obtain unprecedented insights into LIBs non-destructively on a length scale ranging from particles to entire electrodes and has contributed markedly to our understanding [29-33]. The pioneering research of employing synchrotron X-ray tomography by Ebner *et al*. features a direct observation and quantification of electrochemical and mechanical degradation in a SnO anode [34]. Meanwhile, Gonzalez *et al*. have visualized the

expansion of large Si particles during the first lithiation step in three-dimensions (3D) by means of tomography based on a laboratory X-ray source [35].

Herein, by employing both laboratory X-ray tomography and radiography, we re-inspect the underlying mechanism of performance degradation of Si based half cells from the perspective of entire electrodes, which implies spanning the length scales from individual active particles to the macroscopic electrode ensemble. On the one hand, X-ray microtomography grants us the ability to track the structural evolution induced by volume changes in three dimensions. On the other hand, *in operando* micro X-ray radiography enables us to directly observe the changes of the active particles and an entire electrode during lithium insertion and extraction. By the combinatorial X-ray tomography and radiography, for the first time we highlight that, apart from the huge volume expansion/contraction of Si particles during cycles, the striking inhomogeneous lithiation/delithiation mechanism amongst ensemble active particles observed in an electrode, which cannot be easily detected in conventional electrochemical measurements and, the unprecedented electrochemical "deactivation" of original electrochemical active particles are another two key factors contributing to the substantial performance degradation. This study expands the inherent explanations for performance deterioration of Si-anode material based LIBs, and the new sights would open new design principles and opportunities for high-capacity electrode materials for next-generation energy storage systems.

Experimental Section

Materials:

Silicon was received from Elkem AS, Norway. Polyvinylidene difluoride (PVDF) binder, carbon black, Celgard separator, CR2032 coin cells and lithium were purchased from MTI Cor. USA. N-methyl pyrrolidone solvent (NMP) and 1M $LiPF_6$ in a volume-ratio (1:1) mixture of ethylene carbonate (EC) and dimethyl carbonate (DMC) were purchased from Sigma Aldrich. Titanium foil is from ANKURO Int. GmbH, Germany. The housing of proof-of-concept beamline battery is made of polyamide-imide (Torlon), from McMaster-Carr company.

Characterization:

Scanning electron microscopy (SEM) image were taken using a Zeiss ultraplus microscope. The electrochemical characterizations were conducted by using an Ivium CompactStat station, Iviumtechnology.

Battery Preparation:

The composite electrode is made of slurries with weight ratios of Si:carbon black:binder of 75:15:10 in NMP. For the tomo-cell, the slurry was first sandwiched between two glasses and put into an oven at 60 ℃ to dry and form a block, which was then cut into small pieces with a razor blade and put directly onto the top of the screws. The resultant Si composite electrode was a small piece of 1.7 x 1.7 x 0.2 mm (length x width x height). Before the Si composite was assembled into the tomo-cell, it was weighed by a digital balance and the amount of Si particles was determined from the origian mass ration. The Si composite electrode mass in the tomo-cell was around 0.9 mg. For the radio-cell, the slurry was casted onto the 5µm thick titanium (Ti) foil. The area of the slurry was around 4 x 3 mm (length x width). To remove the NMP, the casted Ti foil was also dried in an oven at 60 ℃. Before and after the casting process, Ti foil was weighted

to determine the weight of the electrode materials. The Si composite in the radio-cell was around 1 mg. These two proof-of-concept batteries were assembled in an argon filled glovebox with humidity and oxygen levels below 0.1 ppm. During battery assembly, these two cells were only hand-assembled without exerting extra pressures. For the tomo-cell, metallic lithium (2.5 mm diameter, 1 mm thick) was placed on top of the other screw, and served as a counter and reference electrode. For the radio-cell, a lollipop shape copper foil without inner region (out diameter is 10 mm and inner diameter is 6 mm) was used as a current collector and the Ti foil was placed on top of it. Metallic lithium (6 mm diameter, 1 mm thick) was used as the opposite electrode. A polymer separator was placed between the lithium electrode and the Si electrode in both cells. After filling these two cells with sufficient electrolyte, they were sealed off and then taken out of the glovebox. For a further comparison of the electrochemical activity of Si composite electrode in the two proof-of-concept cells, commercial CR2032 coin-cell with the same Si electrode was assembled and tested.

Micro X-ray Tomography & Radiography Characterizations:

X-ray tomography was conducted on the tomo-cell in the original state and after the voltage had dropped to 0.03V, 0.02V, 0.01V and 0V during discharge. During the discharge process, the current was set to be 0.04 mA. The five tomographies are implied by alphabet a, b, c, d and e in Fig. 4, Fig. 5 and Fig. 6. The particular parameters for the X-ray tomography are as follows: the energy is 60 kV, the current is 166 µA, the source detector distance (SDD) is 500 mm, the source object distance (SOD) is 58 mm. Given the resulting magnification, each detector pixel therefore represented 5.76 µm/voxel in the sample. The exposure time is 2.1 s. During the 360° rotation, 800 projections were recorded. During the charge process, the current was switched to 0.01mA and the tomography was conducted after the voltage had risen to 0.5 V, 0.7 V, 1 V, 1.5 V and 2 V. The five tomographies are implied by alphabet f, g, h, i, and j in Fig. 4, Fig. 5 and Fig. 6. The locations of the particles shown in Fig. 3, Fig. 4 and Fig. 5 are marked in SI Fig. 4. More information is given in the Supporting Information (SI).

For the X-ray radiography measurements, characterization was conducted in situ during the whole discharge/charge process of the radio-cell. During the discharge process, the current was 0.07 mA for 0-18h and then was switched to 0.04 mA for the rest of discharge process. During the charge process, the current was set to be 0.015mA for 6.5 h and then was changed to 0.01 mA until the voltage was 2 V. The radio-cell was facing the X-ray source during the characterization.

Data Processing:

To keep the validity of the measurements, only a median filter (1×1×1) was performed in ImageJ. 3D particle visualization was performed by VGStudio MAX. Analysis of the particles is conducted by Imaje J. More information is given in the SI.

Results and Discussion

X-ray microtomography and radiography was conducted with a laboratory X-ray CT system [43]. To be fully compatible with X-ray imaging and at the same time to completely represent working LIBs, we have designed and manufactured two dedicated proof-of-concept electrochemical cells: a cell for tomography (tomo-cell) and a cell for radiography (radio-cell). Fig. 1 displays

photographs and the corresponding schematic illustrations of the two proof-of-concept batteries as well as a schematic representation of the X-ray micro CT setup [44].

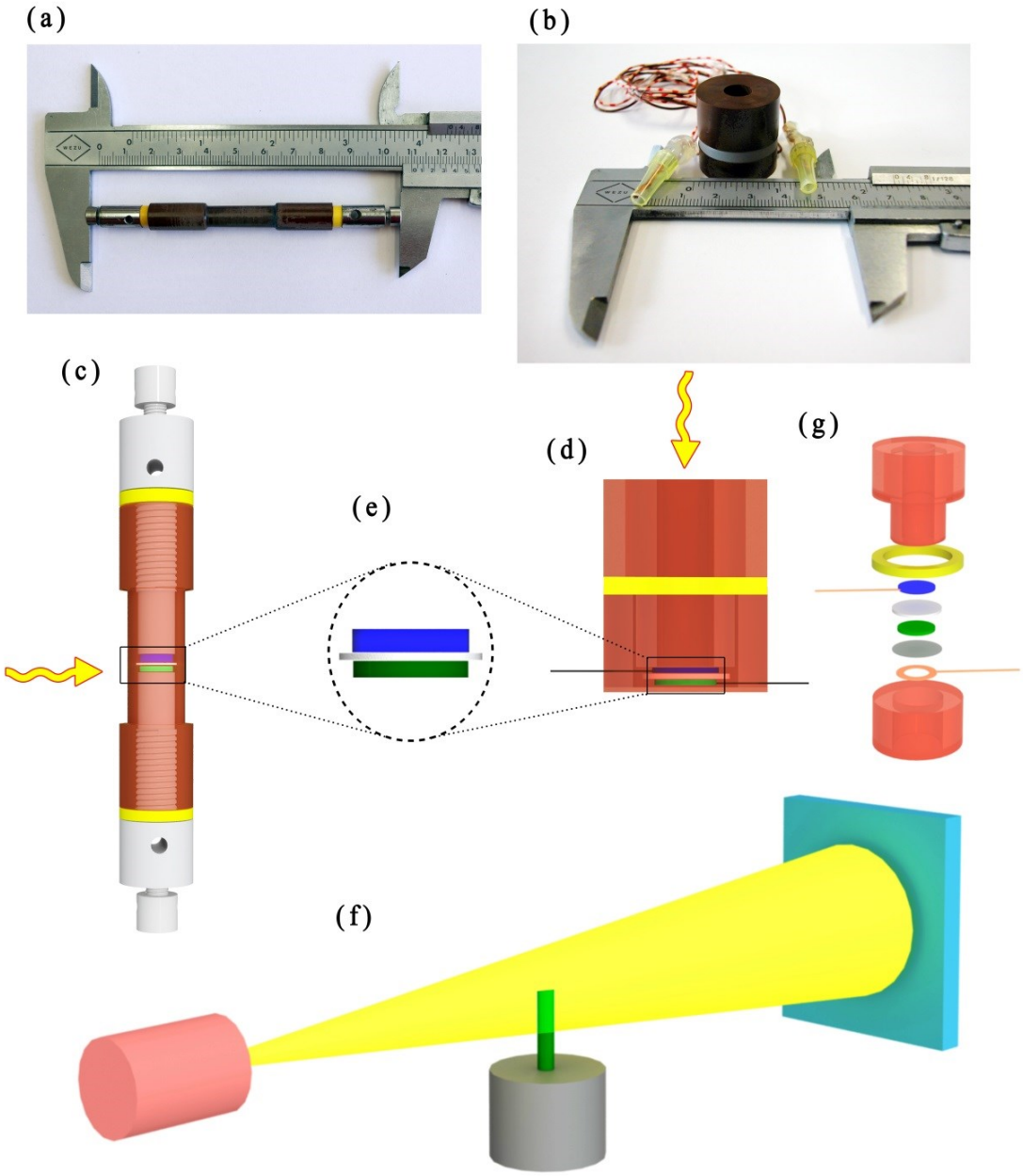

Fig. 1. Images of the proof-of-concept batteries: a) tomo-cell and b) radio-cell. c) Corresponding schematic representation of the tomo-cell. d) and g) Corresponding schematic representations of the radio-cell. e) Enlarged region of interest comprising from top to bottom: lithium (blue), separator (grey) and electrode material (green). g) Schematic illustration of the radio-cell, from top to bottom are, the upper housing (brown), sealing ring (yellow), lithium plate (blue) with copper wire, separator (white), Si/carbon/binder composite (green), titanium foil current collector (gray), lollipop-shaped copper current collector (copper), the lower housing (brown). f) Schematic representation of the X-ray micro CT setup. From left to right: X-ray source (red), cone X-ray beam (yellow), sample representing either of the two

cells (green) and rotation table (grey), detector (blue). The waves in c) and d) represent the direction of X-rays.

After assembling the two proof-of-concept batteries, cyclic voltammetry (CV) was performed to verify the reduction and oxidation characteristics of Si. The insets of Fig. 2 show the CV curves of the two batteries scanned at rate of 1 mV s^{-1} in the potential window of 0-2.5 V. Although there are parasitic redox peaks (arrows in CV figure) associated with contamination and/or electrolyte decomposition [45, 46], the clearly visible cathodic peak above 0 V and an anodic peak at 0.5 V are related to the Li alloying and de-alloying with Si, respectively. The results are in good agreement with previously reported Si/Carbon composites [9, 47], thus confirming the electrochemical reactions inside our proof-of-concept batteries.
Then we conduct the X-ray imaging investigations by galvanostatically discharge/charge these two electrochemical batteries: for tomography, the discharge/charge process was stopped during the tomographic data acquisition and continued afterwards (i.e. the measurement is quasi *in situ*). For radiography, the measurement is continuously conducted simultaneously during the discharge/charge process of the radio-cell (i.e. imaging is truly *in situ*). The discharge/charge curves of both cells, showing the typical characteristic feature of Si are displayed in Fig. 2 and they are in good agreement with previous results [9]. Note that for the tomographic imaging, a newly assembled battery is used, while for radiographic imaging, the battery is first used to obtain the CV scans and then directly used for *in situ* radiography measurement (read more in Supporting Information (SI)). For a further comparison of the electrochemical activity of Si materials in the two proof-of-concept cells, commercial coin-cell assembled with the same Si electrode was conducted and the resultant discharge/charge curve is shown in SI Fig. 1. It is found that these three cells have a low coulomb efficiency during the first charge and the reason may stem from the significant particle pulverization of the large Si particles currently used [19].

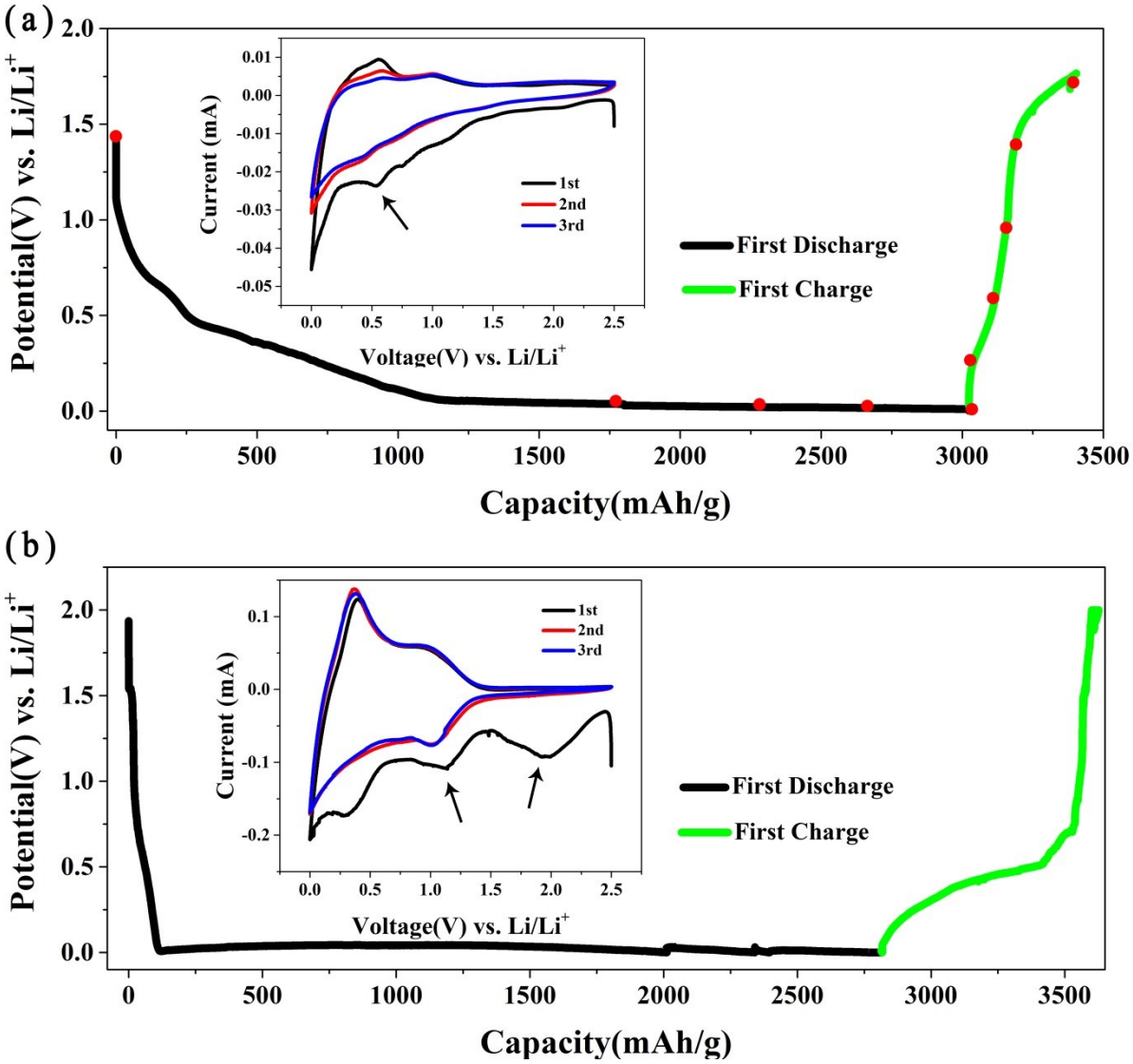

Fig. 2. Electrochemical characterization of the tomo-cell and radio-cell: a) the first discharge-charge curve of the tomo-cell, the inset shows the CV curves; b) same as a) for the radio-cell.

Micro-computed X-ray imaging is an emerging analytical technique that measures variations in X-ray attenuation of samples and it is particularly well suited to track changes from particles morphological evolution to electrode architecture changes over time as characterizations can be conducted *in situ* and non-destructively [48]. Consequently, previously unprecedented degradation mechanisms are highlighted here for the first time. In the present work, a distribution of micron sized Si particles ranging from 125 to 180 µm in diameter are used for both tomo-cell and radio-cell because of the renewed interest in using micron sized particles as commercial LIBs [49]. To begin with, 3D visualization of Si particles evolution within an operating LIB during the first discharge/charge process is presented by micro X-ray tomography. First, the pristine state of the freshly prepared tomo-cell is tomographically recorded with 800 projections covering an angular range of 360° with 2.1 s exposure time. Then the battery is galvanostatically discharged to 0.03V [35]. At this point, the discharge process is stopped and the 2nd tomography is conducted.

After this, the discharge is continued and followed by a 3rd tomography. Altogether 10 tomograms during the first discharge/charge process are made (5 during the discharge and 5 during the charge). All the tomograms conducted during the first discharge/charge process are implied by red spots in Fig. 2a and all the parameters are the same. Fig. 3a and Fig. 3b show projection images of the Li electrode|separator|Si electrode assembly within the proof-of-concept batteries. While the Li electrode and the porous plastic separator appear nearly invisible due to their low X-ray absorption coefficients, the Si electrode is clearly visible. Fig. 3c shows a grayscale slice after reconstruction of the tomo-cell and Fig. 3d an enlarged part of the radio-cell. In order to qualitatively validate our X-ray imaging techniques, scanning electron micrographs (SEM), as shown in Fig. 3e, are given to compare with the reconstructed raw grayscale slice images and the radiography images. The unambiguous agreement indicates that the X-ray imaging technique accurately captures the morphology of Si electrode.

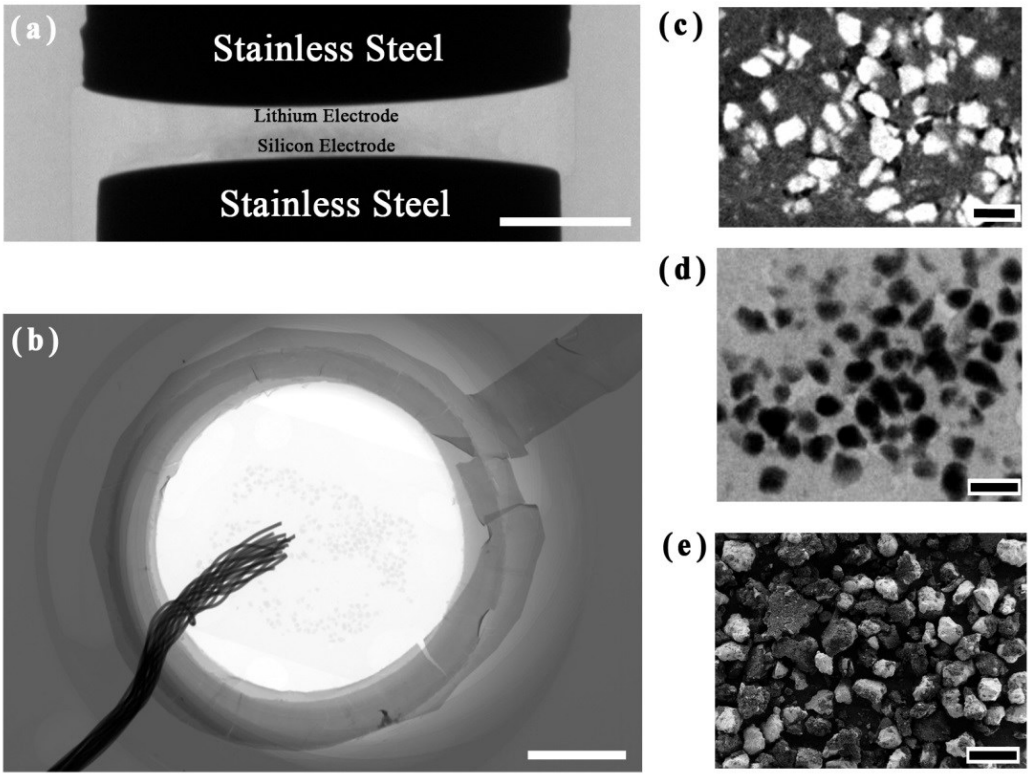

Fig. 3 X-ray imaging results of the assembled Li electrode|separator|Si electrode: a) X-ray projection image of the tomo-cell, the scale bar is 1 mm. b) 2D radiography of the radio-cell, the scale bar is 2 mm. c) Example of a reconstructed slice image of the tomo-cell. d) Cutout of a radiographic image of the radio-cell. e) Scanning electron micrograph of the mixed Si electrode material. The scale bar in c-e) are all 200µm.

We now track in detail the morphological changes during lithium insertion and extraction of one randomly chosen particle, illustrating other electroactive particles evolution as a function of

discharge/charge. Fig. 4 shows a series of cross-sectional slices taken from tomographies of the Si particle in different stages of discharge/charge. The corresponding 3D rendering of this particle is displayed in SI Fig. 1. Histograms of the attenuation coefficients in sub volumes containing the particle are displayed as a function of discharge/charge process see Fig. 4k and Fig. 4l. The leftmost peak corresponds to the weakly absorbing carbon black, binder and electrolyte surrounding the particle. Feature changes to the rightmost peak are directly related to the evolution of the active Si particle. Prior to the electrochemical reduction, the attenuation coefficient histogram for the particle consists of one peak located gray level of 6000. During lithium insertion, see Fig. 4k, along with the magnitude of this peak progressively decreases and moves to the left, the particle evolves gradually into a weakly X-ray attenuating material. This implies that the particle has completely transformed from the high-density Si phase to a low-density Li_xSi phase ($1<x<4.4$). Meanwhile, a notable volume expansion to around 200% (compared with pristine state) is observed in the fully lithiated state. These results are in good agreement with previous results [19, 35]. During lithium extraction, see Fig. 4l, along with the attenuation peak increases and shifts towards the original direction, we observe a homogeneous increase in attenuation coefficient. However, it is worth noting that, neither the peak position nor the peak shape of Si is restored to the original state by the end of the first charge process. This may stem from incomplete delithiation and/or significant trapping of lithium by the electrolyte decomposed byproducts [50], which is considered as one of the reasons of the performance decay during the first cycle.

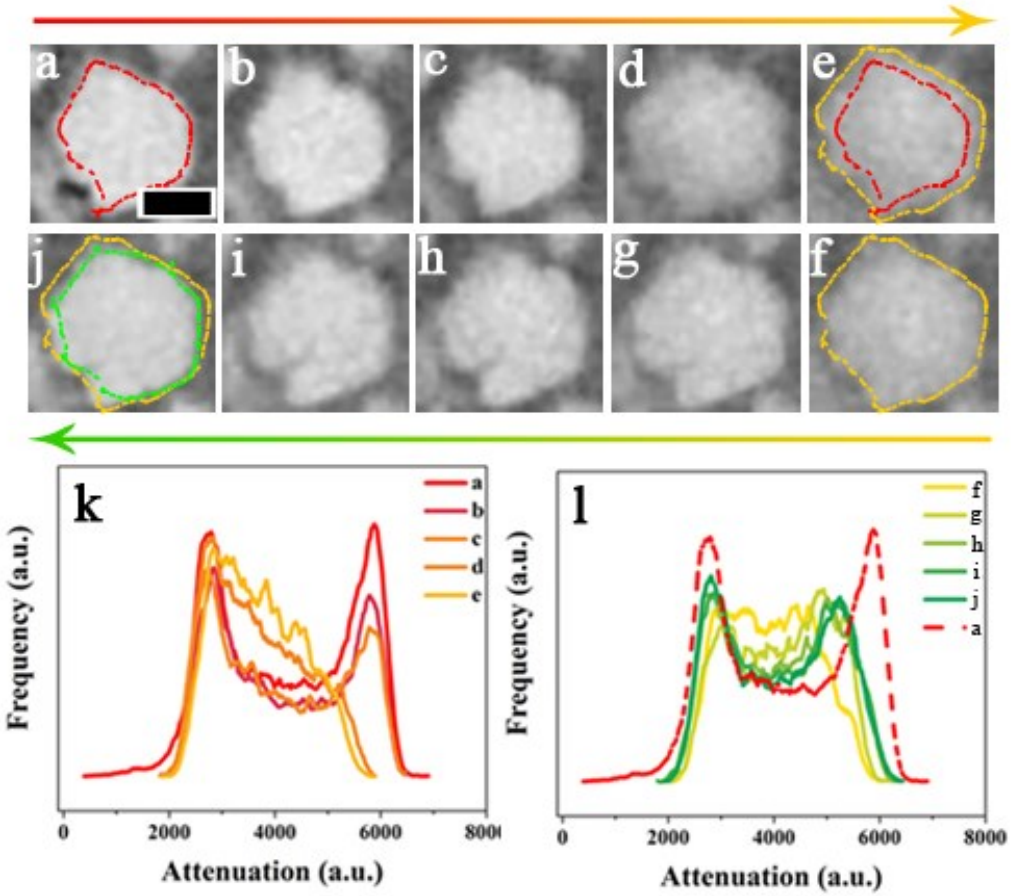

Fig. 4. Evolution of an electrochemically active Si particle: a)-e), tomographic slices through the particle during the first discharge step (see arrow direction); f)-j), tomograms of the first charge process (see arrow direction). k) and l), attenuation coefficient histograms of the specific particle as a function of discharge and charge (dashed red line is the pristine state). Outline of the pristine state (red outline in a)) and outlines of the discharged state (yellow outline in e)) and charged state (green outline in j)) are shown for visual comparison. The scale bar in a) is 100 µm long and is the same in all the images.

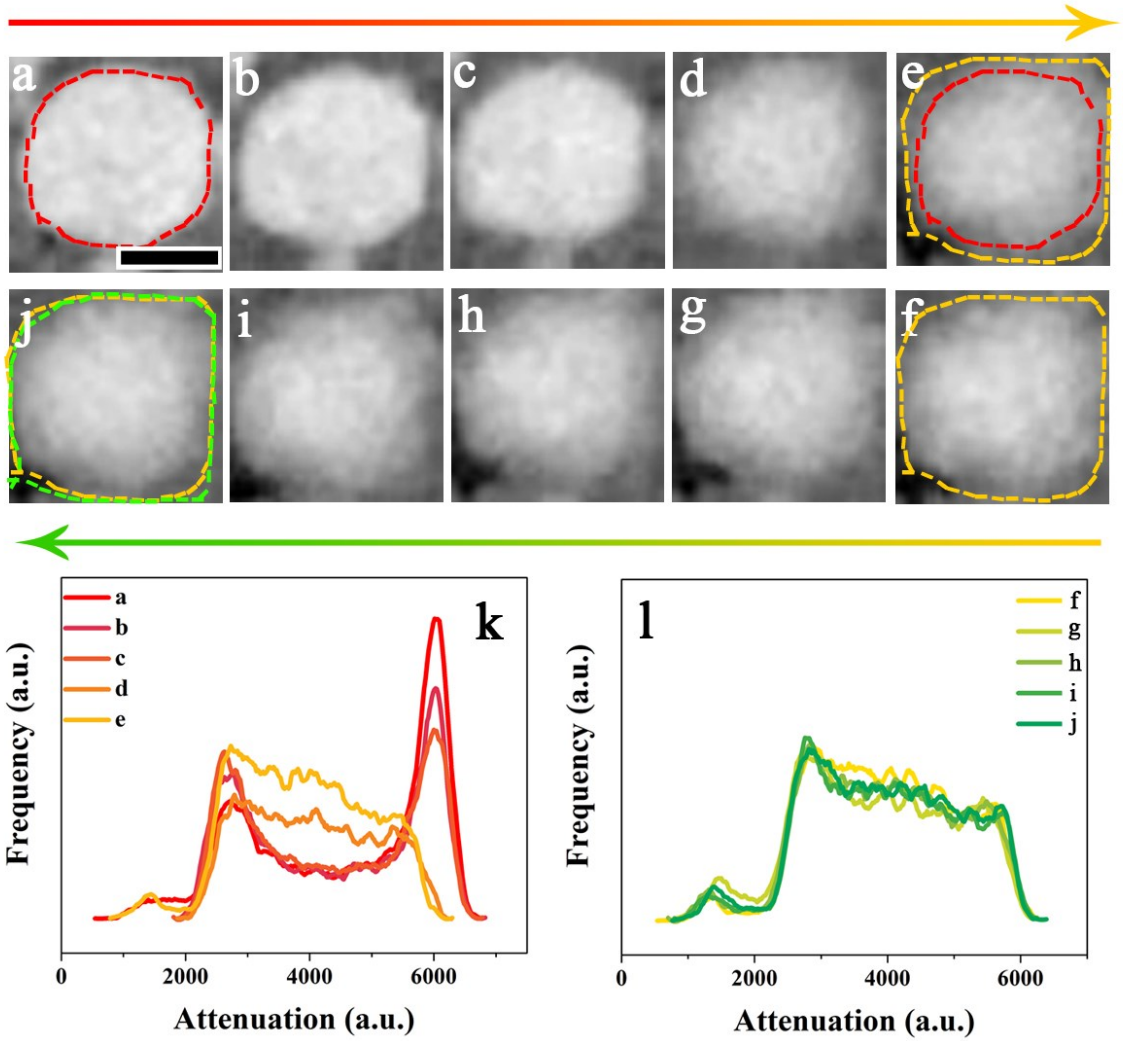

Fig. 5. Evolution of electrochemical deactivation of a Si particle: a)-e), tomographic slices during the first discharge step (see arrow direction); f)-j), tomographic slices during the first charge step (see arrow direction). k) and l), attenuation coefficient histograms during discharge and charge, respectively. Outline of the pristine state (red outline in a)) and outlines of the discharged state (yellow outline in e)) and charged state (green outline in j)) are shown for visual comparison. The scale bar is 100 µm long and applies to all the images.

Surprisingly, we have also detected an unprecedented phenomenon that many electroactive Si particles become electrochemically inactive during the first delithiation process. This electrochemically deactivation progress is illustrated in Fig. 5, in which, the electroactive particle originally effectively participates in the discharge process, from Fig. 5a to Fig. 5e, but turns to be inactive during the subsequent charge process, contributing to the capacity loss during the first charge process, as we can clearly see the unchanged shape of the particle, from Fig. 5f to Fig. 5j, and the stationary attenuation profile during delithiation, Fig. 5l. Another unexpected phenomenon is that several Si particles never undergo lithiation/delithiation during the

discharge/charge process, i.e., they are electrochemically inactive during the whole macroscopic battery level lithium insertion and extraction process, as shown in Fig. 6. On the whole, from an entire electrode-scale point of view, as displayed in SI Fig. 4, we can unambiguously observe that some electrochemically active Si particles undergo a continuous phase transformation during macroscopic battery level discharge/charge, some electrochemically active Si particles undergo an electrochemical deactivation process after the lithium insertion and some non-electroactive Si particles are completely inactive during the first cycle even as the voltage drops to zero against Li^+/Li. In addition, we also observe that some Si particles emerge and/or disappear in the same slice as a function of discharge/charge process. These distinctive phenomena clearly imply that apart from the large volume expansion during lithiation/delithiation, there are many other factors that contribute to the ultimate performance deterioration in Si-based LIBs.

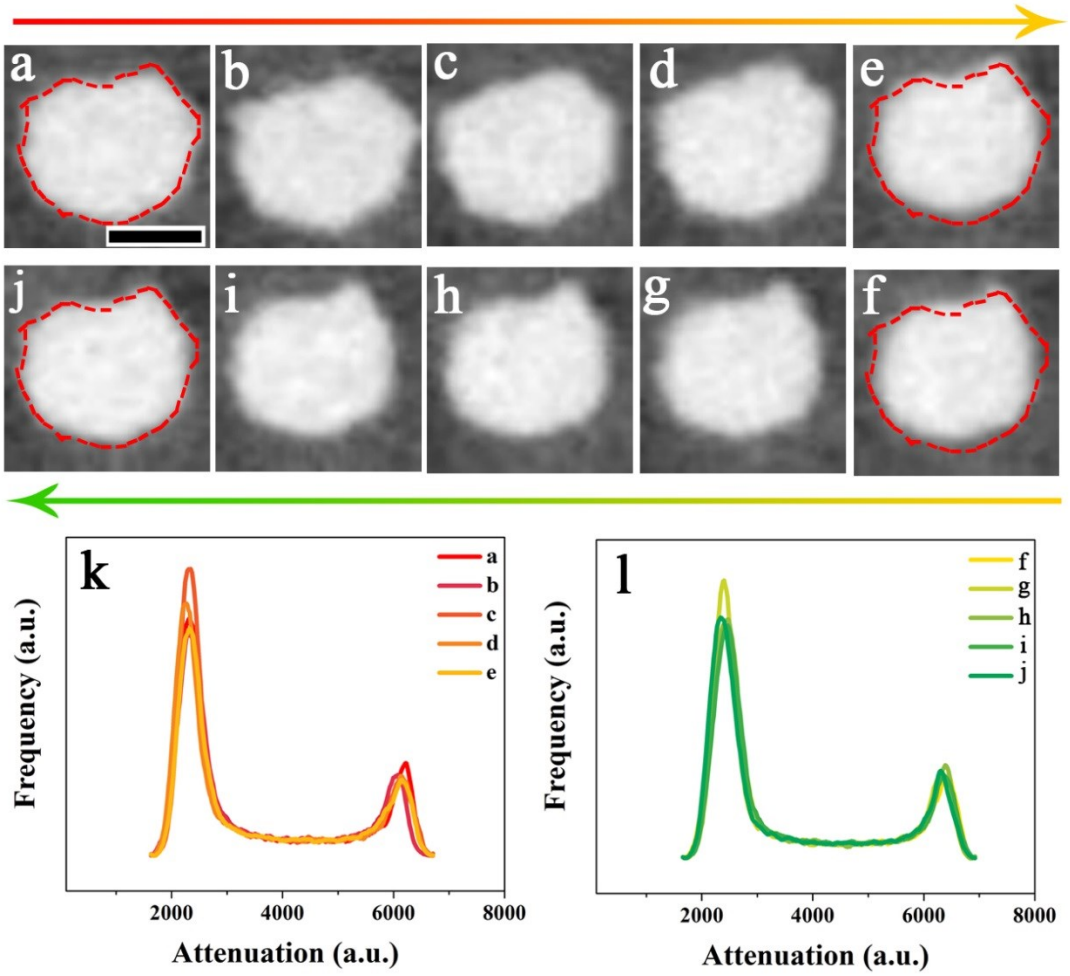

Fig. 6. Evolution of the electrochemically non-active Si particles: a)-e), tomographic slices of the first discharge process (see arrow direction); f)-j), tomographic slices of the first charge process (see arrow direction). k) and l), attenuation coefficient histograms as a function of discharge and charge, respectively;

Outline of the pristine state (red in a)) is duplicated to the discharged state e) and charged state j) for visual comparison. The scale bar is 100 µm.

Moreover, *in operando* 2D X-ray microradiography provides more sophisticated temporal information within the LIB. As shown in Fig. 7, we can clearly observe the expansion/contraction of the whole electrode material (dotted blue contours from D01 to C10), the expansion and contraction of the electrochemically active particles (green panel), the deactivation phenomenon of originally electroactive Si particles (red panel) and a few Si particles that are not electrochemically active throughout the whole discharge/charge process (yellow outlines from D01 to C10). Furthermore, the "core-shell" model reaction is clearly observed during the discharge/charge process (see the evolution of particle from Fig. 7a to 7j) [8]. The significant volume expansion-induced pulverization (see the green panel) may lead to electric disconnection of active particles from current collectors [25]. These results are in good agreement with the 3D X-ray microtomography and the whole *in operando* discharge/charge process is presented in a movie in SI.

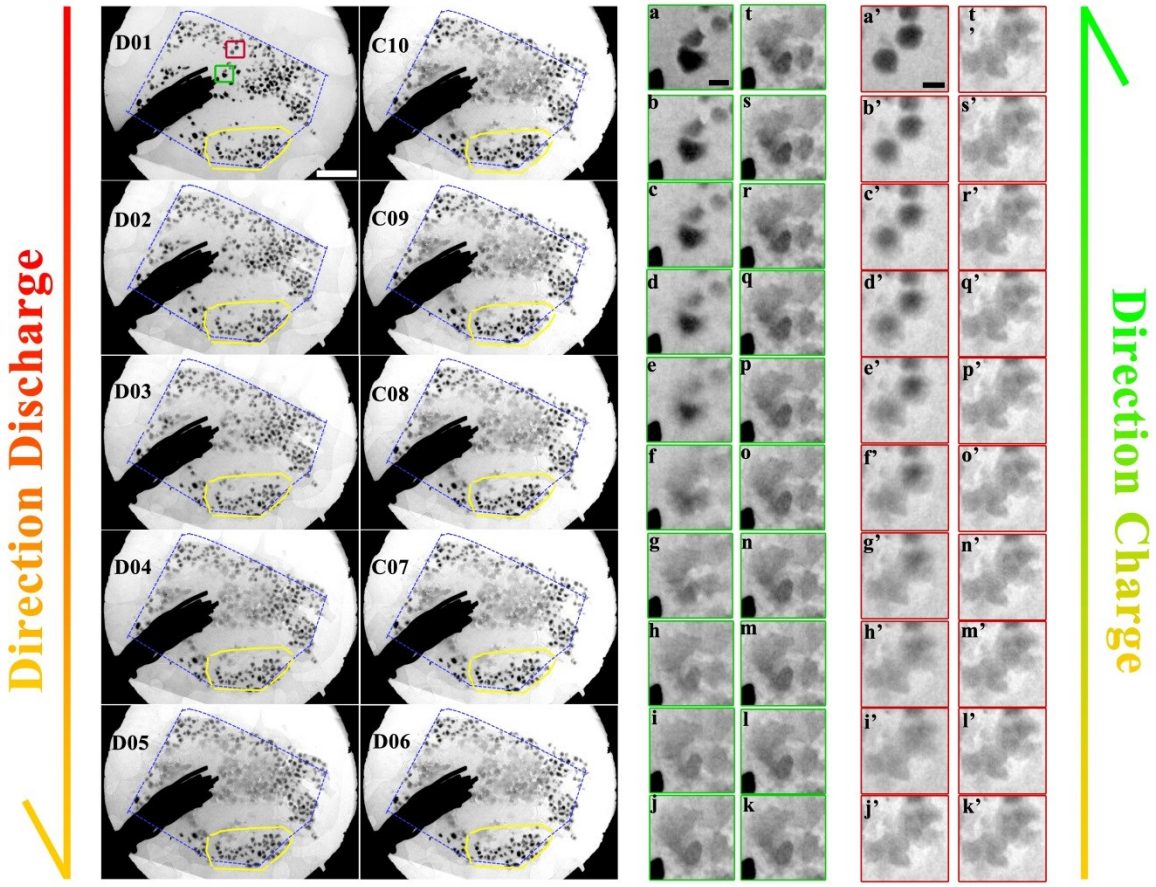

Fig. 7. *In situ* radiographic characterization of the radio-cell: D01 to C10 represent stages in the first discharge (D) and charge (C) step. The region encircled in blue is the original area that covers the

electrode material, increasing numbers refer to elapsing time. The region in green boxes represents the evolution of an electrochemical active Si particle from a to t (the copper lead is seen at the bottom left of each frame). The region in red boxes displays the evolution of electrochemical deactivation from a' to t'. The region encircled in yellow contains many electrochemically inactive particles. The scale bar in D01 is 1 mm long, that in the small boxes 100 µm. More information is provided in SI.

Fundamentally speaking, LIBs operate through the reversible insertion into or removal of lithium from electroactive host materials, respectively [51]. The ability of the materials to accommodate the changes associated with the chemical phase transformations that accompany the variations in lithium concentration determines the electrode's utility and battery performance. From an electrochemical point of view, lithium insertion or extraction process entails Li^+ and e^- simultaneously [52]. Contrary to proposed idealised electrochemical models and simulation that [53] electrochemically driven phase conversion is homogeneous and isotropic, such conditions are hardly satisfied in a real commercial LIB due to the complex electrode structures (ensemble of active materials, conductive agents and binders) and the complicated morphology and conditions with respect to porosity, tortuosity, conductivity and percolation ability for the electrolyte [54]. In fact, increasingly more attention is being paid to the investigation of local electrochemical reactions and their relationship with electrochemical performance on a macroscopic and electrode performance [55, 56]. For example, experimentally a discrepancy is observed between electrochemical measurements that represent the overall state of a cell and spectroscopic data that reflect the local state [57, 58]. In addition, the heterogeneous local depth of discharge (DOD) and the non-uniform local current distribution have been directly demonstrated by Zhang *et al.* [59, 60] and Ng *et al.* [61] respectively, by customizing multiple working electrode LIBs. Similarly, significant inhomogeneity of local DOD in different locations of a commercial LIB have been directly detected by Cai *et al*. [62] and Paxton *et al*. [63] through neutron diffraction and energy-dispersive X-ray diffraction. Moreover, by using µm-resolved Raman spectroscopy, Nanda *et al.* [64] presented visually the local "spectroscopic" electrochemical variations on an LIB electrode. Finally, recent modeling investigations by Zhao *et al.* [65] show a direct correlation between energy density and the non-uniformity in local current distribution, demonstrating a potential gain as high as 40% in energy density through an improved current distribution. Apparently, these locally non-uniform electrochemical reactions, current distributions, ionic/electric conductivity within electrodes will impact on battery performance in a variety of ways, including reduced energy and power, underutilization of capacity, localized heat generation and overcharge or over-discharge of active materials [56, 66].

As in our case, it are these electrochemically active Si particles which are ionically and electronically accessed by the electrolyte and connected to the conducting network that directly dictate battery performance. In other words, the total electrode discharging/charging current concentrates only on the electrochemically active Si particles, as clearly shown in Fig. 4, SI Fig. 4 and Fig. 7. These electrochemically active Si particles undergo lithium insertion and extraction to store and release energy, evidenced by the X-ray attenuation coefficient change. During lithium uptake and release, these electroactive Si particles undergo notable volume expansion

accompanied by the generation of substantial compressive and tensile stresses [67]. The mechanical forces generated will drive local displacement and rearrangement of other Si particles within the composite electrode, leading to the phenomena that some Si particles emerge and some disappear in one and the same slice, as shown in SI Fig. 4 and Fig. 7. On the other hand, the observed "deactivation" mechanism of originally electrochemically active Si particles probably has three sources: First, an electric contact disconnection. Under the influence of the mechanical forces generated, a lot of displacement/rearrangement of the particles occurs with numerous losses or variations in the contacts. Taking into account that in a stack of particles the electrons are transferred between particles by hopping or tunneling with the contact resistivity depending exponentially on the gap between the contacts, and that a gap of 8-10 nm makes a contact electronically insulating [68], it is plausible to say that the deactivation mechanism is attributed to electric disconnection. The second possibility is the insulating crystalline Li_2O oxide layer. By using *in situ* TEM, He *et al*. report that upon initial Si lithiation, the formed crystalline Li_2O, the product of Li reaction with the native silicon oxide layer, will partially insulate the particles during subsequent delithiation cycle [69]. The third possible reason is the unshrinkable conductive matrix. Weker *et al*. proposed that upon the delithiation, when the particles begin to contract, the conductive matrix does not necessarily shrink back to fill the space created by the contracting particles, thus leading to the deactivation of, in their case, germanium particles [70]. Right now we cannot identify a single dominant factor. However, special focus in the future work should be placed to eliminate this phenomenon due to the resultant substantial capacity losses. It is also worth noting that the unexpected electrochemically inactive Si particles within the electrode. From the fact that they are electrochemically inactive from the beginning, it is assumed these Si particles are disconnected into locations of ionically or electronically insulating islands during the electrode preparation, for example binder redistribution during drying, calendaring, cutting and compacting [52]. To get a further quantitative analysis of the influence of different types of Si particles on the obtained discharge/charge capacity, we investigated 78 particles in the same slice in tomo-cell with diameters larger than 50 µm, as shown in SI Fig. 6. It was found that 13% (10) of the Si particles were electrochemically in-active through the first cycle, 87% (68) of the Si particles experienced the first lithiation process and only 24% (19) of the Si particles experienced the first delithiation process. Assuming the theoretical capacity of Si is 3500 mAh/g, the obtained firstly discharged capacity (3000 mAh/g that is around 85% of the theoretical capacity) and the obtained firstly charged capacity (500 mAh/g that is around 14% of the theoretical capacity) agree with the results from the quantitative analysis (fraction of 87% and 24% (within error consideration)). More information can be found in SI.

The unexpected electrochemical "deactivation" mechanism and the presence of many electrochemical inactive Si particles are alarming because they cannot be easily characterized by conventional macroscopic electroanalytical characterization techniques and should draw attentions from electrode engineers and simulation experts. From an electrode engineer's point of view, the electrode architecture engineering optimization is crucially important. On the one hand, in addition to focusing only on individual particle features to develop next-generation LIBs, more

and more efforts should be put in optimizing the entire electrode architecture, which can involve all active material particles ionically and electronically connecting to electrolyte and electric conducting network to maximize the utilization of active materials. On the other hand, new conductive/binder agents are highly needed. The matrix of carbon/binder is supposed to sustain the active material's expansion/contraction during cycles as well as to provide an efficient dynamic electric/ionic conducting pathway even under significant electrode transformation. Currently, some exploratory research of developing self-healing polymer [49] and electric and ionic conductive polymer [71] is underway. From a simulation expert's point of view, in order to develop an electrochemical model that can be used to gain insight into internal processes, to predict performance and operation and optimize cell design, the homogeneous and flawless idealized microstructure characteristics should be compromised with the real complex composite electrodes.

Conclusions

In summary, we re-explore the mechanisms of dynamic deterioration of Si anode LIBs on an electrode scale by employing X-ray imaging tomography and radiography and for the first time highlight that, apart from the significant volume expansion-induced pulverization and electric disconnection from current collectors, electrochemical "deactivation" contributes significantly to the capacity loss during the first charge process. In addition, the presence of a notable number of electrochemically inactive Si particles is also believed to substantially decrease energy density due to the inefficient utilization of loaded active materials. These unexpected findings, which cannot be obtained by macroscopic electrochemical characterizations and conventional structural/compositional characterizations, provide us with novel insights into the mechanisms of performance degradation of Si anode LIBs. From practical point of view, commercially oriented researches into the local microscopic electrochemical reactions could be motivated and aroused as it governs directly the energy density and capacity retention of a real LIB. And more attention should be paid to the further investigation of the correlation between macroscopic electrochemical performance and local behavior of active materials, to guide the selection and optimization of electrode materials and the manufacture of the electrode.

Supporting Information

Supporting Information is available in the online version or from the author.

Acknowledgements

We thank Norbert Beck for fabricating the beamline battery and Elkem AS for providing us with Si particles. This work was sponsored by the Helmholtz Association and the China Scholarship Council.

References

[1] A. Barai, G.H. Chouchelamane, Y. Guo, A. McGordon, P. Jennings, J Power Sources, 280 (2015) 74-80.
[2] B. Sun, K. Huang, X. Qi, X. Wei, J. Zhong, Adv Funct Mater, 25 (2015) 5633-5639.

[3] D.X. Liu, J. Wang, K. Pan, J. Qiu, M. Canova, L.R. Cao, A.C. Co, Angew Chem Int Ed, 53 (2014) 9498-9502.
[4] B. Wang, X. Li, B. Luo, L. Hao, M. Zhou, X. Zhang, Z. Fan, L. Zhi, Adv Mater, 27 (2015) 1526-1532.
[5] F. Sun, K. Huang, Y. Liu, T. Gao, Y. Han, J. Zhong, Appl Surf Sci, 266 (2013) 300-305.
[6] F. Sun, K. Huang, X. Qi, T. Gao, Y. Liu, X. Zou, J. Zhong, Ceram Int, 40 (2014) 2523-2528.
[7] M. Gu, Y. Li, X. Li, S. Hu, X. Zhang, W. Xu, S. Thevuthasan, D.R. Baer, J.-G. Zhang, J. Liu, C. Wang, ACS Nano, 6 (2012) 8439-8447.
[8] J.M. Yuk, H.K. Seo, J.W. Choi, J.Y. Lee, ACS Nano, 8 (2014) 7478-7485.
[9] F. Sun, K. Huang, X. Qi, T. Gao, Y. Liu, X. Zou, X. Wei, J. Zhong, Nanoscale, 5 (2013) 8586-8592.
[10] N. Suzuki, R.B. Cervera, T. Ohnishi, K. Takada, J Power Sources, 231 (2013) 186-189.
[11] T.H. Hwang, Y.M. Lee, B.-S. Kong, J.-S. Seo, J.W. Choi, Nano Lett, 12 (2012) 802-807.
[12] A. Gohier, B. Laïk, K.-H. Kim, J.-L. Maurice, J.-P. Pereira-Ramos, C.S. Cojocaru, P.T. Van, Adv Mater, 24 (2012) 2592-2597.
[13] Y. He, X. Yu, Y. Wang, H. Li, X. Huang, Adv Mater, 23 (2011) 4938-4941.
[14] H. Kim, B. Han, J. Choo, J. Cho, Angew Chem Int Ed, 47 (2008) 10151-10154.
[15] C.K. Chan, H. Peng, G. Liu, K. McIlwrath, X.F. Zhang, R.A. Huggins, Y. Cui, Nat Nano, 3 (2008) 31-35.
[16] Y. Yao, M.T. McDowell, I. Ryu, H. Wu, N. Liu, L. Hu, W.D. Nix, Y. Cui, Nano Lett, 11 (2011) 2949-2954.
[17] L.-F. Cui, L. Hu, J.W. Choi, Y. Cui, ACS Nano, 4 (2010) 3671-3678.
[18] S.W. Lee, M.T. McDowell, J.W. Choi, Y. Cui, Nano Lett, 11 (2011) 3034-3039.
[19] X.H. Liu, L. Zhong, S. Huang, S.X. Mao, T. Zhu, J.Y. Huang, ACS Nano, 6 (2012) 1522-1531.
[20] J. Li, J.R. Dahn, J Electrochem Soc, 154 (2007) A156-A161.
[21] K. Ogata, E. Salager, C.J. Kerr, A.E. Fraser, C. Ducati, A.J. Morris, S. Hofmann, C.P. Grey, Nat Commun, 5 (2014).
[22] S. Ramdon, B. Bhushan, S.C. Nagpure, J Power Sources, 249 (2014) 373-384.
[23] B. Key, M. Morcrette, J.-M. Tarascon, C.P. Grey, J Am Chem Soc, 133 (2011) 503-512.
[24] E. Sarasketa-Zabala, F. Aguesse, I. Villarreal, L.M. Rodriguez-Martinez, C.M. López, P. Kubiak, J Phys Chem C, 119 (2015) 896-906.
[25] X.H. Liu, Y. Liu, A. Kushima, S. Zhang, T. Zhu, J. Li, J.Y. Huang, Adv Eng Mater, 2 (2012) 722-741.
[26] H.A. Bale, A. Haboub, A.A. MacDowell, J.R. Nasiatka, D.Y. Parkinson, B.N. Cox, D.B. Marshall, R.O. Ritchie, Nat Mater, 12 (2013) 40-46.
[27] J. Moosmann, A. Ershov, V. Weinhardt, T. Baumbach, M.S. Prasad, C. LaBonne, X. Xiao, J. Kashef, R. Hofmann, Nat. Protocols, 9 (2014) 294-304.
[28] T. dos Santos Rolo, A. Ershov, T. van de Kamp, T. Baumbach, Proc Natl Acad Sci, 111 (2014) 3921-3926.
[29] P.R. Shearing, N.P. Brandon, J. Gelb, R. Bradley, P.J. Withers, A.J. Marquis, S. Cooper, S.J. Harris, J Electrochem Soc, 159 (2012) A1023-A1027.
[30] J. Wang, Y.-c.K. Chen-Wiegart, J. Wang, Angew Chem Int Ed, 53 (2014) 4460-4464.
[31] Y.-c.K. Chen-Wiegart, R. DeMike, C. Erdonmez, K. Thornton, S.A. Barnett, J. Wang, J Power Sources, 249 (2014) 349-356.
[32] J. Wang, ChemElectroChem, 1 (2014) 329-331.
[33] S. Komini Babu, A.I. Mohamed, J.F. Whitacre, S. Litster, J Power Sources, 283 (2015) 314-319.
[34] M. Ebner, F. Marone, M. Stampanoni, V. Wood, Science, 342 (2013) 716-720.
[35] J. Gonzalez, K. Sun, M. Huang, J. Lambros, S. Dillon, I. Chasiotis, J Power Sources, 269 (2014) 334-343.
[36] M. Ebner, F. Geldmacher, F. Marone, M. Stampanoni, V. Wood, Adv Eng Mater, 3 (2013) 845-850.
[37] L. Zielke, T. Hutzenlaub, D.R. Wheeler, I. Manke, T. Arlt, N. Paust, R. Zengerle, S. Thiele, Adv Eng Mater, 4 (2014) 1301617.
[38] L. Zielke, C. Barchasz, S. Waluś, F. Alloin, J.C. Leprêtre, A. Spettl, V. Schmidt, A. Hilger, I. Manke, J. Banhart, R. Zengerle, S. Thiele, Scientific Reports, 5 (2015) 10921.

[39] L. Zielke, T. Hutzenlaub, D.R. Wheeler, C.-W. Chao, I. Manke, A. Hilger, N. Paust, R. Zengerle, S. Thiele, Adv Eng Mater, 5 (2015) 1401612.
[40] P.R. Shearing, L.E. Howard, P.S. Jørgensen, N.P. Brandon, S.J. Harris, Electrochem Commun, 12 (2010) 374-377.
[41] A. Haibel, I. Manke, A. Melzer, J. Banhart, J Electrochem Soc, 157 (2010) A387-A391.
[42] I. Manke, J. Banhart, A. Haibel, A. Rack, S. Zabler, N. Kardjilov, A. Hilger, A. Melzer, H. Riesemeier, Appl Phys Lett, 90 (2007) 214102.
[43] O. Hampe, H. Franke, C.A. Hipsley, N. Kardjilov, J. Müller, J Morphol, 276 (2015) 564.
[44] A.R. Benetti, J. Jacobsen, B. Lehnhoff, N.C.R. Momsen, D.V. Okhrimenko, M.T.F. Telling, N. Kardjilov, M. Strobl, T. Seydel, I. Manke, H.N. Bordallo, Sci. Rep., 5 (2015).
[45] C. Pereira-Nabais, J. Światowska, A. Chagnes, F. Ozanam, A. Gohier, P. Tran-Van, C.-S. Cojocaru, M. Cassir, P. Marcus, Appl Surf Sci, 266 (2013) 5-16.
[46] M. Nie, D.P. Abraham, D.M. Seo, Y. Chen, A. Bose, B.L. Lucht, J Phys Chem C, 117 (2013) 25381-25389.
[47] X. Zhou, Y.-X. Yin, L.-J. Wan, Y.-G. Guo, Adv Eng Mater, 2 (2012) 1086-1090.
[48] D.S. Eastwood, V. Yufit, J. Gelb, A. Gu, R.S. Bradley, S.J. Harris, D.J.L. Brett, N.P. Brandon, P.D. Lee, P.J. Withers, P.R. Shearing, Adv Eng Mater, 4 (2014) 1300506.
[49] C. Wang, H. Wu, Z. Chen, M.T. McDowell, Y. Cui, Z. Bao, Nat Chem, 5 (2013) 1042-1048.
[50] S.P.V. Nadimpalli, V.A. Sethuraman, S. Dalavi, B. Lucht, M.J. Chon, V.B. Shenoy, P.R. Guduru, J Power Sources, 215 (2012) 145-151.
[51] U. Boesenberg, F. Meirer, Y. Liu, A.K. Shukla, R. Dell'Anna, T. Tyliszczak, G. Chen, J.C. Andrews, T.J. Richardson, R. Kostecki, J. Cabana, Chem Mater, 25 (2013) 1664-1672.
[52] G. Chen, T.J. Richardson, J Power Sources, 195 (2010) 5387-5390.
[53] M. Doyle, T.F. Fuller, J. Newman, J Electrochem Soc, 140 (1993) 1526-1533.
[54] F. Lin, D. Nordlund, T.-C. Weng, Y. Zhu, C. Ban, R.M. Richards, H.L. Xin, Nat Commun, 5 (2014).
[55] N. Balke, S. Kalnaus, N.J. Dudney, C. Daniel, S. Jesse, S.V. Kalinin, Nano Lett, 12 (2012) 3399-3403.
[56] J. Liu, M. Kunz, K. Chen, N. Tamura, T.J. Richardson, J Phys Chem Lett, 1 (2010) 2120-2123.
[57] G. Brunetti, D. Robert, P. Bayle-Guillemaud, J.L. Rouvière, E.F. Rauch, J.F. Martin, J.F. Colin, F. Bertin, C. Cayron, Chem Mater, 23 (2011) 4515-4524.
[58] Y. Li, F. El Gabaly, T.R. Ferguson, R.B. Smith, N.C. Bartelt, J.D. Sugar, K.R. Fenton, D.A. Cogswell, A.L.D. Kilcoyne, T. Tyliszczak, M.Z. Bazant, W.C. Chueh, Nat Mater, 13 (2014) 1149-1156.
[59] G. Zhang, C.E. Shaffer, C.-Y. Wang, C.D. Rahn, J Electrochem Soc, 160 (2013) A610-A615.
[60] G. Zhang, C.E. Shaffer, C.-Y. Wang, C.D. Rahn, J Electrochem Soc, 160 (2013) A2299-A2305.
[61] S.-H. Ng, F. La Mantia, P. Novák, Angew Chem Int Ed, 48 (2009) 528-532.
[62] L. Cai, K. An, Z. Feng, C. Liang, S.J. Harris, J Power Sources, 236 (2013) 163-168.
[63] W.A. Paxton, Z. Zhong, T. Tsakalakos, J Power Sources, 275 (2015) 429-434.
[64] J. Nanda, J. Remillard, A. O'Neill, D. Bernardi, T. Ro, K.E. Nietering, J.-Y. Go, T.J. Miller, Adv Funct Mater, 21 (2011) 3282-3290.
[65] W. Zhao, G. Luo, C.-Y. Wang, J Power Sources, 257 (2014) 70-79.
[66] P. Maire, A. Evans, H. Kaiser, W. Scheifele, P. Novák, J Electrochem Soc, 155 (2008) A862-A865.
[67] M.J. Chon, V.A. Sethuraman, A. McCormick, V. Srinivasan, P.R. Guduru, Phys Rev Lett, 107 (2011) 045503.
[68] B.P.N. Nguyen, J. Gaubicher, B. Lestriez, Electrochim Acta, 120 (2014) 319-326.
[69] Y. He, D.M. Piper, M. Gu, J.J. Travis, S.M. George, S.-H. Lee, A. Genc, L. Pullan, J. Liu, S.X. Mao, J.-G. Zhang, C. Ban, C. Wang, ACS Nano, 8 (2014) 11816-11823.
[70] J.N. Weker, N. Liu, S. Misra, J.C. Andrews, Y. Cui, M.F. Toney, Energ Environ Sci, 7 (2014) 2771-2777.
[71] D. Mazouzi, Z. Karkar, C. Reale Hernandez, P. Jimenez Manero, D. Guyomard, L. Roué, B. Lestriez, J Power Sources, 280 (2015) 533-549.

2.4.1 Supporting Information

Investigation of failure mechanisms in silicon based half cells during the first cycle by micro X-ray tomography and radiography

Fu Sun [a,b,], Henning Markötter [b], Kang Dong [a,b], Ingo Manke [b], Andre Hilger [b], Nikolay Kardjilov [b] and John Banhart [a,b]*

[a] Institute of Material Science and Technologies
Technical University Berlin
10623 Berlin, Germany

[b] Helmholtz Centre Berlin for Materials and Energy
Hahn-Meitner-Platz 1
14109 Berlin, Germany

*Corresponding Author: fu.sun@helmholtz-berlin.de

This section includes:

Data Acquisition and Processing:

The obtained tomography raw data are first flat-field and dark-field corrected and rearranged into sinograms. A median filter with a kernel size of 1 ×1 voxels is applied to the original image for noise reduction while maintaining the validity of the dataset. The reconstruction software Octopus (8.8.2-64 bit) is used to reconstruct the obtained dataset. Because of the huge electrode expansion or contraction during discharge or charge, the reconstructed 2D slices shown in Fig. 4, Fig. 5 and Fig. 6 do not necessarily represent exactly the same plane from one tomography to another. However, we compare with one slice to another to find the closest slices for each particle.

For the particles shown in Fig. 4, it is located 46 µm from the bottom stainless screw current collector and is marked by green circle in SI Fig. 5. For the particles shown in Fig. 5, the distance

is 40 µm from the bottom stainless screw current collector and is marked by yellow rectangular in SI Fig. 5. For the particles shown in Fig. 6, the distance is 80 µm from the bottom stainless screw current collector and is marked in red round rectangle in SI Fig. 5. Note that all the locations are measured in the pristine state.

For the calculated volume expansion, we assume that the Si particles are round and measure their diameter in the pristine state and then compare with that of discharged state. The formula is:

$$V=\frac{4}{3}\pi(\frac{D}{2})^3$$

D is the diameter measured through Image J.

For 3D particle presentation, the software VGStudio MAX 2.2 is employed. Different threshold grey values are employed to best depict the particle shape.

The obtained radiographic raw data are only flat-field and dark-field corrected. To minimise the dataset, we used Grouped Z Project to compress every 20 images into one image. The frame rate of the movie is 20 fps.

The figures shown in Fig.7 represent states as a function of the following discharge or charge times:

State	Time	State	Time	State	time
D01	0 h	a	0 h	a’	0 h
D02	6 h	b	3.35 h	b’	6.78 h
D03	9.9 h	c	4.85 h	c’	8.25 h
D04	13.6 h	d	6.35 h	d’	9.76 h
D05	17.4 h	e	7.85 h	e’	11.28 h
D06	22.8 h	f	9.76 h	f’	12.85 h
		g	11.28 h	g’	14.35 h
C01	23.4 h	h	12.8 h	h’	15.85 h
C02	27.2 h	i	14.7 h	i’	18.12 h
C03	31 h	j	23.4 h	j’	23.4 h
C04	32 h	k	26.9 h	k’	25.4 h
		l	25.2 h	l’	25.9
		m	26.3 h	m’	26.3 h
		n	26.8 h	n’	26.8 h
		o	27.2 h	o’	27.2 h

p	27.7 h	p’	27.7 h
q	28.2 h	q’	28.2 h
r	28.65 h	r’	28.65 h
s	29.1 h	s’	29.1 h
t	29.5 h	t’	29.5 h

For the quantitative analysis of the influence of different types of Si particle on the obtained discharge/charge capacity, we have chosen 78 particles in the same slice in tomo-cell with diameter larger than 50 µm, the locations of the chosen particles are shown in SI Fig. 6. It should be noted that, during the discharge/charge process, the locations of some Si particles (electrochemically active through the first cycle, electrochemically active during the first lithiation but turn into electrochemically in-active during the first delithiation process and electrochemically in-active particles through the first cycle) will change continuously due to lithium insertion into/ extraction from the Si electrode. We only choose the particles that experienced minor movement during the discharge/charge process (they stayed almost in the same slice) and the Si particles that experienced significant movement (they were not in the same slice) were out of consideration. It should be also noted that, we only choose the Si particles whose diameter were larger than 50 µm due to the limited resolution of the laboratory X-ray source. Considering the limited resolution of our laboratory X-ray source, we have not taken Si particles with diameter lower than 50 µm into account. Due to the same reason, we cannot quantify the lithiation or delithiaiton sate of individual particles. That is to say, the individual lithium storage and release ability of electrochemically active Si particles during the first discharge and first charge process cannot be calculated. Nevertheless, by calculating the fraction of Si particles of electrochemically in-active, electrochemically active and electrochemical deactivated, we get a similar result by calculating the discharged/charged capacity.

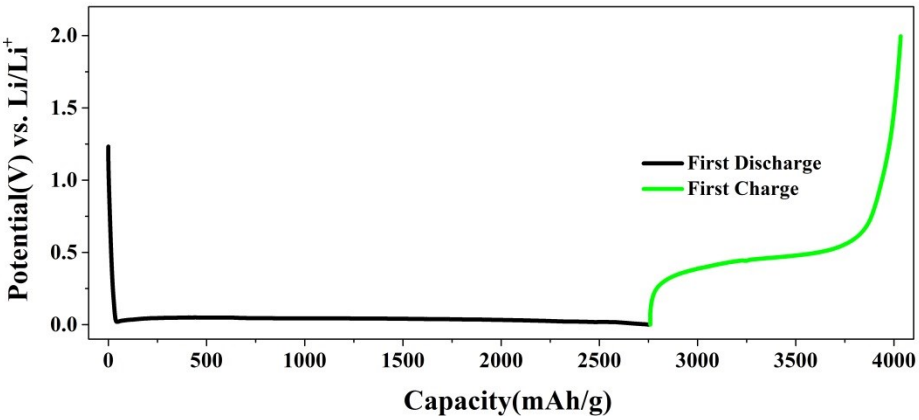

SI Fig. 1 Electrochemical characterization of the coin cell with the same Si electrode: the first voltage-capacity profile. The mass of the loaded Si was 4 mg and the discharge/charge current was 0.075 Ag^{-1}. Note that the Si composite was cast directly to the coin cell casing without using copper current collector.

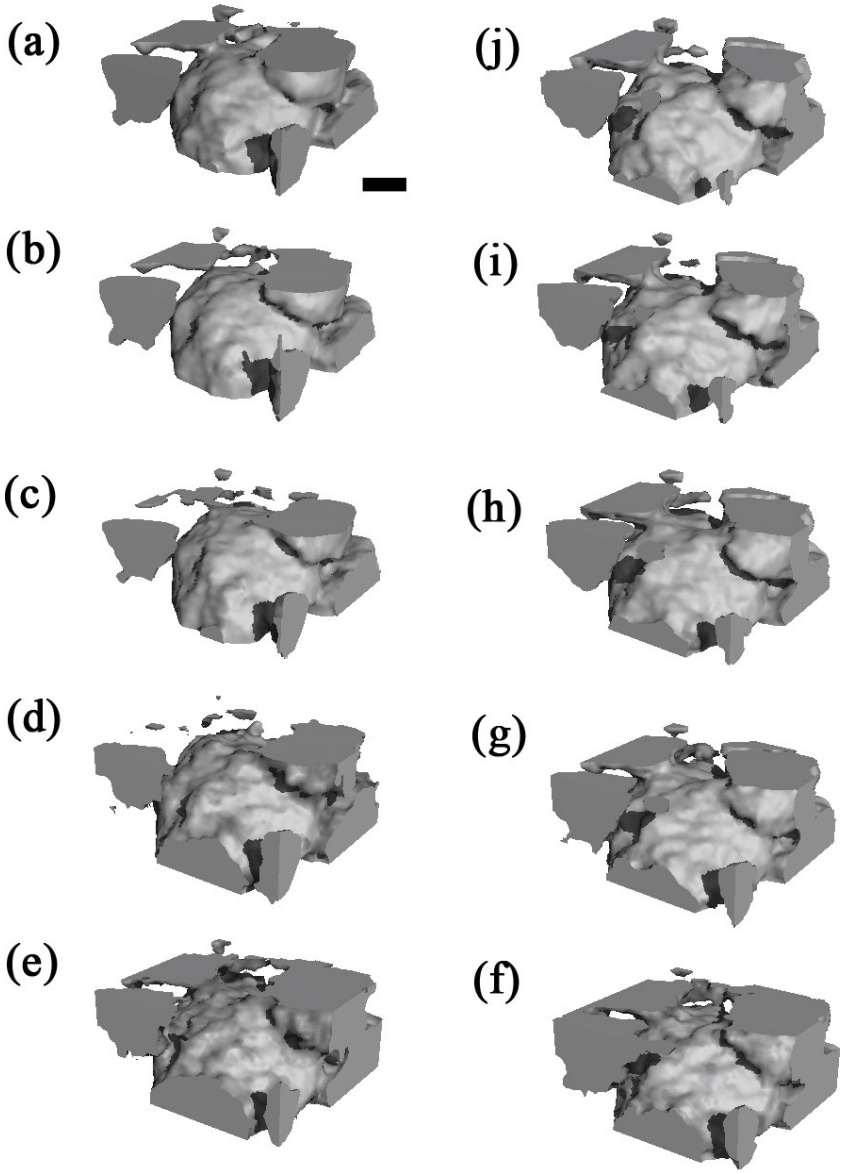

SI Fig. 2. 3D evolution of the electrochemically active Si particle as shown in Fig. 4. a)-e), during the first discharge process; f)-j), during the first charge process; the scale bar is 50 µm long.

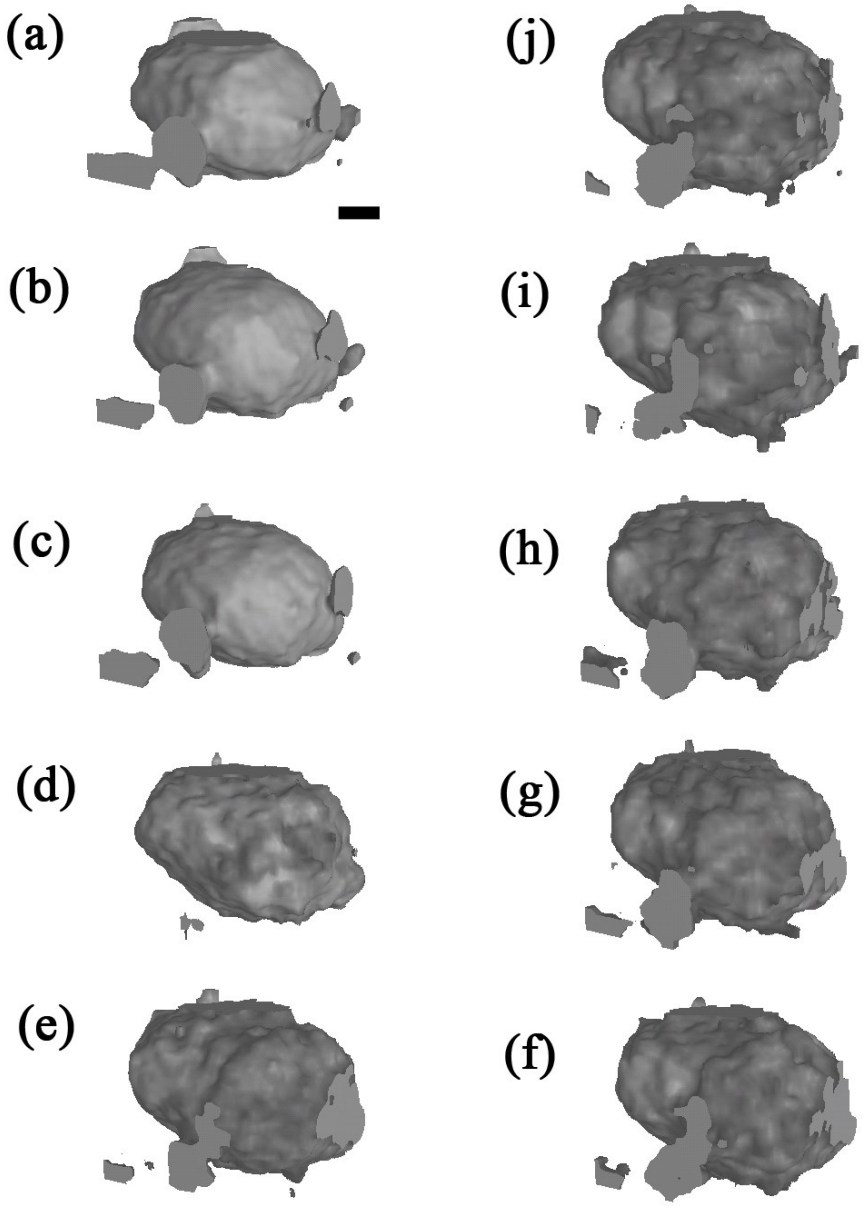

SI Fig. 3. 3D evolution of the electrochemical deactivation of Si particles as shown in Fig. 5. a)-e), during the first discharge process; f)-j), during the first charge process; the scale bar is 50 µm long.

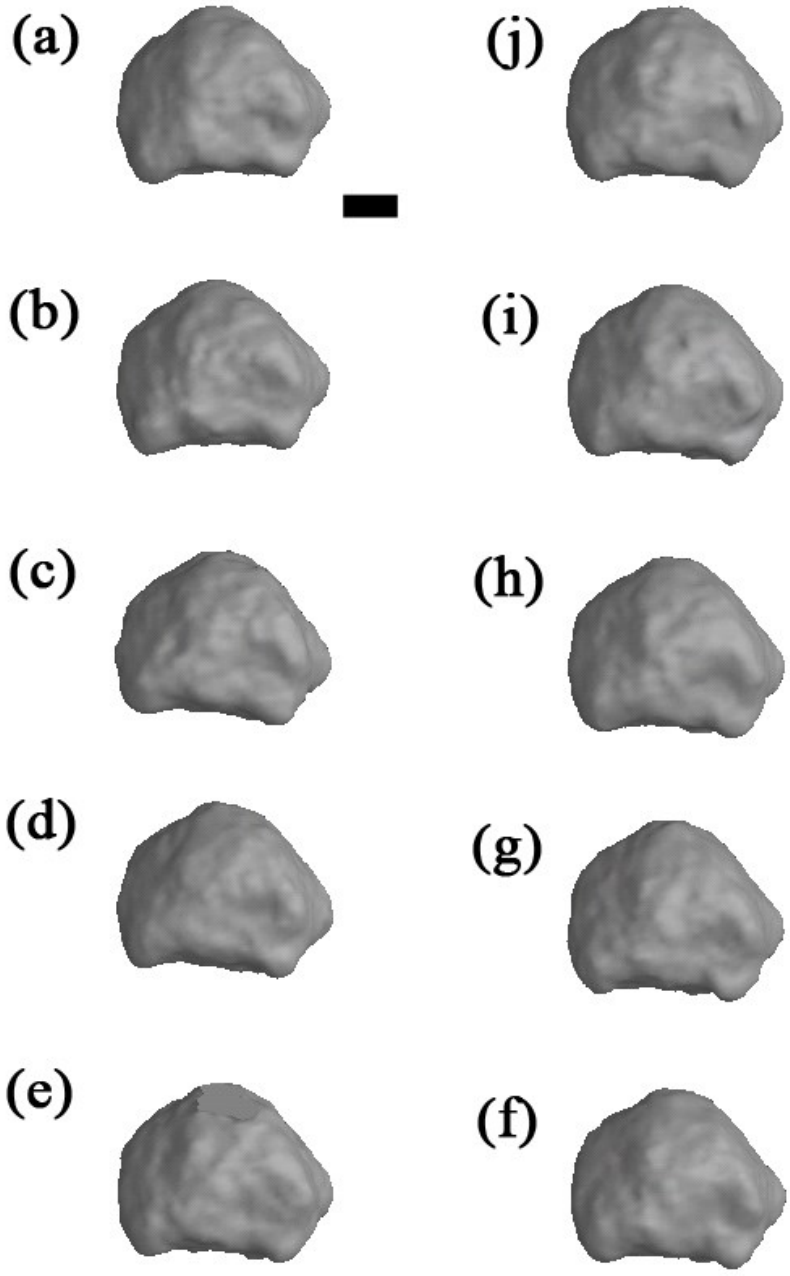

SI Fig. 4. 3D evolution of the electrochemically inactive Si particles shown in Fig. 6. a)-e), during the first discharge process; f)-j), during the first charge process; the scale bar is 50 µm long.

2.4 Degradation of lithium ion batteries based on ~100 µm-sized Si particles

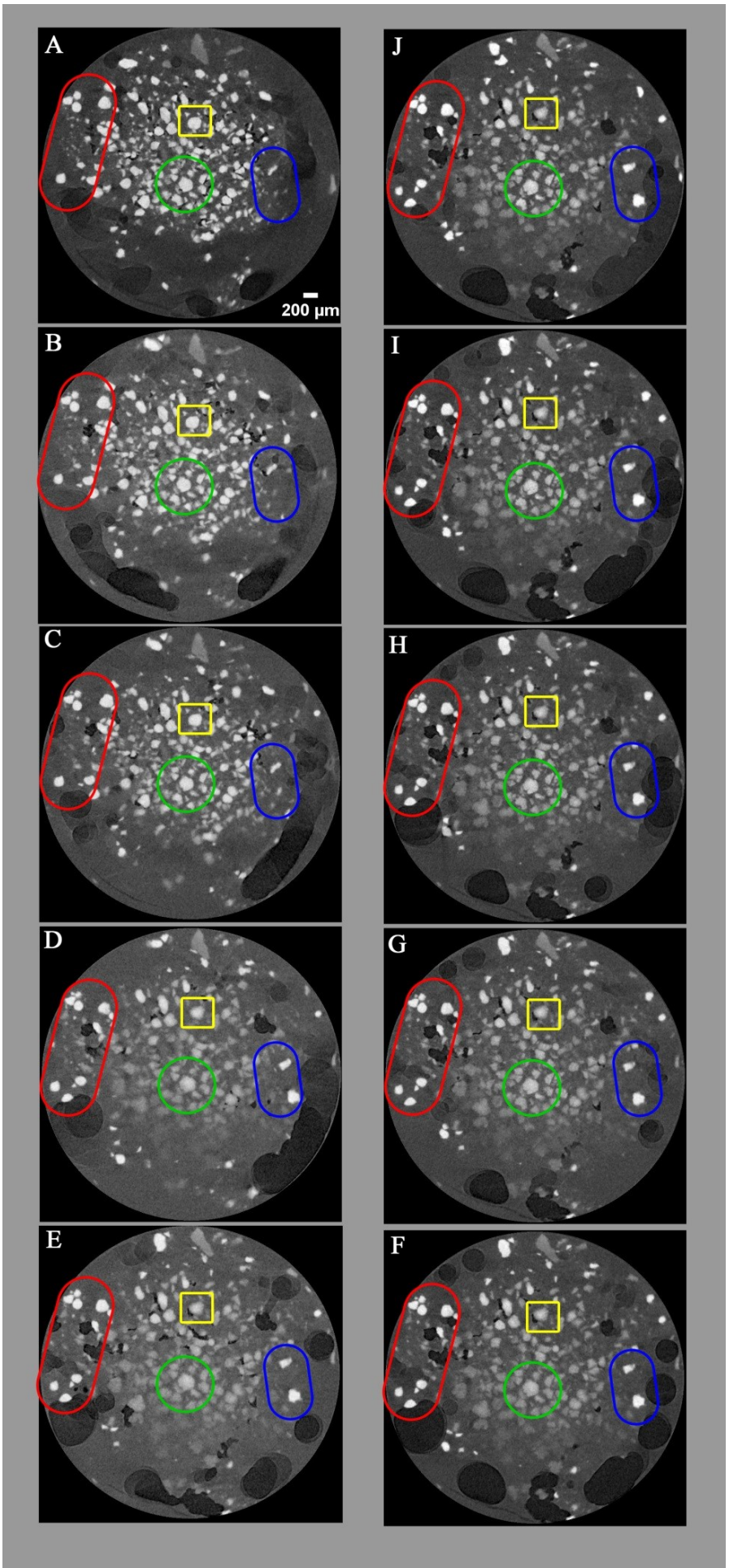

SI Fig. 5. Evolution of Si particles in a larger area of the electrode: A)-E), during the first discharge process; F)-J), during the first charge process; green circle shows regions of electrochemically active particles; yellow rectangular shows regions of electrochemically deactivated particles; red round rectangle shows regions of inactive particles; blue round rectangle shows regions of particle displacement. The slice location is 61 μm from the bottom stainless screw current collector in the pristine state.

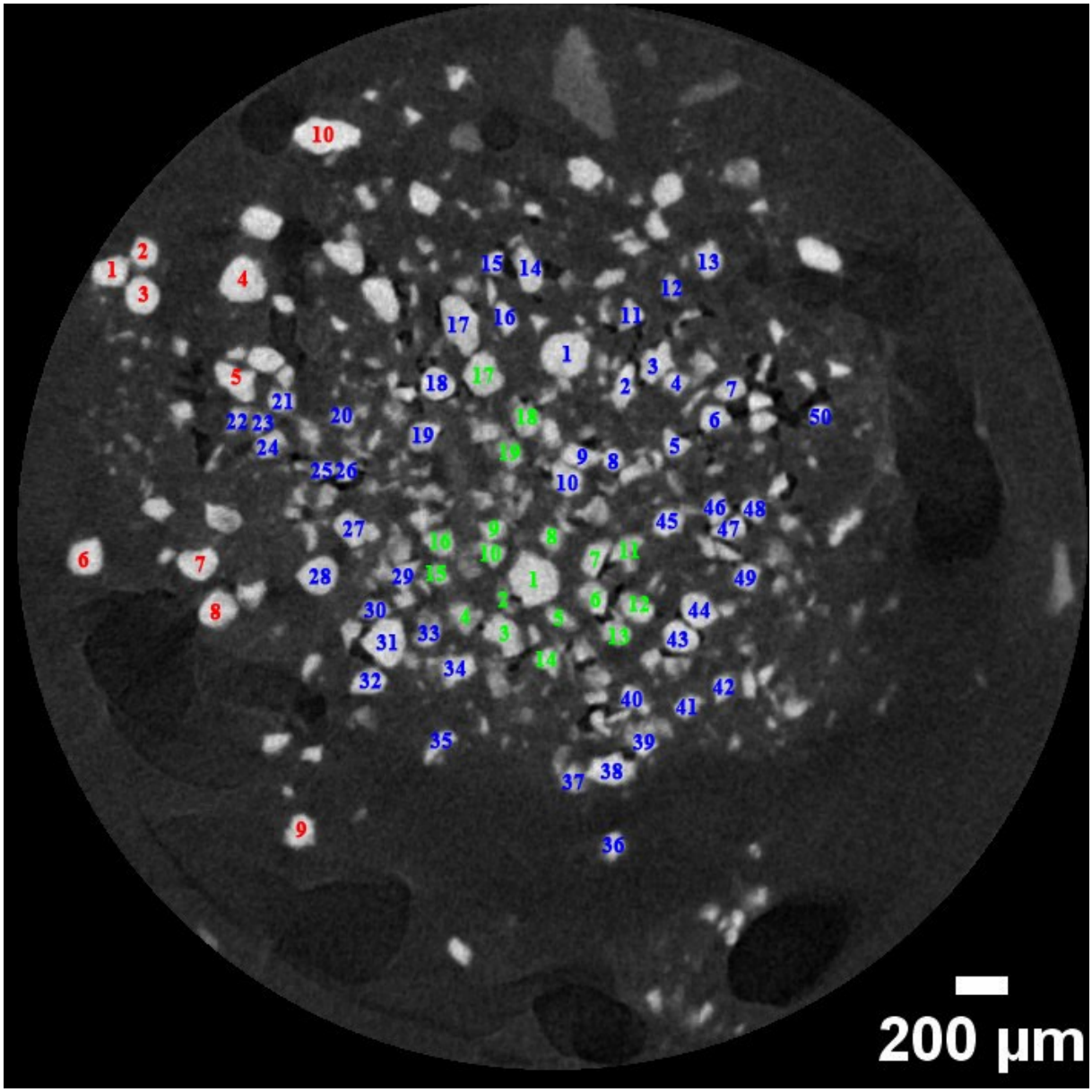

SI Fig. 6. Locations of the chosen 78 Si particles for quantitative analysis. Red numbers denote the Si particles that are electrochemically in-active through the first cycle (from 1 to 10). Blue numbers denote the Si particles that experience the first lithiation but turn into electrochemically in-active during the first delithiation (from 1 to 49). Green numbers denote the Si particles that are electrochemically active through the first cycle (from 1 to 19).

Caption for the Supplementary Movie:

http://www.sciencedirect.com/science/article/pii/S0378775316305109

In situ 2D radiography of radio-cell during the first cycle

Note that during the *in situ* radiography measurement we have stopped the micro CT once to cool down the X-ray source for around 30 minutes.

2.5 Fracture behavior of ~20 µm Si particles

Reprinted with permission from **DOI**: 10.1002/celc.201600219.

Synchrotron X-ray tomographic study of a Silicon electrode before and after discharge and the effect of cavities on particle fracturing

Lukas Zielke[a], Fu Sun[b], Henning Markötter[b], André Hilger[b], Riko Moroni[a], Roland Zengerle[a, c], Simon Thiele[a, d], John Banhart[b] and Ingo Manke[b]*

Lukas Zielke, Riko Moroni
a Laboratory for MEMS Applications, IMTEK Department of Microsystems Engineering, University of Freiburg, Georges-Koehler-Allee 103, 79110 Freiburg, Germany
E-mail: Lukas.Zielke@imtek.de, Riko.Moroni@imtek.de

Prof. Dr. John Banhart, Dr. Ingo Manke, Fu Sun, Dr. André Hilger, Dr. Henning Markötter
b Helmholtz Zentrum Berlin, Hahn-Meitner-Platz 1, 14109 Berlin, Germany
E-mail: banhart@helmholtz-berlin.de, manke@helmholtz-berlin.de, fu.sun@helmholtz-berlin.de, hilger@helmholtz-berlin.de, markoetter@helmholtz-berlin.de

Prof. Dr. Roland Zengerle
a Laboratory for MEMS Applications, IMTEK Department of Microsystems Engineering, University of Freiburg, Georges-Koehler-Allee 103, 79110 Freiburg, Germany
c Hahn-Schickard, Georges-Köhler-Allee 103, 79110 Freiburg, Germany
Zengerle@imtek.de

Dr. Simon Thiele
a Laboratory for MEMS Applications, IMTEK Department of Microsystems Engineering, University of Freiburg, Georges-Koehler-Allee 103, 79110 Freiburg, Germany
d FIT, University of Freiburg, Georges-Köhler-Allee 105, 79110 Freiburg, Germany,
Simon.Thiele@imtek.de

Abstract
Silicon (Si) has been proposed as one of the most promising anode materials for next-generation lithium ion batteries (LIBs). However, unsatisfactory discharge capacity/energy density and inevitable performance worsening prevent their commercialization. Herein, an in-depth investigation on the same Si composite electrode before and after the first discharge by employing in situ synchrotron X-ray tomography is presented. It is found that i) on the electrode level, the Si particles located in the central part of the electrode preferentially experience crack

formation; ii) on the individual particle level, heterogeneous electrochemical lithiation behaviour is observed; iii) cavities are formed during the electrode preparation and battery operation. Moreover, the correlation between the electrochemical activities of Si particles and their individual electrical contact to the electron conducting network is investigated. For the first time it is quantified that Si particles will experience lithiation only under the condition that at least 40% of their surface is electrically connected. These novel insights are possible explanations for low discharge capacity/energy of Si electrode LIBs, and would open new design principles and opportunities for high-capacity electrode materials for next-generation energy storage systems.

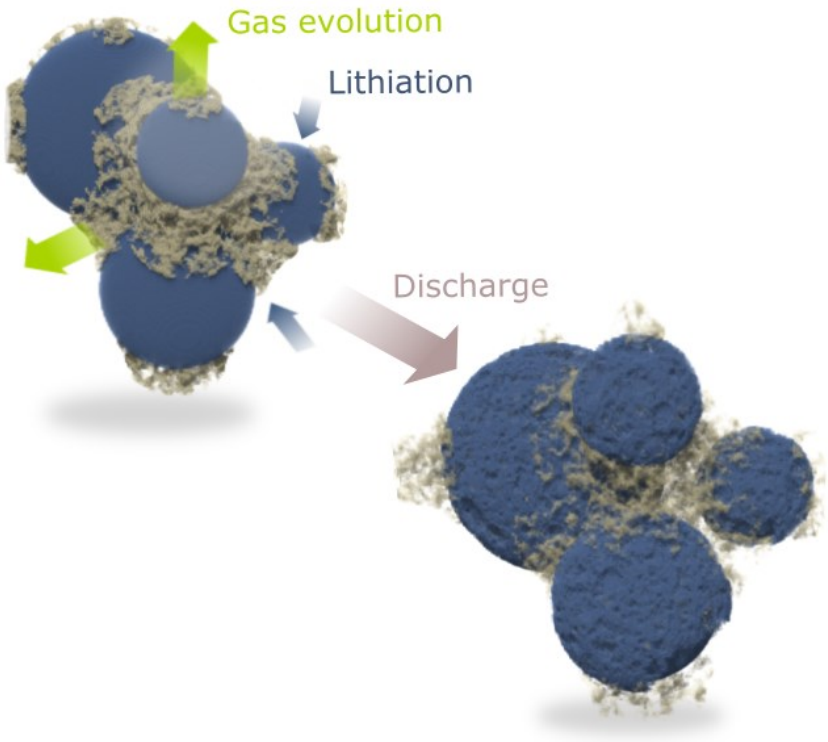

Abstract Graphic

Keywords lithium ion batteries, silicon particles, lithiation mechanisms, degradation mechanisms, Synchrotron X-ray tomography

1. Introduction

Next-generation lithium ion batteries (LIBs) with improved specific power and energy density have been proposed for a variety of demanding applications from electric vehicles to large-scale grid storage facilities.[1] Worldwide efforts are therefore underway to find novel electrode materials that will be considered as alternative options to replace the currently commercialized cathode and anode materials.[2] On this search for high-capacity anode materials, silicon (Si) has been identified as one of the most promising candidates to substitute graphite [3]: In contrast to graphite, where fully lithiated graphite stores one Li-ion per six carbon atoms through intercalation, fully lithiated Si-anodes can theoretically store four Li-ions per Si atom by

chemical bonding. This leads to larger theoretical capacities up to 3579 $mAhg^{-1}$, which is about 10 times larger than that of graphite anodes, 372 mAh g^{-1}. [4] However, Si anodes exhibit an unsatisfactory discharge capacity/energy density when discharged using high currents. They additionally show irreversible capacity fading during cycling. Previous studies, employing various characterization tools such as scanning electron microscope (SEM) [5], transmission electron microscope (TEM) [6] and X-ray tomography [7], have suggested that the inevitable capacity decay is associated intimately with the dramatic volume change of ~300% during cycling, with preferential de/lithiation pathway along the [110] direction of crystalline Si.[8] In addition, it was found that a two-phase boundary between a crystalline Si core and an amorphous Li-Si shell induces stress within the anode particles, resulting in significant particle fracture and pulverisation. [6,7,9]

Apart from boundary-induced fracture mechanisms, other factors also contribute to the decrease in energy density and the irreversible capacity fading. The central issue is related to the weakening or even complete loss of electrical contact between Si particles and the conductive network, consisting of carbon binder domain (CBD) and current collector.[10] Insufficient contact to the conductive network leads to partial electrochemical inactivation of these active materials, resulting in a reduced utilization of loaded material and unsatisfactory dis/charge capacity retention. Unfortunately, extensive characterizations of the evolution of a complete Si based electrode within an operational LIB have not been conducted due to i) the incompatibility between conventional investigation tools and commercial LIBs [11] and ii) the inability to characterize ensembles of active particles contained within a realistic multi-particle electrode. [11] Furthermore, no experimental framework of investigating the lower energy/capacity caused from insufficient contact between active materials and CBD has been reported, although it shows that the rate performance of a LIB electrode composite can be markedly improved by providing alternative electron paths.[12]

Here, we report the imaging of the same Si based electrode in pristine and the firstly discharged state in three-dimensions using in situ synchrotron X-ray tomography. Using high fluxes from synchrotron sources, [13] this characterization technique allows us to obtain large and representative datasets to track the evolution of the entire Si electrode on the electrode level (millimetres) and on the level of individual particles (~5µm) simultaneously. Studies on the de/lithiation of Si and other Li-alloying metals (e.g. Sn and Ge) using X-ray tomography/microscopy were conducted in the past [7,11,14–16], in which volume expansions/contractions, the relation between X-ray absorption and lithiation as well as fracturing mechanisms were investigated. Specifically, Taiwo et al. suggested that mechanical stress generated from the significant volume changes can decrease the contact of single Si particles to the conducting network. [16]

By employing in-situ synchrotron X-ray tomography, we observed what Taiwo et al. suggested and expanded this theory by a further quantitative analysis. Other important findings were i) on the electrode level, the Si particles located in the central part of the electrode preferentially experienced crack formation compared with the Si particles located in the peripheral region. And ii) on the individual particle level, heterogeneous electrochemical lithiation behaviour was

observed compared with the widely employed macro-homogeneuos model for battery simulation. [17] Finally, we quantified the fracturing of Si particles and related particles that remain unfractured with a loss of electrical/ionic contact to either the electron conductive network (current collector or to the carbon binder domain (CBD)) or the Li ion conductive electrolyte. Possible reasons for the contact loss have also been proposed. The current study fundamentally expands the inherent explanations for low discharge capacity/energy of Si electrode LIBs, and would open new design principles and opportunities for high-capacity electrode materials for next-generation energy storage systems.

2. Results

2.1 Morphology of the Pristine Electrode and Electrochemical Characterization

X-ray tomography is based on measuring variations in X-ray attenuation coefficients in a rotating sample and three-dimensional (3D) reconstructions of samples with high spatial resolution can be obtained by using high-flux synchrotron X-ray facilities.[18] Since all phases present (Si particles, CBD and cavity) exhibited excellent contrast due to different X-ray attenuation coefficients, morphological changes of particles, local CBD destruction and cavity formation could be studied in detail in 3D.

In the present study, a proof-of-concept battery, fully compatible with a synchrotron X-ray tomography setup (**Figure 1**a and b) and simultaneously representative of commercial LIBs, was used. We focused on morphological changes in the entire Si composite electrode before and after the first discharge. The experimental setup is shown in Figure 1a. The custom made cell allows imaging all inner components within the proof-of-concept battery (Figure 1b). Before starting the in-situ X-ray tomography we conducted scanning electron microscope (SEM) characterization of the prepared Si composite electrode surface for a reliable interpretation of the X-ray tomography data. An exemplary image is shown in Figure S1: It can clearly be seen, that the Si particles are well mixed with the CBD, which agrees with the tomography data (Figure 1c, inset), where the spherical Si particles can clearly be discriminated from the CBD filled pore space. The nano pores in the CBD cannot be resolved using synchrotron X-ray tomography with a pixel size of 438 nm. [19,20] Therefore, in the following CBD denotes a mixture of small, electrolyte filled pores and carbon black particles glued together with binder.

In a first step, we performed cyclic voltammetry to verify the reduction and oxidation characteristics of the Si particles (Figure S2). The observed anodic/cathodic peaks are in good agreement with those of previously reported silicon/carbon/binder (Si/C) composites [2,21]. Subsequently, a tomography in the pristine state (without any cycling) was made for reference. It is shown in Figure 1c: The battery contains a Si/C composite electrode, a separator (24 µm thick) and a lithium metal electrode (as counter and reference electrode). It can clearly be seen that the currently investigated Si/C composite electrode consists of an ensemble of active particles hold together by the electron conducting CBD, as in most realistic electrodes.

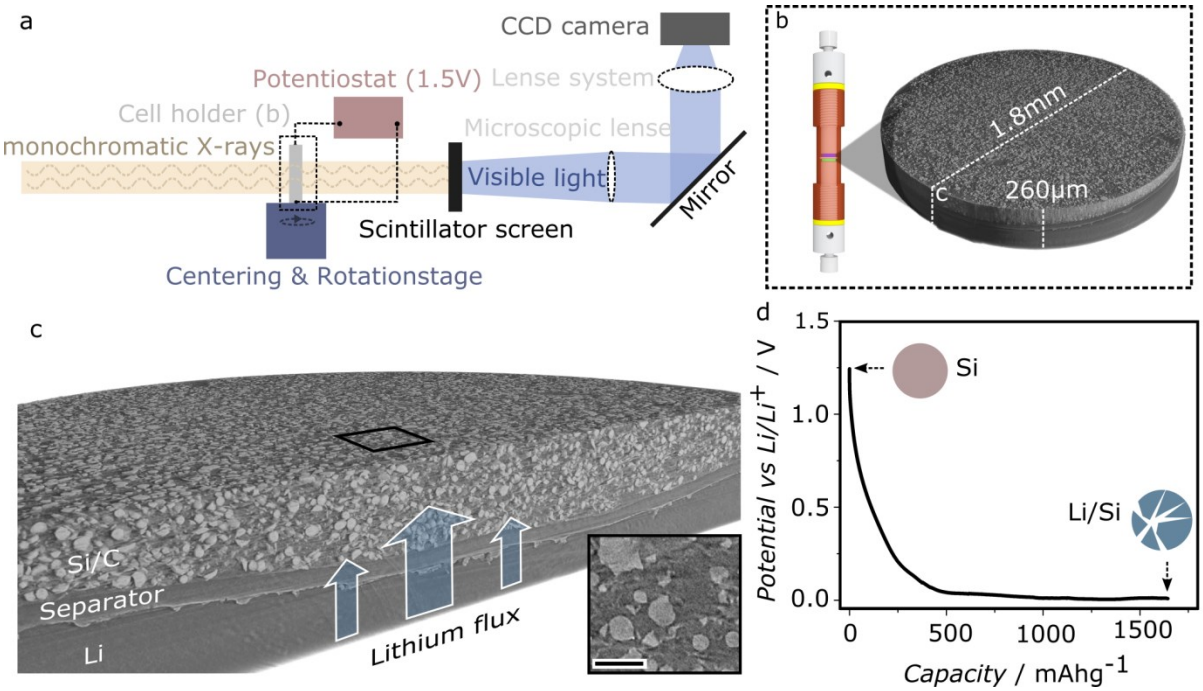

Figure 1 a) Schematic illustration of experimental setup at the BAMline at the electron storage ring BESSY II in Berlin, Germany. b) Battery cell holder design. c) Cell with lithium metal (bottom), separator (24 µm, centre) and a silicon/carbon/binder electrode (top). The lithium flux during discharge is indicated by arrows. An exemplary part of the electrode is shown in the inset. The scale bar represents 50 µm. d) First discharge curve of the battery at 0.13 Ag^{-1}, where the schematic sketch of an intact Si particle represents the pristine state and the cracked Li/Si particle represents the discharged state.

After the tomography in the pristine state, the battery was discharged at 0.13 Ag^{-1} (~0.03 C) based only on the mass of the loaded Si. The corresponding discharge curve is shown in Figure 1d. The obtained specific capacity was around 1700 $mAhg^{-1}$, which is lower than the theoretical specific capacity of Si (3579 $mAhg^{-1}$). In order to find explanations for the low specific capacity of the Si electrode, another tomography of the same electrode was conducted.

2.1 Morphology of the Discharged Electrode

2.1.1 Heterogeneous Lithiation on the Electrode Level

The firstly discharged state tomography is shown in **Figure 2**a, b and c. Compared with the pristine state tomography (Figure 1c), it can be unambiguously discerned that Si particles located in the central part of the electrode preferentially undergo crack formation, denoted by a blue circle in Figure 2b.

2.5 Fracture behavior of ~20 µm Si particles

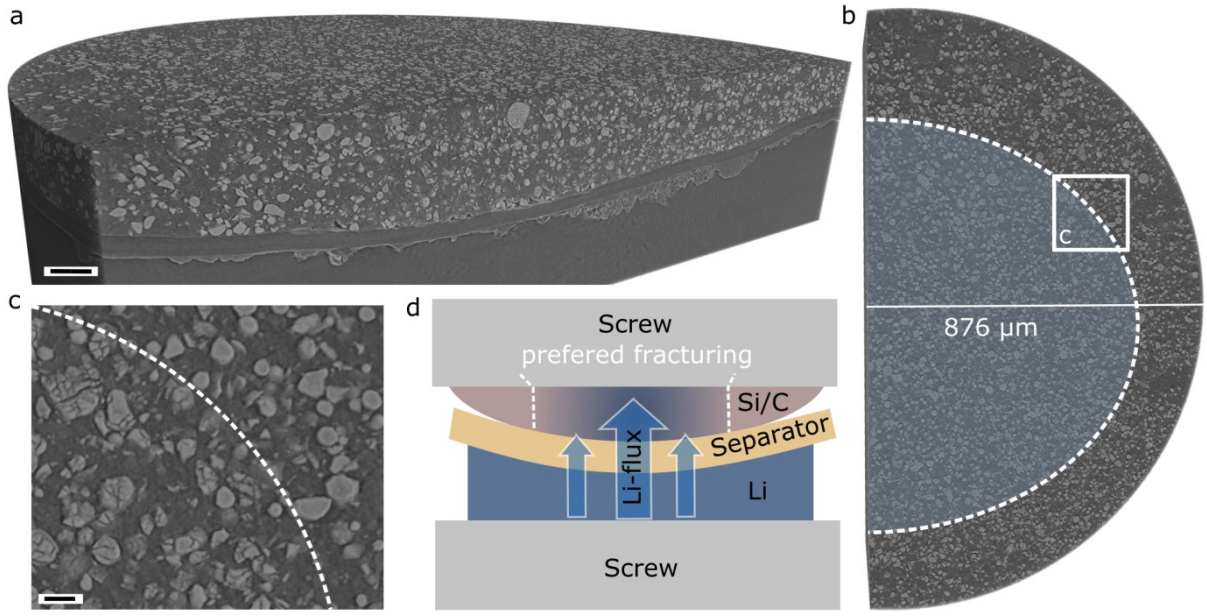

Figure 2 a) Three-dimensional representation of the discharged Si/C composite electrode in through-plane direction. The scale bar represents 50 µm. b) Top-view of the half-cropped reconstruction, showing the region where Si particles fractured preferentially (blue circle). c) Zoom in on the border of the region with preferred fracturing. The scale bar represents 10 µm. d) Schematic illustration showing the 1D Li ions flow paths in the inner part of the Si/C composite electrode.

In contrast, particles located in the peripheral regions are kept intact during the whole discharge process (hereafter, we denote the fractured Si particles as electrochemically active particles or lithiated particles; the unfractured Si particles as electrochemically inactive particles or un-lithiated particles). This finding was further checked by employing two-dimensional particle size distributions, shown in Figure S3. In the region with preferred fracturing (blue circle Figure 2b), the particle size is systematically smaller, confirming the suggestion from the visual analysis of the tomographic dataset. The observed inhomogeneity of lithiation on the entire electrode level corresponds well with previous reports, [22] in which, Cai *et al.* observed an significant inhomogeneous deterioration in a commercial LIB by using in situ neutron diffraction. They found that near the edges of the battery, both the graphite anode and the spinel-based cathode showed a decreased capacity while near the central area, both electrodes functioned properly. They propose some potential factors, such as the electrolyte solution loss, separator pore clogging and non-uniform temperature can contribute to this phenomenon. In our case, we propose that an inhomogeneous Li ion flux resulting from an inhomogeneous pressure subjected on Si/C composite electrode cause the inhomogeneous lithiation on the electrode level. As schematically shown in Figure 2d, owning to a convex shape of the Si/C electrode, an inhomogeneous pressure (a larger pressure in the inner part of the electrode compared with a smaller pressure at the outer parts) can be generated when screwing the Si/C electrode and Li electrode together using the two current collector pins (Figure 1b). This is further evidenced by the curvature of the separator between the two electrodes (Figure 1c and 2a). Assuming a homogeneous and electrically well conducting CBD [23], the lithiation process only occurs in regions with strongly promoted Li

conduction pathways.[24] Considering that the flow of Li ions, driven by the electrochemical potential between the Li electrode and Si electrode, is faster in the central part (shorter distances) than that of the outer part of Si/C electrode (longer distances), the currently observed well-defined one dimensional (1D) Li ions pathway (indicated by arrow in Figure 2d) agrees well with previous reports.[24] Therefore it is reasonable that Si particles located along the 1D Li ions pathway experience significant crack formation (lithiation) while others, located outside the pathway, are kept intact. A direct detrimental effect of the inhomogeneous lithiation on the electrode level is that the discharge current subjected on the complete battery (0.13 Ag^{-1}) concentrates only on the central part of the Si/C electrode, resulting in i) high localized current density and current hotspots that could induce fracture and accelerate capacity fading [25] and ii) significant under-utilization of active materials that could decrease the capacity/energy density. [26] We therefore conclude that it is crucial to design sophisticated electrode architecture that guarantees uniform Li ion flow pathways over the whole electrode.

2.1.2 Particle Sizes and Volume Fractions

To further investigate causes leading to low capacity/energy density, a rectangular region of interest (ROI) located within the 1D Li-ion flow pathway was chosen, as defined in Figure S3 and the results are shown in **Figure 3**. First, we quantified the fracturing of particles in this particular ROI for which we calculated the particle size distribution for the pristine and discharged electrode. As a result, we found a significant thinning of the distribution after discharging the battery, which reflects a general fracturing of particles. The results agree well with previous report. [1] In our case, the fracturing of particles leads to a decreased mean particle diameter from 7 µm to 3 µm (Figure 3a).

2.5 Fracture behavior of ~20 µm Si particles

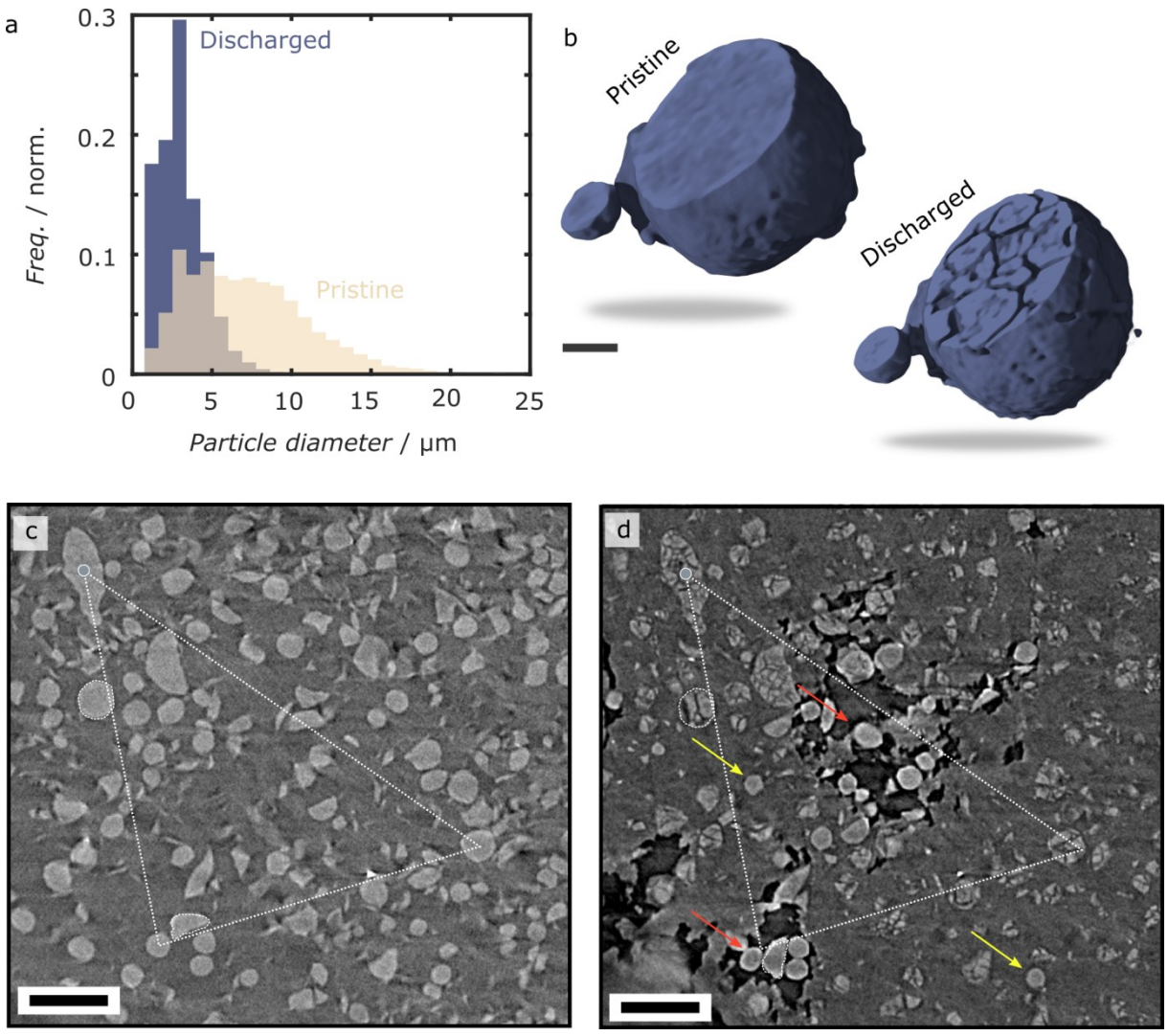

Figure 3 a) Particle size distribution of the pristine (beige) and discharged electrode (blue). b) 3D representation of a large particle, pristine and fractured. c, d) Reconstructed slices of the pristine electrode (c) and the same position after discharge (d) of a small part of the region of interest. The arrows indicate intact particles with good contact to the conducting network (yellow) and bad contact (red). The scale bar is 40 µm long. The white triangle is shown for orientation.

The height of the first bar in the particle size distribution of the discharged electrode in Figure 3a indicates that the size of a certain amount of fractured particles is below the estimated resolution limit of ~1 µm (~2 times the pixel size of 438 nm). To confirm this, we calculated the Si volume per electrode area. The calculation yielded 31.5 µm³/µm² in the pristine state and 24.0 µm³/µm² in the discharged state, which is a difference of 24%. This difference corresponds very well with another group's value of 25%, which implies a reasonable segmentation. [16] The difference before and after the first discharge indicates that approximately a quarter of the original Si after the first lithiation has fractured into pieces smaller than 1 µm in diameter. In Figure 3b a particle

before and after discharge is shown for illustration, indicating the fracturing into multiple smaller parts while keeping the originally spherical shape.

2.1.3 Size and Distribution of Cavities

Apart from particle fracture, other phenomena in the ROI are demonstrated in Figure 3c and d. Here, the same in-plane region of the electrode is shown in the pristine (Figure 3c) and discharged state (Figure 3d). The white triangle shows that there is little in-plane distortion, even though most of the particles exhibit strong fracturing. The limited volume expansion during the first discharge process suggests limited lithium uptake/storage ability of Si particles. [22] Moreover, it can be observed that some Si particles still undergo no lithiation (no crack formation, indicated by yellow arrows in Figure 3d) even though they are located within the 1D Li ions flow pathway, with CBD surrounding them. Actually, the observed inhomogeneous lithiation behaviour among individual particles is in agreement with previous reports that uncharged $FePO_4$ phases are often surrounded by charged $LiFePO_4$ phases [27] and that the statistical measure of local "spectroscopic" state-of-charge (SOC) state in an LIB is heterogeneous. [28] It has been suggested that in a realistic commercial LIB electrode, conditions for a homogeneous electrochemical reaction are hardly satisfied since any fluctuations on the electrolyte exposure, electrical contact or crystal defects can result in an inhomogeneous reaction. [29] In the present study we quantitatively investigated the correlation between the electrochemical activities of Si particles and the influence of their contact to both the ionically conducting electrolyte and the electrically conducting network.

Another worthy observation is that particles in the dark regions in Figure 3d show no or weak fracturing (indicated by red arrows). As a matter of fact, due to the different X-ray absorption coefficients of Si particles, CBD and large pores, we could identify the dark regions as cavities in the CBD. It is already known that gas evolution, which is intimately related with the solid electrolyte interphase (SEI) formation and the electrolyte decomposition, can locally destroy CBD and induce electrolyte displacement. [30,31] Goers et al. have observed gas formed channels during cycling within a LIB by neutron radiography (NR). [32]

In the following, we analyse the cavities in 3D in terms of size, distribution and their influences on Si particle lithiation. Results are shown in **Figure 4**. First, we present the quantitative analysis of the cavities. The mean diameter of the cavities within the complete Si/C electrode was found to be ~5 µm. However, diameters of up to ~18 µm were measured as shown in the size distribution in Figure 4a.

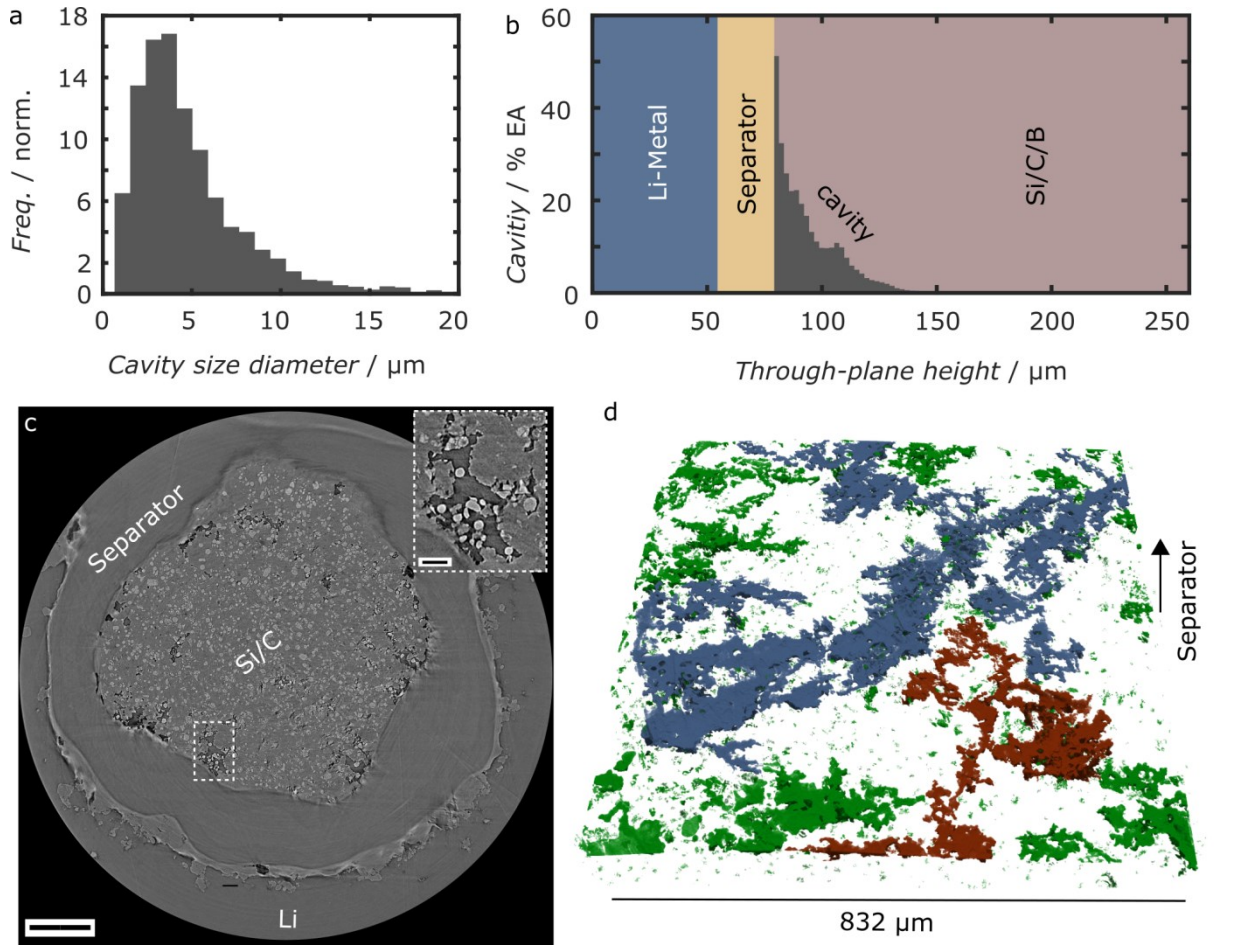

Figure 4 a) Cavity size distribution in the discharged state. b) Fraction of cavity area per electrode area in the through-plane direction, starting at the separator. c) Exemplary tomogram showing inhomogeneously distributed cavities. One of them is shown in the inset. The scale bars represent 25 µm (inset) and 200 µm. d) Three-dimensional representation of the cavity network. The largest connected cluster is shown in blue and the second largest in red. Remaining cavity clusters are shown in green.

We also found that cavities were mostly located in the vicinity of the separator (Figure 4b) and were not homogeneously distributed throughout the electrode as depicted in Figure 4c (exemplary tomogram) and Figure 4d (3D distributions of cavities). It has to be noted that in Figure 4d, the colours represent connected cavity clusters: the largest connected cavity comprises 63 vol. % of the total cavity volume (Figure 4d, blue) and spans the whole length of the ROI; the next largest cavity region comprises 17 vol. % (Figure 4d, red).

2.1.1 A Correlation between Particle Fracture and Cavities

Furthermore a quantitative analysis of the influence of cavities on the fracturing of particles in close contact to them was conducted. The results are shown in **Figure 5**.

2.5 Fracture behavior of ~20 µm Si particles

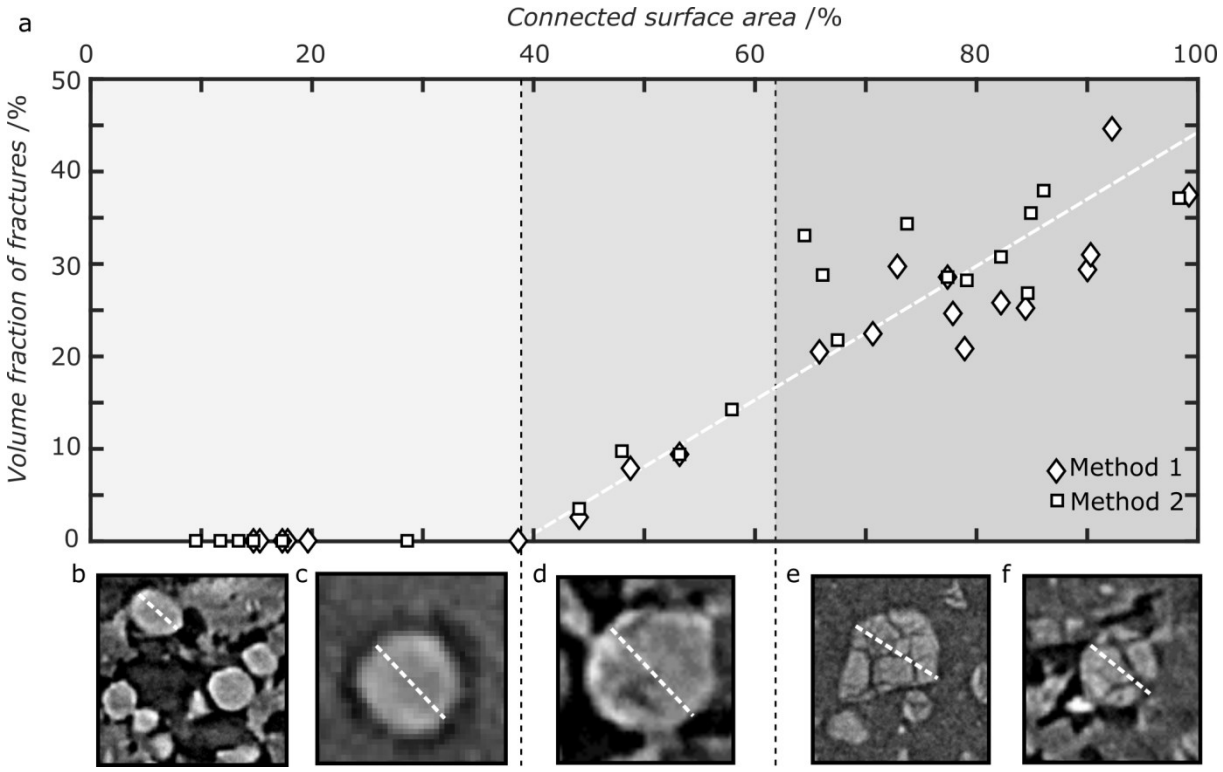

Figure 5 a) Relative volume of fractures within silicon particles versus connected surface area, calculated using two different segmentation methods (diamonds and squares)). b, c) Structurally intact and poorly connected particles: b) within the large cavity network (shown diameter was 16 µm) and c) with localized CBD destruction around it (shown diameter was 9 µm). d) Partially connected particle with a few fractures (~48% connected surface area, diameter was 14 µm). e, f) Well connected Si particle e) with fractures aside of the cavity network (90% connected surface area, diameter of 27 µm) and f) inside of the cavity network (77% connected surface area and a diameter of 14 µm). The white dotted line in a) is a guide to the eye.

Four types of particles were found: i) Particles well connected to the CBD that exhibited large fractures (Figure 5 e, f), ii) particles with only partial contact to the CBD but with fractures (Figure 5 d), iii) particles with only partial contact to the CBD but without fractures (Figure 5 b) and iv) particles almost fully surrounded by a cavity (Figure 5 c). It needs to be noted that the cavity around the particles in iv) is not part of the large cavity network but is strongly localized around single particles. Actually, this kind of particle (type iv) is representative of a class of Si particles that often undergo no crack formation within the 1D Li ions flow pathway (see Figure 3d). The reason for these strongly localized cavities lies probably in the electrode preparation process, e.g. in the material mixture and/or in the drying process. [33] Further information on type iv particles can be found in the supplementary information.

For a representative quantification of the correlation between particle fracturing and contact loss to both the electrical and ionic network, we investigated 21 different particles in the vicinity or within cavities (both gas generated cavities and localized cavities). Relative volume of fractures within the particles, serving as an indicator for lithiation, versus the electrically/ionically

connected surface area of the particles is shown in Figure 5a. We found that, above a threshold of 40%, the degree of fractures intensifies with increasing connected surface area. Since the determination of contact areas is highly critical, all particles and cavities were segmented predominantly manually using two different methods (diamonds and squares), which are described in detail in the Methods section. Despite the scatter of the data a clear trend is observed: the relation between fracturing and electrical/ionic contact of Si particles in the battery shows a threshold. That is, a connected surface area below 40% leads to no electrochemical activity of Si particles. To the authors' knowledge, this is the first investigation on the correlation between the electrochemical activities of Si particles and the influence of their contact area to the conducting electronic/ionic network in the battery.

From an electrochemical point of view, lithium insertion into Si particles during the lithiation process entails Li-ions (from the electrolyte or Li electrode) and electrons (from CBD, conductive network or adjacent active particles) simultaneously. [12] The dependence of the electrochemical performance of LIBs on the contact between active materials and the electrically/ionically conducting network is an important electrode design consideration. [34] Actually, it has been suggested that the electron transference between difference phases is through hopping or tunnelling mechanism with contact resistivity depending exponentially on the gap between the contacts. A gap of 8-10 nm is large enough to make a contact electrically insulating. [35] Thus, the cavities (either from electrode preparation or battery operation) surrounding Si particles will block the flow of electrons into the active particles during the lithiation process to some extent, resulting in the observed electrochemically in-active (unfractured) particles. After an in-depth quantitative analysis, it is discovered for the first time that, Si particles will experience lithiation only under the condition that at least 40% of its surface is electronically/ionically connected.

3. Conclusion

In summary, we performed an in-situ analysis of a Si/C electrode in its pristine and firstly discharged states. Firstly, we found that the Si particles in the centre of the electrode preferentially undergo crack formation while particles located in the peripheral regions are kept intact during the whole first discharge process. We propose that the one-dimensional Li ions flow behaviour and a non-uniform contact pressure subjected on the Si/C electrodes could be the reason. Secondly, we revealed the presence of large non-uniformly distributed cavities (either from electrode preparation or battery operation) within the discharged Si/C electrodes. We further quantified their size and distribution within the electrode in three-dimensions. In addition, an in-depth quantitative analysis was conducted to investigate the dependence of the electrochemical activities of active materials and their contact surfaces to the electrically/ionically conducting network. We found that silicon particles experience fracture only when their contact area to the conducting network is at least 40% of their total surface area. These results show that synchrotron X-ray tomography is a powerful characterization tool to quantitatively investigate the dependence of the electrochemical performance of LIBs on the electrical contact between active materials and conducting network. The novel insights into possible causes for the lower capacity/energy density

of LIBs are crucial because they cannot be easily obtained by conventional macroscopic electroanalytical characterization techniques. Our findings provide potential guidelines to further enhance the performance of LIBs. On the one hand, future electrode engineering should concentrate on optimizing the whole electrode architecture, which can involve all active material particles ionically and electronically connecting to electrolyte and electric conducting network to maximize the utilization of active materials. Particularly, an efficient electrically conducting CBD network and an ionically well-conducting pore space are highly desirable to eliminate the observed electrochemically in-active material. On the other hand, our analysis shows that it is important to develop new electrolytes with reduced gas formation to eliminate gas induced cavities.

4. Experimental Section

Materials: Silicon was received from Elkem AS, Norway. Conductive carbon black, Polyvinylidene difluoride (PVDF) binder, Celgard separator and lithium were purchased from MTI Cor. USA. N-methyl pyrrolidone solvent (NMP) and 1M $LiPF_6$ in a volume-ratio mixture (1:1) of ethylene carbonate (EC) and dimethyl carbonate (DMC) were purchased from Sigma Aldrich. The housing of the proof-of-concept beamline battery is made of polyamide-imide (Torlon) from the McMaster-Carr company.

Battery Preparation: The electrode was made of electrode slurries with weight ratios of Si:carbon black:binder of 70:20:10 in NMP. As binder, PVDF was used. Subsequently, the slurry was cast onto an aluminium foil. To remove the NMP, the cast aluminium foils were dried in an oven at 60 ℃ overnight. After drying, the completed composite electrode was diced into smaller pieces of around 1.7 mm × 1.7 mm × 0.2 mm (length×width×height) with a razor blade. Before the Si composite was assembled into the battery, it was weighed and the amount of Si particles was determined from the original mass ratio. The mass of the Si composite electrode was 0.17 mg. The proof-of-concept battery was assembled in an argon-filled glovebox with humidity and oxygen levels below 0.1 ppm. Metallic lithium was placed on the top of a screw, acting as a counter and reference electrode. The polymer separator was placed between the lithium electrode and the Si electrode. Finally, the housing tube was filled with the liquid electrolyte. Current leads were connected to a potentiostat for electrochemical tests.

Electrochemical Measurement: Cyclic voltammetry (CV) and galvanostatic charge/discharge of the battery were carried out with an IviumStat form Ivium Technologies, Netherlerlands. A freshly assembled battery was measured from 2.5 V to 0 V at a scan rate of 1 mVs^{-1} to obtain CV curves. During galvanostatic cycling at the beamline, the assembled battery was measured at a discharge current of 0.13 Ag^{-1} based only on the mass of Si active material.

Settings of Tomography Measurements: Synchrotron X-ray tomography was carried out at the BAMline at BESSY II of the Helmholtz-Centre Berlin, Germany. The synchrotron beam was monochromatized to 20 keV using a double multilayer monochromator with an energy resolution of about 1.5 %. The detector system comprised a 60-µm thick $CdWO_4$ scintillator, a microscopic optic and a pco4000 camera with a 4008×2672 $pixel^2$ CCD chip that is kept out of the direct

beam by using a mirror. For tomography, 2200 projections during a 180° battery rotation, each with 4 s exposure time were recorded before or after discharge.

Data Processing: The Si/C/B domains were segmented using the software FIJI and applying a median filter and Otsu's method for binarization, followed by a slight opening [36,37]. The cavity domain was segmented using the statistical region-merging tool and followed by individual thresholds for subsets. They were chosen by visual judgement. Pore and particle size distributions were calculated using the Delerue method, implemented in the software packages GeoDict (3D global) and Matlab (3D local). The phase distributions (2D and 3D) were calculated using self-programmed Matlab functions. Segmentation of contact areas was conducted using manual segmentation, and two different approaches. Manual segmentation of particles and a global threshold from visual judgement was used to segment the contact area between Si particles and CBD. A dilation of the particle followed, resulting in an overlap of particle and cavity. To avoid edge effects, the segmented particle was eroded once and subsequently the thresholds for the segmentation of fractures were chosen from visual judgment (Method 1). Based on these datasets, the particle-cavity contact area was manually corrected in every main direction, followed by a slight 3D median filter (Method 2).

Supporting Information

Supporting Information is available from the Wiley Online Library or from the author.

Acknowledgements

We thank Dr. Heinrich Riesemeier, the beamline scientist at BESSY II, for his valuable assistance, Anna Manzoni for conducting scanning electron microscope (SEM) characterization and Norbert Beck for fabricating the beamline battery. We also thank Elkem AS for providing us with the Si particles. This work is sponsored by the Helmholtz Association and the China Scholarship Council.

References

[1] D. S. Eastwood, V. Yufit, J. Gelb, A. Gu, R. S. Bradley, S. J. Harris, D. J. L. Brett, N. P. Brandon, P. D. Lee, P. J. Withers, P. R. Shearing, *Adv. Energy Mater.* **2014**, *4*, n/a.
[2] F. Sun, K. Huang, X. Qi, T. Gao, Y. Liu, X. Zou, X. Wei, J. Zhong, *Nanoscale* **2013**, *5*, 8586.
[3] D. Larcher, S. Beattie, M. Morcrette, K. Edstrom, J.-C. Jumas, J.-M. Tarascon, *J. Mater. Chem.* **2007**, *17*, 3759.
[4] U. Kasavajjula, C. Wang, Appleby, A. John, *Selected Papers presented at the FUEL PROCESSING FOR HYDROGEN PRODUCTION SYMPOSIUM at the 230th American Chemical SocietyNational Meeting Washington, DC, USA, 28 August – 1 September 2005* **2007**, *163*, 1003.
[5] S. W. Lee, M. T. McDowell, L. A. Berla, W. D. Nix, Y. Cui, *Proceedings of the National Academy of Sciences* **2012**, *109*, 4080.
[6] X. H. Liu, L. Zhong, S. Huang, S. X. Mao, T. Zhu, J. Y. Huang, *ACS Nano* **2012**, *6*, 1522.
[7] J. Gonzalez, K. Sun, M. Huang, J. Lambros, S. Dillon, I. Chasiotis **2014**, *269*, 334.

[8] M. Gu, Y. Li, X. Li, S. Hu, X. Zhang, W. Xu, S. Thevuthasan, D. R. Baer, J.-G. Zhang, J. Liu, C. Wang, *ACS Nano* **2012**, *6*, 8439.
[9] M. T. McDowell, S. W. Lee, W. D. Nix, Y. Cui, *Advanced Materials* **2013**, *25*, 4966.
[10] C. K. Chan, H. Peng, G. Liu, K. McIlwrath, X. F. Zhang, R. A. Huggins, Y. Cui, *Nat Nano* **2008**, *3*, 31.
[11] J. Wang, Y.-c. K. Chen-Wiegart, J. Wang, *Angewandte Chemie International Edition* **2014**, *53*, 4460.
[12] G. Chen, T. J. Richardson **2010**, *195*, 5387.
[13] I. Manke, J. Banhart, A. Haibel, A. Rack, S. Zabler, N. Kardjilov, A. Hilger, A. Melzer, H. Riesemeier, *Applied physics letters* **2007**, *90*, 214102.
[14] J. Gonzalez, K. Sun, M. Huang, S. Dillon, I. Chasiotis, J. Lambros **2015**, *285*, 205.
[15] Weker, J. Nelson, N. Liu, S. Misra, Andrews, J. C., Y. Cui, Toney, M. F., *Energy Environ. Sci.* **2014**, *7*, 2771.
[16] O. O. Taiwo, D. S. Eastwood, P. D. Lee, J. M. Paz-García, S. A. Hall, Brett, Daniel J. L, P. R. Shearing, *ECS Transactions* **2015**, *69*, 81.
[17] D. Kehrwald, P. R. Shearing, N. P. Brandon, P. K. Sinha, S. J. Harris, *J. Electrochem. Soc.* **2011**, *158*, A1393.
[18] F. R. Brushett, L. Trahey, X. Xiao, J. T. Vaughey, *ACS Appl. Mater. Interfaces* **2014**, *6*, 4524.
[19] L. Zielke, T. Hutzenlaub, D. R. Wheeler, I. Manke, T. Arlt, N. Paust, R. Zengerle, S. Thiele, *Adv. Energy Mater.* **2014**, *4*, 1301617.
[20] L. Zielke, T. Hutzenlaub, D. R. Wheeler, C.-W. Chao, I. Manke, A. Hilger, N. Paust, R. Zengerle, S. Thiele, *Adv. Energy Mater.* **2015**, *5*.
[21] X. Zhou, Y.-X. Yin, L.-J. Wan, Y.-G. Guo, *Adv. Energy Mater.* **2012**, *2*, 1086.
[22] L. Cai, K. An, Z. Feng, C. Liang, S. J. Harris **2013**, *236*, 163.
[23] C. Villevieille, M. Ebner, J. L. Gómez-Cámer, F. Marone, P. Novák, V. Wood, *Advanced Materials* **2015**, *27*, 1676.
[24] N. Balke, S. Jesse, Y. Kim, L. Adamczyk, A. Tselev, I. N. Ivanov, N. J. Dudney, S. V. Kalinin, *Nano Lett* **2010**, *10*, 3420.
[25] Y. Li, F. El Gabaly, T. R. Ferguson, R. B. Smith, N. C. Bartelt, J. D. Sugar, K. R. Fenton, D. A. Cogswell, Kilcoyne, A. L. David, T. Tyliszczak, M. Z. Bazant, W. C. Chueh, *Nat Mater* **2014**, *13*, 1149.
[26] G. Zhang, C. E. Shaffer, C.-Y. Wang, C. D. Rahn, *J. Electrochem. Soc.* **2013**, *160*, A2299.
[27] J. Liu, M. Kunz, K. Chen, N. Tamura, T. J. Richardson, *J. Phys. Chem. Lett.* **2010**, *1*, 2120.
[28] J. Nanda, J. Remillard, A. O'Neill, D. Bernardi, T. Ro, K. E. Nietering, J.-Y. Go, T. J. Miller, *Advanced Functional Materials* **2011**, *21*, 3282.
[29] F. Lin, D. Nordlund, T.-C. Weng, Y. Zhu, C. Ban, R. M. Richards, H. L. Xin, *Nat Commun* **2014**, *5*.
[30] E. Sarasketa-Zabala, F. Aguesse, I. Villarreal, Rodriguez-Martinez, L. M., López, C. M., P. Kubiak, *J. Phys. Chem. C* **2015**, *119*, 896.
[31] M. Holzapfel, A. Würsig, W. Scheifele, J. Vetter, P. Novák, *13th International Meeting on Lithium Batteries* **2007**, *174*, 1156.
[32] D. Goers, M. Holzapfel, W. Scheifele, E. Lehmann, P. Vontobel, P. Novák, *Journal of Power Sources* **2004**, *130*, 221.
[33] D. Mazouzi, Z. Karkar, C. Reale Hernandez, P. Jimenez Manero, D. Guyomard, L. Roué, B. Lestriez, *Journal of Power Sources* **2015**, *280*, 533.

[34] B. Orvananos, R. Malik, H.-C. Yu, A. Abdellahi, C. P. Grey, G. Ceder, K. Thornton, *Electrochimica Acta* **2014**, *137*, 245.
[35] Nguyen, B. P. N., J. Gaubicher, B. Lestriez, *Electrochimica Acta* **2014**, *120*, 319.
[36] M. D. Abràmoff, P. J. Magalhães, S. J. Ram, *Biophotonics International* **2004**, *11*, 36.
[37] Nobuyuki Otsu, *Trans. Syst., Man, Cybern.* **1979**, *9*, 62.

2.5.1 Supporting Information

Synchrotron X-ray tomographic study of a Silicon electrode before and after discharge and the effect of cavities on particle fracturing

Lukas Zielke[a], Fu Sun[b], Henning Markötter[b], André Hilger[b], Riko Moroni[a], Roland Zengerle[a, c], Simon Thiele[a, d], John Banhart[b] and Ingo Manke[b]*

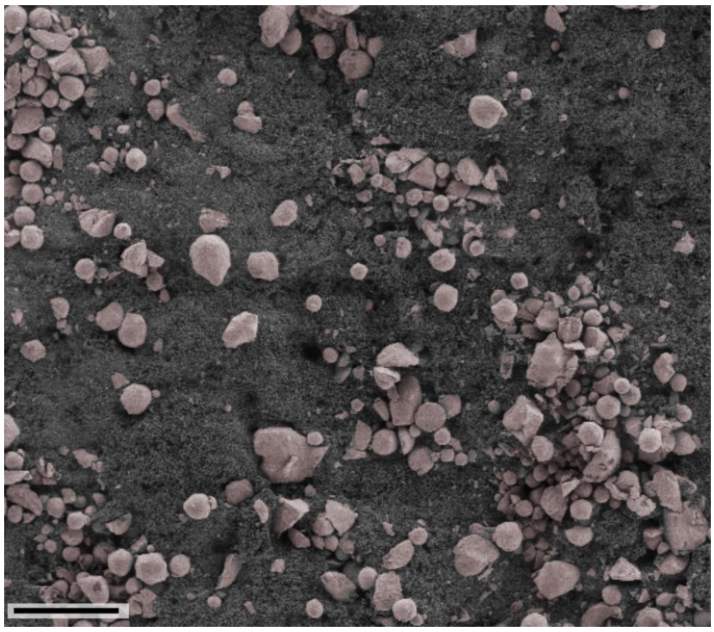

Fig. S1 False color scanning electron micrograph of the mixed Si/Carbon/binder composite electrode in the pristine state. The rose particles are the silicon particles and the pore-filling material is the carbon binder mixture. The scale bar represents 50µm. The image was scanned with a voltage of 2kV.

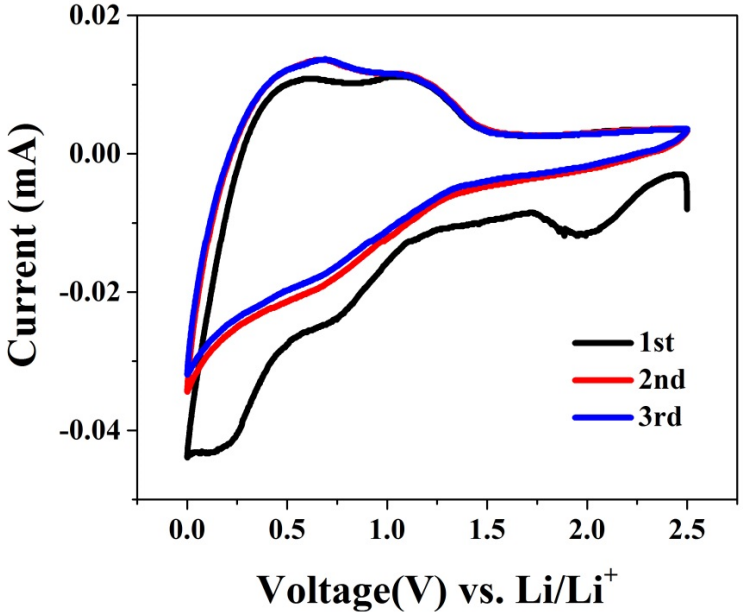

2.5 Fracture behavior of ~20 µm Si particles

Fig. S2 The cyclic voltammetry (CV) curves scanned at 1 mV s^{-1} in the potential window of 0-2.5V of the assembled proof-of-concept beamline battery

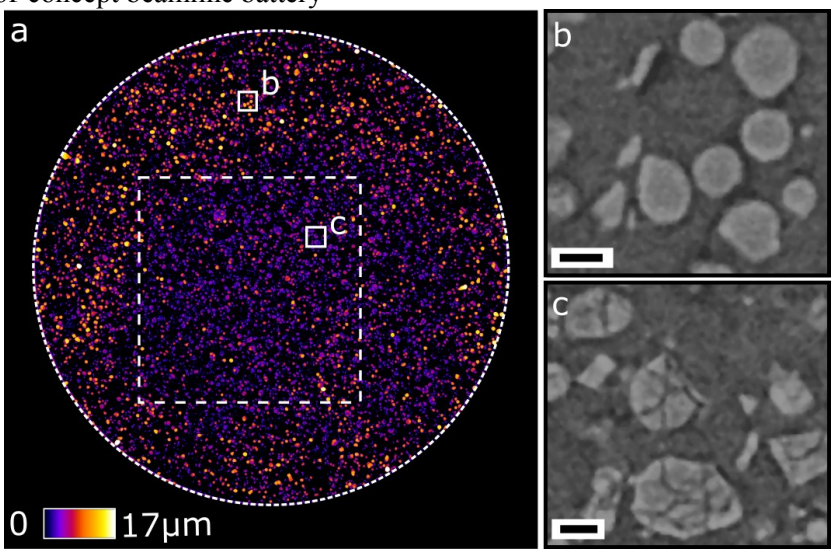

Fig. S3 a) Exemplary segmented in-plane image showing particles of the discharged electrode. The particles are generally larger in the outer region since they kept their original shape (b) and fractured to smaller sizes in the inner region (c). Scale bars in b and c are 10 µm long.

On the search for sufficient morphological parameters determining if single particles with strongly localized cavities around them fractured or not, we calculated characteristic sizes of multiple particles (volume:surface area). The calculated characteristic sizes were calculated in the pristine electrode reconstruction and whether the particles cracked was checked in the discharged reconstruction. The calculation is shown in Fig. S4: the fracturing of those particles did not depend solely on the characteristic size. Finding a parameter solely determining whether type iv particles fracture or not bears a large potential for increasing the performance of Si composite electrodes.

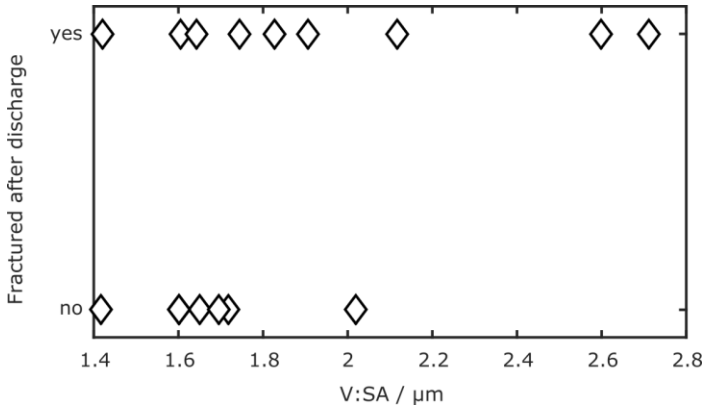

Fig. S4 Influence of characteristic size (volume divided by surface area) on whether the particle with strongly localized cavities around them fractured or not.

2.6 Different (de)lithiation behaviors of Sn particles

Reprinted with permission from **DOI**: 10.1002/cssc.201600220.

In situ radiographic investigation of lithiation and delithiation mechanisms in a Sn-electrode lithium ion battery

Fu Sun,*[a, b] Henning Markötter, [a, b] Dong Zhou, [a, b] Saad Sabe Sulaiman Alrwashdeh, [a, b, c] Andre Hilger, [b] Nikolay Kardjilov, [b] Ingo Manke[b] and John Banhart [a, b]

[a] Fu Sun, Prof. Dr. John Banhart, Dr. Henning Markötter, Dong Zhou, Saad Sabe Sulaiman Alrwashdeh
Institute of Material Science and Technologies
Technical University Berlin
10623 Berlin, Germany
E-mail: fu.sun@helmholtz-berlin.de
john.banhart@tu-berlin.de
[b] Fu Sun, Dr. Henning Markötter, Dong Zhou, Saad Sabe Sulaiman Alrwashdeh, Dr. Andre Hilger, Dr. Nikolay Kardjilov, Dr. Ingo Manke and Prof. Dr. John Banhart
Helmholtz Centre Berlin for Materials and Energy
Hahn-Meitner-Platz 1
14109 Berlin, Germany
[c] Saad Sabe Alrwashdeh
Mechanical Engineering Department
Faculty of Engineering, Mu'tah University
P.O Box 7, Al-Karak 61710 Jordan

Abstract

The lithiation and delithiation mechanisms of multiple-Sn particles in a customized flat radiography cell were investigated by *in situ* synchrotron radiography. For the first time, four hitherto unknown de/lithiation phenomena in a Sn-electrode battery system are highlighted: 1 The de/lithiation behavior varies between different Sn particles; 2 The time required to lithiate individual Sn particle is markedly different from the time needed to discharge the complete battery; 3 Electrochemical deactivation of originally electrochemically active particles is reported; 4 A change of electrochemical behavior of individual particles during cycling is found and explained by dynamic changes of de/lithiation pathways amongst particles within the electrode.

2.6 Different (de)lithiation behaviors of Sn particles

These unexpected findings fundamentaly expand the understanding of the underlying de/lithiation mechanisms inside commercial lithium ion batteries (LIBs) and would open new design principles for high-performance next-generation LIBs.

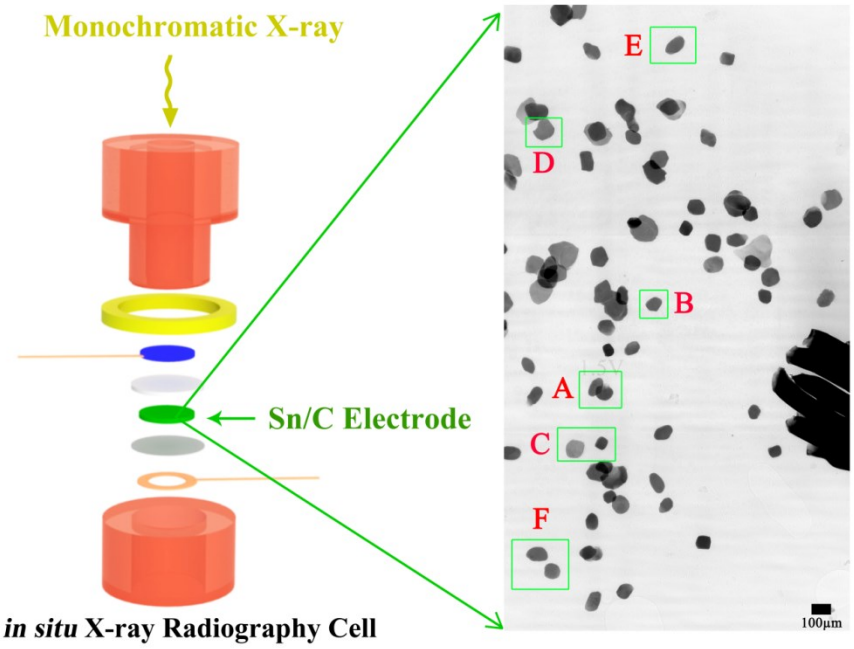

Abstract Graphic

Key words
lithium ion battery; Sn particles; in-situ; Synchrotron X-ray; radiography

Lithium ion batteries (LIBs) are the dominant energy carrier in many applications ranging from portable electronics to hybrid electric vehicles.[1-4] The development of next-generation LIBs with superior energy and power density and long-term cycling stability necessitates a fundamental understanding of de/lithiation mechanisms inside battery systems. Currently, direct visualization into de/lithiation process has been largely provided by *in situ* transmission electron microscopy (TEM) investigations.[5, 6] However, Zhong *et al.* argue that the "end/point contact" architecture of active materials used in the *in situ* TEM technique may deviate from the commercial "flooding geometry" contacts and they find the multiple-stripe lithiation mechanism in a flooding geometry by investigating SnO_2 nanowires.[7] Furthermore, Gu *et al.* suggest that the open-cell configuration and the ionic/Li_2O electrolyte are also inherently different from real commercial batteries and they have developed a sealed *operando* TEM electrochemical cell and found that the lithiation of Si nanowire immersed in the liquid electrolyte progresses in the core-shell fashion.[8] Previous work carried out based on the *in situ* TEM have provided insightful

information into the structural and chemical evolution of electrodes during de/lithiation. Nevertheless, one typical deficiency associated with the *in situ* TEM studies is that they are limited to explore the de/lithiation mechanism on atomic or single nanowire/nanoparticle level only, missing the interplay amongst multiple particles and the interactions between active material and conductive/binder agent composite. Realistically, a commercial LIB electrode is an assembly of active particles, organic polymeric binder and conducting agent.[9] Thus, direct observation of the de/lithiation process on the multiple-particle scale can provide additionally realistic insights into the operation of LIBs and guide engineers designing the electrode architecture in developing more advanced next-generation LIBs.

Herein a cell suitable for *in situ* radiography was built and the de/lithiation process of multiple-Sn particles was investigated by synchrotron X-ray radiography. Some de/lithiation behaviors of Sn particles obtained from this *in situ* radiography cell are consistent with previous results.[8] However, contrary to the widespread belief that the lithium ions are proposed to diffuse uniformly from the separator to the current collector with the formation of an electrode-level de/lithiation front,[10] we find a number of phenomena in the battery systems that cast doubts on this belief. These unexpected findings, which cannot be obtained by the overall macroscopic electrochemical characterizations and a single-particle de/lithiation model, fundamentally expand our understanding of underlying de/lithiation mechanisms in practical commercial LIBs and would open new design principles and opportunities for high-performance next-generation LIBs.

The design of the *in situ* 2D radiography cell (radio-cell) and the schematic illustration of the synchrotron setup are illustrated in Figure 1a,c, along with a photograph of the radio-cell, Figure 1b. Figure SI of the SI (Supporting Information) shows a projection image of the Li electrode/separator/Sn electrode assembly within the cell obtained after the synchrotron X-ray measurements by using a laboratory micro X-ray source.[11] A weight-ratio of Sn:Carbon:Binder of 60:30:10 was used to prevent possible particle overlapping in the radiographs. More details of the cell and the measurement procedure are described in the experimental section and SI. After assembling the radio-cell, cyclic voltammetry (CV) was performed to verify the reduction and oxidation characteristics of Sn, as shown in Figure S2. The clearly observed anodic/cathodic peaks shown in SI Figure 2b are in good agreement with previously reported Sn/Carbon composite LIBs.[12] In a next step, the cell was dis/charged while conducting synchrotron X-ray radiography. Typical dis/charge curves shown in SI Figure 2a also agree with previous results.[13]

2.6 Different (de)lithiation behaviors of Sn particles

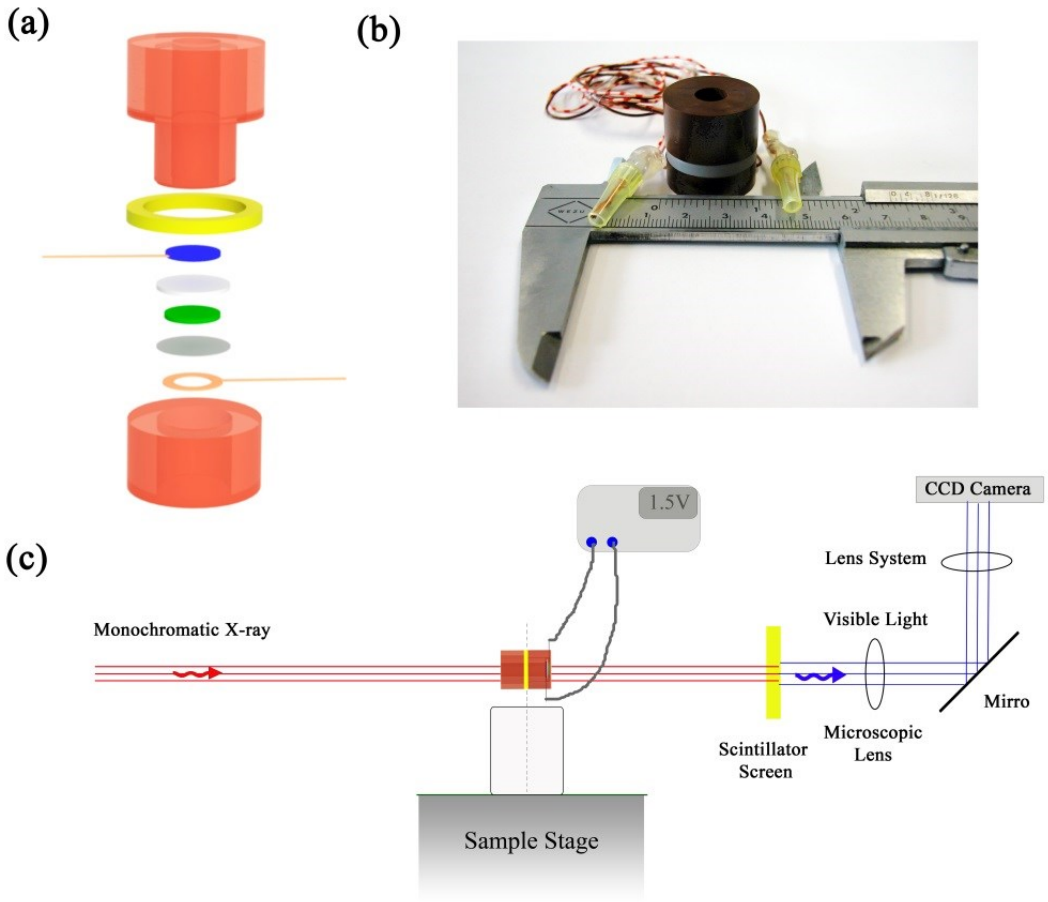

Figure 1. (a) Schematic illustration of the radiography cell used for in situ synchrotron radiography. From top to bottom: upper housing (orange), sealing ring (yellow), lithium plate (blue) with copper wire, separator (light gray), Sn/carbon/binder composite (green), titanium foil current collector (gray), annular copper current collector (copper), lower housing (orange); (b) Photograph of the radio-cell; (c) Schematic illustration of the experimental setup at the BAMline, BESSY II, Helmholtz-Zentrum Berlin, Germany. The radio-cell is arranged coaxially to the beam throughout radiography.

Synchrotron X-ray imaging is an analytical technique that maps the X-ray attenuation coefficients of samples. Since characterizations can be conducted *in situ* and non-destructively,[14] it is particularly well suited to track the morphological evolution of particles and changes of an entire electrode as a function of discharge/charge state. The presented synchrotron X-ray radiography was conducted at the BAM*line* at BESSY II, Helmholtz-Zentrum Berlin, Germany.[15] A beam energy of 17 keV was chosen for optimal beam transmission and image contrast using a double multilayer monochromator with an energy resolution of about 1.5%. A PCO4000 camera with a 4008×2672 pixel^2 CCD chip was used with optics resulting in a pixel size of 0.438 µm and a field of view (FoV) of 1.7×1.2 mm^2 (width×height). One radiographic image was acquired every 60 s at a relatively low X-Ray flux (synchrotron was operated in the single bunch mode). In order to obtain large and representative data of the de/lithiation

mechanism inside the radio-cell during dis/charge process, consecutively three different regions as marked region 1-3 in Figure S1 were characterized.

All normalized projections acquired from the *in situ* radiography are shown in the Supporting Movies (SM) and Figure S3 displays an enlarged view of the pristine state of the consecutively characterized three regions. Different de/lithiation behaviors inside the multi-Sn particles battery during dis/charge process are shown in Figure 2. We track in detail structural changes of one Sn particle (green dotted circle in Figure 2A at time 00:00) during de/lithiation, representing the class of electroactive particles' evolution as a function of the dis/charge process. The location of this particle is shown in Figure S3. As can be clearly seen from the 1st row of Figure 2A, following the first lithiation (from left to right), the sharp contour of the electrochemically active Sn particle becomes progressively blurry during which its volume increases upon further lithiation. Finally, a sudden disintegration involving multiple cracks and fragments occurs and the particle resembles cauliflower-type morphology. During the 1st delithiation process, as shown in the 2nd row in Figure 2A (from right to left), the volume decreases gradually. The 3rd row in Figure 2A shows the 2nd lithiation process of this particle. It is worthy to note that compared with the 1st lithiated state, there is a limited volume expansion during the 2nd lithiation, suggesting a limited lithium uptake capability and a resultant capacity loss during the 2nd discharge. Additional evidence for Li insertion and extraction into or from the Sn particle are the changes of the histogram of transmission values in regions containing this particle as shown in Figure 3A (includes the 1st discharge, 1st charge and 2nd discharge). The rightmost peak corresponds to the weakly absorbing carbon, binder and electrolyte, the leftmost peak corresponds to the Sn particles and the changes to the middle peaks are directly related to the electrochemical evolution of Sn particle. Following the 1st lithiation process, the peak moves progressively from left to right, implying that the Sn particle is gradually transforming from the high-density Sn phase to a low-density Li_XSn phase ($1<x<4.4$).[16] During the 1st delithiation process, we find that the peak shifts gradually towards the original direction. The present demonstrations that the de/lithiation-induced volumetric expansion/contraction by Sn lattice dislocation and plastic deformation during dis/charge process are in good agreement with previous reports.[7, 17] However, it is worth noting that, neither the peak position nor the peak shape of Sn is restored to that of the original state by the end of the 1st charge process. This may stem from the incomplete delithiation and/or a significant amount of lithium trapped in the decomposed electrolyte byproducts.[18]

2.6 Different (de)lithiation behaviors of Sn particles

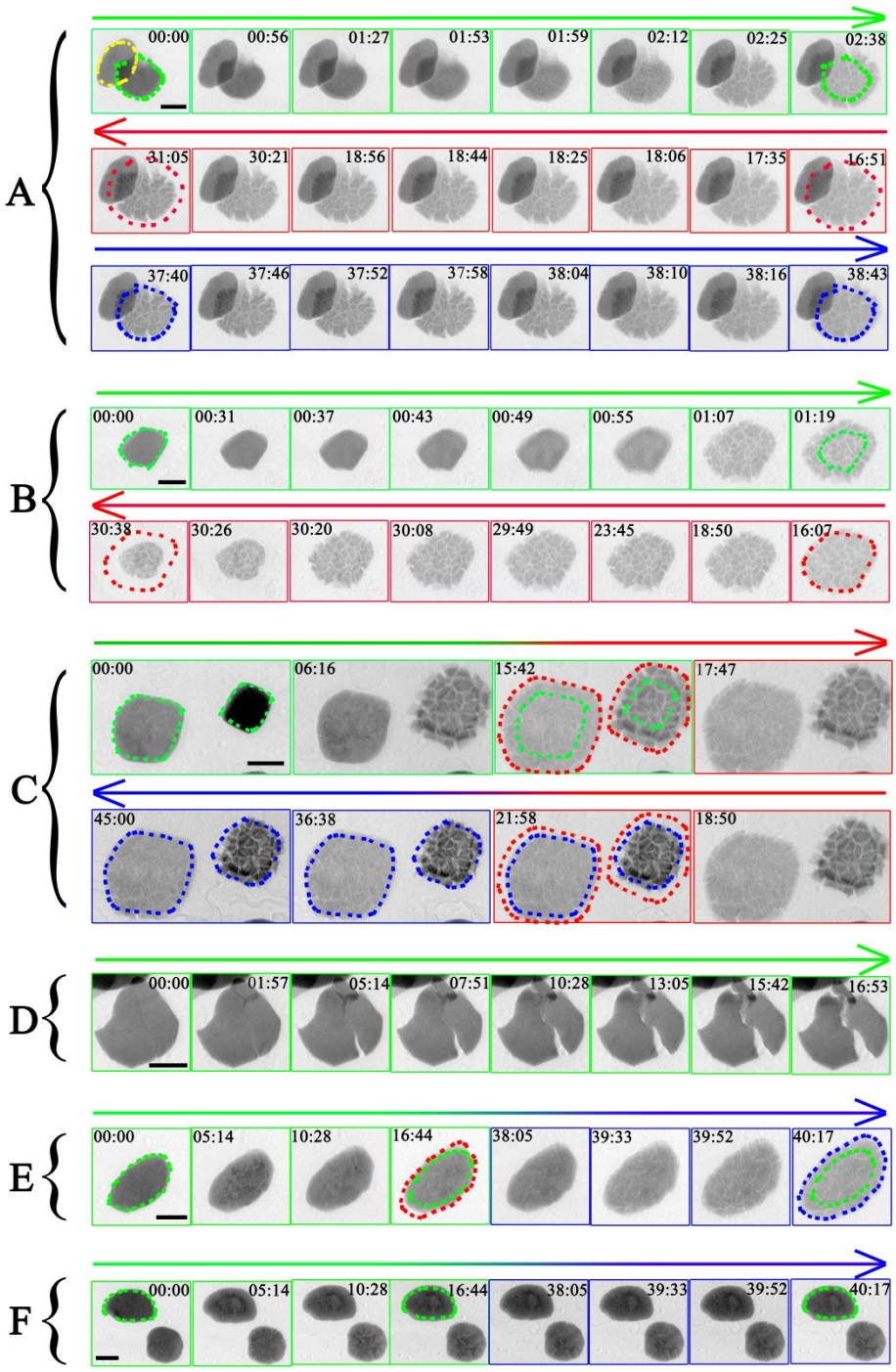

Figure 2. Demonstration of different de/lithiation behavior in the radio-cell: Panel A displays one electrochemically active and one electrochemically inactive Sn particle (green and yellow circles, respectively, in the figure labeled 00:00); Panel B shows that the time required to lithiate individual Sn particle is different from the time needed to discharge the complete battery; Panel C demonstrates the electrochemical deactivation of two Sn particles after the first cycle; Panel D shows an unexpected lithiation pathway, namely fracture instead of volume expansion occurs during first lithiation; Panel E shows one Sn particle becoming electrochemically active after the first cycle incubation period; Panel F features one Sn particle that remains electrochemically inactive after the first cycle incubation period. The locations of all the above particles are shown in Figure S3. In all figures, green rectangles mark the 1st

discharge, red rectangles 1st charge, blue rectangles the 2nd discharge. Green dots encircle particles in the pristine state, red dots refer to the 1st delithiated state, blue to the 2nd lithiated state. Arrows indicate progress in time. All the scale bars shown are 50 μm long.

Surprisingly, we have also observed that many Sn particles never undergo de/lithiation during the dis/charge processes, that is to say, they are electrochemically inactive during the whole macroscopic electrode level dis/charge process, as, for example, shown in Figure 2A where the particle encircled in yellow does not show any visible evolution. Actually, the observation of electrochemically inactive Sn particles corresponds to the previous report by Wang *et al* on $LiFeO_4$ batteries, in which it was found that some particles remain intact during the whole cycle.[19] In another study on NiO electrodes by He *et al,* it was found that not all the NiO nanosheets can be reduced even as the voltage dropped to zero against Li^+/Li.[20] These recent investigations of the locally microscopic inhomogeneous electrochemical reaction with respect to the macroscopically and electrode level electrochemical performance suggest that the electrochemically driven reactions are hardly homogeneous in a commercial LIB due to the complex electrode structure and the complicated interactions.[21] The unexpected locally inhomogeneous de/lithiation behavior amongst multiple-Sn particles could have two side effects. On the one hand, the electrochemically inactive Sn particles are believed to substantially decrease the energy density due to the inefficient utilization of loaded active materials.[22] On the other hand, the inhomogeneous electrochemical reactions suggest that the overall dis/charge current is heterogeneously distributed in the electrode, that is to say, only the electrochemically active Sn particles carry the current.[9] More specifically, we have calculated the time required to lithiate the electrochemically active Sn particle shown in Figure 2B in the 1st lithiation process to be approximately 1 h. In contrast, the time required to discharge the whole cell is approximately 15 h. The present time difference differs from a previous demonstration and the reason may stem from the different rates subjected to the electrochemical cells.[9]

2.6 Different (de)lithiation behaviors of Sn particles

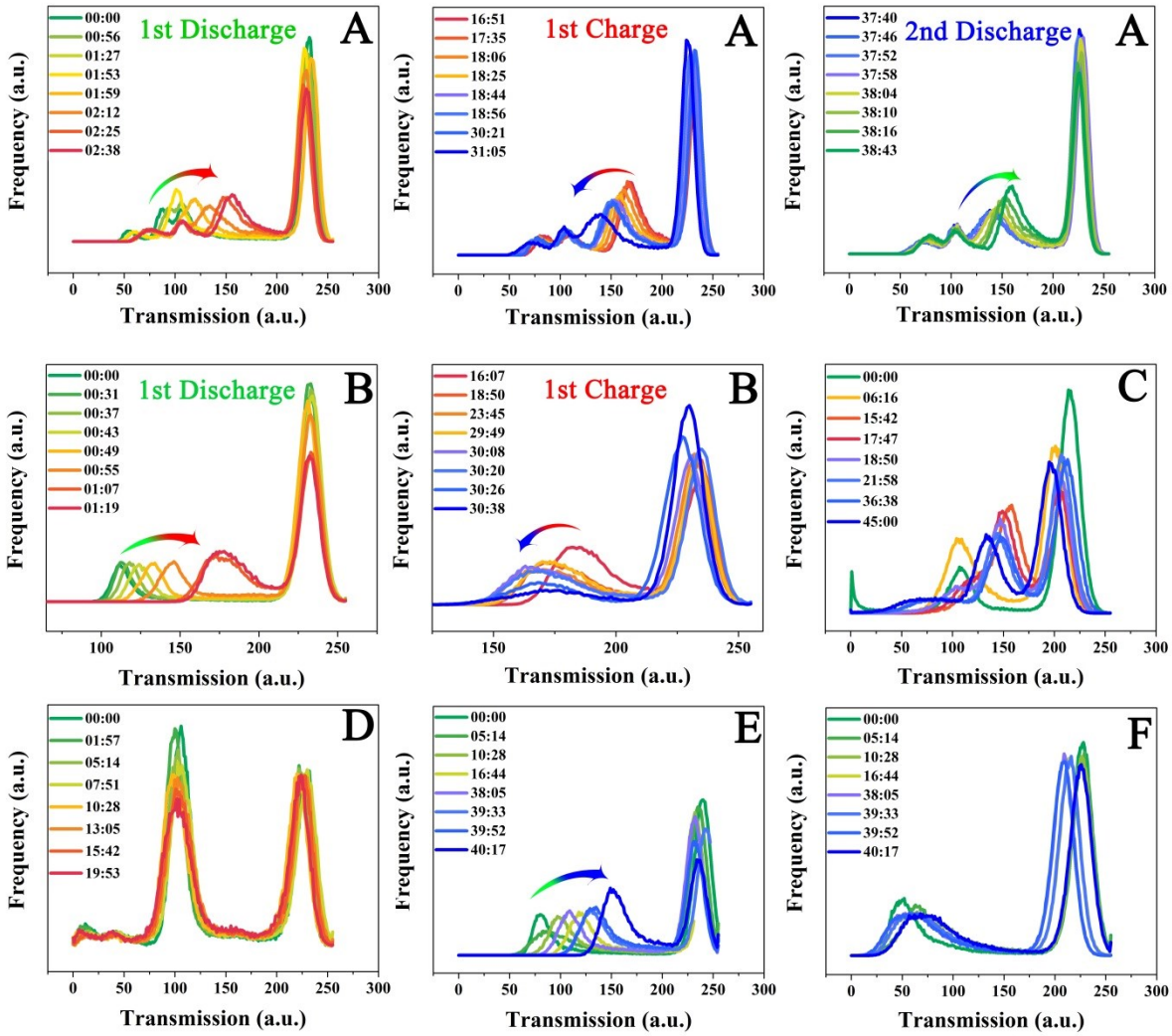

Figure 3. Transmission histograms of various regions shown in Figure 2. Color changes from green to red denote the 1st discharge, changes from red to blue the 1st charging step, changes from blue to green the 2nd discharge. Letters in each graph correspond to the letters in Figure 2 and S3.

In addition, we have also found that some Sn particles that originally participated in the de/lithiation process in the first cycle, as shown in the first row (from left to right) and the second-haft row (with time stamp 18:50 and 21:58) of Figure 2C, turned out to be electrochemically inactive during the 2nd lithiation process, as shown in the second-half row (with time stamp 36:38 and 45:00) in Figure 2C. This electrochemical deactivation process is also evident by the transmission values (barely a peak shift in the 2nd discharge, from light blue to dark blue) as shown in Figure 3C. In fact, He *et al.* proposed that the electrochemically deactivation upon silicon lithiation is caused by crystalline Li_2O, formed as a product of Li reaction with the native silicon oxide layer which partially electrically insulates the silicon particles.[23] However, as in our case, the reason may be the complex interplays between Sn particles and adjacent carbon/binder composite agents. Actually, Toney *et al.* have

experimentally discovered the electrochemical deactivation of Ge particles by *in operando* transmission X-ray microscopy and they also attribute the electrochemical deactivation process to the complex interplays between Ge particles and adjacent carbon/binder agents.[24] As clearly shown in Figure 2D, during the initial lithiation process, there is a cleavage formed in this Sn particle and compared with other electrochemically active Sn particles, this Sn particle continues to further disintegrate instead of showing a volume expansion. The underlying mechanism may be related to a partial electrical contact between this Sn particle and its adjacent carbon/binder composite. Fundamentally speaking, the lithiation process entails lithium ions and electrons simultaneously,[25] i.e., only when ionically and electronically connected to electrolyte and the electrically conducting network Sn can alloy with lithium. During the lithium uptake these electrochemically active Sn particles undergo significant volume expansion accompanied by the generation of substantial stresses[26] and the associated mechanical forces will drive local displacement and rearrangement of adjacent carbon/binder composite. Taking into account that the electron transfer between adjacent materials is based on a hopping or tunneling mechanism with a contact resistivity decaying exponentially with the gap between the contacts and that a gap of just 8-10 nm makes a contact electronically insulating,[27] it is plausible to say that the deactivation mechanism is attributed to the electric disconnection. In Figure 3D, the barely peak shifts of the disintegrated particle also suggests a limited lithiation.

Finally, we have observed that one Sn particle was partially electrochemically active in the first discharge and then turned into fully electrochemically active in the second discharge. As clearly shown in first-half row of Figure 2E, the Sn particle first undergoes a limited lithiation during the 1st lithiation step, resulting in limited volume expansion (red dot line at 16:44) and then a large volume expansion after the 2nd lithiation process (blue dot line at 40:17). This has been further demonstrated in Figure 3E, where a small peak shift from green to brawn during the 1st lithiation vs. a big peak shift from purple to blue during the 2nd lithiation. In contrast, as clearly shown in Figure 2F, another Sn particle keeps electrochemically inactive through the second discharge process and the barely shifted peaks of transmission histograms are shown in Figure 3F. Actually, He *et al.* proposed an "incubation" time to define the time required from the partial "finger" lithiation phenomenon to the fully intrinsic NiO lithiation phenomenon.[20] The incubation time observed here varies significantly from particle to particle (e.g. one particle became active after the first cycle, as show in Figure 2E; another particle might need more than one cycle to become electrochemically active, as shown in Figure 2F) and the reason may again lie in the different local environments surrounding the particles since not all Sn particles are electronically and ionically connected to electrolyte and the current collector and/or the carbon conductive network.[28] The resulting dynamic de/lithiation pathway amongst different particles can perfectly explain the previous report, in which Wang *et al.* found a monotonic specific capacity increase during cycling of a Sn/graphene half LIB.[29]

In summary, the presented study suggests that much potential benefit can be derived from experiments with electrochemical cells that can adequately simulate commercial LIBs. The firstly highlighted four cases of de/lithiation behavior in such electrochemical cells are crucially alarming because they can hardly be detected by conventional macroscopic electro-analytical or

atomic single nanowire/nanoparticle characterization techniques and should draw attentions of battery research communities. In the future, examinations of electrodes prepared with different active material loading and the use of different current rates will be conducted to further obtain insights into the underlying de/lithiation mechanisms under different conditions.

Experimental Section

Sn particles were purchased from Sigma Aldrich. Conductive carbon black, polyvinylidene difluoride (PVDF), Celgard separators and lithium metal were purchased from MTI Corp. USA. N-methyl pyrrolidone solvent (NMP) and 1M $LiPF_6$ in a volume ratio (1:1) mixture of ethylene carbonate (EC) and dimethyl carbonate (DMC) were purchased from Sigma Aldrich. Titanium (Ti) foil was acquired from ANKURO Int. GmbH, Germany. The housing of the battery is made of polyamide-imide (Torlon) from McMaster-Carr Company.

The composite electrode is made of slurries of Sn: carbon black: binder in NMP with weight ratios of 60:30:10. The slurry was cast onto a 5-μm thick titanium foil. To remove the NMP, the material cast on Ti foil was dried at 60 ℃ for 15 h. Before and after casting, the Ti foil was weighed and a mass of the electrode material of 0.4 mg determined. The cell was assembled in an argon-filled glovebox with humidity and oxygen levels below 0.1 ppm. An annular copper foil was used as a current collector and the Ti foil placed on top. Lithium disks (6 mm diameter, 1 mm thick) were used as counter and reference electrodes. A polymer separator was placed between the lithium electrode and the Sn electrode. After filling with electrolyte the cell was sealed and then taken out of the glovebox to the experimental station. Different sized Sn particles will be employed to further investigate the correlation between the de/lithiation behavior and the size effect.

Cyclic voltammetry (CV) was performed by using an Ivium CompactStat station in a potential range of 0-2.5 V. Synchrotron X-ray radiography measurements were conducted in situ throughout discharge and charge of the cell. The current was calculated only on the mass of Sn. The discharge current was set to 0.75 mA/mg and after the voltage has dropped to 0 V the current was switched to 0.0225 mA/mg. The charging current was 0.015 mA/mg. There was a cell resting after the 1st charge of the cell. Finally, during the second discharge the current was set to 0.0225 mA/mg.

The detector system comprised a 60-μm thick $CdWO_4$ scintillator, a microscopic optic and a pco4000 camera with a 4008×2672 pixel^2 CCD chip that is kept out of the direct beam by using a mirror. Radiographic images of region 1 were acquired every 60 s with 60 s exposure time. After this, regions 2 and 3 were consecutively measured. After measuring one particular region, 2 open beam images were recorded in order to normalize the acquired radiographic projections. The cell was kept discharging or charging throughout all the experiments. More information can be found in the SI.

Acknowledgements

The assistance by the beamline scientist of the BAMline, Dr. Heinrich Riesemeier, is gratefully acknowledged. We thank Norbert Beck for preparing the beamline battery. This work was sponsored by the Helmholtz-Zentrum Association and China Scholarship Council.

References

[1] Y. Takahashi, A. Kumatani, H. Munakata, H. Inomata, K. Ito, K. Ino, H. Shiku, P. R. Unwin, Y. E. Korchev, K. Kanamura, T. Matsue, *Nat Commun* **2014**, *5*, 5450-5457.
[2] B. Sun, K. Huang, X. Qi, X. Wei, J. Zhong, *Adv. Funct. Mater.* **2015**, *25*, 5633-5639.
[3] F. Sun, K. Huang, X. Qi, T. Gao, Y. Liu, X. Zou, X. Wei, J. Zhong, *Nanoscale* **2013**, *5*, 8586-8592.
[4] F. Sun, H. Markötter, I. Manke, A. Hilger, N. Kardjilov, J. Banhart, *ACS Appl. Mater. Interfaces* **2016**, DOI: 10.1021/acsami.1026b00708.
[5] J. Y. Huang, L. Zhong, C. M. Wang, J. P. Sullivan, W. Xu, L. Q. Zhang, S. X. Mao, N. S. Hudak, X. H. Liu, A. Subramanian, H. Fan, L. Qi, A. Kushima, J. Li, *Science* **2010**, *330*, 1515-1520.
[6] X. H. Liu, J. W. Wang, S. Huang, F. Fan, X. Huang, Y. Liu, S. Krylyuk, J. Yoo, S. A. Dayeh, A. V. Davydov, S. X. Mao, S. T. Picraux, S. Zhang, J. Li, T. Zhu, J. Y. Huang, *Nat Nano* **2012**, *7*, 749-756.
[7] L. Zhong, X. H. Liu, G. F. Wang, S. X. Mao, J. Y. Huang, *Phys. Rev. Lett.* **2011**, *106*, 248302-248306.
[8] M. Gu, L. R. Parent, B. L. Mehdi, R. R. Unocic, M. T. McDowell, R. L. Sacci, W. Xu, J. G. Connell, P. Xu, P. Abellan, X. Chen, Y. Zhang, D. E. Perea, J. E. Evans, L. J. Lauhon, J.-G. Zhang, J. Liu, N. D. Browning, Y. Cui, I. Arslan, C.-M. Wang, *Nano Lett.* **2013**, *13*, 6106-6112.
[9] Y. Li, F. El Gabaly, T. R. Ferguson, R. B. Smith, N. C. Bartelt, J. D. Sugar, K. R. Fenton, D. A. Cogswell, A. L. D. Kilcoyne, T. Tyliszczak, M. Z. Bazant, W. C. Chueh, *Nat. Mater.* **2014**, *13*, 1149-1156.
[10] T. R. Ferguson, M. Z. Bazant, *J. Electrochem. Soc.* **2012**, *159*, A1967-A1985.
[11] A. R. Benetti, J. Jacobsen, B. Lehnhoff, N. C. R. Momsen, D. V. Okhrimenko, M. T. F. Telling, N. Kardjilov, M. Strobl, T. Seydel, I. Manke, H. N. Bordallo, *Sci. Rep.* **2015**, *5*, 8972-8980.
[12] Z. Shen, Y. Hu, Y. Chen, X. Zhang, K. Wang, R. Chen, *J. Power Sources* **2015**, *278*, 660-667.
[13] N. Li, H. Song, H. Cui, C. Wang, *Nano Energy* **2014**, *3*, 102-112.
[14] D. S. Eastwood, V. Yufit, J. Gelb, A. Gu, R. S. Bradley, S. J. Harris, D. J. L. Brett, N. P. Brandon, P. D. Lee, P. J. Withers, P. R. Shearing, *Adv. Energy Mater.* **2014**, *4*, 1300506-1300513.
[15] I. Manke, J. Banhart, A. Haibel, A. Rack, S. Zabler, N. Kardjilov, A. Hilger, A. Melzer, H. Riesemeier, *Appl. Phys. Lett.* **2007**, *90*, 214102-214105.
[16] K. Eom, J. Jung, J. T. Lee, V. Lair, T. Joshi, S. W. Lee, Z. Lin, T. F. Fuller, *Nano Energy* **2015**, *12*, 314-321.
[17] X. Li, A. Dhanabalan, L. Gu, C. Wang, *Adv. Energy Mater.* **2012**, *2*, 238-244.
[18] S. P. V. Nadimpalli, V. A. Sethuraman, S. Dalavi, B. Lucht, M. J. Chon, V. B. Shenoy, P. R. Guduru, *J. Power Sources* **2012**, *215*, 145-151.
[19] J. Wang, Y.-c. K. Chen-Wiegart, J. Wang, *Nat Commun* **2014**, *5*, 4570-4580.
[20] K. He, H. L. Xin, K. Zhao, X. Yu, D. Nordlund, T.-C. Weng, J. Li, Y. Jiang, C. A. Cadigan, R. M. Richards, M. M. Doeff, X.-Q. Yang, E. A. Stach, J. Li, F. Lin, D. Su, *Nano Lett.* **2015**, *15*, 1437-1444.
[21] F. Lin, D. Nordlund, T.-C. Weng, Y. Zhu, C. Ban, R. M. Richards, H. L. Xin, *Nat Commun* **2014**, *5*, 3358-3367.
[22] W. Zhao, G. Luo, C.-Y. Wang, *J. Power Sources* **2014**, *257*, 70-79.
[23] Y. He, D. M. Piper, M. Gu, J. J. Travis, S. M. George, S.-H. Lee, A. Genc, L. Pullan, J. Liu, S. X. Mao, J.-G. Zhang, C. Ban, C. Wang, *ACS Nano* **2014**, *8*, 11816-11823.
[24] J. N. Weker, N. Liu, S. Misra, J. C. Andrews, Y. Cui, M. F. Toney, *Energy Environ. Sci.* **2014**, *7*, 2771-2777.

[25] U. Boesenberg, F. Meirer, Y. Liu, A. K. Shukla, R. Dell'Anna, T. Tyliszczak, G. Chen, J. C. Andrews, T. J. Richardson, R. Kostecki, J. Cabana, *Chem. Mater.* **2013**, *25*, 1664-1672.
[26] M. J. Chon, V. A. Sethuraman, A. McCormick, V. Srinivasan, P. R. Guduru, *Phys. Rev. Lett.* **2011**, *107*, 045503-045507.
[27] B. P. N. Nguyen, J. Gaubicher, B. Lestriez, *Electrochim. Acta* **2014**, *120*, 319-326.
[28] R. Malik, A. Abdellahi, G. Ceder, *J. Electrochem. Soc.* **2013**, *160*, A3179-A3197.
[29] C. Wang, Y. Li, Y.-S. Chui, Q.-H. Wu, X. Chen, W. Zhang, *Nanoscale* **2013**, *5*, 10599-10604.

2.6 Different (de)lithiation behaviors of Sn particles

2.6.1 Supplementary Information

In situ radiographic investigation of lithiation and delithiation mechanisms in a Sn-electrode lithium ion battery

Fu Sun,*[a, b] Henning Markötter, [a, b] Dong Zhou, [a, b] Saad Sabe Sulaiman Alrwashdeh, [a, b, c] Andre Hilger, [b] Nikolay Kardjilov, [b] Ingo Manke[b] and John Banhart [a, b]

[a] Fu Sun, Prof. Dr. John Banhart, Dr. Henning Markötter, Dong Zhou, Saad Sabe Sulaiman Alrwashdeh
Institute of Material Science and Technologies
Technical University Berlin
10623 Berlin, Germany
E-mail: fu.sun@helmholtz-berlin.de
john.banhart@tu-berlin.de
[b] Fu Sun, Dr. Henning Markötter, Dong Zhou, Saad Sabe Sulaiman Alrwashdeh, Dr. Andre Hilger, Dr. Nikolay Kardjilov, Dr. Ingo Manke and Prof. Dr. John Banhart
Helmholtz Centre Berlin for Materials and Energy
Hahn-Meitner-Platz 1
14109 Berlin, Germany
[c] Saad Sabe Alrwashdeh
Mechanical Engineering Department
Faculty of Engineering, Mu'tah University
P.O Box 7, Al-Karak 61710 Jordan

Data processing

For the normalization (N) of X-ray radiography (R), flat field (FF, without samples) and dark field images (DF, without beam) are used. The normalization process is expressed by:

$$\mathrm{N} = \frac{R - DF}{FF - DF}$$

and conducted by ImageJ.
The originally obtained radiographies are 4008 x 2627 pixels in size. For the movie, we have used Bilinear Interpolation to reduce the size. The repetition frequency of the image series is 15 fps.

Battery information

In a normal electrode, the weight ratios of active material:conductive agent:binder agent is usually set to 80:10:10[1]. In the present investigation, in order to reduce possible particle overlapping in the radiographs, a weight ratio of Sn:Carbon:Binder of 60:30:10 was used. From Figure S1 and Figure S3, we can see that the individual Sn particles can be clearly separated from one to another, thus facilitating our investigations.
The cyclic voltammetry (CV) diagram of the radio-cell is shown in Figure S2b. The cathodic peaks at around 1.0 and 0.5 V of the first scan are caused by the formation of solid electrolyte interface (SEI)[2], and the peak at 0V is due to the Li-Sn alloying reaction[2]. The anodic peaks at around 0.25V and 0.6V are due to the de-alloying of Li-Sn and the decomposition of the electrolyte, respectively[3].
SI Figure 3 shows the locations of different Sn particles displayed in Figure 2. Specifically, the electrochemically active particle is located in location A in SI Figure 3; the particle which is shown to have different lithiation time with relation to the whole battery discharge time is located in location B in SI Figure 3; the particles show electrochemically de-active processes after the first cycle are located in location C in SI Figure 3; the particle shows cleavage is located in location D in SI Figure 3; the incubation-active particle is located in location E in SI Figure 3, the incubation-inactive particles are located in location F in SI Figure 3.

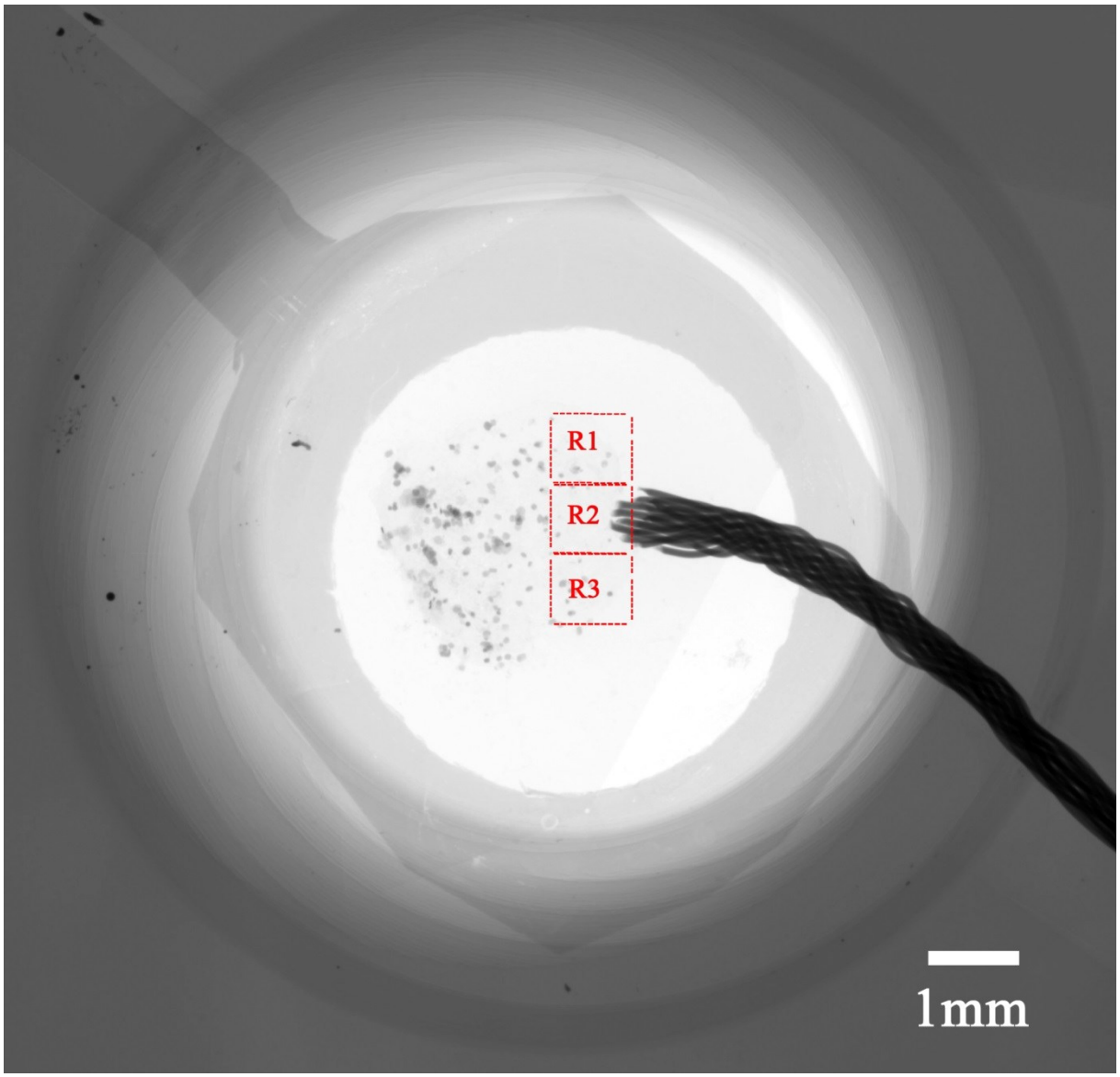

Figure S1. A projection image of the Li electrode/separator/Sn electrode assembly within the radio-cell characterized by a laboratory micro X-ray source after synchrotron X-ray measurement. The radio-cell is arranged coaxially to the beam throughout radiography. Region 1 (R1) is the region that firstly measured, after which regions R2 and R3 were acquired. The acquired images of these three images from synchrotron X-ray were composed to one image, as shown in Figure S3. Note that due to the low X-ray absorption of the radio-cell, housing, lithium electrode, separator and titanium foil are nearly invisible, only the Sn particles, the annular copper current collector and the copper wire are visible.

2.6 Different (de)lithiation behaviors of Sn particles

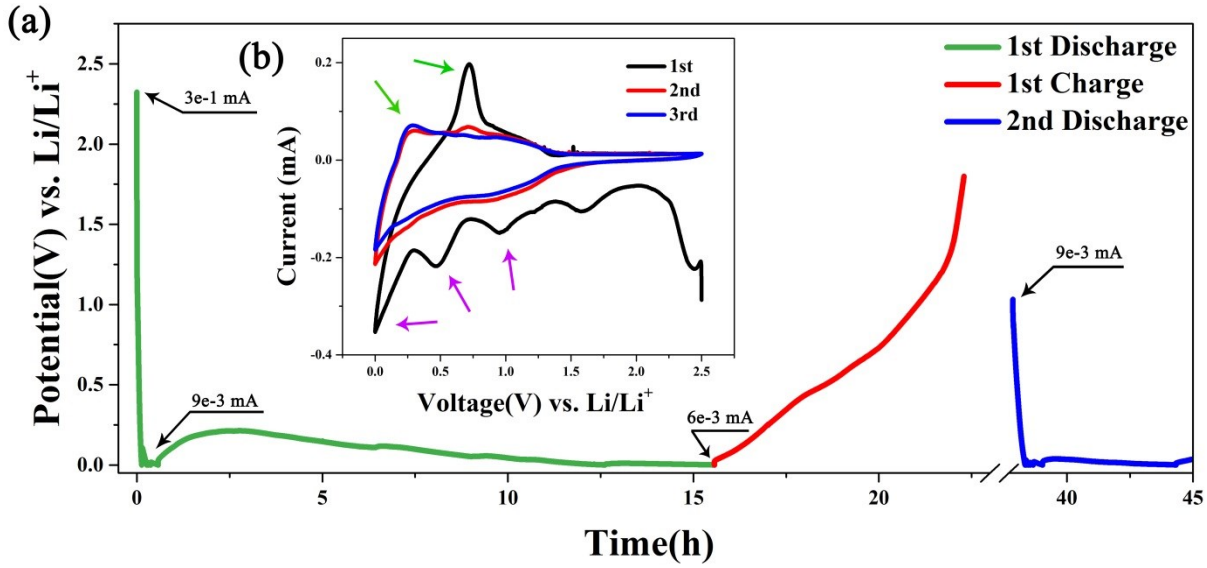

Figure S2. Electrochemical characterization of the battery: a) Discharge and charge curves of the cell. Inset figure (b): cyclic voltammetry (CV) curves scanned at 1 mV s^{-1} in the potential window 0-2.5V. Purple arrows point at the cathodic peaks, green arrows point the anodic peaks.

2.6 Different (de)lithiation behaviors of Sn particles

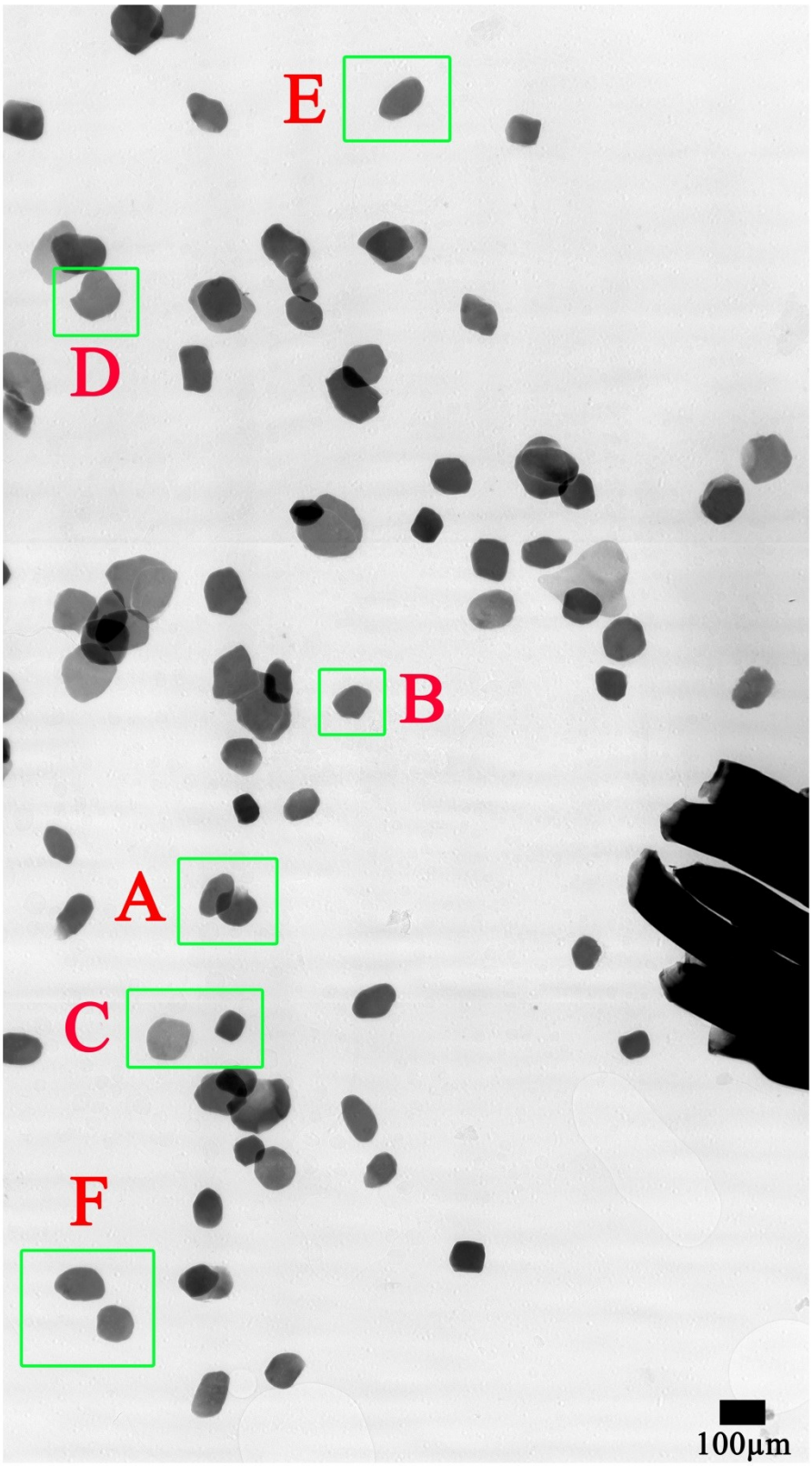

Figure S3. Locations of the particles in the electrode in the pristine state shown in Figure 2 in the main text. A: electrochemically active particles, B: particle whose lithiation time is different from the whole battery's discharge time, C: deactivated particles, D: particle hat has formed a cleavage, E: active particle after incubation, F: inactive particle after incubation.

Captions for Supplementary Movies

http://onlinelibrary.wiley.com/wol1/doi/10.1002/cssc.201600220/abstract

Position_1-Movie

Position_2-Movie

Position_3-Movie

Reference

[1] H. Qiao, K. Chen, L. Luo, Y. Fei, R. Cui, Q. Wei, *Electrochimica Acta* **2015**, *165*, 149-154.
[2] N. Li, H. Song, H. Cui, C. Wang, *Nano Energy* **2014**, *3*, 102-112.
[3] Z. Shen, Y. Hu, Y. Chen, X. Zhang, K. Wang, R. Chen, *J. Power Sources* **2015**, *278*, 660-667.

3 Summary

The direct observation of the evolution of electrochemically stripped/plated LmSs presented in section 2.1 shed new lights on a range of processes that previously have not been acknowledged or barely considered. Firstly, the proposed mechanism of LmS evolution can explain the origin of the electrochemically generated PLI (Porous Lithium Interface) that grows towards the Li bulk electrode. Based on our observations, both the electrochemical dissolution of the initial Li bulk electrodes and the following electrochemical deposition of nascent LmSs contribute to the inward growth of the PLI. Secondly, the evaluation using Coulombic efficiency to investigate the cycling efficiency of Li in Li symmetrical cells is compromised by the electrochemically inert LmSs. According to our observations, a significant amount of Li is stripped from the initial Li bulk instead from the generated nascent (electrochemically inactive) LmSs to compensate for the depletion of Li ions in the electrolyte used to be plated. Thirdly, concerns about using Li metal as a standard counter electrode for the evaluation of the performance of new battery materials using half-cells are raised. In fact, it has been confirmed that the PLI, which continuously grows in each cycle, can markedly increase the inner cell resistance and is the actual origin of the onset of cell degradation and failure. Finally, considering that the dissolution of the initial Li bulk electrodes and the deposition of nascent LmSs (necessitated by the charge transfer within cells) remain intrinsic and unavoidable, the present results suggest that novel fundamental strategies that involve direct engineering of Li electrodes are desirable and necessary. For example, strategies such as introducing surface patterns to Li electrodes to direct and control Li deposition, replacing conventional Li foil electrodes by organic-coated Li powder or employing different substrates to selectively deposit and then encapsulate the LmS, appear more suitable than conventional mechanical suppression or formation of protective passivation layers.

As shown in section 2.2, trilayer Celgard® 2325 separators can deform significantly and can be pushed into the large cavity within the Li anode by the LmSs growing from the Li cathode. In addition, the strong mechanical stress exerted by the growing LmSs causes delamination of the separator into its three native layers. According to the manufacturer, the Celgard® separator has a high mechanical strength (in terms of tensile strength along both the machine direction (MD) and the transverse direction (TD)) and puncture strength. Specifically, the trilayer Celgard® 2325 separator possesses a tensile strength along MD and TD direction of 1900 and 135 kg/cm^{-2}, respectively, and a puncture strength of 300 g/cm^{-2}. From the direct internal view of the electrochemically short-circuited cell, one can safely conclude that considerable force caused by the growing LmSs was generated during their formation. Finally, it is clearly observed that the PE layer can be melted during penetration of the LmS. Once the LmS has pierced through the separator and induced a short circuit, the overall cell current is concentrated on the penetration location, leading to a localized very high current density. It has been simulated that such a high current could induce a large localized Joule heating (~108 $W\ m^{-3}$) and result in the melting of the trilayer Celgard® 2325 separator.

3 Summary

Section 2.3 presents a detailed study of gas evolution within an operating LIB. By employing synchrotron X-ray imaging, the gas and channel evolution occurring in an operating LIB have been directly visualized in their inherent 3D state as a function of discharge and charge. In addition, using the spatial 3D distribution of gas voids and channels, the active particles that dictate the performance of a functional LIB were identified and visualized in 3D. Meanwhile, delithiation and lithiation are interpreted as the process of activating particles continuously in a step-by-step way. The present work not only demonstrates the generation and evolution of gas within LIBs in 3D, but also reveals the distribution of active particles. The current study connects the gas bubble or channel evolution with the evolution of effectively or potentially active particles in a functional LIB. This opens new perspectives in optimizing the overall performance of a battery. From the viewpoint of electrode engineering, it is important to find optimal battery operating conditions or to develop new materials with reduced gas formation. It is also crucial to optimize the electrode architecture to significantly increase the population of active particles to sustain overall galvanostatic current and at the same time to improve the homogeneity of distribution of active particles to prevent extent of shocks and fractures induced by high local currents. From the perspective of numerical simulation, it is important to identify the impact of SEI (solid electrolyte interface) formation with the associated gas release within electrodes on the transport properties of Li ions and cycling performance of LIBs during discharge and charge. Altogether, the three dimensional microscale investigations of gas in the present study contribute to the understanding of the complex discharge and charge processes.

Section 2.4 presents potential mechanisms of dynamic deterioration of Si anode LIBs on an electrode scale by employing laboratory X-ray imaging tomography and radiography and highlights that, apart from the significant volume expansion-induced pulverization and electric disconnection from current collectors, electrochemical “deactivation” contributes significantly to the capacity loss during the first charge process. In addition, the presence of a notable number of electrochemically inactive Si particles is also believed to substantially decrease energy density due to the inefficient utilization of loaded active materials. These observations are helpful for future battery design. From an electrode engineer’s point of view, the optimization electrode architecture engineering is crucially important. On the one hand, in addition to focusing only on individual particle features, more and more efforts should be put in optimizing the entire electrode architecture, which can involve all active material particles ionically and electronically connecting to the electrolyte and electric conducting network to maximize the utilization of active materials. On the other hand, new conductive/binder agents are highly needed. The matrix of carbon/binder is supposed to sustain the active material’s expansion/contraction during cycles as well as to provide an efficient dynamic electric/ionic conducting pathway even under significant electrode transformation. From a simulation expert’s point of view, in order to develop an electrochemical model that can be used to gain insight into internal processes, to predict performance and operation and optimize cell design, the homogeneous and flawless idealized microstructure characteristics should be compromised with the real complex composite electrodes.

3 Summary

Section 2.5 presents an in-depth investigation on the same Si composite electrode before and after the first discharge by employing in situ synchrotron X-ray tomography. It is found that i) on the electrode level, the Si particles located in the central part of the electrode preferentially experience crack formation; ii) on the individual particle level, heterogeneous electrochemical lithiation is observed; iii) cavities are formed during electrode preparation and battery operation. Moreover, the correlation between the electrochemical activities of Si particles and their individual electrical contact to the electron conducting network is investigated. It is quantified that Si particles will experience lithiation only under the condition that at least 40% of their surface is electrically connected. These results show that synchrotron X-ray tomography is a powerful characterization tool to quantitatively investigate the dependence of the electrochemical performance of LIBs on the electrical contact between active materials and conducting network. The novel insights into possible causes for the lower capacity/energy density of LIBs are crucial because they cannot be easily obtained by conventional macroscopic electroanalytical characterization techniques. These results suggest an efficient electrically conducting CBD network and an ionically well-conducting pore space and are highly useful to eliminate the observed electrochemically in-active material.

The lithiation and delithiation mechanisms of multiple Sn particles in a customized flat radiography cell were investigated by in situ synchrotron radiography and the results are shown in section 2.6. Four hitherto unknown de/lithiation phenomena in a Sn-electrode battery system are highlighted: 1 The de/lithiation behavior varies between different Sn particles; 2 The time required to lithiate individual Sn particles is markedly different from the time needed to discharge the complete battery; 3 Electrochemical deactivation of originally electrochemically active particles is reported; 4 A change of electrochemical behavior of individual particles during cycling is found and explained by dynamic changes of de/lithiation pathways amongst particles within the electrode. The highlighted four cases of de/lithiation behavior in such electrochemical cells can raise serious concerns because they can hardly be detected by conventional macroscopic electro-analytical or atomic single nanowire/nanoparticle characterization techniques and should attract attention of the battery research community. In the future, examinations of electrodes prepared with different active material loadings and the use of different current rates will be conducted to further obtain insights into the underlying de/lithiation mechanisms under different conditions.

4 Outlook

From the electrode point of view, sulfur (S) is currently considered to be one of the most interesting cathodes for future mobile and stationary applications due to its inherently high energy density and its abundance. During last few years research activities either in industry or scientific laboratories on S composite electrodes for LIBs have increased significantly. The number of publications in this field has increased by more than one order of magnitude during last two decades. Unfortunately, a major obstacle for battery systems based on S composite electrodes is the inevitable electrode microstructure degradation which can seriously influence battery performance and lifetime. Understanding and avoiding degradation phenomena in electrochemical systems is a fundamental research influencing many systems including S-based electrode batteries. Unfortunately, there is no adequate set of tools to quantitatively characterize and predict degradation phenomena.

Meanwhile, using solid electrolytes in S-based electrode batteries can break the standard of conventional S-based LIBs. It has been suggested that replacing the flammable organic liquid electrolyte by a non-flammable solid-state electrolyte would improve device safety tremendously. As for S-based LIBs, the electrolyte-changing shift from liquid to solid electrolytes will fundamentally eliminate the polysulfide shuttle effect and enable a stable cycling performance. With the emergence of solid electrolytes with ionic conductivities comparable to those of liquid electrolyte, all-solid-state LIBs based on S are proposed to be the next breakthrough for energy storage. However, the build-up of inner resistance between the solid state S composite electrode and the solid state electrolyte during cycling can lead to ultimate battery degradation. Unfortunately, no fundamental investigation regarding the relation of S-based electrode and the evolution of the interface between the S-based electrode and the solid state electrolyte has been reported.

Based on the investigations we have already accomplished and investigations based on X-ray imaging the degradation mechanisms in S-based electrode LIBs (using either liquid electrolyte or solid electrolyte) is planned. In-operando characterizations can also be conducted to directly track the morphological evolution of S-based electrodes during lithium insertion and extraction due to the advanced X-ray radiographic techniques available. Furthermore, X-ray tomography enables us to obtain the evolution of entire electrodes non-destructively and in three-dimension (3D).

5 Acknowledgements

I would like to thank my advisor Prof. John Banhart for providing an opportunity for me to pursue my Ph.D. at the Technische Universität Berlin and the Helmholtz Zentrum Berlin. I would like to also thank Dr. Ingo Manke, who has always supported my ideas and helped me in all possible ways to explore them. In addition, I would like to take this opportunity to thank Dr. Henning Markötter, Dr. André Hilger, Dr. Nikolay Kardjilov, Dr. Tobias Arlt, Dong Zhou, Kang Dong, Christiane Förster and Norbert Beck for providing valuable help during my experiments. Also, I would like to take this opportunity to thank Lukas Zielke, Riko Moroni, Dr. Simon Thiele and Prof. Roland Zengerle for helping analyzing my datasets.

I would like to thank China Scholarship Council for providing me financial support.

At last, I would like to convey my deepest gratitude to my parents. Without their persistent efforts and accompanies, enormous sacrifice and love, it would have been impossible for me to go so far.

6 References

[1] A. Yoshino, The birth of the lithium-ion battery, Angewandte Chemie International Edition 51 (2012) 5798-5800.
[2] J.M. Tarascon, M. Armand, Issues and challenges facing rechargeable lithium batteries, Nature 414 (2001) 359-367.
[3] J.M. Tarascon, Key challenges in future li-battery research, Philosophical Transactions of the Royal Society of London A: Mathematical, Physical and Engineering Sciences 368 (2010) 3227-3241.
[4] V. Etacheri, R. Marom, R. Elazari, G. Salitra, D. Aurbach, Challenges in the development of advanced li-ion batteries: A review, Energy & Environmental Science 4 (2011) 3243-3262.
[5] D. Deng, Li-ion batteries: Basics, progress, and challenges, Energy Science & Engineering 3 (2015) 385-418.
[6] B. Scrosati, J. Garche, Lithium batteries: Status, prospects and future, Journal of Power Sources 195 (2010) 2419-2430.
[7] J.B. Goodenough, K.-S. Park, The li-ion rechargeable battery: A perspective, Journal of the American Chemical Society 135 (2013) 1167-1176.
[8] G. Jian, S. Si-Qi, L. Hong, Brief overview of electrochemical potential in lithium ion batteries, Chinese Physics B 25 (2016) 018210.
[9] A. Van der Ven, J. Bhattacharya, A.A. Belak, Understanding li diffusion in li-intercalation compounds, Accounts of Chemical Research 46 (2013) 1216-1225.
[10] C.-X. Zu, H. Li, Thermodynamic analysis on energy densities of batteries, Energy & Environmental Science 4 (2011) 2614-2624.
[11] Y.-U. Kim, C.K. Lee, H.-J. Sohn, T. Kang, Reaction mechanism of tin phosphide anode by mechanochemical method for lithium secondary batteries, Journal of The Electrochemical Society 151 (2004) A933-A937.
[12] J. Motavalli, Technology: A solid future, Nature 526 (2015) S96-S97.
[13] M.S. Whittingham, Lithium batteries and cathode materials, Chemical Reviews 104 (2004) 4271-4302.
[14] J.W. Fergus, Recent developments in cathode materials for lithium ion batteries, Journal of Power Sources 195 (2010) 939-954.
[15] J.B. Goodenough, Y. Kim, Challenges for rechargeable li batteries, Chemistry of Materials 22 (2010) 587-603.
[16] M.R. Palacin, Recent advances in rechargeable battery materials: A chemist's perspective, Chemical Society Reviews 38 (2009) 2565-2575.
[17] W. Kong, H. Li, X. Huang, L. Chen, Gas evolution behaviors for several cathode materials in lithium-ion batteries, Journal of Power Sources 142 (2005) 285-291.
[18] K. Kumai, H. Miyashiro, Y. Kobayashi, K. Takei, R. Ishikawa, Gas generation mechanism due to electrolyte decomposition in commercial lithium-ion cell, Journal of Power Sources 81–82 (1999) 715-719.
[19] K.W. Schroder, H. Celio, L.J. Webb, K.J. Stevenson, Examining solid electrolyte interphase formation on crystalline silicon electrodes: Influence of electrochemical preparation and ambient exposure conditions, The Journal of Physical Chemistry C 116 (2012) 19737-19747.
[20] D. Goers, M. Holzapfel, W. Scheifele, E. Lehmann, P. Vontobel, P. Novák, In situ neutron radiography of lithium-ion batteries: The gas evolution on graphite electrodes during the charging, Journal of Power Sources 130 (2004) 221-226.

6 References

[21] F. Sun, H. Markötter, I. Manke, A. Hilger, N. Kardjilov, J. Banhart, Three-dimensional visualization of gas evolution and channel formation inside a lithium-ion battery, ACS Applied Materials & Interfaces 8 (2016) 7156-7164.
[22] Y. Kim, Mechanism of gas evolution from the cathode of lithium-ion batteries at the initial stage of high-temperature storage, Journal of Materials Science 48 (2013) 8547-8551.
[23] V.A. Agubra, J.W. Fergus, The formation and stability of the solid electrolyte interface on the graphite anode, Journal of Power Sources 268 (2014) 153-162.
[24] R. Marom, S.F. Amalraj, N. Leifer, D. Jacob, D. Aurbach, A review of advanced and practical lithium battery materials, Journal of Materials Chemistry 21 (2011) 9938-9954.
[25] F. Sun, K. Huang, Y. Liu, T. Gao, Y. Han, J. Zhong, Hierarchical structure of co3o4 nanoparticles on si nanowires array films for lithium-ion battery applications, Applied Surface Science 266 (2013) 300-305.
[26] W.-J. Zhang, A review of the electrochemical performance of alloy anodes for lithium-ion batteries, Journal of Power Sources 196 (2011) 13-24.
[27] R. Malini, U. Uma, T. Sheela, M. Ganesan, N.G. Renganathan, Conversion reactions: A new pathway to realise energy in lithium-ion battery—review, Ionics 15 (2009) 301-307.
[28] H. Kim, G. Jeong, Y.-U. Kim, J.-H. Kim, C.-M. Park, H.-J. Sohn, Metallic anodes for next generation secondary batteries, Chemical Society Reviews 42 (2013) 9011-9034.
[29] H. Ikeda, Saito, T. & Tamura, H., Proc. Manganese Dioxide Symp. Vol. 1 (1975) IC sample Office, Cleveland, OH.
[30] M.S. WHITTINGHAM, Electrical energy storage and intercalation chemistry, Science 192 (1976) 1126-1127.
[31] A. Jana, D.R. Ely, R.E. García, Dendrite-separator interactions in lithium-based batteries, Journal of Power Sources 275 (2015) 912-921.
[32] W. Xu, J. Wang, F. Ding, X. Chen, E. Nasybulin, Y. Zhang, J.-G. Zhang, Lithium metal anodes for rechargeable batteries, Energy & Environmental Science 7 (2014) 513-537.
[33] M. Mohri, N. Yanagisawa, Y. Tajima, H. Tanaka, T. Mitate, S. Nakajima, M. Yoshida, Y. Yoshimoto, T. Suzuki, H. Wada, 4th international meetings on lithium batteriesrechargeable lithium battery based on pyrolytic carbon as a negative electrode, Journal of Power Sources 26 (1989) 545-551.
[34] J. Steiger, D. Kramer, R. Mönig, Mechanisms of dendritic growth investigated by in situ light microscopy during electrodeposition and dissolution of lithium, Journal of Power Sources 261 (2014) 112-119.
[35] Y.S. Cohen, Y. Cohen, D. Aurbach, Micromorphological studies of lithium electrodes in alkyl carbonate solutions using in situ atomic force microscopy, The Journal of Physical Chemistry B 104 (2000) 12282-12291.
[36] M. Dollé, L. Sannier, B. Beaudoin, M. Trentin, J.-M. Tarascon, Live scanning electron microscope observations of dendritic growth in lithium/polymer cells, Electrochemical and Solid-State Letters 5 (2002) A286-A289.
[37] A.J. Leenheer, K.L. Jungjohann, K.R. Zavadil, J.P. Sullivan, C.T. Harris, Lithium electrodeposition dynamics in aprotic electrolyte observed in situ via transmission electron microscopy, ACS Nano 9 (2015) 4379-4389.
[38] R. Bhattacharyya, B. Key, H. Chen, A.S. Best, A.F. Hollenkamp, C.P. Grey, In situ nmr observation of the formation of metallic lithium microstructures in lithium batteries, Nat Mater 9 (2010) 504-510.
[39] S. Chandrashekar, N.M. Trease, H.J. Chang, L.-S. Du, C.P. Grey, A. Jerschow, 7li mri of li batteries reveals location of microstructural lithium, Nat Mater 11 (2012) 311-315.

6 References

[40] D. Aurbach, Review of selected electrode–solution interactions which determine the performance of li and li ion batteries, Journal of Power Sources 89 (2000) 206-218.
[41] Z.-i. Takehara, Future prospects of the lithium metal anode, Journal of Power Sources 68 (1997) 82-86.
[42] F.B. Dias, L. Plomp, J.B.J. Veldhuis, Trends in polymer electrolytes for secondary lithium batteries, Journal of Power Sources 88 (2000) 169-191.
[43] A. Zhamu, G. Chen, C. Liu, D. Neff, Q. Fang, Z. Yu, W. Xiong, Y. Wang, X. Wang, B.Z. Jang, Reviving rechargeable lithium metal batteries: Enabling next-generation high-energy and high-power cells, Energy & Environmental Science 5 (2012) 5701-5707.
[44] A.N. Dey, Electrochemical alloying of lithium in organic electrolytes, Journal of The Electrochemical Society 118 (1971) 1547-1549.
[45] F. Sun, K. Huang, X. Qi, T. Gao, Y. Liu, X. Zou, X. Wei, J. Zhong, A rationally designed composite of alternating strata of si nanoparticles and graphene: A high-performance lithium-ion battery anode, Nanoscale 5 (2013) 8586-8592.
[46] X. Su, Q. Wu, J. Li, X. Xiao, A. Lott, W. Lu, B.W. Sheldon, J. Wu, Silicon-based nanomaterials for lithium-ion batteries: A review, Advanced Energy Materials 4 (2014) n/a-n/a.
[47] P. Limthongkul, Y.-I. Jang, N.J. Dudney, Y.-M. Chiang, Electrochemically-driven solid-state amorphization in lithium-silicon alloys and implications for lithium storage, Acta Materialia 51 (2003) 1103-1113.
[48] S. Goriparti, E. Miele, F. De Angelis, E. Di Fabrizio, R. Proietti Zaccaria, C. Capiglia, Review on recent progress of nanostructured anode materials for li-ion batteries, Journal of Power Sources 257 (2014) 421-443.
[49] D. Ma, Z. Cao, A. Hu, Si-based anode materials for li-ion batteries: A mini review, Nano-Micro Letters 6 (2014) 347-358.
[50] C. Du, M. Chen, L. Wang, G. Yin, Covalently-functionalizing synthesis of si@c core-shell nanocomposites as high-capacity anode materials for lithium-ion batteries, Journal of Materials Chemistry 21 (2011) 15692-15697.
[51] H. Wu, G. Chan, J.W. Choi, I. Ryu, Y. Yao, M.T. McDowell, S.W. Lee, A. Jackson, Y. Yang, L. Hu, Y. Cui, Stable cycling of double-walled silicon nanotube battery anodes through solid-electrolyte interphase control, Nat Nano 7 (2012) 310-315.
[52] Y. Yu, L. Gu, C. Wang, A. Dhanabalan, P.A. van Aken, J. Maier, Encapsulation of sn@carbon nanoparticles in bamboo-like hollow carbon nanofibers as an anode material in lithium-based batteries, Angewandte Chemie International Edition 48 (2009) 6485-6489.
[53] J. Qin, C. He, N. Zhao, Z. Wang, C. Shi, E.-Z. Liu, J. Li, Graphene networks anchored with sn@graphene as lithium ion battery anode, ACS Nano 8 (2014) 1728-1738.
[54] N. Li, H. Song, H. Cui, G. Yang, C. Wang, Self-assembled growth of sn@cnts on vertically aligned graphene for binder-free high li-storage and excellent stability, Journal of Materials Chemistry A 2 (2014) 2526-2537.
[55] W. Li, R. Yang, J. Zheng, X. Li, Tandem plasma reactions for sn/c composites with tunable structure and high reversible lithium storage capacity, Nano Energy 2 (2013) 1314-1321.
[56] M. Winter, J.O. Besenhard, Electrochemical lithiation of tin and tin-based intermetallics and composites, Electrochimica Acta 45 (1999) 31-50.
[57] S.S. Zhang, A review on the separators of liquid electrolyte li-ion batteries, Journal of Power Sources 164 (2007) 351-364.
[58] P. Arora, Z. Zhang, Battery separators, Chemical Reviews 104 (2004) 4419-4462.
[59] V. Deimede, C. Elmasides, Separators for lithium-ion batteries: A review on the production processes and recent developments, Energy Technology 3 (2015) 453-468.

6 References

[60] H. Lee, M. Yanilmaz, O. Toprakci, K. Fu, X. Zhang, A review of recent developments in membrane separators for rechargeable lithium-ion batteries, Energy & Environmental Science 7 (2014) 3857-3886.
[61] Z. Li, J. Huang, B. Yann Liaw, V. Metzler, J. Zhang, A review of lithium deposition in lithium-ion and lithium metal secondary batteries, Journal of Power Sources 254 (2014) 168-182.
[62] H.A. Bale, A. Haboub, A.A. Macdowell, J.R. Nasiatka, D.Y. Parkinson, B.N. Cox, D.B. Marshall, R.O. Ritchie, Real-time quantitative imaging of failure events in materials under load at temperatures above 1,600°c, Nature Materials 12 (2013) 40-46.
[63] J. Moosmann, A. Ershov, V. Weinhardt, T. Baumbach, M.S. Prasad, C. LaBonne, X. Xiao, J. Kashef, R. Hofmann, Time-lapse x-ray phase-contrast microtomography for in vivo imaging and analysis of morphogenesis, Nat. Protocols 9 (2014) 294-304.
[64] F. Sun, H. Markötter, D. Zhou, S.S.S. Alrwashdeh, A. Hilger, N. Kardjilov, I. Manke, J. Banhart, In situ radiographic investigation of (de)lithiation mechanisms in a tin-electrode lithium-ion battery, ChemSusChem 9 (2016) 946-950.
[65] M. Ebner, F. Marone, M. Stampanoni, V. Wood, Visualization and quantification of electrochemical and mechanical degradation in li ion batteries, Science 342 (2013) 716-720.